

NON-THERMAL FIXED POINTS AND
SUPERFLUID TURBULENCE
IN ULTRACOLD QUANTUM GASES

Boris Nowak

Dissertation
Fakultät für Physik und Astronomie
Universität Heidelberg
2012

Inaugural-Dissertation zur
Erlangung der Doktorwürde der
Naturwissenschaftlich-Mathematischen Gesamtfakultät der
Ruprecht-Karls-Universität Heidelberg

vorgelegt von
Dipl.-Phys. Boris Nowak
aus Dieburg

Tag der mündlichen Prüfung: 05.12.2012

NON-THERMAL FIXED POINTS AND
SUPERFLUID TURBULENCE
IN ULTRACOLD QUANTUM GASES

Gutachter: Prof. Dr. Thomas Gasenzer
Prof. Dr. Markus Oberthaler

Nicht-thermische Fixpunkte und superfluide Turbulenz in ultrakalten Quantengasen

In der vorliegenden Arbeit wird die Nicht-Gleichgewichts-Dynamik ultrakalter Quantengase numerisch und analytisch in ein, zwei und drei Raumdimensionen studiert. Der Schwerpunkt liegt auf dem Bereich hoher Besetzungszahlen, in welchem das System durch ein Ensemble nichtlinearer Wellen beschrieben werden kann. Ein Ziel dieser Arbeit ist es die Existenz von nicht-thermischen Fixpunkten in der Dynamik ultrakalter Bose-Gase zu untersuchen. Es wird gezeigt, dass ein zwei- oder dreidimensionales Bose-Gas einen nicht-thermischen Fixpunkt besitzt, der durch einen verdünnten Zustand zufällig verteilter Wirbel oder Wirbellinien gekennzeichnet ist. Dieser Zustand ist durch Teilchen- und Energieflüsse gekennzeichnet und zerfällt unter Bildung von Wirbel-Antiwirbel-Korrelationen. Unter Verwendung von Methoden für die Beschreibung suprafluider Turbulenz führen wir eine detaillierte Analyse der zugrundeliegenden Wirbel-Dynamik durch. Weiterhin untersuchen wir die Bedeutung des nicht-thermischen Fixpunktes für den Prozess der Phasenordnung und der Bose-Einstein-Kondensation, sowie die Möglichkeit eines nicht-thermischen Fixpunktes in einem eindimensionalen ultrakalten Bose-Gas. Darauf aufbauend diskutieren wir die Realisierung eines nicht-thermischen Fixpunktes, sowohl in einer relativistischen skalaren Theorie, als auch in einem zwei-komponentigen Bose-Gas in zwei Raumdimensionen. Nach einer kurzen Diskussion möglicher Experimente geben wir eine Zusammenfassung der Ergebnisse und schließen mit einem Ausblick.

Non-thermal fixed points and superfluid turbulence in ultracold quantum gases

In this thesis the non-equilibrium dynamics of ultracold quantum gases is studied numerically and analytically in one, two, and three spatial dimensions. We focus on the regime of large occupation numbers, where the system can be described by an ensemble of non-linear waves. A goal of this work is to investigate the existence of non-thermal fixed points in the dynamics of ultracold Bose gases. It is shown that a two- or three-dimensional Bose gas features a non-thermal fixed point which is characterised by a dilute random distribution of vortices or vortex lines. This state is accompanied by particle and energy fluxes and decays via the formation of vortex-antivortex correlations. By making use of superfluid turbulence methods, we give a detailed analysis of the underlying vortex dynamics. Furthermore, we focus on the relevance of the non-thermal fixed point for the dynamics of phase ordering kinetics and Bose-Einstein condensation. Then, we explore the possibility of a non-thermal fixed point in a one-dimensional ultracold Bose gas as well as a two-component Bose gas in two dimensions. Finally, we discuss the realisation of a non-thermal fixed point in a relativistic scalar field theory as well as for the case of a two-component Bose gas in two dimensions. After a brief discussion of experimental prospects, we summarise our results and close with an outlook.

Publications

This thesis contains the discussions and results from a number of publications I have coauthored as listed below.

1. B. Nowak, D. Sexty, and T. Gasenzer, Superfluid turbulence: Nonthermal fixed point in an ultracold Bose gas, *Phys. Rev. B* **84**, 020506(R) (2011)
2. T. Gasenzer, B. Nowak, and D. Sexty, Charge separation in reheating after cosmological inflation, *Phys. Lett.* **B710**, 500 (2012)
3. B. Nowak, J. Schole, D. Sexty, and T. Gasenzer, Nonthermal fixed points, vortex statistics, and superfluid turbulence in an ultracold Bose gas, *Phys. Rev. A* **85**, 043627 (2012)
4. M. Schmidt, S. Erne, B. Nowak, D. Sexty, and T. Gasenzer, Nonthermal fixed points and solitons in a one-dimensional Bose gas, *New J. Phys.* **14**, 075005 (2012)
5. J. Schole, B. Nowak, and T. Gasenzer, Critical dynamics of a two-dimensional superfluid near a non-thermal fixed point, *Phys. Rev. A* **86**, 013624 (2012)
6. B. Nowak and T. Gasenzer, On a new twist in the dynamics of Bose-Einstein condensation, arXiv:1206.3181 [cond-mat.quant-gas] (2012)
7. C. Bodet, M. Kronenwett, B. Nowak, D. Sexty, and T. Gasenzer, Non-equilibrium Quantum Many-Body Dynamics: Functional Integral Approaches, in N. Proukakis, S. Gardiner, M. Davis, and M. Szymanska, eds., *Proc. Int. Workshop FINESS 2009, Durham, UK*, Quantum Gases: Finite Temperature and Non-Equilibrium Dynamics (Vol. 1 Cold Atoms Series), Imperial College Press, London (in press) (2012)

These publications represent the result of collaborative work. To clearly separate my contribution to each project from the work of others, I give a summary of contributions made to references 1-7.

Statement of contribution to jointly authored works

- Ref. 1: I carried out all numerical simulations for this project.
- Ref. 2: The numerical results reported in Ref. 1 initiated this project. I analysed scaling properties of charge-domain structures.
- Ref. 3: I performed simulations in 3D and analytical calculations in 2D and 3D, presented in sections 2, 3 and 4.
- Ref. 4: I guided the numerical and analytical research work done by Maximilian Schmidt and Sebastian Erne.
- Ref. 5: I contributed the central idea of how to locate the non-thermal fixed point. I guided the numerical research of Jan Schole who carried out the numerical simulations. I further performed calculations on the initial atomic scattering dynamics as well as the kinetic theory for vortex scattering.
- Ref. 6: I carried out all numerical simulations for this publication.
- Ref. 7: I provided the results presented in section 4.3.

Declaration by the author

This thesis is composed of my original work, and contains no material previously published or written by another person except where due reference has been made in the text. I have clearly stated the contribution by other authors to jointly-authored works that I have included in my thesis. The content of my thesis is the result of work I have carried out since the commencement of my graduate studies at the Heidelberg Graduate School of Fundamental Physics, Institut für Theoretische Physik, Universität Heidelberg and does not include material that has been submitted by myself to qualify for the award of any other degree or diploma in any university or other tertiary institution.

Danksagung

Diese Arbeit ist für mich untrennbar mit der Unterstützung und Freundschaft vieler Menschen verbunden, denen ich im Folgenden danken möchte.

Besonders am Herzen liegt mir die Danksagung bei meinen Doktorvater Prof. Dr. Thomas Gasenzer, der mich seit unserem ersten Treffen in Boulder als Mensch und Wissenschaftler begeistert hat. Danke für ein atemberaubendes Forschungsprojekt, für eine immer freundschaftliche Arbeitsatmosphäre, für gemeinsame Forschungsreisen, Diskussionen bis in die Nacht und die vielen lobenden und aufmunternden Worte.

Mein herzlicher Dank gebührt außerdem Prof. Dr. Markus Oberthaler für die Zweitkorrektur der Arbeit, die Teilnahme am Advisory Committee und viele spannende Diskussionen über die Physik ultrakalter Gase.

Prof. Dr. Heinz Horner und Prof. Dr. Aeschbach-Hertig sei herzlich für die Teilnahme an meiner Doktorprüfung gedankt.

An dieser Stelle möchte ich mich auch bei Prof. Dr. Jan M. Pawlowski bedanken, der als dritter Mitbetreuer diese Arbeit aufmerksam begleitet hat.

Es ist mir ein großes Bedürfnis der gesamten Arbeitsgruppe Gasenzer meinen Dank auszusprechen. Ich habe mich immer wohl gefühlt in der Gemeinschaft mit Sebastian Bock, Dr. Cédric Bodet, Sebastian Erne, Martin Gärtner, Roman Hennig, Markus Karl, Dr. Matthias Kronenwett, Andreas Leonhardt, Steven Mathey, Nikolai Philipp, Maximilian Schmidt, Jan Schole, Dr. Dénes Sexty, Martin I. Trappe, Pascal Weckesser und Jan Zill. Herzlichen Dank für die hervorragende wissenschaftliche und persönliche Zusammenarbeit.

Für das Korrekturlesen des Manuskripts bedanke ich mich bei Sebastian Bock, Emer Brady, Markus Karl, Steven Mathey, David Mesterházy, Dr. Konrad Schade und Martin I. Trappe.

Dankbar bin ich ebenfalls für Forschungsaufenthalte am Kavli Institute for Theoretical Physics, Santa Barbara, USA, der Arbeitsgruppe von Prof. Dr. Shih-Chuan Gou, Changhua, Taiwan, dem Yukawa Institute, Kyoto, Japan, der Arbeitsgruppe von Prof. Dr. Makoto Tsubota, Osaka, Japan, der Arbeitsgruppe von Prof. Dr. Schlagheck, Liege, Belgien und der Arbeitsgruppe von Prof. Dr. Jörg Schmiedmayer, Wien, Österreich.

Für spannende wissenschaftliche Diskussionen danke ich Prof. Dr. B. Anderson, Prof. Dr. J. Berges, Prof. Dr. E. Bodenschatz, R. Bücker, Prof. Dr. M. J. Davis, Dr. S. Diehl, Prof. Dr. G. Falkovich, Dr. S. Flörchinger, D. Gelfand, Prof. Dr. S.-C. Gou, Prof. Dr. H. Horner, Prof. Dr. R. Kerr, Dr. G. Krstulovic, Prof. Dr. I. Mazets, Prof. Dr. L. McLerran, D. Mesterházy, E. Nicklas, Prof. Dr. Schlagheck, S. Schlichting, Prof. Dr. M. G. Schmidt, Prof. Dr. J. Schmiedmayer, Prof. Dr. B. Shivamoggi und Prof. Dr. M. Tsubota.

Für den wissenschaftlichen Austausch und die kollegiale Atmosphäre danke ich den Arbeitsgruppen des Instituts für Theoretische Physik, sowie den Arbeitsgruppen von Prof. Dr. S. Jochim, Prof. Dr. M. Oberthaler und Prof. Dr. M. Weidemüller.

Ganz herzlich danke ich Dr. Eduard Thommes und dem gesamten Sekretariatsteam am Institut für Theoretische Physik für die freundliche Hilfe in allen administrativen Belangen, sowie Dr. Elmar Bittner und Prof. Dr. Werner Wetzels für die EDV-Unterstützung. Die Diskussionen mit renommierten Gastwissenschaftlern oder den erfahrenen Emeriti habe ich außerdem sehr geschätzt. Seminare, Feste, Kaffeegespräche und Mittagsrunden in der Villa am Philosophenweg 16 werde ich immer in positiver Erinnerung behalten.

Mein Dank gilt außerdem den noch nicht genannten Freuden- und Leidensgenossen aus dem Kellerbüro, Fabian Gross, Thomas Lübbert, Mariele Motta, Dr. Behnam Nikoobakht und Andreas Samberg.

Ich bedanke mich bei der Heidelberg Graduate School of Fundamental Physics, insbesondere bei Prof. Dr. Sandra Klevansky und ihrem Team für die Unterstützung meiner Doktorarbeit. Ich bin dankbar für die vielfältigen Angebote des Extreme Matter Institutes (EMMI) und des Center for Quantum Dynamics (CQD), die meine Doktorarbeit sehr bereichert haben. Der Deutschen Forschungsgemeinschaft (DFG), sowie der Wilhelm und Else Heraeus-Stiftung danke ich für die finanzielle Förderung.

Zu guter Letzt möchte ich mich bei meiner lieben Frau Shu-Wei bedanken, die mir mit Ihrer Lebensfreude und Spontanität das Leben außerhalb des Instituts versüßt hat. Ebenso bin ich sehr glücklich über die stete Unterstützung durch meine wunderbaren Eltern und meinen Bruder.

Contents

1	Introduction	1
2	Background	9
2.1	Ultracold atomic gases	9
2.1.1	Bose-Einstein condensation	10
2.1.2	Lower dimensions	11
2.1.3	Theoretical description out of equilibrium	12
2.2	Classical field theory	14
2.2.1	(Quasi-) topological defects	15
2.2.2	(Quantum-) hydrodynamics	17
2.3	Non-thermal fixed points	19
2.3.1	Classical Kolmogorov turbulence	20
2.3.2	Superfluid turbulence	21
2.3.3	Wave turbulence	21
2.3.4	Heuristic derivation	26
2.4	Summary	28
3	Superfluid turbulence as a non-thermal fixed point	29
3.1	Observation of wave-turbulent spectra	29
3.2	Observation of vortices	32
3.3	Summary	34
4	Vortex statistics	35
4.1	Vortices in $d = 2$	35
4.1.1	Independent vortices	37
4.1.2	Independent vortex-antivortex pairs	37
4.1.3	Pair correlated vortices	38
4.2	Vortex loops in $d = 3$	42
4.2.1	Uncorrelated vortex loops	44
4.2.2	Straight vortex lines and rings	45
4.3	Velocity distribution	48
4.4	Summary	49

5	Properties near the non-thermal fixed point	51
5.1	Bose gas approaching the non-thermal fixed point	52
5.1.1	Time evolution of the single-particle spectrum	53
5.1.2	Fluxes	56
5.2	Vortices, acoustic turbulence and the departure from the fixed point	58
5.2.1	Superfluid turbulence and statistics of vortices	59
5.2.2	Acoustic turbulence	60
5.2.3	Vortex velocities	61
5.2.4	Pairing and departure from the fixed point	62
5.3	Summary	64
6	Critical dynamics near a non-thermal fixed point	65
6.1	Creation of vortices and turbulence	65
6.2	Vortex density decay	67
6.3	Vortex correlations	69
6.4	Energy equilibration	70
6.5	Possible relation to classical turbulence	71
6.6	Kinetic theory of vortex scattering	72
6.7	Phase correlations	73
6.8	Summary	77
7	A three-dimensional Bose gas near a non-thermal fixed point	79
7.1	Mean field scattering dynamics	79
7.2	Isotropisation and mean field decay	81
7.3	Vortex density decay	83
7.4	Energy equilibration and condensation	86
7.5	Summary	87
8	Dynamics of Bose-Einstein condensation	89
8.1	Evolution of the zero mode	91
8.2	Momentum distribution	91
8.3	Hydrodynamic condensation	92
8.4	Defect formation	95
8.5	Summary	95
9	Non-thermal fixed points and solitons	97
9.1	Momentum spectra of soliton ensembles	97
9.1.1	Random-soliton model: uniform gas	98
9.1.2	Relation to non-thermal fixed points and vortices	101
9.1.3	Random-soliton model: trapped gas	104
9.2	Soliton spectra in dynamical simulations	107
9.2.1	Soliton formation and tracking in position space	108
9.2.2	Number of solitons after cooling ends	110
9.2.3	Time evolution of single-particle spectra	111
9.3	Summary	112

10 From cosmological inflation to table-top experiments	115
10.1 Charge separation in reheating after inflation	115
10.1.1 The model	116
10.1.2 Scaling of the momentum distribution	117
10.1.3 Charge separation	119
10.2 Domain formation in a two-component Bose gas	122
10.2.1 Dynamics in the immiscible regime	123
10.2.2 Outlook into the miscible regime	124
10.3 Experimental prospects	125
11 Summary and outlook	127
A Numerical techniques	133
B Condensation	139
References	141

Introduction

Far-from-equilibrium dynamics of interacting many-body systems has become a topic of intense focus in very different areas of physics. Applications range from the formation of Bose-Einstein condensates in ultracold atomic gases to quark-gluon plasmas produced in heavy-ion collisions, and thus over a range of twenty-two orders of magnitude in temperature. An important question is whether one can identify universal aspects of non-equilibrium dynamics in ultracold quantum gases that also have the potential to be applied to systems at vastly different energy scales. With present-day technology that allows one to precisely prepare initial non-equilibrium states and determine theoretical model parameters, researchers in the field of ultracold atomic gases are given the unique opportunity to clarify such challenging questions of global, interdisciplinary significance [1–4].

Exciting examples within the realm of non-equilibrium physics studied in ultracold gases include driven-dissipative systems [5], which have the potential to improve the control of quantum information devices, and non-equilibrium evolution across phase transitions [6, 7] – a question of long-standing interest in areas from cosmology to solid-state physics [8, 9]. Researchers from various fields are intensively investigating the dynamics of thermalisation of closed quantum systems [10–12]. Questions concerning the existence of non-thermal equilibrium states [13–17], superfluid turbulence [18], as well as prethermalised states [19–23] are heavily discussed. Recently, this topic has also attracted considerable attention in the context of thermalisation of the quark-gluon plasma [4]. The controversial idea of dynamical Bose-Einstein condensation in this system [24] is one example of a phenomenon that is very familiar to ultracold atomic physicists.

Among the wealth of possible non-equilibrium many-body configurations, the most interesting candidates for theoretical and experimental study are those at which the time evolution gets stuck for an extraordinarily long time. This is a common feature near equilibrium phase transitions where the dominance of low momentum modes slows down the dynamics of the system. Simultaneously, universal properties like the power-law behaviour of correlation functions appear. These critical points can be described as fixed points of renormalisation group transformations [25]. In

analogy to that, one can define far-from-equilibrium non-thermal fixed points as stationary states which are characterised by power-law scaling of correlation functions¹. In closed systems these solutions are transient and decay towards thermal equilibrium at late times. They correspond to situations in which scattering processes are almost negligible, which enhances their life time beyond experimentally relevant time scales. In driven systems, non-thermal fixed-point solutions can be stationary within a certain region of momentum space due to the presence of local transport of globally conserved quantities [28–33].

Classical fluid turbulence is among the earliest phenomena described by such scaling behaviour out of equilibrium [34–39]. It comprises a quasi-stationary flow of energy from large to small scales [40]. This flow is fed by some stirring mechanism at large scales and stabilises a non-equilibrium steady state whose correlation functions exhibit characteristic scaling [34, 35].

Now, we draw attention to non-equilibrium *quantum* many-body systems. In this context wave turbulence phenomena [41–43] have been studied in dilute ultracold Bose gases [29, 31, 32, 44–51], the inflating and reheating early universe [28, 30, 52–55] and quark-gluon matter created in heavy-ion collisions [24, 56–61]. In contrast to Kolmogorov’s theory of classical turbulence [34, 35], the wave turbulence approach does not reference vortical flow in the fluid under consideration, but mathematically analyses possible non-thermal fixed point solutions of the dynamic equations.

In a regime where kinetic theory is applicable, a weak-wave-turbulence theory has been developed [41, 42] – it aims at the analysis of non-thermal fixed points defined by quasi-stationary, self-similar momentum distributions, $n(k) \sim k^{-\zeta}$, with scaling exponent ζ obtained from kinetic wave equations. Equations of this type are well suited to describe scattering phenomena of particles and waves in a regime where interactions are sufficiently weak. Applications reach from vibrating plates [62] and capillary waves [63] to models of the inflationary early universe [52, 64] and dynamics of Bose-Einstein condensates [42, 50, 65, 66].

However, in an ultracold Bose gas occupation numbers necessarily grow large in the low-momentum region and the kinetic approximation becomes invalid. An extension of weak-wave turbulence by non-perturbative quantum field theory methods leads to the prediction of new scaling laws [27, 28, 53]. Calculations for a non-relativistic ultracold Bose gas were presented in Ref. [29]. The authors propose strong matter-wave turbulence in the regime of long-range excitations. The main result is the prediction of various non-thermal fixed-point scaling solutions for the case of an ultracold Bose gas. They correspond to constant particle and energy flux solutions. Particularly interesting is the prediction of large scaling exponents in the low-momentum region that go beyond the weak-wave-turbulence analysis.

¹Note that non-thermal fixed points are not defined as fixed points of renormalisation group equations throughout this thesis. Intuitively, they can be understood as dynamical fixed points known from the theory of dynamical systems. However, a formulation in terms of a renormalisation group approach might well be possible and is a topic of current research [26, 27].

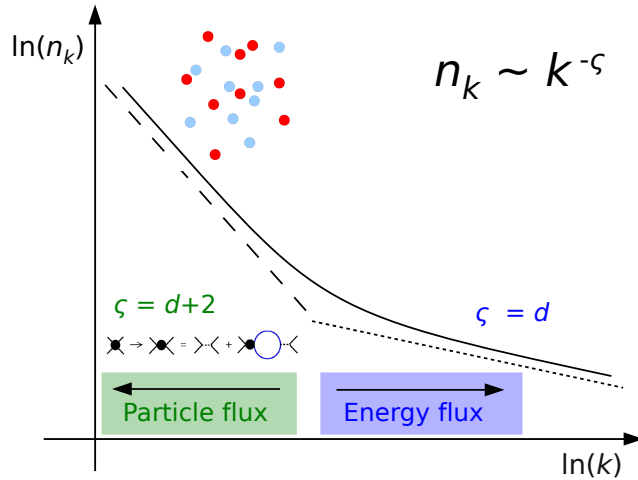


Figure 1.1: Sketch of the single-particle mode occupation number $n(k)$ as a function of the radial momentum k for the non-thermal fixed point solutions found numerically [31, 32]. We provide evidence for the presence of a bimodal distribution in the presence of an inverse particle flux at low momenta and a direct energy flux at high momenta. Importantly, the momentum distribution in the low momentum region is explained by the presence of a random distribution of vortices and antivortices, which provides an intuitive understanding for the strong turbulence phenomena predicted in Ref. [29].

In the non-equilibrium regime of a quantum many-body system multiple types of excitations can be present. In the case of an ultracold Bose gas, one encounters linear excitations like those of single particles or collective sound waves and non-linear ones such as (quasi-) topological excitations [67–70]. Topological defects are robust states of interacting many-body systems and are classified by the values of an order parameter field on the boundary of the system [71]. One prominent example is a quantised vortex which exists as a topological excitation of superfluids or superconductors, liquid crystals, magnets and cosmic fields [69]. Its fundamental properties have been studied since the 1940s [72–74] and are of great importance, e.g. for bosonic superfluids such as ^4He [75, 76] and dilute atomic gases [77–81] in two and three spatial dimensions. In contrast to eddies in classical fluids, vorticity in a superfluid is quantised [73, 74], and the creation and annihilation processes of quantised vortices are distinctly different from their classical counterparts [76, 82, 83]. Rapidly rotating Bose-Einstein condensates have been shown to form lattices of singly-quantised vortices [84–86], and the dynamics of interacting vortices are also experimentally accessible [87–90]. To obtain statistical information on vortex dominated flows ensembles of vortices were considered [73, 91–94]. This approach is closely related to the phenomenon of superfluid turbulence, also referred to as quantum turbulence [18, 95]. Turbulent quantised vortices have been the subject

of extensive studies in the context of helium [76, 82, 96–104] and, more recently, dilute Bose gases [44–46, 48, 49, 90, 105–111]. For example, the observation of a Kolmogorov 5/3-law [34, 35] in experiments with superfluid helium [102, 112, 113] received much attention [18, 114–119].

In this thesis we study the non-equilibrium dynamics of ultracold quantum gases in one, two, and three spatial dimensions within the semi-classical regime of the underlying quantum field theory [120–122]. This task requires us to extend the (quasi-) equilibrium studies of these systems and to investigate the creation, characterisation and destruction of turbulence. A key feature of our method is the possibility to investigate single realisations of the inhomogeneous non-equilibrium ensemble, as well as ensemble averaged quantities. This way, we simultaneously address wave turbulence phenomena observed in correlation functions and superfluid turbulence. Our main achievement is to reveal a connection between the dynamics of (quasi-) topological field configurations and field-theoretic methods which offers great prospects for a unified description of non-equilibrium dynamics. Moreover, it provides hints of how the proposed non-thermal fixed points in relativistic systems [27, 28, 30, 53, 57, 58] are realised in nature. In the following, we present a review and general discussion of the main results contained in this thesis.

Before these results are discussed in depth in the main body of this thesis, Chap. 2 will provide background information on the physics of ultracold gases and their theoretical description – there we will carefully introduce the key concepts and ideas necessary to appreciate the subsequent chapters.

In Chap. 3 we show that a two- or three-dimensional superfluid Bose gas in the vicinity of a non-thermal fixed point is characterised by a dilute random distribution of vortices or vortex lines of positive and negative circulation (see Refs. [31] and [32]). The numerically found quasi-stationary scaling properties are in agreement with quantum-field-theoretic predictions of Ref. [29]. This is remarkable since it provides evidence for a relation between wave turbulence and quantum turbulence not reported in the literature so far. In Fig. 1.1 our findings are schematically summarised. The numerically obtained scaling exponents, discussed in detail in Chap. 5, equal the exponents obtained analytically for particle transport towards low momenta and energy transport towards high momenta [29, 32]. The nature of these transport processes is corroborated by calculations of the respective fluxes [32]. Furthermore, the momentum distribution in the low-momentum region is analytically explained by the presence of a random distribution of vortices and antivortices (see Chap. 4). An inverse particle flow is invoked through vortex-antivortex annihilations. Moreover, we show that the decay of strong turbulent scaling is caused by vortex-antivortex pairing or shrinking of vortex rings.

The decay of superfluid turbulence is typically accompanied by a build-up of coherence and quasi-condensation [44–50, 105, 106]. In Chaps. 6 and 7 we explore this process in detail and describe the role of non-thermal fixed points during the out-of-equilibrium evolution. A central result obtained for two spatial dimensions

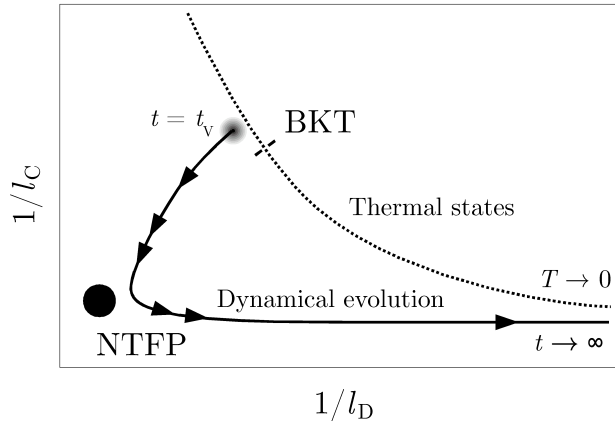


Figure 1.2: Dynamical evolution of a two-dimensional superfluid near a non-thermal fixed point. The sketch shows the equilibration process after a quench, in the space of inverse coherence length l_C and inverse mean vortex-antivortex pair distance l_D [33]. The trajectory denoted by ‘Dynamical evolution’ illustrates the decay of superfluid turbulence starting at the time where vortices appear, $t = t_V$, approaching the non-thermal fixed point and finally evolving towards equilibrium. The line marked as ‘Thermal states’ qualitatively illustrates these quantities for thermal configurations [123–125], featuring a steady decrease of inverse coherence with inverse mean vortex-antivortex distance and including a Berezinskii-Kosterlitz-Thouless phase transition. An unbinding of vortices of opposite circulation characterises the approach to the non-thermal fixed point before finally all vortices decay, i.e. $l_D \rightarrow 0$, to establish equilibrium phase coherence at a temperature below the phase transition.

is depicted schematically in Fig. 1.2, see Ref. [33]. Here, we sketch the projection of the phase ordering process onto the space spanned by the coherence length l_C of the bulk matter and the mean inter-vortex pair distance l_D . In this way, the dynamical evolution towards and away from a non-thermal fixed point can be compared to the properties of near-equilibrium states of a two-dimensional degenerate Bose gas [73, 123–127]. Arrows mark the direction of the flow and indicate that critical slowing down occurs near the non-thermal fixed point. An unbinding of vortices of opposite circulation emerges during the approach of the fixed point before finally all vortices decay to establish full equilibrium phase coherence. In three dimensions, the analogous process involves the decay of vortex line density and an increase of mean vortex ring radius.

A fundamental and long-debated question in the field of ultracold gases concerns the formation of a Bose-Einstein condensate from a completely disordered initial state in three dimensions [45–48, 50, 65, 105, 106, 128–139]. We address this issue in Chap. 8 in order to clarify the particularly interesting aspect of superfluid turbulence in this process [45, 46, 48, 106, 130]. Our main finding is that the superfluid turbulence period can appear in two different forms [140]. The two possible paths to Bose-Einstein condensation are shown schematically in Fig. 1.3. If a sufficiently small

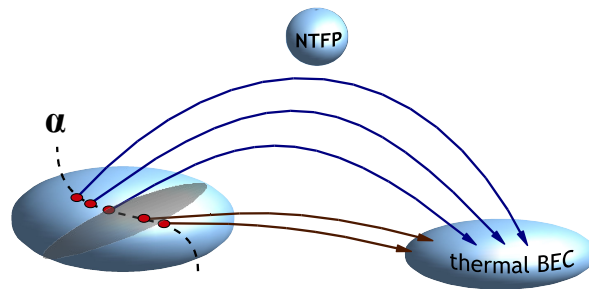


Figure 1.3: Depending on the strength α (parametrising the UV fall-off $n(k) \sim k^{-\alpha}$) of an initial cooling quench, the gas can thermalise directly to a Bose-Einstein condensate, or it can first approach and critically slow down near a non-thermal fixed point. There, it is characterised by a self-similar particle spectrum $n(k) \sim k^{-5}$ and strong superfluid turbulence.

amount of energy is removed, a thermal Rayleigh-Jeans distribution forms in a quasi-adiabatic way. The chemical potential increases, and a fraction of particles is deposited in the lowest mode, forming a Bose-Einstein condensate. In the second scenario, after a sufficiently strong cooling quench, the system develops transient scaling behaviour in the momentum distribution prior to condensate formation. We show that the power law can be traced back to the flow pattern around undistorted vortex lines and is interpreted as a signature of the non-thermal fixed point discussed in Chaps. 3-7.

To emphasise the importance of our results we point out that understanding the dynamics of Bose-Einstein condensation is of fundamental interest to physics beyond that of ultracold gases. Today, many-body dynamics of coherent bosonic excitations is intensively studied in solid-state systems consisting of magnons [141–144] or polaritons [145–148]. Recently, condensation has even been discussed for the case of gluons as an intermediate stage of heavy-ion collisions [4, 24, 61].

After exploring the non-equilibrium behaviour of ultracold Bose gases in two and three dimensions, we will turn our attention to one-dimensional Bose gases in Chap. 9. The non-equilibrium dynamics of these systems is under intense investigation by the quantum gas community [2, 7, 149–154]. Extending our studies on universal properties of vortex ensembles, we focus on solitary waves and show that these exhibit analogous scaling behaviour. Solitons are non-dispersive wave solutions which can arise in many non-linear systems spanning a wide range from the earth’s atmosphere [155] or water surface waves [156] to optics [157]. The characteristics of single or few solitons in ultracold Bose gases have been studied during the last decade regarding their movement and interaction in traps [149, 151, 152, 154], as well as their formation and creation [158–161] and their decay [162, 163], see Ref. [153] for a review. See Refs. [164–166] for related studies in relativistic field theory.

The last part of this thesis, Chap. 10, begins with a recent study on non-thermal fixed points and superfluid turbulence in the context of reheating after cosmological

inflation. Here, instabilities are shown to induce the formation of domain structures of opposite charge. We simultaneously observe quasi-stationarity and scaling in the occupation number spectrum, which is interpreted as a signature of a non-thermal fixed point.

We have taken a first step in the direction of studying multi-component fields by investigating the ultracold two-component Bose gas, see Chap. 10 [167]. There, we discuss non-equilibrium dynamics triggered by instabilities for different inter- and intraspecies couplings and reveal the possibility for different quasi-stationary scaling solutions [168–170]. An extension of this study to the regime of ultracold spin-1 and spin-2 Bose gases [133, 171–177] poses an interesting challenge for future research.

The chapter ends with an overview of prospects for experimental studies on non-thermal fixed points with ultracold alkali atoms. Here, we briefly introduce the set-ups by the groups in Vienna, Austria (1D) [150, 178, 179], Heidelberg, Germany (1D) [7, 151], Tucson, USA (2D) [89, 90, 138] and São Carlos, Brazil (3D) [109, 111] and show that a verification of our results is readily feasible.

The results contained in this thesis contribute to the understanding of non-equilibrium dynamics of quantum fields – this statement is particularly motivated by the abundant appearance of topological defects in nonlinear field theories. As a famous example, metastable multi-vortex states or, in one spatial dimension, solitary waves, are known to appear from strong fluctuations in the vicinity of the normal-fluid to superfluid transition [180]. Rapidly crossing such a transition by varying an equilibrium macroscopic parameter like the temperature at a certain rate is well known to induce defects. In this case, their number can be estimated from the coherence length at the point where the parameter variation ceases to be adiabatic [8, 181, 182]. Experiments with ultracold Bose gases following such Kibble-Zurek-type protocols [138, 183] as well as generating superfluid turbulence [109, 111] are pursued with increasing effort and could serve to discover and study non-thermal fixed points systematically.

Our work motivates the development and application of non-perturbative techniques to study superfluid turbulence. A unified field-theoretic description of classical and superfluid turbulence might ultimately clarify the similarities and differences between the two, a project that is of major interest for the fluid-dynamics community [18, 101].

The concept of non-thermal fixed points appears to be very significant for the understanding of thermalisation of interacting many-body systems [1, 2]. Across different fields of physics one encounters the possibility of non-thermal equilibrium states [13–17] as well as prethermalised states [19–23]. Among these classes of states non-thermal fixed points are the most dramatic ones, living a metastable life far away from equilibrium. However, their long-range and steady nature offers good prospects to tame the non-equilibrium regime.

Background

In this chapter we provide theoretical and experimental background on ultracold atomic quantum gases and lay out the key theoretical concepts used in the forthcoming chapters. After a brief sketch of the historical developments and technical achievements of cooling and trapping dilute atomic vapour, we discuss the equilibrium phenomenon of Bose-Einstein condensation in three dimensions. We highlight effects specific for lower dimensions, $d < 3$, where Bose-Einstein condensation is strictly speaking statistically forbidden in the thermodynamic limit. Instead, constrained quantum gases develop long-range order in the form of quasi-condensates. A brief introduction to the theoretical descriptions of quantum gases out-of-equilibrium is followed by an outline of the powerful classical-field method, which is extensively used in this thesis. Special attention is paid to the appearance of (quasi-) topological excitations and (quantum-) hydrodynamic behaviour of the gas. Finally, the quantum field theoretic approach based on the 2-particle irreducible (2PI) effective action for correlation functions is introduced, which lead to the proposal of non-thermal fixed points and strong wave turbulence. With that, we are going to be prepared for a thorough and multi-sided analysis of non-equilibrium Bose fluids.

2.1 Ultracold atomic gases

Since the groundbreaking experiments on Bose-Einstein condensation in dilute atomic alkali gases [184–186] at JILA [187], MIT [188] and Rice University [189], in 1995, the field of ultracold quantum gases has seen a wide spectrum of developments [190]. Starting from the characterisation of the condensed bosonic gas in thermal equilibrium [79, 191], researchers investigated the formation of ultracold Fermi gases [192–200] and mixtures [201–203], the few-body physics of ultracold atoms and molecules [204–210], properties of matter waves [211, 211], soliton and vortex formation [86, 87, 149, 151, 160, 163] as well as many-body phase transitions in magnetic traps and optical lattices [212–214]. Today, questions concerning the non-equilibrium dynamics of quantum gases [1, 2, 5, 8, 18, 215, 216], quantum mag-

netism [217], artificial gauge fields [218], squeezing and entanglement [219–222] are examples for topics at the forefront of experimental and theoretical research. Nevertheless, these new developments build on the understanding and control of some basic physical properties of ultracold gases, which we want to review in this section. Our considerations are guided by excellent reviews, see Refs. [79, 191, 223–228]. Due to its relevance for the subsequent chapters of this thesis we focus on the case of bosonic atoms.

2.1.1 Bose-Einstein condensation

Experimental studies of atomic quantum gases rely on elaborate trapping and cooling techniques. A well established scheme to produce a Bose-Einstein condensate starts with laser cooling in a magneto-optical trap [223, 229]. Alkali atoms are well suited for that, since their internal structure can be addressed with available laser systems. A magneto-optical trap consists of a magnetic field gradient produced by a quadrupole field. It makes use of the position-dependent Zeeman shift of the electronic levels to focus atoms in the centre. When atoms move in a radially increasing magnetic field, they feel an energy increase towards larger radii. This can be designed to act as an external harmonic potential, characterised by the length scale a_{ho} , which is typically a few μm . Red-detuned optical beams are intercepting at right angles in the centre. They provide additional confinement by means of radiation trapping and are essential for cooling due to the Doppler-effect. Fast atoms are forced to absorb counter-propagating photons, thus damping atomic motion from hundreds of meters per second to tens of centimetres per second. Typically, magneto-optical traps capture up to 10^{10} atoms at densities n close to 10^{11}cm^{-3} and temperatures below $100\mu\text{K}$. The phase space density $n\lambda_{\text{dB}}^3$, with $\lambda_{\text{dB}} = \hbar/\sqrt{2\pi mk_{\text{B}}T}$ being the thermal de Broglie wavelength, and m the atomic mass, does not increase beyond 10^{-6} [226].

Evaporative cooling is the method of choice to finally reach ultracold temperatures in the nanokelvin regime [230]. Here, one applies a spatially selective, radio-frequency coupling between different hyperfine states. Since the magnetic trapping potential sensitively depends on the direction of the hyperfine spin orientation, this can induce an expulsion force removing the most energetic atoms on the outside of the trap. An evaporative cooling ramp consists of many cycles in which fast atoms are expelled from the outer regions of the trapping potential, carrying much of the energy with them. Subsequently, the remaining gas thermalises at a lower temperature. Although interactions are not required for the existence of Bose-Einstein condensation, they are indispensable for creating the respective equilibrium state. The strength of two-body collisions in a Bose-Einstein condensate sensitively depends on the s-wave scattering length a . This length scale is the only relevant interaction parameter at ultra-low energies, i.e. for momenta $p/\hbar \ll 1/r_0$, where r_0 is the effective range of the interaction potential (typically $r_0 \sim a$). Since near condensation $p/\hbar \sim 1/\lambda_{\text{dB}} \sim n$, a description in terms of elastic s-wave collisions requires the diluteness condition $na^3 \ll 1$. The manipulation of the scattering

length by means of a Feshbach-resonance offers the possibility to study quantum gases from weak to strong interactions [231, 232].

It is worth noticing, that the atomic Bose-Einstein condensate can only be a metastable state, since at low temperatures the atoms would favour the solid phase. However, to cross this phase transition requires three-body collisions which are suppressed at low densities. The number of recombinations per unit time is proportional to $a^4 n^3 \hbar/m$ [233, 234].

Combining laser and evaporative cooling, experimenters eventually succeeded in observing the formation of a Bose-Einstein condensate. This requires phase space densities greater than one, $n\lambda_{\text{dB}}^3 \gtrsim 1$, which means that the wave functions of individual atoms overlap. For a homogeneous, non-interacting gas in $d = 3$ dimensions this condition can be inverted at the critical point, where $n\lambda_{\text{dB}}^3 = \zeta(3/2)$, to give the critical temperature

$$k_{\text{B}}T_c = \frac{2\pi\hbar^2}{m} \left(\frac{n}{\zeta(3/2)} \right)^{2/3}. \quad (2.1)$$

At this point, the chemical potential μ equals the ground state energy E_0 and the ground state mode becomes macroscopically occupied. Effects of interactions on a mean-field level yield a shift in the critical temperature $\delta T_c/T_c \simeq -1.3n^{1/3}a$, which is typically on the order of a few percent. For simplicity we have discussed the thermodynamics of Bose-Einstein condensation only for the case of a homogeneous density. Quantitative modifications arise from the trapping potential present in laboratory experiments with ultracold alkali gases [79].

Superfluidity

Superfluidity is most prominently defined as the property of matter to flow with zero viscosity. It was first discovered by Kapitza [235], Allen and Misener [236] in liquid ^4He below the so called λ -point ($T_\lambda = 2.17\text{K}$). Immediately after, a connection to Bose-Einstein condensation was proposed [237, 238]. In 1941, Landau clarified this relation by giving the Landau-criterion of frictionless flow, which requires that the low-lying excitations have linear dispersion. This is fulfilled for Bose-Einstein condensates and liquid helium [239]. Superfluidity emerges to be closely related to the existence of an order parameter field, which also includes the existence of quantised vortices. The properties of these excitations are going to be introduced in Sect. 2.2.1.

2.1.2 Lower dimensions

So far we have discussed the trapping and cooling of dilute bosonic gases as well as condensate properties and superfluidity in three-dimensional space. Now, we turn our attention to lower-dimensional systems which show very peculiar statistical properties. Most importantly, thermal fluctuations inhibit Bose-Einstein conden-

sation of an interacting homogeneous gas in $d = 1$ and $d = 2$ dimensions in the thermodynamic limit [240]. This can already be suspected by considering the Bose-Einstein distribution function for free particles in the limit $\mu \rightarrow 0$

$$n_{\text{BE}}(k) = \frac{1}{e^{\beta\hbar^2 k^2/2m} - 1}, \quad (2.2)$$

with $\beta = 1/k_{\text{B}}T$. In the thermodynamic limit the low momentum behaviour of the finite temperature distribution features a $1/k^2$ -divergence. This yields a divergent contribution to the number of non-condensed particles $N - N_0 = \int d^d k n_{\text{BE}}(k)$ for $d < 3$ dimensions [79, 191, 241]. In fact, a harmonic trap can weaken this theorem in two dimensions even in the thermodynamic limit due to the modified density of states. In a one-dimensional system this is not enough, instead condensation is only possible for a finite system [79, 230, 241]. For the case of interacting bosonic gases interesting features show up beyond that, like the Berezinskii-Kosterlitz-Thouless transition in $d = 2$. This can be seen as a disorder-order transition that separates a disordered state of freely moving topological defects from an ordered state of tightly bound defects [126, 127]. The ramifications of this transition in trapped ultracold gases have been investigated in Refs. [124, 125, 138, 242–246]. It turns out that the ordered state below the Berezinskii-Kosterlitz-Thouless transition shows long-range coherence very similar to a true Bose-Einstein condensate, which coined the name quasi-condensate. Similar signatures have recently been observed in ultracold atomic gases confined to one spatial dimension [247, 248]. This concerns solely the weakly-correlated regime $\gamma \ll 1$, with γ the Lieb-Liniger parameter defined in terms of the coupling constant g_{1D} as $\gamma \equiv mg_{1D}/\hbar^2 n_{1D}$ [248].

2.1.3 Theoretical description out of equilibrium

Time evolution of many-body systems in which effects of quantum physics play an important role belong to the least understood physical phenomena. Whereas the problem of two interacting bodies can be solved within elementary mechanics, the motion of three and more objects is complicated to predict. For large numbers of particles, continuum descriptions like quantum field theory or hydrodynamics are very successful. However, quantum and classical statistical effects prevent a fully deterministic description of the system. Two main aspects constitute the complexity connected with non-equilibrium phenomena and their theoretical description: long-time evolution and strong correlations arising from non-linear interactions [2, 249].

Commonly, theoreticians attempt to obtain time evolution equations for correlation functions of quantum fields, which are solved analytically or numerically. In this respect, functional-integral approaches including the two-particle irreducible (2PI) effective-action and the real-time functional flow equation methods for quantum field dynamics represent promising techniques that allow to go beyond perturbative approximations [19, 215, 249–260]. A completely different approach is to construct a (stochastic) differential equation, which mimics the ‘micro-canonical’ evolution of a many-body system. From such a process, correlation functions of quantum fields

are obtained by numerical averaging of many trajectories followed by the stochastic field. Hence, out-of-equilibrium trajectory-methods are complementary to methods based on averaged correlation functions. It is important to note that there exists a mapping from one to the other. Examples from statistical physics include the mapping of Langevin-trajectories to Fokker-Planck equations or quantum Monte Carlo wave function trajectories to Master equations [261]. It is crucial that usually trajectory methods are much cheaper to process on the computer than evolution equations for correlation functions. Due to this major advantage we have, for the most part of this thesis, chosen a trajectory method to investigate the non-equilibrium dynamics of ultracold Bose gases.

We want to remark that special cases exist, where the exact solution of the time-evolution equations can be given. An example is provided by the Lieb-Liniger solutions for homogeneous one-dimensional systems with contact interactions [262]. However, computing observables for large numbers of particles is still a computational challenge. The solution simplifies only in the strongly correlated regime, where the interacting Bose gas can be mapped onto a free gas of fermions [263–265].

The model

Before the semi-classical field method is explained, we introduce the theoretical model under consideration. Throughout this thesis, we describe an ultracold Bose gas of atoms with mass m in $d = 1, 2, 3$ space dimensions interacting through s -wave collisions by the Hamiltonian

$$H = \int d^d x \left[-\Phi^\dagger \left(\frac{\hbar^2 \nabla^2}{2m} + V(\mathbf{x}) \right) \Phi + \frac{g}{2} \Phi^\dagger \Phi^\dagger \Phi \Phi \right], \quad (2.3)$$

where the time and space dependent fields $\Phi \equiv \Phi(\mathbf{x}, t)$ satisfy Bose commutation relations, $V(\mathbf{x})$ is an external potential¹, and the coupling g measures the interaction strength. In $d = 3$, the coupling constant g is given by $g = g_{3D} = 4\pi\hbar^2 a/m$ [227]. In $d = 2$, one has $g = g_{2D} = -(4\pi\hbar^2/m)[\ln(\mu m a_{2D}^2/4)]^{-1}$ where μ is the chemical potential and a_{2D} is a scattering length in two dimensions. In experiments with ultracold atomic gases, reduced dimensions are established by confining the gas via tight transverse trapping potentials. The conditions that allow to neglect transverse degrees of freedom are $T, \mu < \hbar\omega_T$. For a two-dimensional gas created by trapping a three-dimensional one, with transverse harmonic-oscillator length l_T , the effective 2D scattering length is given by $a_{2D} = 4l_T(\pi/B)^{1/2} \exp\{-\sqrt{\pi}l_T/a\}$, where $B \simeq 0.915$ [266]. In quasi-1D systems, generated by two transverse confining fields, the coupling constant in the limit $l_T \gg a$ is given by $g_{1D} = 2\hbar a \omega_T$ [267].

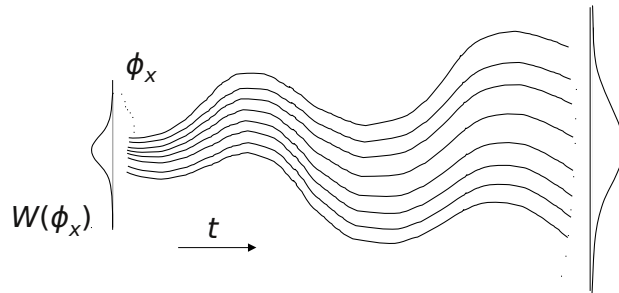


Figure 2.1: Illustration of the decomposition of the time evolution of the Wigner function $W[\phi, \phi^*]$ into Gross-Pitaevskii trajectories.

2.2 Classical field theory

By looking at the Bose-Einstein distribution function, Eq. (2.2), we observe that the limit of large occupation numbers, $n(k) \gg 1$, corresponds to low momenta² $k \ll 1/\lambda_{\text{dB}}$. In this limit, the momentum distribution has the form of a Rayleigh-Jeans distribution,

$$n_{\text{RJ}}(k) = \frac{2mT}{k^2}, \quad (2.4)$$

which is typical for classical waves [268]. Even in the non-equilibrium regime, one can show that the low-momentum region of an ultracold Bose gas can be described by a collection of classical waves [120–122, 269]. The statistical nature of the gas is captured by a probability distribution for the complex field $\phi(\mathbf{x})$ and its conjugate momentum $\phi^*(\mathbf{x})$ on each point in space, called the Wigner function $W[\phi, \phi^*]$ which is positive in this limit. Since quantum effects are small because they arise from coupling to sparsely occupied modes, the dynamics of the Wigner function follows a classical Liouville equation. Moreover, in this so-called truncated Wigner approximation, the evolution of the Wigner function can be represented by many trajectories evolving according to the Gross-Pitaevskii equation

$$i\partial_t \phi(\mathbf{x}, t) = \left[-\frac{\nabla^2}{2m} + V(\mathbf{x}) + g|\phi(\mathbf{x}, t)|^2 \right] \phi(\mathbf{x}, t), \quad (2.5)$$

illustrated in Fig. 2.1. Correlation functions are obtained by averaging over many trajectories. The number of runs is chosen such that the statistical error arising from run-to-run fluctuations is reduced to a small value. Please refer to App. A for details of the numerical techniques and grid units.

The classical field method has proven to be very powerful in describing Bose gases

¹In this thesis we will mainly consider the case $V \equiv 0$. Thereby, we neglect effects from the trapping potential which are inevitable in a realistic experimental set-up. However, for sufficiently large traps, we expect the essential bulk properties of the gas to be well described by our approach.

²In the following we use units where $\hbar = k_B = 1$.

in the degenerate regime, both in equilibrium and out-of-equilibrium since the 1950's [78, 270, 271]. This is particularly true due to its non-perturbative nature, which captures scattering processes of the underlying quantum field theory to all orders in the coupling [257]. Recent examples include dynamics of Bose-Einstein condensation [47], Bose fields at non-zero temperature [136, 272–274], dynamical quantum noise [275], damping of collective excitations [276], vortex formation during Bose-Einstein condensation [138], thermal vortices in a two-dimensional superfluid [125, 245], one dimensional systems [277, 278], squeezing [222], and dynamics of solitons [279]. For a discussion of the condensation properties of the classical field theory, see App. B.

2.2.1 (Quasi-) topological defects

The classical field equation, Eq. (2.5), has some peculiar properties, that shall be discussed in the following. The first one is the existence of topologically nontrivial solutions and nonlinear stationary states [69]. The second one is a mapping to hydrodynamic equations invoking so-called quantum hydrodynamic behaviour [227].

Solitons

First, we discuss quasi-topological one-dimensional solutions of Eq. (2.5), called solitons. They travel with a fixed velocity but are non-dispersive, i.e. stationary in shape [153, 280]. However, due to the interaction with sound they can continuously vanish, which means they are not topologically stable. In dimensions $d > 1$, solitons decay into vortices [87, 281]. For positive coupling constant $g_{1D} > 0$, the solitons are characterised by an exponentially localised density depression with respect to the surrounding bulk matter and a corresponding shift in the phase angle φ of the complex field $\phi = |\phi| \exp\{i\varphi\}$. Depending on the depth of this depression, the 'dark' soliton is either called grey or, for maximum depression, black. On the background of a homogeneous bulk density n it is described by

$$\phi_\nu(x, t) = \sqrt{n} \left[\gamma^{-1} \tanh \left(\frac{x - x_s(t)}{\sqrt{2}\gamma\xi} \right) + i\nu \right], \quad (2.6)$$

where $x_s(t) = x_0 + \nu t$ is the position of the soliton at time t . Here, $\xi = [2mng_{1D}]^{-1/2}$ is the healing length, $\gamma = 1/\sqrt{1 - \nu^2}$ is the 'Lorentz factor' corresponding to the velocity v of the grey soliton in units of the speed of sound, $\nu = v/c_s = |\phi_\nu(vt, t)|/\sqrt{n}$. Being related to the density minimum, ν is also termed the 'greyness' of the soliton, ranging between 0 (black soliton, $|\phi_\nu(vt, t)| = \nu\sqrt{n} = 0$) and 1 (no soliton, $|\phi_\nu(vt, t)| = \sqrt{n}$).

The energy to create a soliton on top of a uniform background yields the intriguing result [227]

$$E_S = \frac{4}{3}nc(1 - \nu^2)^{3/2}. \quad (2.7)$$

For small velocities $\nu \ll 1$, the bracket can be expanded and gives $E_S \sim 4nc/3 - 2nc\nu^2$, which is an expression for a classical point particle with negative mass. The energy of a soliton monotonously decreases with increasing velocity, hinting at a dynamical instability.

Vortices

In $d > 1$ dimensions, topologically stable solutions for ϕ do exist. To see that, we recall that the ground-state manifold given by the minimum of the effective potential $V(\phi) = \mu|\phi|^2 + g|\phi|^4$ of the classical field $\phi(\mathbf{x}) = \sqrt{n(\mathbf{x})}e^{i\varphi(\mathbf{x})}$ requires constant density $n(\mathbf{x}) = n$, but is degenerate in the phase $\varphi(\mathbf{x})$. Of course, the true ground state has a constant phase, and is therefore called topologically trivial. On the other hand, we can consider field configurations, e.g. in two dimensions, which have constant density on the boundary, but varying phase. If we use this freedom to evolve the phase $\varphi(\mathbf{x})$ of the classical field from 0 to 2π when going around the boundary, we arrive at a topologically nontrivial state. Configurations are topologically distinct, because one can not define a continuous function, that transforms one into the other. A phase winding of 2π needs to persist also when we leave the boundary towards the origin. Inevitably, we are lead to the conclusion that the phase can not be defined in the very centre, which justifies the name topological defect. Such a field configuration is still mathematically well defined once the density goes to zero at that point. The stationary state of Eq. (2.5), which fulfils these properties is called a vortex [227].

A singly quantised vortex with circulation $\kappa = \pm 1$ in two dimensions is described, in polar coordinates, by the solution $\phi(r, \varphi) = f(r) \exp\{i\kappa\varphi\}$ of the Gross-Pitaevskii equation Eq. (2.5), where $f(r)$ is real and approaches the square root of the bulk density n for large distances r from the vortex core, whereas $f(r) \sim r$ for $r \rightarrow 0$. A vortex is a stationary solution of Eq. (2.5), evolving as $\phi(\mathbf{r}, t) = \phi(\mathbf{r}, 0) \exp\{-i\mu t\}$ with $\mu = gn$. The velocity field of the vortex $\tilde{\mathbf{v}}(r, \varphi)$ is

$$\tilde{\mathbf{v}}(r, \varphi) = \frac{\kappa}{mr} \mathbf{e}_\varphi. \quad (2.8)$$

Its Fourier transform yields³

$$\tilde{\mathbf{v}}(k, \varphi_k) = \frac{\kappa}{m} \int dr d\varphi \begin{pmatrix} -\sin(\varphi) \\ \cos(\varphi) \end{pmatrix} e^{ikr\cos(\varphi-\varphi_k)} = \frac{\kappa}{m} \frac{2\pi i}{k} \mathbf{e}_{\varphi_k}. \quad (2.9)$$

The energy needed to create a singly quantised vortex in a homogeneous gas in the volume $V = \pi R^2$ is given in Ref. [227] as

$$E_V = \frac{\pi n}{m} \ln \left(\frac{1.46R}{\xi} \right). \quad (2.10)$$

³The Fourier transform can be evaluated with the help of the first-order Bessel function, $\int d\varphi \cos(\varphi) \exp\{i\alpha \cos \varphi\} = 2\pi i J_1(\alpha)$, with normalisation condition $\int d\alpha J_1(\alpha) = 1$.

In $d = 3$ dimensions, point vortices are extended into vortex lines around which the fluid rotates [69]. In the simplest case, a vortex line of length L goes straight from one end of the volume to the other. This requires the excitation energy LE_V . Vortex lines can not end inside the medium, but can form closed loops of all shapes, e.g. rings, ellipses, knots. In fact, Eq. (2.5) supports linear wave excitations on top of vortex lines, so called Kelvin waves [282–285]. Higher dimensional vortices exist whereby the dimensionality of vortex-core geometry is always $d - 2$, for example leading to vortex surfaces in four dimensions.

2.2.2 (Quantum-) hydrodynamics

The presence of vortex excitations reminds us of the properties of classical fluids, which carry angular momentum through so called eddies. In fact, the analogy between the superfluid and the classical fluid can be made even more explicit.

The Gross-Pitaevskii equation Eq. (2.5) can be rewritten in the polar representation

$$\phi(\mathbf{x}, t) = \sqrt{n(\mathbf{x}, t)} e^{i\varphi(\mathbf{x}, t)}, \quad (2.11)$$

which allows to express the particle current $\mathbf{j} = i(\phi^* \nabla \phi - \phi \nabla \phi^*)/2m = n\mathbf{v}$ in terms of the velocity field $\mathbf{v} = \nabla \varphi/m$. Under Eq. (2.11), the field equation transforms into an effective Euler equation for a compressible inviscid (i.e. non-viscous) fluid with modified pressure $\tilde{\mu}$,

$$\partial_t n + \nabla \cdot (n\mathbf{v}) = 0, \quad (2.12)$$

$$\partial_t \mathbf{v} + \mathbf{v} \cdot \nabla \mathbf{v} = -\nabla \tilde{\mu}/m, \quad (2.13)$$

$$\tilde{\mu} \equiv gn - \frac{\Delta \sqrt{n}}{2\sqrt{n}}. \quad (2.14)$$

However, it is important to note that this mapping is valid only outside of vortex cores, where the phase φ is well defined (see Sect. 2.2.1). The compact phase $\varphi \in [0, 2\pi)$, becomes a non-compact velocity potential. As a consequence of this, no quantised vortex creation or annihilation is possible from the dynamics of the effective Euler equation. In fact, due to the Thomson circulation theorem vorticity is locally conserved in an inviscid flow [286].

The effective hydrodynamic equation Eq. (2.14) correctly captures the appearance of collective sound excitations in the Bose gas, which become important on scales larger than the healing length ξ . To see that, we study small density perturbations δn on top of the superfluid density n , $n = n + \delta n$, coupled to small velocity fluctuations $\mathbf{v} = \delta \mathbf{v}$. To first approximation one obtains

$$\partial_t^2 \delta n - \frac{gn}{m} \Delta \delta n = 0, \quad (2.15)$$

and

$$\partial_t^2 \delta \mathbf{v} - \frac{gn}{m} \Delta \delta \mathbf{v} = 0, \quad (2.16)$$

the solutions of which are propagating with dispersion relation $\omega = ck$, with speed of sound $c = \sqrt{gn/m}$.

A non-equilibrium flow features the presence of multiple types of excitations. In order to distinguish longitudinal excitations (sound waves) from rotational excitations (vortices), we continue by discussing a decomposition of the kinetic energy density proposed by Nore et al. [114]. The total kinetic energy

$$E_{\text{kin}} = \frac{m}{2} \int d^d x \langle |\nabla \phi(\mathbf{x}, t)|^2 \rangle, \quad (2.17)$$

can be split, $E_{\text{kin}} = E_v + E_q$, into a ‘classical’ part $E_v = \frac{m}{2} \int d^d x \langle |\sqrt{n} \mathbf{v}|^2 \rangle$ and a ‘quantum-pressure’ component $E_q = \int d^d x \langle |\nabla \sqrt{n}|^2 \rangle / 2m$. The radial energy spectra for these fractions involve the Fourier transform of the generalised velocities $\mathbf{w}_v = \sqrt{n} \mathbf{v}$ and $\mathbf{w}_q = \nabla \sqrt{n}/m$,

$$E_\delta(k) = \frac{m}{2} \int k^{d-1} d\Omega_d \langle |\mathbf{w}_\delta(\mathbf{k})|^2 \rangle, \quad \delta = v, q. \quad (2.18)$$

Note that the superfluid velocity $\mathbf{v} = \nabla \varphi$ of a single vortex diverges as $1/r$ with the distance r from the vortex core. Since it is a potential field it does not reveal a transversal flow component, $\nabla \times \tilde{\mathbf{v}} = 0$ (outside vortex cores). On the contrary, \mathbf{w}_v is not a potential field and the divergence at $r \rightarrow 0$ is circumvented by the function $\sqrt{n(r)}$. Following Ref. [114] the regularised velocity \mathbf{w}_v can be furthermore decomposed into ‘incompressible’ (divergence free) and ‘compressible’ (solenoidal) parts, $\mathbf{w}_v = \mathbf{w}_i + \mathbf{w}_c$, with $\nabla \cdot \mathbf{w}_i = 0$, $\nabla \times \mathbf{w}_c = 0$, to distinguish vortical superfluid and rotationless motion of the fluid. By construction, the generalised velocity of a vortex $\tilde{\mathbf{w}}_v = f(r) \tilde{\mathbf{v}}(r, \varphi)$, Eq. (2.8) has only an incompressible component, since

$$\nabla \cdot \tilde{\mathbf{w}}_v = \nabla f(r) \cdot \tilde{\mathbf{v}}(r, \varphi) + f(r) \nabla \cdot \tilde{\mathbf{v}}(r, \varphi) = 0. \quad (2.19)$$

The first term vanishes due to the transversal nature of the vortex velocity field, the second one equals zero because the superfluid velocity is a potential field. The density of incompressible energy $|\tilde{\mathbf{w}}_i|$ of a vortex is constant up to the healing length and then falls off like $1/r^2$ for $r \rightarrow \infty$. Sound waves, see Eqs. (2.15) and (2.16), are purely compressible excitations. Their oscillating density and phase profiles are visible as scattered maxima and minima in the compressible energy density in position space.

For comparison of the kinetic-energy spectrum with the single-particle spectra $n(k)$, we determine occupation numbers corresponding to the different energy fractions

as

$$n_\delta(k) = k^{-d-1} E_\delta(k), \quad \delta \in \{i, c, q\}. \quad (2.20)$$

Now, we calculate $k^2 n(k)$ in terms of generalised velocities $\mathbf{w}_\delta, \delta \in \{v, q\}$,

$$\begin{aligned} k^2 n(k) &= \langle \mathcal{F}(\mathbf{w}_v e^{i\varphi})(k) \mathcal{F}(\mathbf{w}_v e^{i\varphi})^*(k) \rangle \\ &\quad + 2\Re \langle i \mathcal{F}(\mathbf{w}_v e^{i\varphi})(k) \mathcal{F}(\mathbf{w}_q e^{i\varphi})^*(k) \rangle \\ &\quad + \langle \mathcal{F}(\mathbf{w}_q e^{i\varphi})(k) \mathcal{F}(\mathbf{w}_q e^{i\varphi})^*(k) \rangle. \end{aligned} \quad (2.21)$$

\Re denotes the real part and \mathcal{F} the Fourier transform. The middle term vanishes since the expectation value is purely imaginary due to isotropy. It follows that

$$\begin{aligned} k^2 n(k) &= \langle (\mathbf{w}_v * \mathcal{F}(e^{i\varphi}))(k) (\mathbf{w}_v * \mathcal{F}(e^{i\varphi}))^*(k) \rangle \\ &\quad + \langle (\mathbf{w}_q * \mathcal{F}(e^{i\varphi}))(k) (\mathbf{w}_q * \mathcal{F}(e^{i\varphi}))^*(k) \rangle. \end{aligned} \quad (2.22)$$

Removing correlations between phase and phase velocity, the main contribution to the 4-point correlation functions arises from terms of the form

$$\langle \mathbf{w}_\delta(|\mathbf{p} - \mathbf{k}|) \mathbf{w}_\delta(|\mathbf{q} - \mathbf{k}|) \rangle \langle \mathcal{F}(\exp\{i\varphi\})(p) \mathcal{F}(\exp\{i\varphi\})^*(q) \rangle, \quad (2.23)$$

$\delta \in \{v, q\}$. In the superfluid regime, the phase of the field is a slowly varying function in position space. Therefore, the $\mathcal{F}(\exp\{i\varphi\})^*(q)$ -terms are strongly peaked at zero momentum, effectively acting as regularised delta functions under the convolution. Hence,

$$k^2 n(k) \simeq \langle |\mathbf{w}_v(k)|^2 \rangle + \langle |\mathbf{w}_q(k)|^2 \rangle. \quad (2.24)$$

In situations of strong phase fluctuations $\mathcal{F}(\exp\{i\varphi\})^*(q)$ develops a width, that can be estimated by $q_0 \sim 1/r_0$, with phase coherence length r_0 , which leads to a modification of Eq. (2.24) on scales $k < q_0$.

In this section, we have presented the classical-field method for ultracold bosons and discussed some important properties of the corresponding classical field equation. The definitions and considerations introduced here, will later be applied to analyse the full non-equilibrium time evolution of an ultracold Bose gas. Before that, we spend some time on the introduction of non-thermal fixed points and dynamic equations for correlation functions.

2.3 Non-thermal fixed points

Most generally, a non-thermal fixed point can be defined as a non-equilibrium quasi-stationary state of a many-body system [287, 288]. In reminiscence of equilibrium fixed points, one requires additional power-law scaling of correlation functions [28, 29, 53]. From turbulence research, it is known that such states can be created by

a constant flux of a conserved quantity in momentum space. The most prominent example of this kind is fully developed classical fluid turbulence. It comprises a quasi-stationary flow of energy from large to small scales [40]. The corresponding energy spectrum exhibits the famous Kolmogorov-Obukhov scaling, which shall be recalled in the following [34,35].

2.3.1 Classical Kolmogorov turbulence

The Navier-Stokes equation describes the hydrodynamic motion of Newtonian fluids and gases, such as ocean water, atmospheric clouds and interstellar dust. It is long known to feature turbulent vortical motion in which the trajectories of individual particles show chaotic behaviour. A quote which has been attributed to Werner Heisenberg, and was given in a similar form by Horace Lamb, mirrors the complexity of the matter. It says, "When I meet God, I am going to ask him two questions: Why relativity? And why turbulence? I really believe he will have an answer to the first." A review of interesting historical aspects of classical turbulence can be found in Ref. [289].

A successful approach to turbulent phenomena is given by the concept of a cascade, i.e. a quasi-local transport in momentum space. This way of thinking was initiated by Richardson (1922), who proposed that a turbulent flow is fed by an energy input on large scales [40]. This energy is transported to smaller scales by the break-up of large vortices into smaller ones. This process continues throughout the so called inertial range until energy is dissipated into heat. The length scale where dissipation sets in is called Kolmogorov scale, named after A. N. Kolmogorov, who used the ideas of Richardson to develop a scaling theory of turbulence in 1941. It is based on the insight, that the Richardson cascade yields a self-similar distribution of energy. By using dimensional analysis Kolmogorov found that $E(k) \sim k^{-5/3}$.

Suppose a turbulent fluid of density ρ is driven by an energy input on large scales and a dissipation on small scales. The energy flux density ϵ at the intermediate length scale L can be estimated by a characteristic velocity V_L and a characteristic time T_L as

$$\epsilon \sim \rho \frac{V_L^2}{T_L} \sim \rho \frac{V_L^3}{L}. \quad (2.25)$$

The total kinetic energy density E_L observed at the scale L is $\sim \rho V_L^2$, which can also be expressed in terms of the spectral energy density $E(k)$ as

$$E_L \sim \rho V_L^2 \sim \rho^{1/3} \epsilon^{2/3} L^{2/3} \sim \int_{1/L}^{\infty} dk' E(k'). \quad (2.26)$$

One finds upon inserting $k = 1/L$ and differentiating both sides with respect to k , that

$$E(k) \sim \rho^{1/3} \epsilon^{2/3} k^{-5/3}, \quad (2.27)$$

which is the celebrated Kolmogorov-Obukov 5/3-law [34,35]. It is a prime exam-

ple of self-similarity far from thermal equilibrium. Experiments strongly support the theory, see e.g. Ref. [37]. Nevertheless, a rigorous field theoretic derivation of the Kolmogorov-Obukov law is still missing. In this context, renormalisation group approaches might be a promising tool to capture the essential properties of turbulence, quasi-stationarity and scaling [39].

2.3.2 Superfluid turbulence

Superfluid turbulence or quantum turbulence refers to the turbulent behaviour of quantised vortices [18, 95]. It has been the subject of extensive studies in the context of helium [76, 82, 96–100, 103, 104] and, more recently, dilute Bose gases [90, 107–111]. Particularly interesting is the relation of quantum turbulence to classical fluid turbulence. The observation of a 5/3-law in experiments with superfluid helium [102, 112, 113] and theoretical models [114–118] received much attention [18]. The quasi-classical behaviour is believed to be caused by a polarisation of quantised vortices, i.e. their grouping into bundles, thus mimicking a continuous distribution of vorticity on large scales [290, 291]. Whether polarisation of quantised vortices is a self-organised process or whether it needs to be imprinted by specific steering mechanisms (e.g. locking to the turbulent normal fluid [292, 293]) is currently under debate. Alternatively, quantum turbulence might enter a stage characterised by a random distribution of vorticity, called Vinen turbulence, which is characterised by an energy spectrum defined in Eq. (2.26) [102, 104]

$$E(k) \sim k^{-1}. \quad (2.28)$$

This situation could be especially important for the case of dilute ultracold gases [90, 107–109, 111], where the number of vortices is much smaller than in superfluid helium. In dilute Bose gases, the momentum distribution $n(k)$ is more accessible than the energy spectrum, since it can be obtained from time-of-flight density images [294]. Therefore, we will present an approach that directly addresses the computation of this quantity in the following.

2.3.3 Wave turbulence

Wave turbulence is directly concerned with the analysis of non-thermal fixed points in the (quasi-) particle momentum distribution and therefore well suited to study turbulent ultracold quantum gases. In the beginning of this chapter, we pointed out the possibility to describe the many-body evolution in terms of dynamic equations for correlation functions like the momentum distribution. Although desirable, this approach poses a serious challenge for theoretical physicists. Far from equilibrium one can not treat non-equilibrium dynamics as a small perturbation of the equilibrium state. Additionally, one might not be able to rely on a perturbation expansion which requires a weak coupling. The escape from these restrictions is generally seen in refined approximations which allow to take complex correlations into account over a sufficiently long period of evolution. Here, we review the work of Scheppach et al. [29] which was motivated by the original proposal for non-thermal

fixed points in relativistic quantum fields [28]. They consider Kadanoff-Baym dynamic equations for time-dependent Green functions of an ultracold Bose gas to extract quasi-stationary momentum distributions $\dot{n}(\mathbf{k}, t) = 0$. Furthermore, they investigate the possibility of universal power-law behaviour

$$n(s\mathbf{k}) = s^{-\zeta}n(\mathbf{k}), \quad (2.29)$$

in a certain regime of momenta \mathbf{k} . Here s is some positive, real number and ζ a universal exponent which was determined from the dynamic equations for the field correlation functions. The main goal of this section is to discuss the different exponents which resulted in different momentum regimes, see Fig. 2.3 in Chap. 1.

Weak wave turbulence

Suppose the generic case that for sufficiently large momenta $|\mathbf{k}| = k$ occupation numbers $n(\mathbf{k}, t) = \langle \Phi^\dagger(\mathbf{k}, t)\Phi(\mathbf{k}, t) \rangle$ are small enough to justify a perturbative treatment. Then, for a given coupling g , the quantum Boltzmann equation

$$\begin{aligned} \partial_t n_{\mathbf{k}} &= I(\mathbf{k}, t), \quad (2.30) \\ I(\mathbf{k}, t) &= \int d^d p d^d q d^d r |T_{\mathbf{k}\mathbf{p}\mathbf{q}\mathbf{r}}|^2 \delta(\mathbf{k} + \mathbf{p} - \mathbf{q} - \mathbf{r}) \delta(\omega_{\mathbf{k}} + \omega_{\mathbf{p}} - \omega_{\mathbf{q}} - \omega_{\mathbf{r}}) \\ &\quad \times [(n_{\mathbf{k}} + 1)(n_{\mathbf{p}} + 1)n_{\mathbf{q}}n_{\mathbf{r}} - n_{\mathbf{k}}n_{\mathbf{p}}(n_{\mathbf{q}} + 1)(n_{\mathbf{r}} + 1)], \quad (2.31) \end{aligned}$$

describes the evolution of $n_{\mathbf{k}} \equiv n(\mathbf{k}, t)$ under the effects of collisions. In our case, the transition matrix element squared $|T_{\mathbf{k}\mathbf{p}\mathbf{q}\mathbf{r}}|^2$ is a numerical constant proportional to g^2 and thus independent of momenta. Zeroes of the scattering integral $I(\mathbf{k})$ correspond to fixed points of the time evolution within the regime of applicability of the quantum Boltzmann equation [41]. Most prominent amongst these are the thermal fixed point corresponding to the system in thermal equilibrium and the trivial fixed point where the occupation number is independent of \mathbf{k} . At both fixed points the scattering integral vanishes and $n(\mathbf{k}, t)$ becomes independent of t . Note that both, the trivial distribution and the thermal Bose-Einstein distribution in the Rayleigh-Jeans regime, for $\omega(\mathbf{k}) \sim k^2$, show a power-law behaviour of the form (2.29) with $\zeta = 0$ and $\zeta = 2$, respectively.

The theory of weak wave turbulence [41] allows to analytically derive further, non-thermal fixed points at which the occupation number $n(\mathbf{k})$ obeys a scaling law of the form (2.29) and, in general, $\zeta \neq 2$. As in classical turbulence of an incompressible fluid one assumes that universal scaling appears within a certain regime of momenta, the inertial range. According to this picture, outside the scaling regime excitation quanta enter the system from an external source and/or leave it into a sink, whereas there are no sources and sinks within the inertial interval. Instead, quanta are transported from momentum shell to momentum shell without loss or gain. To a good approximation, this process is described by a continuity equation in momentum space, with a momentum-independent, radially oriented current

vector.⁴ A central aspect of weak-wave-turbulence theory is that the quantum Boltzmann equation can be cast into different such equations [41], for the radial number density $N(k) = (2k)^{d-1}\pi n(k)$ and the energy density $E(k) = (2k)^{d-1}\pi\varepsilon(k)$, $\varepsilon(k) = \omega(k)n(k)$,

$$\partial_t N(k, t) = -\partial_k Q(k), \quad (2.32)$$

$$\partial_t E(k, t) = -\partial_k P(k). \quad (2.33)$$

Depending on whether the radial particle current $Q(k) = (2k)^{d-1}\pi Q_k(k)$ or energy current $P(k) = (2k)^{d-1}\pi P_k(k)$ is taken to be independent of k , one derives different scaling exponents. The resulting exponents⁵ are

$$\zeta_Q^{\text{UV}} = d - 2/3, \quad \zeta_P^{\text{UV}} = d. \quad (2.34)$$

These exponents can be obtained by simple power counting: Combining Eqs. (2.30) and (2.32) gives the radial relation $\partial_k Q(k) \sim k^{d-1}I(k)$ which implies that stationarity requires $k^d I(k)$ to become k -independent, i.e. scale like k^0 . Counting all powers of k in $I(k)$, Eq. (2.31), in the wave-kinetic regime where the terms of third order in the occupation numbers dominate the scattering integral, this requires $n(k) \sim k^{-d+2/3}$. Analogously one infers the exponent ζ_P^{UV} from the balance equation (2.33) for the energy density $\varepsilon(k) \sim k^2 n(k)$. Despite this simple procedure, the existence of the respective scaling solutions has to and can be derived rigorously from the quantum Boltzmann equation by means of Zakharov conformal integral transforms [41]. We note that, similarly as in classical turbulence, the case $d = 2$ is special, where the scaling exponent ζ_P^{UV} equals that of a thermal distribution in the Rayleigh-Jeans regime.

Strong wave turbulence

Given a positive scaling exponent ζ momentum occupation numbers $n(k) \sim k^{-\zeta}$ grow large in the IR regime of small k . As a consequence, for a given coupling g , the quantum Boltzmann equation fails in this regime, where contributions to the scattering integral $I(k)$ which are of higher order than $g^2 n^3$ become important.

To find scaling solutions in the IR, an approach beyond kinetic theory is required [42, 43, 295, 296]. This is available through quantum-field dynamic equations derived from the two-particle irreducible (2PI) effective action or Φ -functional [297–299] beyond the 2-loop order in the expansion of the self-energy [215, 249–258, 300]. See Ref. [29] for details of the procedure summarised in the following⁶. The 2PI

⁴Note that justification of this assumption, i.e., locality of the transport, needs to be checked for each particular wave-turbulent solution [41].

⁵The superscript UV (ultraviolet) in Eq. (2.34) refers to the regime of large momenta where the description in terms of a kinetic equation is expected to be accurate.

⁶Here, we use four-vector notation $x = (x_0, \mathbf{x})$ and averages denote connected averages defined as $\langle \Phi^\dagger(x)\Phi(y) \rangle_c \equiv \langle \Phi^\dagger(x)\Phi(y) \rangle - \langle \Phi^\dagger(x) \rangle \langle \Phi(y) \rangle$. We remark that it has been shown in Ref. [26]

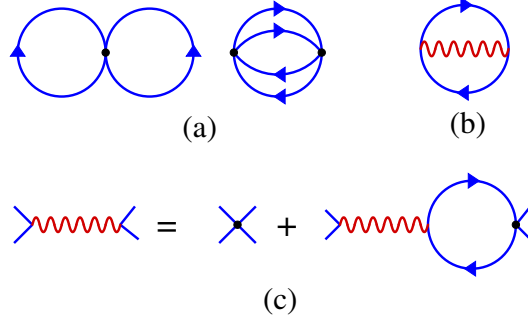


Figure 2.2: 2PI diagrams of the loop expansion of $\Gamma_2[G]$. (a) The two lowest-order diagrams of the loop expansion which lead to the quantum Boltzmann equation. Black dots represent the bare vertex $\sim g\delta(x-y)$, solid lines the propagator $G(x, y)$. (b) Diagram representing the resummation approximation which, in the IR, replaces the diagrams in (a) and gives rise to the scaling of the T -matrix in the IR regime. (c) The wiggly line is the scalar propagator which is represented as a sum of bubble-chain diagrams.

equations include the Dyson equation for the time-ordered Green function $G(x, y) = \langle \mathcal{T} \Phi^\dagger(x) \Phi(y) \rangle_c$, from which a time evolution equation (2.30) for $n(\mathbf{k})$ is derived. As before one considers zeros of the scattering integral which in the dynamic theory reads

$$I(\mathbf{k}) = \int d\omega [\Sigma^\rho(k)F(k) - \Sigma^F(k)\rho(k)]. \quad (2.35)$$

Here, $k \equiv (\omega, \mathbf{k})$, and ρ and F are the spectral and statistical components of G , respectively, defined in coordinate space by $F(x, y) = \langle \{\Phi^\dagger(x), \Phi(y)\} \rangle_c / 2$, $\rho(x, y) = i \langle [\Phi^\dagger(x), \Phi(y)] \rangle_c$, $G(x, y) = F(x, y) - (i/2) \text{sgn}(x_0 - y_0) \rho(x, y)$. The corresponding contributions to the self energy $\Sigma(x, y) = 2i\delta\Gamma_2/\delta G(x, y)$ are defined in terms of G through a loop expansion of the 2PI effective action, see Fig. 2.2. Resumming an infinite set of such loop diagrams contributing to the 2PI effective action, leads to a non-perturbative, effectively renormalised coupling in the dynamic equations [28, 29]. To derive the scaling solutions of the dynamic equations for Green functions $G(\omega, \mathbf{k})$ one assumes separate scaling of its spectral and statistical components according to $\rho(s^z\omega, s\mathbf{k}) = s^{-2+\eta}\rho(\omega, \mathbf{k})$, $F(s^z\omega, s\mathbf{k}) = s^{-2-\kappa}F(\omega, \mathbf{k})$, $s > 0$. Here, z is the dynamical scaling exponent accounting for a different scaling in ω as compared to \mathbf{k} . The scaling exponent ζ is related to κ by $n(s\mathbf{k}) = s^{z-2-\kappa}n(\mathbf{k})$. κ is derived from the condition that the scattering integral (2.35) vanishes, making use of Zakharov transformations, while the anomalous scaling exponent η remains undetermined by this but, for the first, are assumed to be vanishingly small. The IR scaling exponents for radial quasi-particle flow (Q) and radial energy flow (P)

that the disconnected contributions do not alter the non-thermal fixed-point predictions in Ref. [29].

in d dimensions were predicted in Ref. [29] to be

$$\zeta_Q^{\text{IR}} = d + 2, \quad \zeta_P^{\text{IR}} = d + 2 + z. \quad (2.36)$$

In situations where a quasi-particle picture applies the dynamical exponent z corresponds to the homogeneity index of ω : $\omega(s\mathbf{k}) = s^z\omega(\mathbf{k})$. In this case, the non-perturbatively resummed effective coupling can be related to the diagonal elements of an effective many-body T -matrix, $T_{\mathbf{k}\mathbf{p}\mathbf{q}\mathbf{r}}^{\text{eff}} \equiv T_{\mathbf{k}+\mathbf{p},\mathbf{q}+\mathbf{r}}^{\text{eff}}$ in the kinetic Boltzmann formulation. In the scaling regimes this scales as

$$|T_{\mathbf{k}}^{\text{eff}}| \equiv |T_{\mathbf{k},\mathbf{k}}^{\text{eff}}| \sim |gCk^{z-2}/[1 + C'gk^{d-2}n_{\mathbf{k}}]|, \quad (2.37)$$

$k = |\mathbf{k}|$, where C' is some constant which fine-tunes the position of the transition from UV to IR scaling. Generalising the validity criterion of the kinetic equation, Eq. (2.30), given in Ref. [130] to arbitrary dimensions

$$g \int_0^k d^d k' n(\mathbf{k}') \ll \frac{k^2}{2m}, \quad (2.38)$$

and assuming a scaling momentum distribution $n(k) \sim k^{-\zeta}$ this translates into $2\Omega_d m g k^{d-2} n(k) \ll 1$, with Ω_d the surface of a sphere in d dimensions, which shows exactly the same scaling as Eq. (2.37).

For small n_k and $z = 2$ one recovers the UV case discussed in the previous section, i.e., $T_{\mathbf{k}}^{\text{eff}}$ is a constant independent of k . For large n_k , the second term in the denominator dominates which, assuming scaling of $n_{\mathbf{k}} \sim k^{-\zeta}$, implies a power-law behaviour $|T_{\mathbf{k}}^{\text{eff}}|^2 \sim k^{2(\zeta-d+z)}$ and, in turn, the modified scaling (2.36) of $n_{\mathbf{k}}$ in the infrared regime of small wave numbers as compared to the UV regime discussed before. Physically, the renormalised T -matrix implies a reduction of the effective interaction strength in the IR regime of strongly occupied modes [28]. As a consequence, single-particle occupation numbers rise, towards smaller wave numbers, in an even steeper way than in the weak-turbulence regime.

In Fig. 2.3, we summarise the resulting non-thermal fixed point predictions for an ultracold Bose gas in d dimensions given in Ref. [29].

Due to the great computational effort, it has up to date not been possible to confirm the scaling analysis Eq. (2.36) by numerically integrating the 2PI-dynamic equations. However, as we will show in the next chapter, this challenge can be met by the classical-field method introduced in Sect. 2.2.

As an outlook, we point out the possibility to obtain the turbulent scaling solutions from the viewpoint of the renormalisation group [26, 27, 53]. Turbulence has served, since the seminal work of Kolmogorov [34, 35, 37], as one of the first phenomena to develop renormalisation-group techniques out-of-equilibrium. The effectively local transport processes in momentum space, which are at the basis of turbulent cascades, immediately suggest themselves for a renormalisation group analysis. A promising approach might be a formulation in terms of the functional

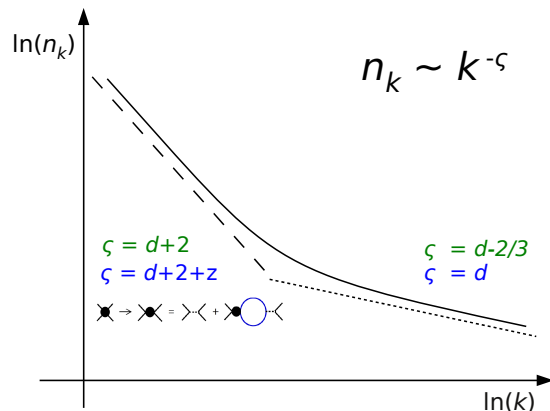


Figure 2.3: Sketch of the single-particle mode occupation number $n(k)$ as a function of the radial momentum k for the non-thermal fixed point solutions predicted in Ref. [29]. At large momenta the theory coincides with weak wave turbulence, predicting the Kolmogorov-Zakharov spectra $\zeta = d - 2/3$ (particle flux) and $\zeta = d$ (energy flux). At low momenta the theory gives new scaling solutions $\zeta = d + 2$ (particle flux) and $\zeta = d + 2 + z$ (energy flux), termed strong turbulence.

renormalisation group [301–307]. Moreover, it has been shown, that dynamic equations can be derived which are similar in structure to the equations obtained from the 2PI effective action. The key idea of the approach is to consider the generating functional for Green functions where all times are smaller than a maximum time τ , implying the closed time path to be cut off at τ [259, 260].

2.3.4 Heuristic derivation

Before this chapter closes with a summary we present an alternative derivation for the strong turbulence scaling exponents, see Eq. (2.36). It is based on a heuristic argument formulated in analogy to the derivation of the Kolmogorov 5/3-law in Sect. 2.3.1. Suppose a turbulent superfluid, which exhibits an inverse particle cascade with stationary particle flux on scale L given by

$$Q_L = \frac{N_L}{T_L} \quad (2.39)$$

with total particle number up to scale L denoted by N_L . The characteristic time for the motion of particles at scale L is $T_L \sim 1/\omega_L \sim L^2$ for free particles⁷ $\omega_k \sim k^2$.

⁷Assuming the presence of quantised vortices, ω_L might also be taken as the turnaround frequency of particles in a vortex $\omega_L \sim v_L/L$, with vortex velocity profile $v_L \sim 1/L$. This again gives $T_L \sim 1/\omega_L \sim L^2$.

Hence, for constant particle flux $Q_L \equiv Q$, we get

$$N_L \sim QL^2 \sim \int_{1/L}^{\infty} dk' k'^{d-1} n(k'). \quad (2.40)$$

One finds upon inserting $k = 1/L$ and differentiating both sides with respect to k , that

$$n(k) \sim k^{-d-2}, \quad (2.41)$$

which coincides with ζ_Q^{IR} in Eq. (2.36). The same idea can be applied to the case of an energy cascade in the superfluid.

$$P_L = \frac{E_L}{T_L} = E_L \omega_L, \quad (2.42)$$

then

$$E_L \sim \frac{P}{\omega_L} \sim \int_{1/L}^{\infty} dk' k'^{d-1} \omega_{k'} n(k'). \quad (2.43)$$

By taking $\omega_L \sim L^{-z}$, one finds upon inserting $k = 1/L$ and differentiating both sides with respect to k , that

$$n(k) \sim k^{-d-2z}, \quad (2.44)$$

which agrees with Eq. (2.36) only for the case $z = 2$.

Here, we want to point out the possibility for obtaining another power law. To do that, we come back to the case of a particle cascade. We saw that the characteristic time T_L is connected to a characteristic velocity, $T_L \sim 1/\omega_L \sim L^2$. To obtain $\zeta = d + 2$, we assumed free streaming of particles. A second natural guess would be that the characteristic velocity in a Bose-Einstein condensate is given by the speed of sound $v_L = c_s$. Then,

$$N_L \sim QL \sim \int_{1/L}^{\infty} dk' k'^{d-1} n(k'). \quad (2.45)$$

One finds upon inserting $k = 1/L$ and differentiating both sides with respect to k , that

$$n(k) \sim k^{-d-1}. \quad (2.46)$$

This scaling behaviour was not predicted by the quantum field theory reviewed in Sect. 2.3.3. However, we will see later that it appears in one-dimensional Bose gases and systems with two species subject to an inverse particle cascade. We end these considerations on a heuristic derivation of turbulent scaling with the remark that these calculations are just meant to give an intuitive approach of a complicated matter, rather than an explanation.

2.4 Summary

This chapter was devoted to the introduction of general properties and dynamics of ultracold Bose gases in one, two, and three spatial dimensions. After a brief review of experimental and theoretical developments in the field, we described the classical field method. This approach will be extensively used in the subsequent chapters to study the non-equilibrium time evolution. We then focused on the discussion of (quasi-) topological excitations as well as hydrodynamical features in order to prepare the reader for the later discussion. Finally, we introduced the concept of non-thermal fixed points and their manifestations in classical- and superfluid turbulence. This provided the background for a discussion of recent predictions on wave-turbulent scaling solutions for an ultracold Bose gas. After that, we gave an intuitive derivation of these scaling laws. The dynamical appearance of quasi-stationary scaling solutions, as well as their microscopic origin and associated transport phenomena will be a central topic of this thesis. In the next chapter, we will present results for the case of an ultracold Bose gas in two and three dimensions.

Superfluid turbulence as a non-thermal fixed point

Here, we study non-equilibrium dynamics in two and three dimensional dilute Bose gases by means of simulations in the classical-wave limit of the underlying quantum field theory (see Sect. 2.2). We show the development of a bimodal scaling of the single-particle momentum distribution after an interaction quench. The results are compared to analytical predictions presented in Ref. [29] and reviewed in Sect. 2.3. While we find excellent agreement, our results provide an interpretation of the dynamical fixed points proposed in Refs. [28, 29] for the case of an ultracold Bose gas: The appearance of non-perturbative infrared scaling reflects the presence of a dilute gas of vortices. This is the main result of this chapter. Moreover, the power spectra of underlying compressible excitations suggest an understanding in terms of acoustic turbulence [41] on top of the vorticity-bearing quasi-condensate.

In Chaps. 4, 5, 6 and 7, we present an in-depth study of the effects highlighted in the present chapter. This includes an extensive analysis of scaling properties of vortex excitations, the approach and decay of the non-thermal fixed point, as well as turbulent features appearing during the time evolution.

3.1 Observation of wave-turbulent spectra

As discussed in Sect. 2.2, a dilute superfluid Bose gas can be described, in the classical-wave limit, by the Gross-Pitaevskii equation, Eq. (2.5). According to the truncated Wigner method, the initial values for the real and imaginary parts of the field $\phi(\mathbf{k}, 0)$ are randomly chosen from a Gaussian distribution with width $1/2$, centred around $\sqrt{n(\mathbf{k}, 0)} \exp\{i\varphi(\mathbf{k}, 0)\}$, where $n(\mathbf{k}, t) = \langle \phi^\dagger(\mathbf{k}, t) \phi(\mathbf{k}, t) \rangle$ is the occupation number at time t and $\varphi(\mathbf{k}, 0)$ is a random phase angle. To induce transport from small to large wave numbers, only a few modes near $\mathbf{k} = 0$ were chosen to be occupied at the initial time with $n(\mathbf{k}, 0) \gg 1$. Such an initial state represents a macroscopically depleted Bose-Einstein condensate and can be prepared, e.g., by Bragg scattering of photons from a Bose-Einstein condensate in equilibrium [308–310].

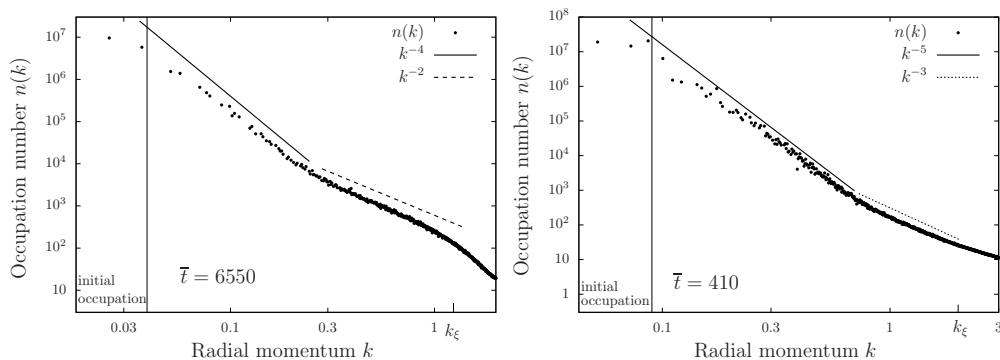


Figure 3.1: Single-particle mode occupation numbers as functions of the radial momentum k at intermediate times of the evolution. Note the double-logarithmic scale. Left panel: For the case of $d = 2$ dimensions. Parameters are: $\bar{g} = 3 \cdot 10^{-5}$, $N = 10^8$, $N_s = 256$. The number of runs ~ 100 . We show the development of a scaling $n(k) \sim k^{-4}$ at low momenta is followed by a scaling with $n(k) \sim k^{-2}$ at larger wave numbers. Right panel: For the case of $d = 3$ dimensions. Parameters are: $\bar{g} = 8 \cdot 10^{-4}$, $N = 10^9$, $N_s = 128$. The number of runs ~ 10 . We show the presence of a bimodal scaling $n(k) \sim k^{-5}$ at low momenta and $n(k) \sim k^{-3}$ at larger wave numbers.

During the evolution to a new equilibrium state, energy is transported to modes with higher wave number, and, given appropriate interaction strength, one observes quasi-stationary distributions to develop prior to final thermalisation.

Power-law behaviour is found in the momentum distributions of particles and energy as we discuss in the following. Fig. 3.1 shows the distribution of the ensemble- and angle-averaged single-particle spectrum at intermediate times of the evolution

$$n(k) = \int d^{d-1}\Omega_d(\mathbf{k}) \langle \phi^*(\mathbf{k})\phi(\mathbf{k}) \rangle_{\text{ensemble}}, \quad (3.1)$$

as a function of radial momentum $k = |\mathbf{k}|$, on a double-logarithmic scale. ($d\Omega_d(\mathbf{k})$ denotes the angular differential in d -dimensional k -space.) During the initial evolution the mode occupations gradually spread to larger wave numbers. At $\bar{t} = 6550$ (2D) and $\bar{t} = 410$ (3D) a power-law regime $n(k) = k^{-\zeta}$ is observed. These power laws are found to be in agreement with the analytical prediction of Ref. [29]. While in the ultraviolet the exponent $\zeta^{\text{UV}} = d = 2$ (left panel) and $\zeta^{\text{UV}} = d = 3$ (right panel) exhibits weak wave turbulence, in the infrared the exponent confirms the result $\zeta = d + 2 = 4$ (left panel) and $\zeta = d + 2 = 5$ (right panel), see Eq. (2.36). These corroborate results for a relativistic model studied in [28]. Note that in $d = 2$, the weak-turbulence exponent $\zeta^{\text{UV}} = 2$ is identical to that in thermal equilibrium in the Rayleigh-Jeans regime, $n(k) \sim T/\omega \sim T/k^2$ [41]. Meanwhile, similar turbulent spectra have been found to appear for relativistic [55] and non-relativistic systems [51, 140, 167], which will be discussed in the successive chapters. From the point of view of wave turbulence the appearance of power-law dependent spectra is connected to the presence of a transport of particles and energy in k -space. In a

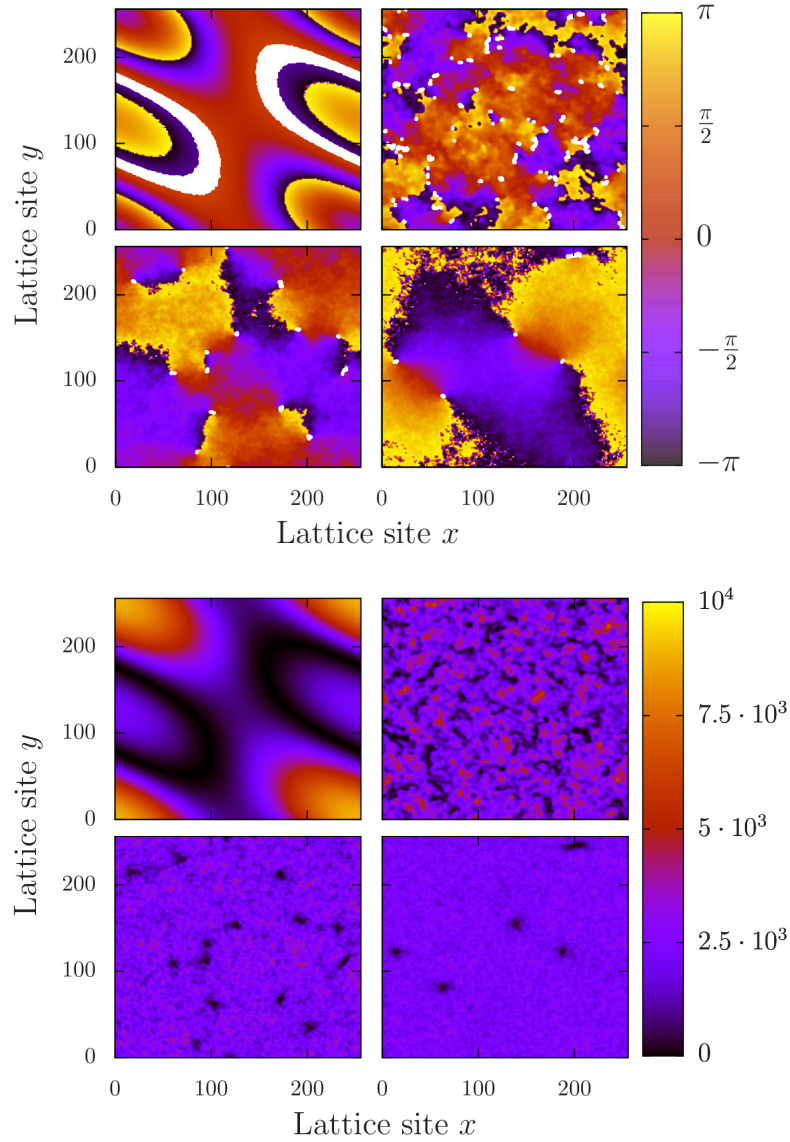


Figure 3.2: Phase angle $\varphi(\mathbf{x}, t)$ (upper panel) and spatial density $n(\mathbf{x})$ (lower panel) at four times during a single run of the simulations in $d = 2$. Parameters are the same as Fig. 3.1(left panel). Shown times are: 1. $\bar{t} = 26$ (top left): Ordered phase shortly after initial preparation. 2. $\bar{t} = 820$ (top right): After creation of vortex-antivortex pairs. 3. $\bar{t} = 6550$ (bottom left): During critical slowing down of the vortex-antivortex annihilation. 4. $\bar{t} = 10^5$ (bottom right): Low-density vortex-antivortex pairs before final thermalisation.

closed many-body system, these transport processes are inevitably going to come to rest at the time when equilibration sets in. Both of these aspects will be discussed in detail in Chap. 5.

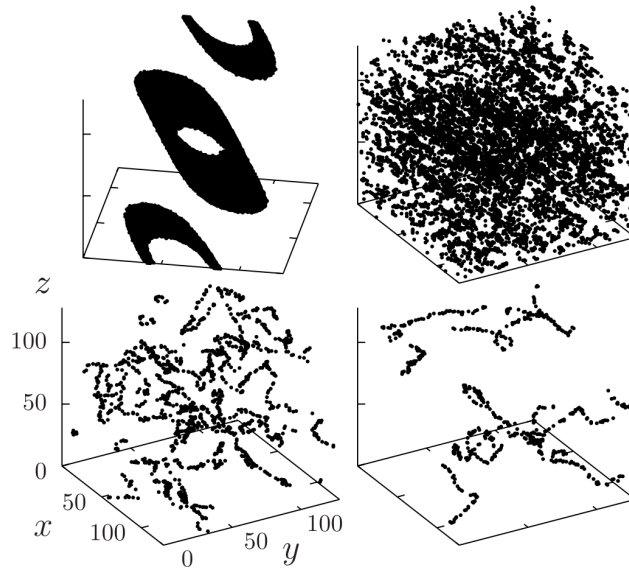


Figure 3.3: Snapshots of a single run of the evolution in $d = 3$ dimensions. The black dots mark positions where the density falls below 5% of the mean density \bar{n} . Parameters are the same as Fig. 3.1(right panel). 1. $\bar{t} = 0$ (top left) 2. $\bar{t} = 103$ (top right) 3. $\bar{t} = 410$ (bottom left) 4. $\bar{t} = 1640$ (bottom right)

3.2 Observation of vortices

Here, we will continue in a different direction. Since wave turbulence is based on the properties of correlation functions, we have used the classical field method to compute the ensemble averaged correlation function Eq. (3.1). However, the trajectory approach enables us to investigate single trajectories as well. Doing so, we reveal that quantised vortices appear during the intermediate stage of the non-equilibrium evolution. For videos of the evolution see [311]. Characteristic properties of vortices, see Sect. 2.2.1 and App. A, can be used to track their creation, motion and decay. To exhibit the rotational flow we use the polar representation $\phi(\mathbf{x}, t) = \sqrt{n(\mathbf{x}, t)} \exp\{i\varphi(\mathbf{x}, t)\}$ of the field in terms of the density $n(\mathbf{x}, t)$ and a phase angle $\varphi(\mathbf{x}, t)$. In Fig. 3.2, we show the phase angle $\varphi(\mathbf{x}, t)$ and the spatial density $n(\mathbf{x})$ during a single run in $d = 2$ dimensions, while in Fig. 3.3 the evolution in $d = 3$ is illustrated by the near-zero-density points. Many singly quantised vortex-antivortex pairs (vortex rings) are formed once the initial coherent wave has developed to form shock-wave-like fronts. During the later evolution, the pairs mutually annihilate at a substantially decreasing rate. After the last pair has vanished the gas thermalises. In $d = 3$, the system develops a dense chaotic tangle. Decreasingly tangled vortex lines are observed during a near-stationary evolution.

To understand these findings in the context of superfluid we analyse kinetic-energy spectra as proposed in [114] and discussed in Sect. 2.2 and App. A. This enables us to distinguish different excitations present in the gas. In the cases we consider, the

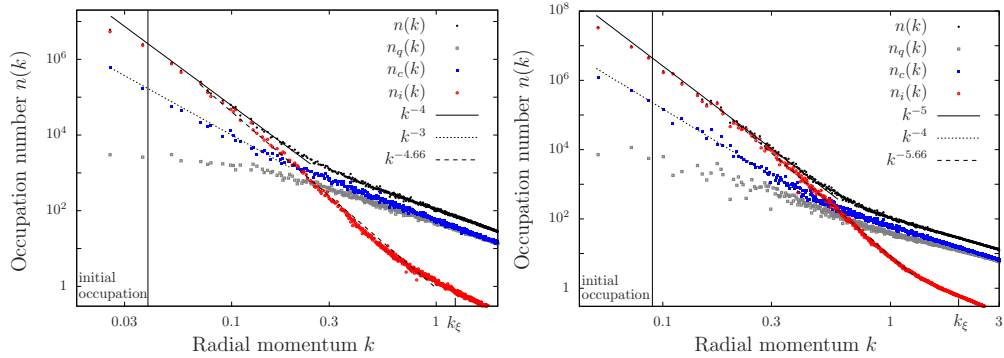


Figure 3.4: Single-particle occupation numbers of different fractions of the system. Colours distinguish the fractions n_i (red circles), i.e., the divergence-free part of the flow field $\mathbf{w}_v = \sqrt{n}\mathbf{v}$, n_c (filled blue squares), i.e., the solenoidal part of \mathbf{w}_v , and the quantum-pressure part n_q (open grey squares). $k_\xi = 2\pi/\xi$ marks the scale corresponding to the healing length $\xi = 1/\sqrt{2mgn}$. Note the double-logarithmic scale. (Left panel) At time $\bar{t} = 10^5$ of the run in $d = 2$ dimensions shown in Figs. 3.1 and 3.2. A scaling with $k^{-4.66}$ corresponds to a 5/3-law for the kinetic energy in $d = 2$. (Right panel) For the run in $d = 3$ dimensions shown in Figs. 3.1 and 3.3, at the time $\bar{t} = 1640$. A scaling with $k^{-5.66}$ corresponds to a 5/3 law for the kinetic energy in $d = 3$.

resulting spectra $n_i(k)$, $n_c(k)$, and $n_q(k)$ add up to the single-particle spectrum $n(k)$ discussed before. The components and their sum are shown separately, for $d = 2$ (left panel) and $d = 3$ (right panel), in Fig. 3.4. Red circles denote n_i , filled blue squares show the dependence of n_c , and open grey squares that of n_q . Qualitatively, the results are the same for $d = 2$ and $d = 3$. Excitations with large wave numbers are thermally distributed. In this regime, the spectrum $n(k) \sim k^{-2}$ is dominated by the compressible and quantum-pressure components. For smaller wave numbers the scaling changes to $n(k) \sim k^{-d-2}$, being dominated by the velocity \mathbf{w}_v . Moreover, we find that it is this decomposition into n_i and n_c which, for intermediate wave numbers, allows the incompressible part of the energy to develop a Kolmogorov-like scaling $\sim k^{-5/3-d-1}$ above the scale $k_l \sim 2\pi/l$ determined by the mean distance l between vortex cores. While the scaling of the sum of these components is predicted by the field-theoretic analysis in Ref. [29], a rising compressible part allows the incompressible contribution to deviate from the IR power law and to develop the observed scaling. Towards the IR limit, the compressible part becomes too weak such that the scaling of n_i goes over to $\zeta = d + 2$.

As we will show in Chap. 4, one can obtain the analytically predicted infrared power law $n(k) \sim k^{-4}$ in $d = 2$ from a finite density of independent vortices and antivortices. The IR scaling $\sim k^{-d-1}$ of the compressible (blue) component suggests an interpretation in terms of acoustic turbulence [41, 45, 50]. Our results presented in Chap. 5, show that this component survives for a limited period beyond the time when all vortical excitations have mutually annihilated.

It was found that the annihilation processes which eventually destroy the vortical

structure while coherence builds up in the system are very slow and thus stabilise the scaling solution over a long time. This is interesting, since it gives us an explanation for the quasi-stationarity of the wave turbulent spectra from the point of view of vortex dynamics. In particular, only after the last vortex-antivortex pair has annihilated and the last ring shrunk to zero the power law $n(k) \sim k^{-\zeta_{\text{Q}}^{\text{IR}}}$ breaks down and a thermal distribution of particles is left over. Characteristic times are $\bar{t} \sim \mathcal{O}(10^2)$ for vortex formation, $\bar{t} \sim \mathcal{O}(10^3)$ for stabilisation of the scaling solution and $\bar{t} \sim \mathcal{O}(10^4) - \mathcal{O}(10^5)$ for the last vortices to annihilate.

3.3 Summary

In summary, our results show a distinct power-law behaviour $k^{-\zeta}$ of the single-particle momentum spectrum $n(k)$ as well as of different components of the kinetic-energy distribution over the radial wave number k . Scaling exponents ζ of $n(k)$ corroborate the analytical predictions of Ref. [29]. Our findings suggest that local field expectation values and short- to intermediate-range coherence, including topological excitations, are at the basis of the infrared power laws predicted within non-perturbative dynamical field theory [28, 29, 53, 58]. This shows that both, weak wave turbulence and macroscopic, topological excitations of the field can be described within a unified field-theoretic approach. Weak turbulent flow and non-linear solitary bulk excitations are described in a unified manner as representing a non-thermal critical fixed point of the system. In turn, the approach also implies that superfluid turbulence can be studied in a new way, in the frame of a universal quantum field theoretical approach.

In the following two chapters, we will have a close look at different aspects pointed out here. Chap. 4 is concerned with momentum spectra arising from vortex dominated flows. To this end, we analyse statistical distributions of vortices and antivortices in the framework of the Onsager point vortex model. In this way, we are able to give a thorough interpretation of the IR-non-thermal fixed point solutions in terms of vortices. In Chap. 5, wave-turbulent properties such as the particle and energy cascades are studied. Additional scaling laws found in the single-particle momentum distribution at late times are related to pairing of vortices, allowing for a comprehensive understanding of the approach and decay of the non-thermal fixed point.

Vortex statistics

As we have seen in Chap. 3, the scaling of the momentum occupation numbers in the IR regime of large wave numbers, predicted within a non-perturbative analysis of strong wave-turbulence, correspond, for 2- and 3-dimensional degenerate Bose gases, to the appearance of macroscopic vortical excitations. In the following, we analyse the observed scaling spectra by comparing them to the single-particle momentum distributions for a set of randomly positioned point vortices (vortex lines) in $d = 2$ ($d = 3$) dimensions. With this approach, non-thermal fixed points in an ultracold Bose gas can be related to the statistics of vortices. We will show that uncorrelated vortices (vortex lines) are sufficient to yield the infrared scaling with exponent ζ_Q^{IR} , see Eq. (2.36). We will also show that beyond this, pair correlations between vortices and antivortices as well as configurations with small rings well separated from each other can give rise to a further scaling exponent deviating from ζ_Q^{IR} . See Fig. 4.1 for an illustration of different vortex distributions. Numerical calculations, sampling field configurations of static randomly positioned vortices, confirm the analytical result. Finally, the velocity probability distribution of a vortex-dominated flow [312, 313] is derived and numerically confirmed.

The point (line) vortex model employed here was introduced by Onsager in 1949 [73]. It describes the complex flow pattern in terms of the statistical mechanics of interacting classical point objects. This model has been constructed as a discrete vorticity approximation of classical fluid turbulence, but it is even more suitable to describe superfluid turbulence consisting of quantised vortices. Further applications include plasma physics or stellar dynamics [92, 314, 315].

4.1 Vortices in $d = 2$

In two dimensions, an isolated, singly quantised vortex is described by the complex field $\phi(r, \varphi) \equiv \sqrt{n(r)}e^{i\varphi}$ (see Sect. 2.2.1). As the r -dependence of the density $n(r)$ only becomes important at small scales on the order of the healing length $\xi = 1/\sqrt{2mgn}$ where our simulations are dominated by thermal excitations, we will omit it in the following and assume n to be uniform.

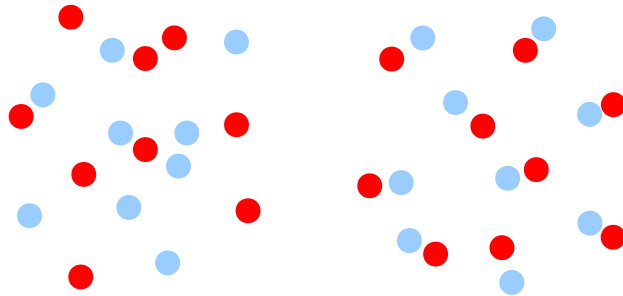


Figure 4.1: Left panel: Sketch of a random vortex-antivortex distribution underlying the IR scaling close to the non-thermal fixed point. Right panel: Correlated vortex distribution causing a modification to weaker pair scaling in the IR, for momenta smaller than the inverse of the average pairing length.

A system of M vortices in $d = 2$ dimensions can be described by $\phi(\mathbf{x}) = \prod_i^M \phi_i(\mathbf{x})$, where $\phi_i(\mathbf{x}) = \phi(\mathbf{x} - \mathbf{x}_i)$ is the single vortex field centred around \mathbf{x}_i . We derive the corresponding particle spectrum by considering the hydrodynamic velocity field $\mathbf{v} = \nabla\varphi/m$. Denoting the velocity field of a single vortex as $\tilde{\mathbf{v}}(\mathbf{x})$ (see Sect. 2.2.1) we can express the mean classical kinetic energy density of the velocity field as

$$\begin{aligned} E_v(\mathbf{x}) &= \frac{m}{2} \langle |\mathbf{v}(\mathbf{x})|^2 \rangle \\ &= \frac{m}{2} \langle \left| \int d^2x' \tilde{\mathbf{v}}(\mathbf{x} - \mathbf{x}') \rho(\mathbf{x}') \right|^2 \rangle, \end{aligned} \quad (4.1)$$

where $\rho(\mathbf{x}) = \sum_{i=1}^M \kappa_i \delta(\mathbf{x} - \mathbf{x}_i)$ defines the spatial distribution of vortices with winding number $\kappa_i = \pm 1$. Here and in the following, $\langle \cdot \rangle$ denotes an ensemble average over different realisations of the classical field $\phi(\mathbf{x})$. We derive the low- k scaling of $n(k)$ from the kinetic-energy spectrum $E_v(k)$, given by the angle-averaged Fourier transform of $E_v(\mathbf{x})$, taking into account that at low k , the single-particle spectrum is dominated by the superfluid velocity field \mathbf{v} , i.e.,

$$n(k) \simeq 2mk^{-2} E_v(k). \quad (4.2)$$

One has, from Eq. (4.1)

$$E_v(\mathbf{k}) \sim \langle |\mathbf{v}(\mathbf{k})|^2 \rangle = \langle |\rho(\mathbf{k})|^2 |\tilde{\mathbf{v}}(\mathbf{k})|^2 \rangle, \quad (4.3)$$

with

$$|\rho(\mathbf{k})|^2 = \sum_{i,j}^M \kappa_i \kappa_j e^{i\mathbf{k}(\mathbf{x}_i - \mathbf{x}_j)}. \quad (4.4)$$

Below the healing length scale $k_\xi = 2 \sin(\pi/2\xi)$ (lattice units), the modulus of the velocity field of a single vortex scales as $|\tilde{\mathbf{v}}| \sim k^{-1}$ and is radially symmetric in

momentum space. Hence, the angle-averaged single-particle spectrum scales like

$$n(k) = k^{-4} \left(M + 2 \sum_{i < j} \kappa_i \kappa_j J_0(k l_{ij}) \right). \quad (4.5)$$

Here, $J_0(y) = (2\pi)^{-1} \int_{-\pi}^{\pi} d\theta \cos(y \cos(\theta))$ denotes the zeroth-order Bessel function and $l_{ij} = |\mathbf{x}_i - \mathbf{x}_j|$ is the distance between vortices i and j .

4.1.1 Independent vortices

Assuming that the positions \mathbf{x}_i of the vortices are uncorrelated one can take the average over relative positions l_{ij} within the area $V_R = \pi R^2$,

$$\frac{2\pi}{V_R} \int_0^R dl l J_0(kl) = 2 \frac{J_1(kR)}{kR}, \quad (4.6)$$

and, for fixed k , the limit $R \rightarrow \infty$. Hence, the second term in brackets in Eq. (4.5) vanishes and one finally obtains the scaling [91]

$$n(k) \sim k^{-4}. \quad (4.7)$$

4.1.2 Independent vortex-antivortex pairs

In a two-dimensional superfluid containing vortices and antivortices an effectively attractive force between the two species can lead to pair correlations. We study a signature of this feature in the single-particle momentum spectrum by applying the point vortex model introduced above to the case of vortex-antivortex pairs.

As a first step we calculate the velocity field \mathbf{v}_{VA} for a vortex-antivortex pair with the vortex situated at \mathbf{x}_1 and the antivortex at $-\mathbf{x}_1$,

$$\mathbf{v}_{\text{VA}} = \tilde{\mathbf{v}}(\mathbf{x} - \mathbf{x}_1) - \tilde{\mathbf{v}}(\mathbf{x} + \mathbf{x}_1). \quad (4.8)$$

The squared velocity field far away from the centre of the pair can be obtained via a dipole approximation $|\mathbf{x}| \gg |\mathbf{x}_1|$ which yields the scaling $\mathbf{v}_{\text{VA}} \sim r^{-2}$. Hence, in Fourier space, the pair velocity field scales as $|\mathbf{v}_{\text{VA}}|^2 \sim k^0$ for low momenta. In this regime, the vortex-antivortex pair can again be treated as a point-like object with modified velocity scaling. To obtain the infrared scaling of a set of random vortex-antivortex pairs, we define a spatial pair distribution $\rho_{\text{pair}}(\mathbf{x}) = \sum_i \delta(\mathbf{x} - \mathbf{x}_i)$, with \mathbf{x}_i denoting the centre of the i -th vortex-antivortex pair. Then, the analysis performed for random vortices above can be adopted. Therefore, in the case of independently distributed pairs, the approach predicts the infrared scaling of the occupation number to be the same as for a single pair, i.e. $n(k) \sim k^{-2}$.

4.1.3 Pair correlated vortices

The considerations from Sect. 4.1.2 are only valid in the far IR (or equivalently for pair size going to zero). In our numerical simulations we found, however, that for large evolution times, a finite minimum distance emerged between vortices and antivortices, and also between vortices with the same circulation, see Sect. 5.2.4. To take into account this observation and to analyse the full spectrum, we go back to writing the distribution $\rho(\mathbf{x}) = \rho^V(\mathbf{x}) - \rho^A(\mathbf{x})$ as the sum of distributions $\rho^V(\mathbf{x}) = \sum_{i=1}^M \delta(\mathbf{x} - \mathbf{x}_i^V)$ of M vortices and $\rho^A(\mathbf{x}) = \sum_{i=1}^M \delta(\mathbf{x} - \mathbf{x}_i^A)$ of M antivortices. Hence,

$$\langle |\rho(\mathbf{k})|^2 \rangle = \int d^2x d^2x' e^{i\mathbf{k}(\mathbf{x}-\mathbf{x}')} C(\mathbf{x}, \mathbf{x}'), \quad (4.9)$$

with $C(\mathbf{x}, \mathbf{x}') = \langle \rho_{\mathbf{x}}^V \rho_{\mathbf{x}'}^V \rangle - \langle \rho_{\mathbf{x}}^V \rho_{\mathbf{x}'}^A \rangle - \langle \rho_{\mathbf{x}}^A \rho_{\mathbf{x}'}^V \rangle + \langle \rho_{\mathbf{x}}^A \rho_{\mathbf{x}'}^A \rangle$. This allows for a derivation of the kinetic-energy distribution in terms of correlation functions of vortex positions.

We model pairing by the density-density correlation functions

$$\langle \rho_{\mathbf{x}}^{V(A)} \rho_{\mathbf{x}'}^{V(A)} \rangle = \frac{M}{V_R} \delta(\mathbf{x} - \mathbf{x}') + P_{\mathbf{x}, \mathbf{x}'}, \quad (4.10)$$

$$\langle \rho_{\mathbf{x}}^{V(A)} \rho_{\mathbf{x}'}^{A(V)} \rangle = \frac{M}{V_R V_\Lambda} \theta(\lambda - |\mathbf{x} - \mathbf{x}'|) + P_{\mathbf{x}, \mathbf{x}'}. \quad (4.11)$$

where $V_\Lambda = \pi\lambda^2$ is the area in which the theta function equals one. The contributions

$$P_{\mathbf{x}, \mathbf{x}'} = \frac{M(M-1)}{V_R(V_R - V_\Lambda)} \theta(|\mathbf{x} - \mathbf{x}'| - \Lambda) \quad (4.12)$$

take into account that, besides the pairing, vortices and antivortices avoid each other in the dilute gas, keeping a minimum distance Λ . This is due to vortex-vortex repulsion and fast vortex-antivortex annihilation on small distances. The functions $P_{\mathbf{x}, \mathbf{x}'}$ cancel out in Eq. (4.9).¹

Inserting Eqs. (4.10), (4.11) into Eq. (4.9), evaluating the Fourier transform and angular averaging gives

$$\langle |\rho(k)|^2 \rangle = 2M \left(1 - \frac{2}{k\lambda} J_1(k\lambda) \right). \quad (4.13)$$

The expansion of the integral for $k \ll 2\pi/\lambda$ yields the leading-order result

$$\langle |\rho(k)|^2 \rangle = M(k\lambda)^2/4 + \mathcal{O}(k^4) \quad (4.14)$$

and, from Eqs. (4.2) and (4.3), the same occupation-number scaling as for indepen-

¹If different avoidance scales Λ apply for vortices and antivortices, the terms do not cancel, but the remaining term does not alter the results for pair scaling derived here.

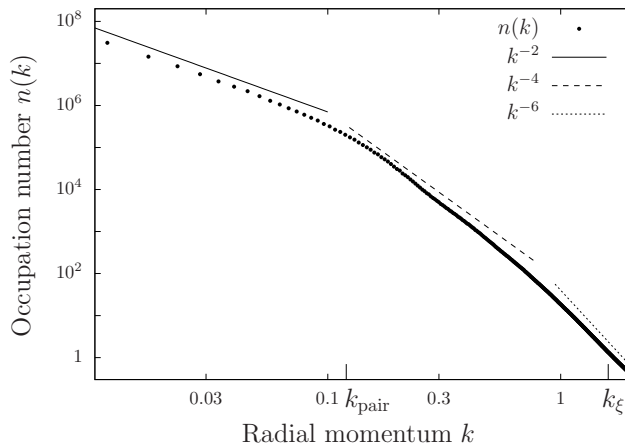


Figure 4.2: Radial momentum distribution for a randomly distributed set of $M = 80$ bound vortex-antivortex pairs, on a $N_s^2 = 1024^2$ grid. Note the double-logarithmic scale. The vortices are positioned according to the probability distribution (4.16). At low momenta the power law is consistent with the existence of random vortex pairs $n_k \sim k^{-2}$. Above k_{pair} , the distribution exhibits the scaling of an ensemble of independent vortices, $n_k \sim k^{-4}$, while at momenta larger than the healing-length scale k_ξ one observes the vortex-core scaling $\sim k^{-6}$.

dent pairs,

$$n(k) \sim k^{-2}. \quad (4.15)$$

At momenta $k \gg 2\pi/\lambda$ the independent-vortex scaling $n(k) \sim k^{-4}$ is restored. We note that the infrared result (4.15) can also be achieved by choosing more general pair correlations of the form $\langle \rho_{\mathbf{x}}^V \rho_{\mathbf{x}'}^A \rangle = \langle \rho_{\mathbf{x}}^A \rho_{\mathbf{x}'}^V \rangle = M\epsilon [2V_R\pi(\lambda_{\text{max}}^\epsilon - \lambda_{\text{min}}^\epsilon)]^{-1} |\mathbf{x} - \mathbf{x}'|^{\epsilon-2} \theta(\lambda_{\text{max}} - |\mathbf{x} - \mathbf{x}'|) \theta(|\mathbf{x} - \mathbf{x}'| - \lambda_{\text{min}}) + P_{\mathbf{x}, \mathbf{x}'}$, with $\epsilon \geq 0$ and $\lambda_{\text{min}} < \lambda_{\text{max}}$, which is closer to our numerical observations and includes the case of a fixed “binding length” $\lambda_{\text{min}} \rightarrow \lambda_{\text{max}}$. As before, pair scaling k^{-2} is found for $k\lambda_{\text{max}} \ll 1$, critical scaling k^{-4} for $k\lambda_{\text{max}} \gg 1$, irrespective of ϵ . We supplement our discussion of scaling in the point vortex model with numerical data obtained by averaging over an ensemble of field configurations in $d = 2$ dimensions. These configurations were constructed by multiplying uncorrelated single-vortex fields centred at positions according to the probability distribution

$$P^{(M)}(\mathbf{x}_1^V, \mathbf{x}_1^A, \dots) = \prod_i^M P^{(1)}(\mathbf{x}_i^V) P^{(2)}(\mathbf{x}_i^V, \mathbf{x}_i^A) \quad (4.16)$$

with $P^{(1)}(\mathbf{x}_i^V) = 1/V_R$, $P^{(2)}(\mathbf{x}_i^V, \mathbf{x}_i^A) = V_\lambda^{-1} \theta(\lambda - |\mathbf{x}_i^V - \mathbf{x}_i^A|)$, where we neglect that unpaired vortices avoid each other, i.e., choose $\Lambda = 0$. They do not represent stable solutions of the classical field equation nor do they contain sound-wave and related excitations yet which would build up through the interactions of the field and the vortices.

The resulting momentum spectrum is presented in Fig. 4.2. Three scaling regimes

can be observed. At low momenta the power law is consistent with the existence of random vortex pairs $n_k \sim k^{-2}$. Above $k_{\text{pair}} = 2\sin(\pi/2\lambda) \simeq \pi/\lambda$, choosing $\lambda = 25$ (lattice units), the distribution exhibits the scaling of an ensemble of independent vortices, $n_k \sim k^{-4}$, while at momenta larger than the healing-length scale k_ξ one observes the vortex-core scaling $\sim k^{-6}$ [316]. The above results reflect that in a vortex dominated flow, particles with low momenta are found far away from vortex cores. In the case of pairing, the flow field far away from the cores is given by the field of a vortex pair, and the low-momentum scaling follows the pair-field scaling. Particles closer to the vortex cores pick up a higher momentum. Above k_{pair} the field will be dominated by the field of a single vortex. Note that Fig. 4.2 shows the result of a numerical calculation in which we have sampled field configurations of random static vortices. Dynamical simulations of the classical field equation Eq. (2.5) will be shown in Sect. 5.1.

It was shown by Novikov (1976), that one can construct a Kolmogorov 5/3-scaling from the statistics of point vortices [91, 316]. This can be achieved by the density-density correlation functions for vortices

$$\langle \rho_{\mathbf{x}}^{V(A)} \rho_{\mathbf{x}'}^{V(A)} \rangle \sim (\mathbf{x} - \mathbf{x}')^{-\alpha} + P_{\mathbf{x}, \mathbf{x}'}, \quad (4.17)$$

$$\langle \rho_{\mathbf{x}}^{V(A)} \rho_{\mathbf{x}'}^{A(V)} \rangle = P_{\mathbf{x}, \mathbf{x}'}. \quad (4.18)$$

The contributions $P_{\mathbf{x}, \mathbf{x}'}$ are assumed to be equal. The integral Eq. (4.9) is convergent for $1/2 < \alpha < 2$, which includes $\alpha = 4/3$. This choice gives $n(k) \sim k^{-4.66}$ and $E(k) \sim k^{-5/3}$. Note that the presence of vortex-antivortex correlations destroys the 5/3-scaling as discussed in Ref. [316].

IR-cutoff

At this point, we want to discuss the appearance of an IR-cutoff in the single-particle momentum distribution. Consider a Bose gas containing a random distribution of vortices of either sign and density n_V . If we were to estimate the coherence of the wave function $\langle \phi(0)\phi(x) \rangle$ (as will be discussed in detail in Sect. 6.7), we would expect a decay of coherence at the scale of the mean vortex distance, $l_V = n_V^{-1/2}$. That is because vortices appear on average at this distance and induce a rapid change of the phase angle $\varphi(x)$. Since the momentum distribution is nothing but the Fourier-transform of the coherence function, a momentum scale $k_V = \pi/l_V$ is created. For momenta $k < k_V$, the momentum distribution $n(k)$ needs to be almost flat in order to insure convergence of the integral that counts the number of particles. This restriction is not forced upon the particle numbers defined by the quantum hydrodynamic decomposition Sect. 2.2, i.e. n_i, n_c, n_q . Hence, we also expect a deviation of $n(k)$ from the incompressible momentum distribution n_i below the scale k_V , as has also been mentioned at the end of Sect. 2.2.2. In Fig. 4.3, we present numerical evidence for our reasoning. The plot shows the single-particle (dots) as well as the incompressible momentum distributions (lines) for three different vortex numbers N_V distributed over a lattice of size $N_s^2 = 1024^2$.

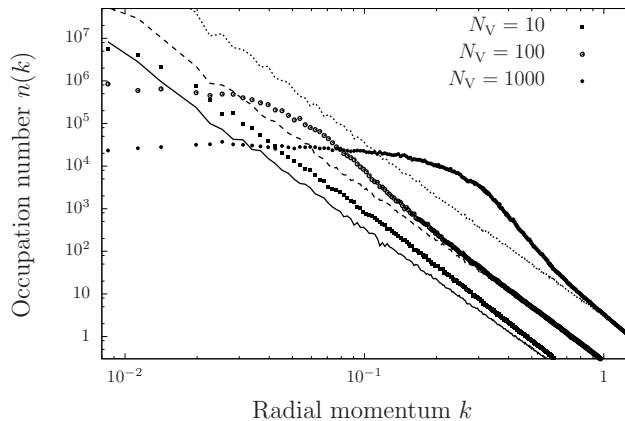


Figure 4.3: Radial momentum distribution for a set of infinitely thin ($\xi=0$) randomly distributed vortices. Note the double-logarithmic scale. At the highest momenta, $n(k)$ (dots) and $n_i(k)$ (lines) follow the k^{-4} scaling of independent vortices. However, at momenta $k < k_V$, with $k_V(N_V = 10) \simeq 10^{-2}$, $k_V(N_V = 100) \simeq 3 \times 10^{-2}$, $k_V(N_V = 1000) \simeq 10^{-1}$, the single-particle momentum distribution $n(k)$ becomes flat. Instead, the incompressible occupation number $n_i(k)$ continues to rise.

One can observe the vortex density dependence of the IR-cutoff in the single-particle momentum distribution. The spectrum of the incompressible velocity field does not show this feature. Instead, the k^{-4} -scaling persists all the way to the lowest momenta. We remark, that a random distribution of vortex-antivortex pairs does not show a sharp IR-cutoff, see Fig. 4.2. The reason behind this is that the phase field of a vortex-antivortex pair is smooth at large distances.

Note that a trapped quantum gas features an IR-cutoff given by the inverse of the cloud diameter. At low temperatures, this size is approximately given by the Thomas-Fermi radius R_{TF} . For low vortex densities we expect k_V and k_{TF} to be of the same order of magnitude.

Onsager model: Non-thermal fixed point as a maximum entropy state

We close with recalling the picture Onsager developed in Ref. [73] of thermodynamic equilibrium states of a fixed number of vortices and antivortices in two dimensions. He used the Hamiltonian of vortical flow in two dimensions [72],

$$H = -\frac{1}{2\pi} \sum_{i>j}^M \kappa_i \kappa_j \ln(|\mathbf{r}_i - \mathbf{r}_j|), \quad (4.19)$$

to describe the dynamics of a system of M vortices in a superfluid which hence behave like a Coulomb gas. Here, the position of the i -th vortex is denoted as $\mathbf{r}_i = (x_i, y_i)$. Due to the fact that the x and y coordinates of each vortex are canonical conjugates, phase space is identical with configuration space of the vortex

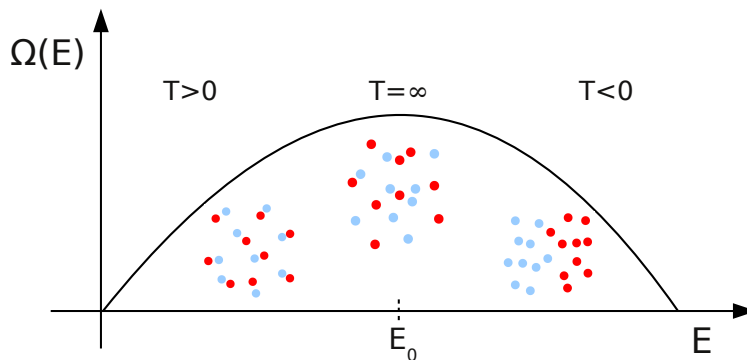


Figure 4.4: Illustration of Onsager’s picture of thermodynamic equilibrium states of the neutral two-dimensional Coulomb gas at fixed particle number. We plot the qualitative form of the number of available states $\Omega(E)$ as a function of energy E as well as snapshots of typical microscopic configurations.

positions. Hence, for vortices moving in a volume V the total phase space is given by V^M . The Hamiltonian (4.19) implies that low-energy configurations feature vortices of opposite sign close to each other, whereas high-energy configurations require vortices of equal sign to group. Due to these constraints, the number of configurations $\Omega(E)$ available for the system at a given energy E decreases towards high and low energies, with a maximum at some intermediate $E = E_0$. This concept is illustrated in Fig. 4.4. According to Boltzmann, the entropy is

$$S(E) = \ln(\Omega(E)), \quad (4.20)$$

and the inverse temperature $1/T = \partial S/\partial E$ is positive for $E < E_0$ and negative for $E > E_0$. It follows that positive-temperature states are characterised by vortex-antivortex pairing, while negative-temperature states feature vortices of the same circulation to cluster. At the point of maximum entropy $S(E_0)$ and infinite temperature, Onsager expected a state of uncorrelated vortices and antivortices. This understanding of the non-thermal fixed point as a quasi-equilibrium state of vortices corroborates our result that the IR scaling behaviour at the fixed point corresponds to the appearance of topological excitations.

4.2 Vortex loops in $d = 3$

We now consider the three-dimensional case of vortex lines and loops. A formulation similar to the Onsager point vortex model in Sect. 4.1.1 is possible [18, 317, 318]. See also Refs. [93, 94, 319, 320] for an extension including the dynamics of tangles of vortex lines.

We write the classical kinetic energy spectrum of the velocity field in terms of the

vorticity density

$$\boldsymbol{\omega}(\mathbf{x}) = m \nabla \times \mathbf{v}(x) \quad (4.21)$$

as

$$E_v(\mathbf{k}) = \frac{\langle |\boldsymbol{\omega}(\mathbf{k})|^2 \rangle}{2mk^2}. \quad (4.22)$$

The vorticity is vanishing everywhere but on the vortex lines, i.e., assuming M individual vortex loops,

$$\boldsymbol{\omega}(\mathbf{x}) = \sum_i^M \int_0^{L_i} d\tau \mathbf{s}'_i(\tau) \delta(\mathbf{s}_i(\tau) - \mathbf{x}). \quad (4.23)$$

In this expression, the vortex filaments are represented by the connected curves $\mathbf{s}_i(\tau)$, parametrised by the one-dimensional coordinate $\tau \in \{0, L_i\}$, L_i being the arc length of filament i . The loops are closed, $\mathbf{s}_i(L_i) = \mathbf{s}_i(0)$, possibly also across the walls of the 3-dimensional volume in accordance with periodic boundary conditions. $\mathbf{s}'_i(\tau)$ is the tangent vector along the filament at $\mathbf{s}_i(\tau)$, of unit length $|\mathbf{s}'_i(\tau)| = 1$. We parametrise the i -th vortex loop in terms of a single centre coordinate and a relative curve, $\mathbf{s}_i(\tau) = \mathbf{R}_i + \mathbf{r}_i(\tau)$ and write the vorticity as

$$\begin{aligned} \boldsymbol{\omega}(\mathbf{x}) = \sum_i^M \int d^3y \delta(\mathbf{y} - \mathbf{R}_i) \int_0^{L_i} d\tau \mathbf{r}'_i(\tau) \\ \times \delta(\mathbf{r}_i(\tau) - \mathbf{x} + \mathbf{y}). \end{aligned} \quad (4.24)$$

Hence, in Fourier space,

$$\boldsymbol{\omega}(\mathbf{k}) = \sum_i^M e^{i\mathbf{k}\mathbf{R}_i} \tilde{\boldsymbol{\omega}}_i(\mathbf{k}), \quad (4.25)$$

where $\tilde{\boldsymbol{\omega}}_i(\mathbf{k})$ is the Fourier transform of the vorticity of the i -th vortex loop, given by

$$\tilde{\boldsymbol{\omega}}_i(\mathbf{x}) = \int_0^{L_i} d\tau \mathbf{r}'_i(\tau) \delta(\mathbf{r}_i(\tau) - \mathbf{x}). \quad (4.26)$$

The ensemble-averaged vorticity $\langle |\boldsymbol{\omega}(\mathbf{k})|^2 \rangle$ becomes

$$\langle |\boldsymbol{\omega}(\mathbf{k})|^2 \rangle = \sum_{i,j}^M \langle e^{i\mathbf{k}(\mathbf{R}_i - \mathbf{R}_j)} \tilde{\boldsymbol{\omega}}_i(\mathbf{k}) \tilde{\boldsymbol{\omega}}_j(\mathbf{k}) \rangle. \quad (4.27)$$

Assuming that the shapes of the individual vortex loops are statistically indepen-

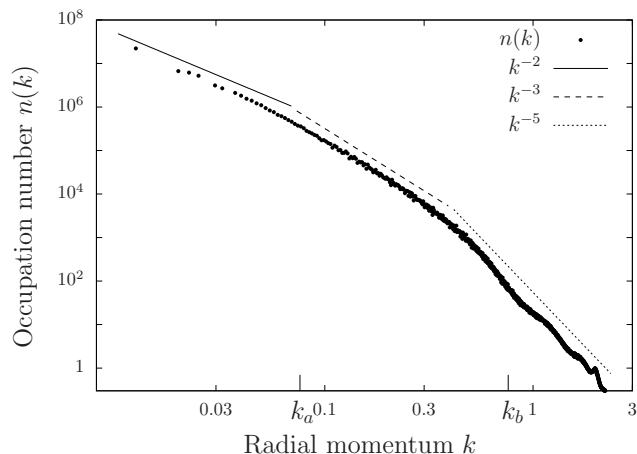


Figure 4.5: Radial momentum distribution of an elliptical vortex loop on a $N_s^3 = 1024^3$ grid. Note the double-logarithmic scale. The major and minor radius scales k_a , for $r_a = 40$, and k_b , for $r_b = 4$, respectively, are indicated. These scales separate pair scaling $n(k) \sim k^{-2}$ as for a near-circular vortex ring, scaling $n(k) \sim k^{-3}$ for two anti-circulating vortex lines, and $n(k) \sim k^{-5}$, as for a vortex ring or of a pair of straight vortex lines, corresponding to the scaling exponent ζ_Q^{IR} at the non-thermal fixed point. See Sect. 4.2 for more details.

dent of their position, it follows that

$$\langle e^{i\mathbf{k}(\mathbf{R}_i - \mathbf{R}_j)} \tilde{\omega}_i(\mathbf{k}) \tilde{\omega}_j(\mathbf{k}) \rangle = \langle e^{i\mathbf{k}(\mathbf{R}_i - \mathbf{R}_j)} \rangle \langle \tilde{\omega}_i(\mathbf{k}) \tilde{\omega}_j(\mathbf{k}) \rangle. \quad (4.28)$$

4.2.1 Uncorrelated vortex loops

If the loops are also uncorrelated among themselves, then $\langle \tilde{\omega}_i(\mathbf{k}) \tilde{\omega}_j(\mathbf{k}) \rangle = \langle |\tilde{\omega}_i(\mathbf{k})|^2 \rangle \delta_{ij}$. Hence, for statistically identical loops,

$$\langle |\omega(\mathbf{k})|^2 \rangle = M \langle |\tilde{\omega}(\mathbf{k})|^2 \rangle, \quad (4.29)$$

which means that the vorticity spectrum scales in the same way as the average vorticity of a vortex loop centred at the origin. Finally, the scaling of the momentum spectrum $n(k) = 2mk^{-2}E_v(k)$ follows from that of the angle-averaged vorticity,

$$n(k) \sim k^{-4} \int d\Omega_k \langle |\omega(\mathbf{k})|^2 \rangle. \quad (4.30)$$

For the case of two straight parallel vortex lines of opposite circulation Eq. (4.29) is evaluated in Sect. 4.2.2, as well as for an ensemble of such paired lines. Making use of the procedure developed there, the case of circular vortex rings of radius r is also discussed. For the latter, the resulting angle-averaged momentum spectrum scales like $n(k) \sim k^{-2}$ for momenta $k \ll k_r = 2 \sin(\pi/2r)$ and $n(k) \sim k^{-5}$ for momenta $k \gg k_r$. To include effects from squeezed vortex loops, we consider elliptical filaments. The ellipse is defined by a major radius r_a and minor radius r_b .

In Fig. 4.5, the angle-averaged momentum spectrum of an elliptical vortex loop is shown. Three scaling regimes can be distinguished. For the lowest momenta, one has $n(k) \sim k^{-2}$, which equals the infrared scaling for a vortex ring. For momenta $k_a \ll k \ll k_b$, one finds $n(k) \sim k^{-3}$, which coincides with the infrared scaling of two anti-circulating vortex lines (see Sect. 4.2.2). For the ellipse, above k_b , the momentum distribution scales like $n(k) \sim k^{-5}$. This is the scaling of a single vortex line and can also be found as the high-momentum scaling of a vortex ring or a pair of straight vortex lines (see Sect. 4.2.2).

4.2.2 Straight vortex lines and rings

The main result of Sect. 4.2 is this derivation of different scaling regimes of a gas of vortex ellipses presented in Sect. 4.2.1 and numerically evaluated in Fig. 4.5. It is intuitive, that in different regimes of k -space, the ellipse shows scaling behaviour similar to vortex lines or rings. Therefore, we give the analytic derivation of the spectra for a single vortex line, an ensemble of parallel vortex lines and a vortex ring in the following.

Straight vortex line

Based on Eq. (4.23), we calculate the vorticity of two straight vortex lines in three dimensions, with circulation κ_i , $i = 1, 2$, placed at positions $(0, -y_0)$ and $(0, y_0)$ in the x - y plane and relate it to the momentum spectrum, see Eq. (4.30). The lines are parametrised by

$$\mathbf{s}_i(\mathbf{x}) = (0, (-1)^i y_0, \kappa_i \tau) \quad (4.31)$$

with $\tau \in [-\infty, \infty]$. In Fourier space, the vorticity density, defined in Eq. (4.21), reads

$$\boldsymbol{\omega}(\mathbf{k}) = \mathbf{e}_z \delta(k_z) (\kappa_1 e^{-ik_y y_0} + \kappa_2 e^{ik_y y_0}). \quad (4.32)$$

The vorticity spectrum follows from Eq. (4.23),

$$|\boldsymbol{\omega}(\mathbf{k})|^2 = 2\delta^2(k_z) [1 + \kappa_1 \kappa_2 \cos(2k_y y_0)]. \quad (4.33)$$

Hence, for co-rotating vortex lines ($\kappa_1 = \kappa_2$)

$$|\boldsymbol{\omega}(\mathbf{k})|^2 = 4\delta^2(k_z) \cos^2(k_y y_0), \quad (4.34)$$

while for counter-rotating vortex lines ($\kappa_1 = -\kappa_2$) one obtains

$$|\boldsymbol{\omega}(\mathbf{k})|^2 = 4\delta^2(k_z) \sin^2(k_y y_0). \quad (4.35)$$

In order to be able to take the angle average over δ^2 we regularise the delta distribution, giving it a finite width $\Delta = 1/L_z$. The angle average of Eq. (4.34) then

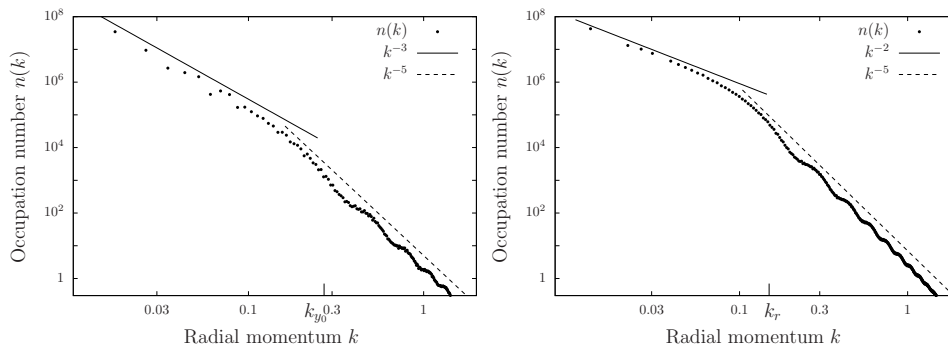


Figure 4.6: Momentum distribution as a function of radial coordinate k , on a $N_s^3 = 1024^3$ lattice. Note the double-logarithmic scale. Left: For the case of two straight vortex lines of circulation $\kappa_1 = -\kappa_2 = 1$. The distance scale k_{y_0} is indicated. Right: For the case of a vortex ring of radius r . The radius scale k_r is indicated.

reads

$$\begin{aligned}
 |\omega(k)|^2 &= \int d\varphi_k du \delta_\Delta(ku)^2 \\
 &\quad \times 4 \cos^2(ky_0 \sqrt{1-u^2} \cos\varphi_k) \\
 &= 8\pi^2 L_z k^{-1} [1 + J_0(2ky_0)],
 \end{aligned} \tag{4.36}$$

where L_z is the length of the system in z -direction and $u = \cos(\theta)$. One obtains the scaling behaviour

$$|\omega(k)|^2 = 16\pi^2 L_z k^{-1} + \mathcal{O}(k), \tag{4.37}$$

which is the scaling of a single line. With Eq. (4.30), we conclude $n(k) \sim k^{-5}$. Following the same reasoning, the angle average of Eq. (4.35) is given as

$$|\omega(k)|^2 = 8\pi^2 L_z k^{-1} [1 - J_0(2ky_0)]. \tag{4.38}$$

For $ky_0 \ll 1$

$$|\omega(k)|^2 = 8\pi^2 L_z y_0^2 k + \mathcal{O}(k^3), \tag{4.39}$$

which gives $n(k) \sim k^{-3}$. For $ky_0 \gg 1$

$$|\omega(k)|^2 = 8\pi^2 L_z k^{-1} \tag{4.40}$$

which gives $n(k) \sim k^{-5}$. These scalings are confirmed in Fig. 4.6 (left).

Ensembles of parallel vortex lines

In Sects. 4.1.2 and 4.1.3, we have discussed the scaling of the momentum distribution for ensembles of independent and pair correlated vortices in two dimensions,

respectively. Here, we generalise the scaling derived above for straight vortex lines to the case of many such lines in $d = 3$. We derive an expression for the momentum spectrum of a system of M straight vortex lines oriented along the z direction. The average vorticity squared is given by Eq. (4.27) where \mathbf{R}_i are vectors in the two-dimensional x - y plane pointing to the i -th vortex line with circulation $\kappa_i = \pm 1$. The vorticity of the single line is

$$\begin{aligned}\tilde{\boldsymbol{\omega}}_i(\mathbf{k}) &= \kappa_i \int d^3x e^{i\mathbf{k}\mathbf{x}} \int d\tau \mathbf{e}_z \delta(\kappa_i \tau \mathbf{e}_z - \mathbf{x}), \\ &= \kappa_i \delta(k_z) \mathbf{e}_z.\end{aligned}\tag{4.41}$$

Hence, Eq. (4.27) has the same form as Eq. (4.4) for $d = 2$,

$$\langle |\boldsymbol{\omega}(\mathbf{k})|^2 \rangle = \delta^2(k_z) \sum_{i,j}^M \langle \kappa_i \kappa_j e^{i\mathbf{k}(\mathbf{R}_i - \mathbf{R}_j)} \rangle,\tag{4.42}$$

up to a $\delta^2(k_z)$ term, which arises from the infinite extent of the vortex lines in z -direction. As in Sect. 4.2.2, we regularise the delta distributions, and averaging (4.42) over solid angles yields

$$\langle |\boldsymbol{\omega}(k)|^2 \rangle \sim \frac{L_z}{k} \sum_{i,j}^M \langle \kappa_i \kappa_j J_0(k|\mathbf{R}_i - \mathbf{R}_j|) \rangle,\tag{4.43}$$

which is analogous to Eq. (4.5) in two dimensions. As the position of the i -th vortex line is determined by \mathbf{R}_i , statistical averaging of (4.43) can be done in the same way as in $d = 2$.

Vortex ring

A vortex ring with radius r lying in the x - y plane can be parametrised as

$$\mathbf{s}(\mathbf{x}) = (r \cos \varphi, r \sin \varphi, 0)\tag{4.44}$$

with $\varphi \in [0, 2\pi]$. In Fourier space, similar steps as above lead to the angle-averaged vorticity density

$$|\boldsymbol{\omega}(k)|^2 = \int d\theta_k |J_1(kr \sin \theta_k)|^2.\tag{4.45}$$

Evaluating the integral numerically shows that the vorticity scales like $\sim k^2$ for $kr \ll 1$ and $\sim k^{-1}$ for $kr \gg 1$, corresponding to $n(k) \sim k^{-2}$ and $n(k) \sim k^{-5}$. This is shown in Fig. 4.6 (right). Both scalings are also found in the momentum spectrum of a vortex ellipse, discussed in Sect. 4.2.

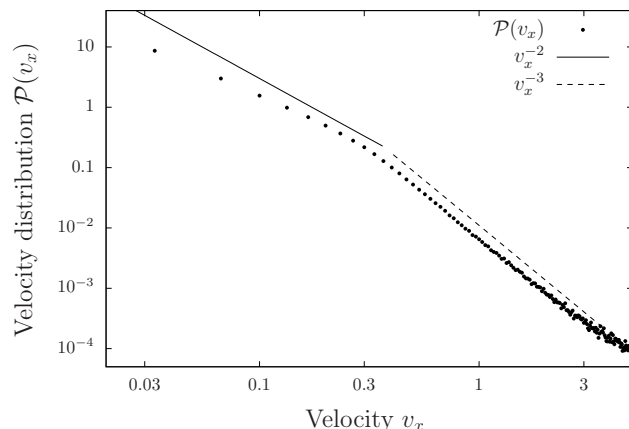


Figure 4.7: Velocity distribution (4.47) as obtained from a random distribution of $M = 80$ bound vortex-antivortex pairs, on a $N_s^2 = 1024^2$ grid, as in Fig. 4.2. Note the double-logarithmic scale. At low momenta the velocity field follows the scaling of vortex-antivortex pairs ($\alpha = 2$), whereas at higher momenta the distribution reflects the presence of vortices ($\alpha = 1$). Note, that there is a deviation from $\alpha = 2$ in the regime of low velocities. From simulations with higher resolution, we find the best agreement for $\alpha = 1.8$. We remark, that in the limit $M \rightarrow \infty$ the velocity distribution is expected to be Gaussian [321].

4.3 Velocity distribution

The vortex model can provide insight into another observable accessible in our numerical simulations, the velocity distribution. See Refs. [312, 321–323] for discussions of the velocity distribution and Ref. [313] for recent experimental results. As discussed above, the velocity field scales, far away from any core, as $\sim r^{-\alpha}$, with $\alpha = 1$ for a single vortex and $\alpha = 2$ for a vortex-antivortex pair in two dimensions. The velocity probability distribution $\mathcal{P}(\mathbf{v})$ is calculated as $\mathcal{P}(\mathbf{v}) = |\partial\mathbf{x}/\partial\mathbf{v}|\rho(\mathbf{x})$, with spatial vortex distribution function $\rho(\mathbf{x})$. For a uniform distribution $\rho(\mathbf{x}) = \text{const.}$, it follows after angular averaging that

$$\mathcal{P}(\mathbf{v}) = |\mathbf{v}|^{-2(\alpha+1)/\alpha}. \quad (4.46)$$

It is numerically convenient to calculate the probability density of a single component of the field, e.g.

$$\mathcal{P}(v_x) = \int dv_y \mathcal{P}(\mathbf{v}) \simeq v_x^{1-2(\alpha+1)/\alpha}. \quad (4.47)$$

In Fig. 4.7, the corresponding velocity distribution $\mathcal{P}(v_x)$ is shown. In accordance with the analytical predictions two scaling regimes are observed. At low momenta the velocity field follows the scaling of vortex-antivortex pairs, whereas at higher momenta the distribution reflects a random distribution of vortices.

4.4 Summary

In summary, we have analysed the momentum distribution of randomly distributed point (line) vortices in two and three dimensions. This work, was motivated by the scaling of the momentum occupation numbers in the IR regime of large wave numbers, predicted within a non-perturbative analysis of strong wave-turbulence, and found to correspond to the appearance of macroscopic vortical excitations in Chap. 3. We have shown that uncorrelated vortices (vortex lines) are sufficient to yield the infrared scaling with exponent ζ_Q^{IR} , see Eq. (2.36). For the two-dimensional case, we could also give an intuitive understanding of the non-thermal fixed point as a maximum entropy state of the Onsager model. We also showed that beyond this, pair correlations between vortices and antivortices as well as configurations with small rings well separated from each other can give rise to a further scaling exponent deviating from ζ_Q^{IR} . The relevance of this finding for the full time evolution will be discussed in the next chapter. We have further discussed the topic of an IR-cutoff in single-particle momentum distribution and the scaling of the velocity distribution of a vortex dominated flow.

Properties near the non-thermal fixed point

In this chapter, we extend our studies of the relaxation of two and three dimensional dilute Bose gases through stages of superfluid turbulence and the approach of a non-thermal fixed point, by means of extensive numerical simulations. In Section 2.3, we have introduced the quantum-field theoretical predictions of Refs. [29, 41], in particular for the wave-turbulent scaling exponents of the single-particle momentum distribution. In simulations discussed in Chap. 3, we found excellent agreement with those predictions. Moreover, our results provided an interpretation of the non-thermal fixed points proposed in Refs. [28, 29] for the case of an ultracold Bose gas: The appearance of non-perturbative infrared scaling reflects the presence of statistically independent vortices [31]. This phenomenon appears to be distinctly different from the weak wave turbulence we observe in the UV part of the spectrum.

In Chap. 4, we described a model of independent as well as pair-correlated vortical excitations [73] which allowed for the introduction of vortex-antivortex correlations. These findings tightened the vortex picture of non-thermal fixed points and revealed the possibility of further scaling exponents depending on vortex correlations. In this chapter, we use this knowledge for a more refined interpretation of the scaling behaviour during the different stages of the evolution presented in Chap. 3. First, we show that the stationary scaling is maintained by energy (UV) and particle (IR) fluxes, further supporting the analytic theory. In Section 5.2, we study the power-law distributions of the compressible and incompressible contributions to the flow pattern in great detail. This adds to the clear understanding of the bimodal scaling laws in the overall momentum spectrum. IR power-law spectra of subdominant compressible excitations suggest the presence of acoustic turbulence [41] on the top of the vorticity-bearing quasi-condensate. In comparison with recent experiments and analytical predictions, the velocity field probability distribution as well as the velocity statistics of individual vortices are studied. This observable is of great interest, since it has recently been used to experimentally verify a distinction between classical and quantum turbulence [313]. We finally show that the complete decay of the turbulent scaling is anticipated by the appearance of weaker IR power laws reflecting vortex-antivortex pairing correlations.

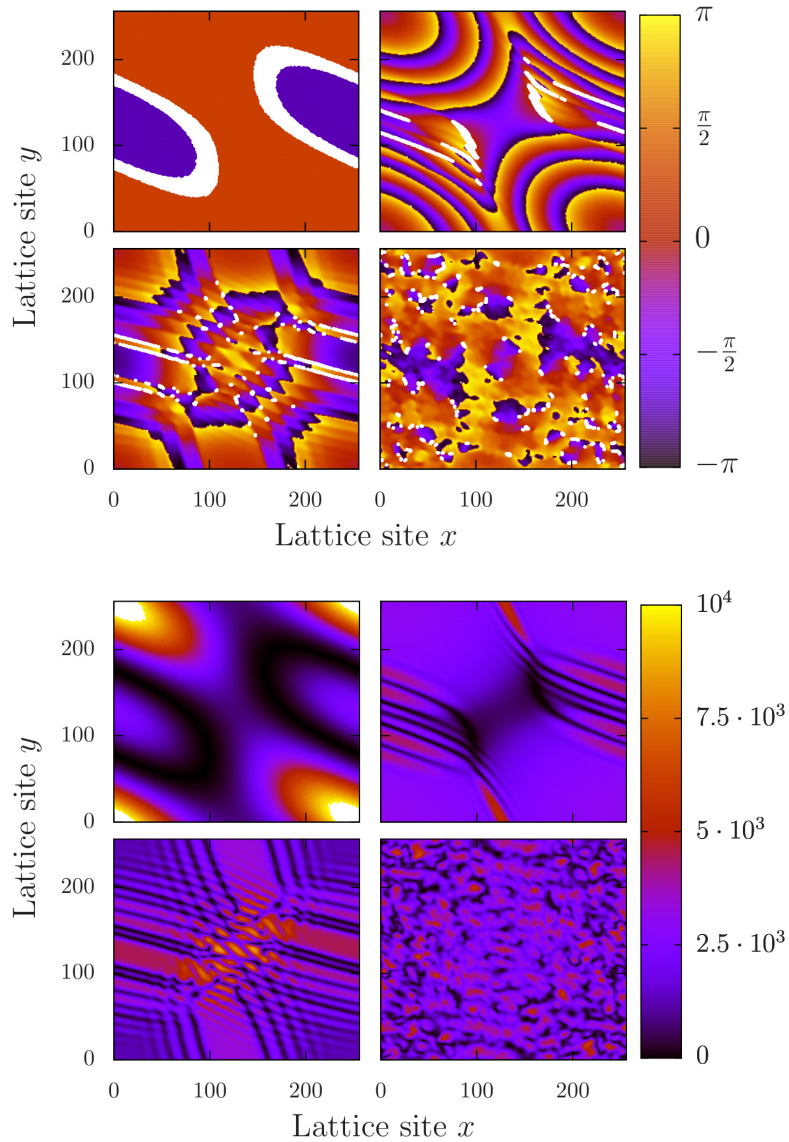


Figure 5.1: Phase angle $\varphi(\mathbf{x}, t)$ (upper panel) and spatial density $n(\mathbf{x})$ (lower panel) at four times during a single run of the simulations in $d = 2$. Parameters are: $\bar{g} = 3 \cdot 10^{-5}$, $N = 10^8$, $N_s = 256$ (same as Fig. 3.1(left panel)). Shown times are: 1. $\bar{t} = 0$ (top left): Ordered phase at initial preparation. 2. $\bar{t} = 52$ (top right): During build-up of strong density and phase gradients. 3. $\bar{t} = 104$ (bottom left): Formation of vortices and antivortices. 4. $\bar{t} = 208$ (bottom right): Isotropisation of density and phase fluctuations.

5.1 Bose gas approaching the non-thermal fixed point

In this section we return to the process of the formation of vortical excitations and of the Bose gas approaching the non-thermal fixed point characterised by the wave-turbulent scaling solutions discussed in Sect. 2.3, Chap. 3 and Refs. [29,31]. Thereby

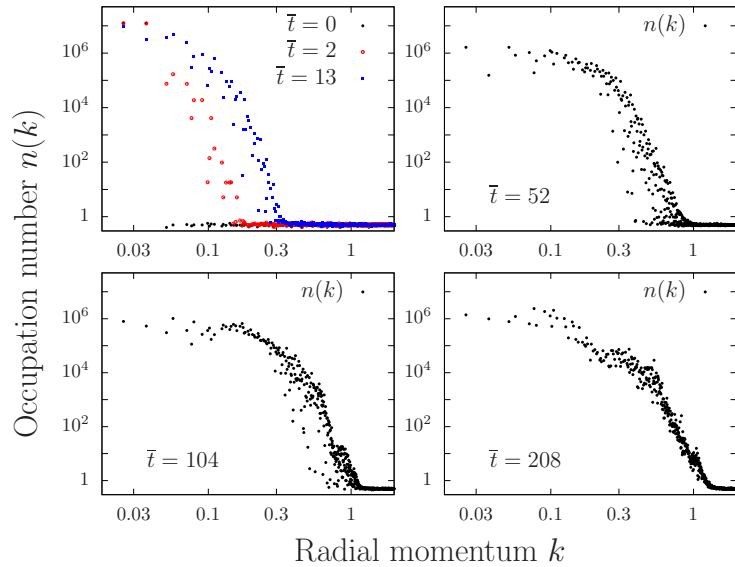


Figure 5.2: Single-particle mode occupation numbers as functions of the radial momentum k , for six different times in $d = 2$ dimensions. The number of runs is ~ 100 . Parameters are the same as in Fig. 5.1. Note the double-logarithmic scale. At early times (top left), scattering between macroscopically occupied modes leads to excitation transfer to high momenta. Vortex formation (bottom left) happens when this process has reached the healing length scale k_ξ .

we first focus on the evolution of the single-particle momentum distributions and the emergence of non-thermal power laws. In order to identify in a clearer way the relevant processes in approaching the fixed point we compute the fluxes in momentum space. Remarkably, we find that the appearance of the particle scaling exponent ζ_Q^{IR} in the IR and of the energy exponent ζ_P^{UV} in the UV are compatible with predictions based on general arguments of energy and number conservation in a collision process [41].

5.1.1 Time evolution of the single-particle spectrum

As discussed in Chap. 3, vortical excitations can be created in large numbers, within shock waves forming during the non-linear evolution of the coherent matter-wave field. The dynamics of this process is best observed from the evolution of phase and density profiles for the case of $d = 2$ dimensions shown in Fig. 5.1. Four snapshots are shown, taken at the dimensionless times \bar{t} as indicated in the caption. See App. A for details on the simulations and on lattice units. The initial field configurations were prepared by macroscopically populating a few of the lowest momentum modes in the computation such that the resulting condensate density in position space varied between zero and some maximum value. One can observe how strong phase gradients form due to the non-linear evolution. At around $t \simeq 100$, these gradients collapse into vortices. Scattering processes between vortices quickly isotropise phase and density fluctuations (bottom right). In Fig. 5.2, we show the

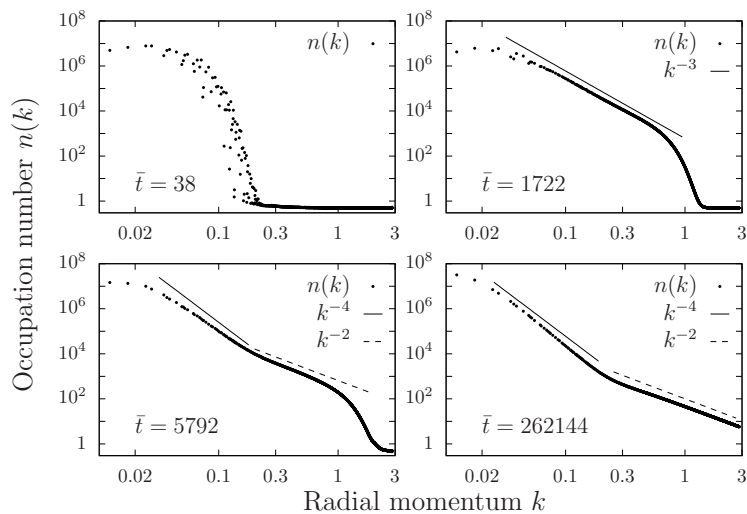


Figure 5.3: Single-particle mode occupation numbers as functions of the radial momentum k , for four different times of a run in $d = 2$ dimensions. Parameters are: $\bar{g} = 3 \times 10^{-5}$, $N = 4 \times 10^8$, $N_s = 512$. Note the double-logarithmic scale. An early development of a scaling $n(k) \sim k^{-3}$ is followed by a quasi-stationary period of bimodal scaling with $n(k) \sim k^{-4}$ in the IR, due to the presence of vortices, and $n(k) \sim k^{-2}$ in the UV, corresponding to weak wave turbulence or thermal equilibrium.

corresponding time evolution of the angle- and ensemble-averaged radial momentum spectrum, Eq. (3.1). The early times (top left) are characterised by scattering between macroscopically occupied modes. Once excitations of the order of the healing length ξ are created, vortex formation sets in.

In the following, we focus on the approach of the non-thermal fixed point scaling solutions. Figs. 5.3 and 5.4 show the long-time evolution of radial momentum spectra, Eq. (3.1), for a Bose gas in $d = 2$ and $d = 3$ dimensions, respectively. Shortly after vortical excitations are created the spectrum in $d = 2$ dimensions exhibits a power-law behaviour $2.85 \lesssim \zeta \lesssim 3.0$ within a range of momenta $k \in [0.04 : 0.4]$, see the upper right panel of Figs. 5.3. Subsequently, the evolution slows down and a quasi-stationary period is entered. During an intermediate stage (bottom left panel of Fig. 5.3 and upper right panel of Fig. 5.4) of the vortex-bearing phase two distinct power laws develop which are in excellent agreement with the analytical prediction in Eqs. (2.34) and (2.36). While in the ultraviolet the exponent $\zeta_P^{\text{UV}} = d$ exhibits weak wave turbulence, Eq. (2.34), in the infrared, the exponent confirms the field theory prediction $\zeta_Q^{\text{IR}} = d + 2$, cf. Eq. (2.36). More specifically, in two dimensions, at $\bar{t} = 5792$, one observes scaling exponents $3.8 \lesssim \zeta \lesssim 4.0$ within a range of momenta $k \in [0.02 : 0.2]$ and $2.0 \lesssim \zeta \lesssim 2.3$ within a range of momenta $k \in [0.2 : 0.7]$, see the lower left panel of Figs. 5.3. At $\bar{t} = 262144$, $4.0 \lesssim \zeta \lesssim 4.2$ within a range of momenta $k \in [0.02 : 0.2]$, see the lower right panel of Figs. 5.3. In $d = 3$ dimensions, at $\bar{t} = 820$, one observes $4.8 \lesssim \zeta \lesssim 5.0$ within a range of momenta $k \in [0.08 : 0.4]$ and $3.0 \lesssim \zeta \lesssim 3.1$ within a range of momenta $k \in [0.5 : 1.7]$, see

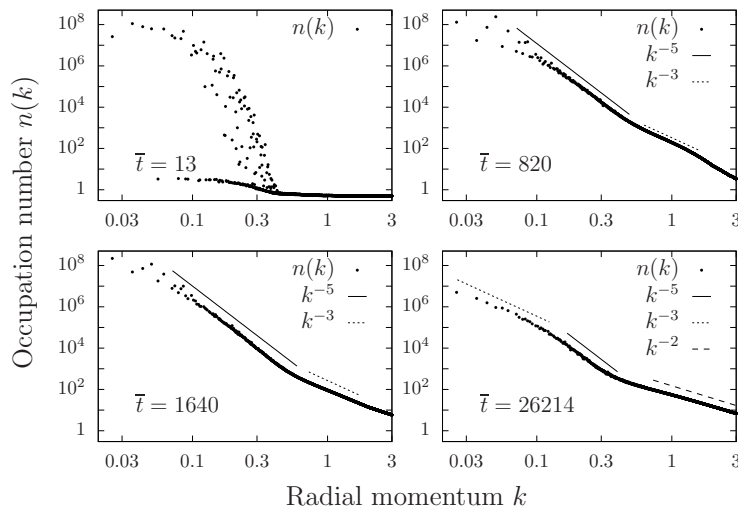


Figure 5.4: Single-particle mode occupation numbers as functions of the radial momentum k , for the four different times of a run in $d = 3$ dimensions. Parameters are: $\bar{g} = 4 \times 10^{-4}$, $N = 8 \times 10^9$, $N_s = 256$. Note the double-logarithmic scale. A period of bimodal scaling $n(k) \sim k^{-5}$ (vortex lines, IR) and $n(k) \sim k^{-3}$ (weak wave turbulence, UV) is followed by trimodal scaling, which also exhibits pairing, i.e., $n(k) \sim k^{-3}$ in the far IR, induced by a set of far separated small vortex rings, in addition to $n(k) \sim k^{-5}$ (IR), and thermal scaling $n(k) \sim k^{-2}$ in the UV.

the upper right panel of Figs. 5.4. At $\bar{t} = 1640$, $5.0 \lesssim \zeta \lesssim 5.1$ within a range of momenta $k \in [0.05 : 0.5]$, see the lower left panel of Figs. 5.4.

During the ensuing evolution, the weak-wave-turbulence scaling decays towards $\zeta = 2$, reflecting a thermal UV tail. Note that in $d = 2$, the weak-turbulence exponent $\zeta_P^{\text{UV}} = 2$ is identical to that in thermal equilibrium in the Rayleigh-Jeans regime, $n(k) \sim T/k^2$ [41]. In $d = 3$ we observe, at late times, a change of the infrared scaling behaviour from $\zeta = d+2 = 5$ to $\zeta = 3$, pointing to the development of pairing correlations, cf. Sects. 4.1.3, Sect. 4.2, and Sect. 5.2.4 below. More specifically, at $\bar{t} = 26214$, one observes a scaling exponent $2.9 \lesssim \zeta \lesssim 3.0$ within a range of momenta $k \in [0.03 : 0.1]$, see the lower right panel of Figs. 5.4.

At late times, after the last vortical excitations have disappeared, we observe the entire spectrum to become thermal, i.e., exhibit Rayleigh-Jeans scaling with $\zeta = 2$ (not shown). We emphasise that thermal scaling of the single-particle occupation number with $\zeta = 2$ applies despite the fact that quasi-particles with a linear dispersion are expected to thermalise in the regime of wave numbers smaller than the inverse healing length $1/\xi \simeq 0.45$ ($d = 2$) and $1/\xi \simeq 0.22$ ($d = 3$). In the Bogoliubov approximation this is seen by taking into account the power-law dependence of the coefficients $u_k^2 \sim v_k^2 \sim k^{-1}$ which contribute to $n(k) \sim (u_k^2 + v_k^2)T/k \sim T/k^{-2}$ [29].

We are going to study more details of the time evolution of the vortex tangle in Chap. 6 and Chap. 7 and focus in the remainder of this chapter on properties of the momentum and velocity correlation functions. An important question in this

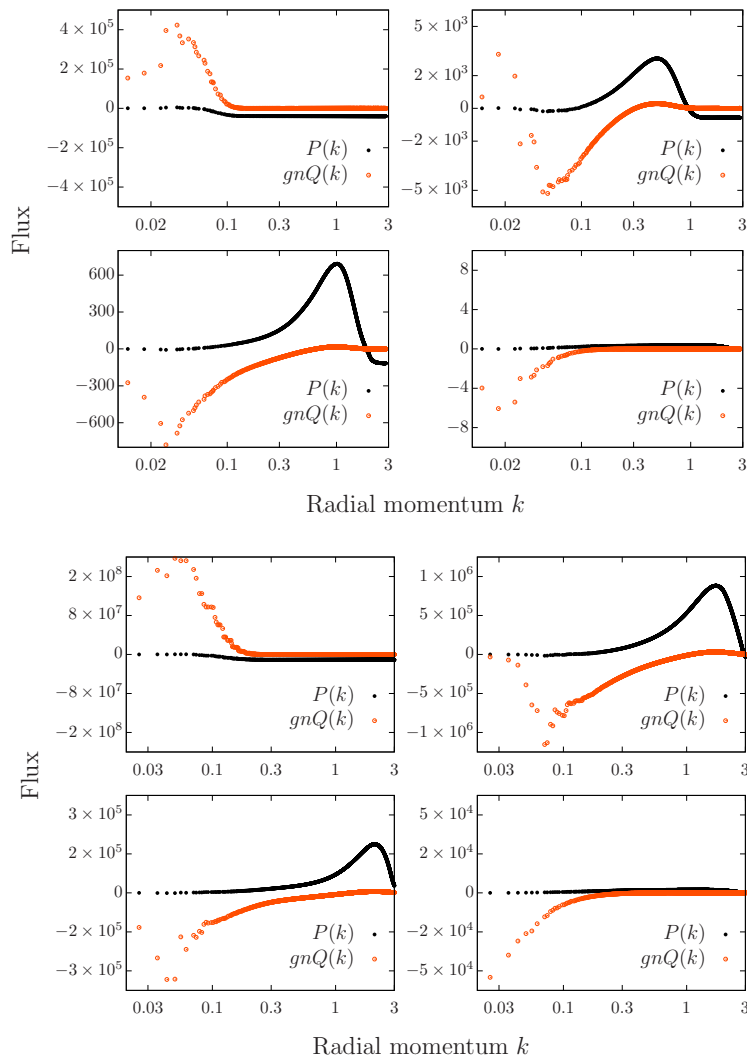


Figure 5.5: Kinetic-energy and particle fluxes in $d = 2$ (upper set) and $d = 3$ (lower set), for the four different snapshots of Figs. 5.3 and 5.4, respectively. Note the logarithmic k -axes. The appearance of the bimodal scaling coincides with a positive kinetic energy flux in the UV, and a negative particle flux in the IR. Flux units: $[P] = [gnQ] = (4m^2 a_s^{d+4})^{-1}$, cf. Sect. 2.2.

context is, why the system selects the particular exponents $\zeta_P^{\text{UV}} = d$ and $\zeta_Q^{\text{IR}} = d+2$ from the set of four possible exponents given in Eqs. (2.34) and (2.36). For this, the fluxes underlying the stationary but non-equilibrium distributions are relevant.

5.1.2 Fluxes

The timeline of distributions shown in Figs. 5.3 and 5.4 suggests that the evolution of the gas involves a transport process from intermediate momenta around $0.05 \dots 0.2$ both towards lower and higher wave numbers, building up a bimodal

power-law distribution. To describe the character of these transport processes we plot, in Fig. 5.5 for $d = 2$ (upper set of four panels) and $d = 3$ (lower set), the radial particle and kinetic-energy flux distributions Q_k and P_k , respectively. Note that the radial particle flux density Q_k is multiplied by gn to have the same units as the energy flux density $P(k)$. These flux densities are defined through the balance equations (2.32) and (2.33), respectively, with kinetic energy density $\varepsilon_k = n_k k^2 / 2m$. They are determined by integrating the numerically obtained particle and energy spectra $N(k)$ and $E(k)$ up to a certain scale. The initial stage is governed by an infrared particle transport towards larger k , also causing a flux gnQ of interaction energy. At intermediate times, $Q(k)$ changes sign. This is accompanied by a positive kinetic energy transport in the UV, as observed in two-dimensional simulations in Ref. [106].

We emphasise that the negative particle flux in the IR and the positive kinetic-energy flux in the UV coincide with the appearance of the bimodal momentum distributions in Figs. 5.3 and 5.4 (bottom left panels). Although the derivation of the IR exponents requires the full dynamical theory with non-perturbatively resummed self-energies, the signs of the fluxes correspond to the respective scaling exponents, i.e., ζ_Q^{IR} in the IR, and ζ_P^{UV} in the UV, cf. Sect. 2.3.3. Moreover, at late times, the kinetic-energy flux P almost vanishes due to a thermalised UV momentum distribution, but Q still reshuffles particles and therefore interaction energy, keeping the system out of equilibrium close to the non-thermal fixed point.

We finally remark that it has been shown in Ref. [41] that a necessary condition for a non-equilibrium stationary distribution in our systems is energy damping in the region of large k . Moreover, energy and particle number conservation in the interaction of different momentum modes can be shown to imply the existence of at least one more sink, i.e., a region where the right-hand sides of Eq. (2.32) effectively has an additional damping term $\sim \Gamma(k)n(k)$, with negative Γ . In between these sinks, a source region supplies the input to the bidirectional flux pattern towards the UV and IR. It was shown in Ref. [41], within wave-kinetic theory, that a positive k -independent flux transports energy, $P > 0$ while a negative flux transfers particles, $Q < 0$. The only exception is the case of $d = 2$ where the thermal and the weak-wave-turbulence exponent ζ_P^{UV} can not be distinguished. Remarkably, this pattern remains valid in our case, beyond the UV weak-wave-turbulence regime, in the IR region where the exponent emerges from a fixed point of the full dynamic equations. As already pointed out in Ref. [29], however, the derivation of the IR exponent $\zeta_Q^{\text{IR}} = d + 2$ requires the existence of a sufficiently well defined quasi-particle dispersion relation, suggesting a treatment in terms of the Quantum Boltzmann equation with a momentum dependent scattering matrix element to be applicable.

From this point of view, the negative flux Q and scaling in the IR and the positive flux P and weak wave turbulence in the UV, as observed in the numerics, emerge as a necessary consequence of conservation laws and transport processes described by wave-kinetic transport equations.

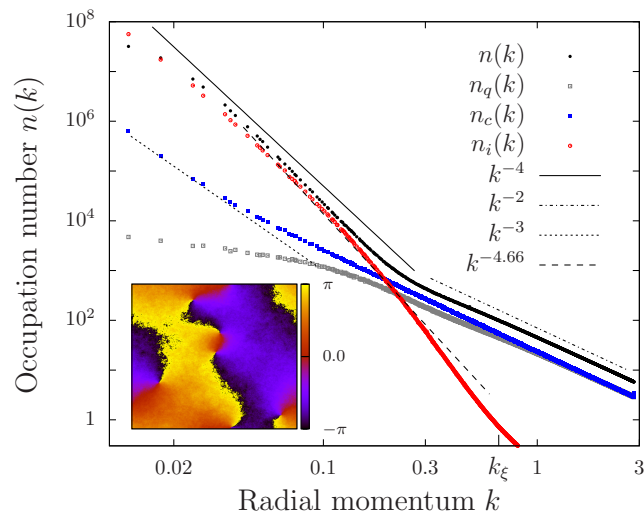


Figure 5.6: Occupation numbers as functions of the radial momentum k , as defined in Sect. 2.2.2: Total single-particle occupation number $n(k)$ (black dots), incompressible (solenoidal-flow) component $n_i(k)$ (red circles), compressible (rotationless) component $n_c(k)$ (blue filled squares), quantum-pressure component $n_q(k)$ (grey open squares). Parameters are the same as in Fig. 5.3 (lower right panel), for the run in $d = 2$ dimensions at the time $\bar{t} = 262144$. Note the double-logarithmic scale. A scaling with $k^{-4.66}$ corresponds to a power-law exponent $5/3$ for the kinetic energy in $d = 2$. See text for more details on the scaling exponents. Inset: Phase angle $\varphi(\mathbf{x}, t)$.

5.2 Vortices, acoustic turbulence and the departure from the fixed point

In this section we analyse the single-particle momentum spectra obtained in our numerical simulations in view of their interpretation in terms of vortical excitations as implied by the point- and line-vortex models introduced in Chap. 4. For this we first decompose the flow pattern of the system which has closely approached the non-thermal fixed point, into transverse (incompressible) and longitudinal (compressible) contributions. In this way we can show that the IR scaling is dominated by the incompressible part while in the UV the particles mainly belong to the compressible as well as a quantum pressure components. We find a further scaling exponent $\zeta \simeq d + 1$ for the sub-dominant compressible component in the IR which is interpreted as a signature of acoustic turbulence.

Moreover, going beyond the results presented in [31] we identify signs of pair formation in the final stage. The scaling caused by this goes beyond the predictions from dynamical quantum field theory summarised in Section 2.3, and we interpret it as a signature for the system leaving the fixed point again for final thermalisation.

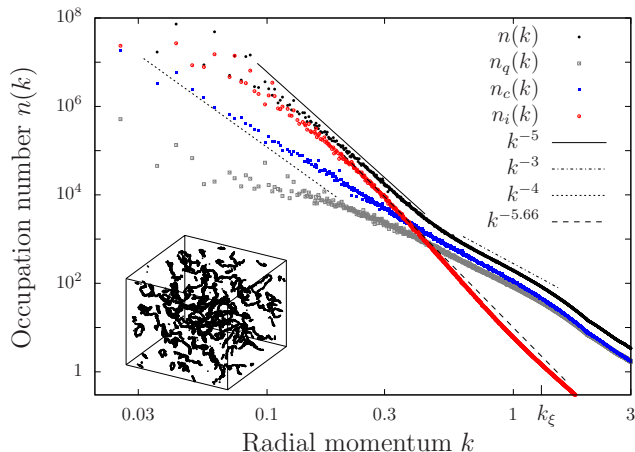


Figure 5.7: Occupation numbers as functions of the radial momentum k , as defined in Sect. 2.2.2 (see caption of Fig. 5.6 for more information). Parameters are the same as in Fig. 5.4 (lower left panel), for the run in $d = 3$ dimensions at the time $\bar{t} = 1640$. Note the double-logarithmic scale. A scaling with $k^{-5.66}$ corresponds to a power-law exponent $5/3$ for the kinetic energy in $d = 3$. Inset: The black spots mark points around the vortex line cores where the density falls below 5% of the mean density n .

5.2.1 Superfluid turbulence and statistics of vortices

To exhibit vortical flow, we make use of the hydrodynamic decomposition, see Sect. 2.2.2. In Figs. 5.6 and 5.7, we depict the momentum distributions of the occupation numbers $n_i(k)$, $n_c(k)$, and $n_q(k)$, together with the previously shown total single-particle spectrum $n(k)$, each at a late time when the system is close to the fixed point, i.e., shows the predicted scaling both in the IR and the UV. Red circles denote n_i , filled blue squares n_c , and open grey squares n_q . Qualitatively, the results are similar for $d = 2$ and $d = 3$.

In the range of large wave numbers, the spectrum is dominated by the compressible and quantum-pressure components. The scaling of these excitations exhibits the weak-wave-turbulence exponent $\zeta_P^{\text{UV}} = d$. For smaller wave numbers the scaling changes to $n(k) \sim k^{-d-2}$. The decomposition into the various components now shows that this switching to a different scaling in the IR is clearly due to the take-over of a different character of the excitations with a modified flow pattern accounted for by the incompressible (solenoidal) component of \mathbf{w}_v . The fact that in this regime contributions from vortical flow n_i dominate is in accordance with our interpretation of the strong IR scaling by a model of an ensemble of vortical excitations. As we have discussed in the previous section the analytically predicted infrared power laws $n(k) \sim k^{-d-2}$ are consistent with a finite density of independent vortices and antivortices ($d = 2$) or vortex lines ($d = 3$).

Moreover, we find that the compressible component in the IR represents the second strongest contribution to the flow and develops a non-thermal scaling as $\sim k^{-d-1}$.

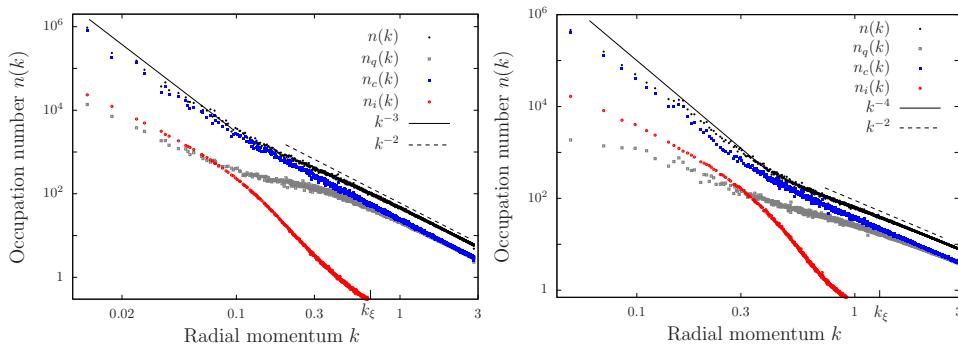


Figure 5.8: Late-stage acoustic turbulence: Occupation numbers defined in Sect. 2.2.2 are shown as functions of the radial momentum k , from an average over ~ 10 single runs in $d = 2$ dimensions (left panel) and $d = 3$ (right panel). The times $\bar{t} = \mathcal{O}(10^6)$ ($d = 2$) and $\bar{t} = \mathcal{O}(10^4)$ ($d = 3$) were chosen right after the decay of the last vortical excitation. See caption of Fig. 5.6 for more information. Parameters are: $d = 2$: $\bar{g} = 3 \times 10^{-5}$, $N = 4 \times 10^8$, $N_s = 512$; $d = 3$: $\bar{g} = 4 \times 10^{-4}$, $N = 10^9$, $N_s = 128$. Note the double-logarithmic scale. The figure shows that, shortly after the last vortex ring has disappeared (incompressible component breaks down), compressible excitations exhibiting acoustic turbulence scaling $\sim k^{-(d+1)}$ remain present.

We will discuss this result in more detail in Sect. 5.2.2 below.

For momenta larger than about $k \simeq 0.2$ for $d = 2$ and $k \simeq 0.4$ for $d = 3$ the compressible and quantum-pressure components dominate the momentum distributions. In the regime of intermediate momenta, above the scale $k_l \sim 2\pi/l$ with l the mean inter-vortex spacing, where the incompressible flow and the rest are of roughly equal strength one finds a scaling of approximately $n_i(k) \sim k^{-d-1-5/3}$, corresponding to $E_i(k) \sim k^{-5/3}$ for both the two- and the three-dimensional case. Scaling with this exponent, which is the same as in classical Kolmogorov turbulence in an incompressible fluid, has been found in simulations of superfluid turbulence in $d = 2, 3$ before [18, 107, 108, 114–118, 324]. In some of these cases, turbulent flow appeared in the time evolution of a system starting from a Taylor-Green configuration of vortex line tangles. We emphasise that our configuration after the creation of vortical excitations resembles more a state of the kind usually termed chaotic (Vinen) turbulence. It is unclear whether chaotic turbulence can be related to classical Kolmogorov turbulence as this does not bear near-classical bundles of equal-orientation vortex lines. Nonetheless we observe such $5/3$ scaling in the range of intermediate momenta where the interplay between the incompressible and compressible components is most pronounced.

5.2.2 Acoustic turbulence

The IR scaling $\sim k^{-d-1}$ of the compressible component (blue filled squares) in Figs. 5.6, 5.7, and also Fig. 5.10 below suggests an interpretation in terms of acoustic turbulence [41, 45, 46, 50] and corroborates the numerical findings reported in

Ref. [325].

In our numerical simulations the scaling is persistent until late times, see, e.g., Fig. 5.10, but decays after the vortices have disappeared. To check that the non-thermal scaling of the incompressible component is not an artifact of the decomposition of the vortical flow into compressible and incompressible parts, we show the momentum spectrum for an average over selected runs in $d = 3$, see Fig. 5.8 (right panel), where the snapshot is taken shortly after the last vortex ring has disappeared. One can observe that acoustic turbulence can survive for a limited period, $\Delta\bar{t} = \mathcal{O}(100)$, beyond the time when vortical excitations are negligible. In the case of $d = 2$, the effect is weaker but still present, see Fig. 5.8 (left panel), where we show the averaged spectrum shortly after the last vortex-antivortex annihilation. Our interpretation of this finding is that acoustic turbulence coexists with the dominant vortical flow. It is driven by vortex motion and especially vortex annihilation processes, which are known to produce compressible excitations. In $d = 2$, signatures of acoustic turbulence are less pronounced, which we attribute to reduced vortex dynamics or, equivalently, weaker driving of compressible excitations.

We remark that scaling predictions for weak wave turbulence on top of a homogeneous condensate have been deduced in Ref. [326]. Decomposing the field $\phi(x, t) = \phi_0 + \delta\phi(x, t)$, the spectrum corresponding to energy transport could be calculated from a 3-wave Boltzmann equation and yields $n(k) \sim k^{-d-d/2}$. In $d = 2$ dimensions the predictions agree with our findings and differ in $d = 3$ dimensions. We remark that the weak-wave turbulence phenomenon consists of a direct energy cascade. [326]. Since we expect decaying vortices to inject energy into compressible excitations at a scale on the order of the healing length, we would rather assume that the turbulence is driven by transport from small to large scales. During the vortex bearing phase modifications due to vortex-sound interactions might also be relevant.

5.2.3 Vortex velocities

We furthermore investigated the velocity-field probability distribution in the turbulent regime to compare our data with the expectations summarised in Sect. 4.3. In $d = 3$ dimensions, see Fig. 5.9 (left), the results corroborate theoretical and experimental results reported in Refs. [312, 313, 327, 328]. The low-momentum distribution is characterised by Gaussian statistics, whereas the UV regime clearly shows scaling $\mathcal{P}(v_x) \sim v_x^{-3}$ predicted by the model of randomly distributed, uncorrelated vortex lines, see Eq. (4.47). Note that even at late times, when vortex rings shrink in size, no signs of vortex pairing, $\mathcal{P}(v_x) \sim v_x^{-2}$, can be seen in the velocity distribution. This is due to dominating Gaussian fluctuations in the low momentum region. In $d = 2$ dimensions, see Fig. 5.9 (right), we compare the distribution of the superfluid velocity field with the distribution of velocity of the individual vortices. Similar to the three-dimensional case the IR part of the velocity-field distribution is characterised by Gaussian statistics, whereas the UV regime shows single-vortex scaling [312]. The vortex velocity distribution is obtained from the statistical analy-

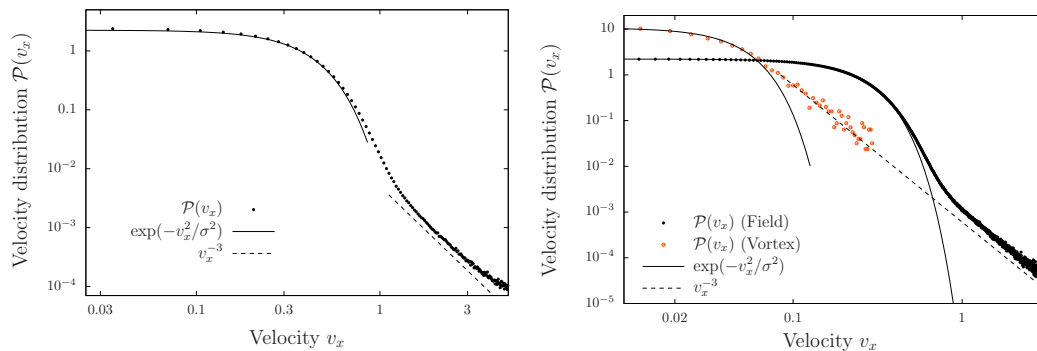


Figure 5.9: Velocity field probability distribution. Note the double-logarithmic scale. Left: Parameters are the same as in Fig. 5.4, for the run in $d = 3$ dimensions, at the time $\bar{t} = 1640$. The black line is a Gaussian fit to the data which shows that in the low-velocity regime, the distribution is dominated by Gaussian fluctuations. A high-velocity scaling with v_x^{-3} reflects the presence of uncorrelated vortices, cf. Eq. (4.47). Right: Comparison of the vortex velocity distribution with the velocity-field probability distribution in $d = 2$ dimensions at $\bar{t} = 32768$. At this time an average of 86 vortices are present in the system. Parameters: $\bar{g} = 3 \times 10^{-5}$, $N = 16 \times 10^8$, $N_s = 1024$. A high-velocity scaling with v_x^{-3} reflects the presence of uncorrelated vortices, cf. Eq. (4.47). Gaussian fluctuations are suppressed in the distribution of velocities of the individual vortices, measured through the motion tracking of the vortex cores.

sis of a vortex-tracking algorithm which is designed to detect regions of low density accompanied by a winding number equal to one. The method is analogous to the experimental set-up of Ref. [313], where particles are trapped inside vortex cores to study vortex velocities in $d = 3$. In agreement with the experiment, Fig. 5.9 (right) shows that Gaussian random motion is suppressed for vortices, but $\sim v^{-3}$ scaling clearly persists. In this way, quantum turbulence can be distinguished from classical turbulence, where a continuous distribution of vorticity favours a Gaussian velocity distribution.

5.2.4 Pairing and departure from the fixed point

In Fig. 5.10 we show the decomposition of the single-particle spectrum into the previously defined incompressible, compressible, and quantum-pressure components, see Sect. 2.2.2, for the 3-dimensional system at $\bar{t} = 26214$, as in the lower right panel of Fig. 5.4. At this time, only a small density of vortex rings has survived, which decays under the influence of the noise field, cf. also Refs. [83, 329]. During the period when only a few small vortex rings remain one can observe a decrease of the infrared scaling exponents of the occupation number and its incompressible part to the value $\zeta = 3$. Since vortical excitations are still dominating the spectrum, we can interpret this observation in terms of the statistical point vortex model introduced in Chap. 4, as vortex-antivortex pair correlations, see Sect. 4.2. This is consistent with the snapshots of individual runs showing small vortex ellipses (see inset of Fig. 5.10). The scaling transition can be identified with the scale

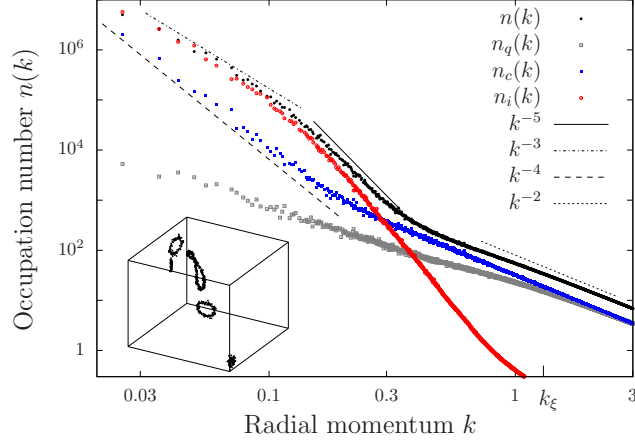


Figure 5.10: Pairing effects: Occupation numbers are shown as functions of the radial momentum k . Parameters are the same as in Fig. 5.4, for the run in $d = 3$ dimensions, at the time $\bar{t} = 26214$ (lower right panel). Note the double-logarithmic scale. The scaling $\sim k^{-3}$ in the far IR reflects pair correlations present in far-separated small vortex loops. (See caption of Fig. 5.6 for more information).

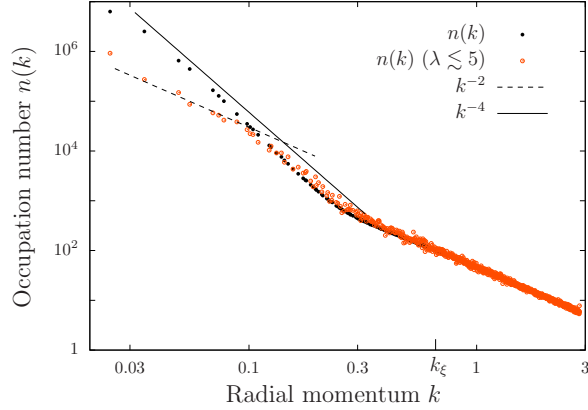


Figure 5.11: Pairing effects: Occupation numbers are shown as functions of the radial momentum k in $d = 2$ dimensions, at the time $\bar{t} = 262144$: Occupation number obtained from averaging over all runs (black dots); Occupation number obtained from averaging over selected runs featuring tightly bound vortex antivortex pairs with maximum pair correlation length $\lambda \lesssim 5$ (red circles). Parameters: $\bar{g} = 3 \times 10^{-5}$, $N = 10^8$, $N_s = 256$. Note the double-logarithmic scale. A scaling with k^{-2} reflects the presence of correlated vortex-antivortex pairs in $d = 2$.

$k_b = 2\pi/2r_b$, with estimated minor radius $r_b \simeq 15$.

Fig. 5.11 shows the average occupation number spectrum at $\bar{t} = 262144$ in $d = 2$ dimensions, as in the lower right panel of Fig. 5.3. In the average over all generated runs pairing effects can hardly be observed. However, for selected runs with small maximum pair correlation length $\lambda \lesssim 5$, as introduced in Sect. 4.1.3, the pair scaling appears. We find that in the selected runs ($\sim 0.2\%$ of total number of runs), at

the chosen point of time one or at most a few vortex-antivortex pairs with pairing length smaller than the distance between pairs are present. This constitutes the final period of the evolution, shortly before the last pair has disappeared through mutual annihilation and the system fully thermalises. The generic configuration in $d = 2$ dimensions during the preceding time interval of critical slowing down close to the non-thermal fixed point is characterised by randomly positioned vortices and antivortices, with pairing correlations nevertheless present. We observe that, in $d = 2$, scattering between the vortices of equal and opposite circulation can lead to the increase of the pairing length between correlated vortices and antivortices. A detailed analysis of this process will be given in Chap. 6. This is in contrast to the situation for $d = 3$ where the scattering between vortex rings rarely leads to an increase in the size of the rings. It is energetically advantageous for the rings to shrink in size, and thus, at a particular late time of the evolution the presence of separated small rings is generic and "pairing" is seen in the spectrum.

5.3 Summary

We have studied the dynamics of superfluid turbulence in two- and three-dimensional dilute Bose gases. A focus was set on the identification and characterisation of stationary scaling solutions, in particular for single-particle momentum distributions. Here, we have shown that the stationary scaling is maintained by the presence of particle (IR) and energy (UV) fluxes, originating at intermediate scales and directed towards the low- and high-frequency limits, respectively. The respective fluxes were found to be consistent with the particular scaling exponents of the momentum distribution in the respective regimes, as predicted within non-perturbative wave turbulence theory. We could successfully employ statistical models of point vortices in two dimensions and vortex rings in three dimensions to interpret the IR scaling exponent of the spectra. Moreover, we observed in our simulations, during the final thermalisation stage, decay of the turbulence scaling into a scaling derived from the assumption of vortex-antivortex pairing. To characterise further the bimodal power spectra developed close to the non-thermal fixed point we have analysed the decomposition of the overall flow pattern into compressible and incompressible components. We found that the IR power spectra of underlying compressible excitations suggest an understanding in terms of acoustic turbulence on top of the vorticity-bearing quasi-condensate. Finally, to compare with the results of recent experiments and analytical predictions, the velocity-field probability distribution as well as the velocity statistics of individual vortices has been studied. This observable is of great interest, as it can be used to experimentally distinguish between classical and quantum turbulence.

Our analysis gives a picture of the necessary conditions and the character of the non-thermal fixed point. It also shows that pairing effects are a first signature for the system leaving this fixed point again for the final move to thermal equilibrium.

Critical dynamics near a non-thermal fixed point

In this chapter, we study the non-equilibrium dynamics of a two-dimensional Bose gas evolving towards and away from a non-thermal fixed point, the (quasi-) stationary properties of which were discussed in Chaps. 3, 4 and 5 and Refs. [29, 31, 32]. Here, we focus on the dynamics of vortices which have been shown to play a crucial role [33]. For example, we monitor the vortex density during equilibration of the turbulent gas and reveal a bimodal scaling behaviour in time. By following vortex-antivortex correlations, we show that this phenomenon is directly related to a non-equilibrium vortex unbinding process. Ultimately, vortex excitations evolve into an almost random distribution which constitutes the universal scaling at the non-thermal fixed point. The main aim of this chapter is to locate the non-thermal fixed point with respect to equilibrium configurations of vortex excitations in the two-dimensional superfluid [126, 127], see Fig. 1.2.

We present mainly numerical simulations of a two-dimensional dilute Bose gas evolving towards a non-thermal fixed point and away from it to thermal equilibrium. In the spirit of Chap. 3, we choose initial states with a few macroscopically occupied modes in momentum space, as illustrated in Fig. 6.1. Fluctuations around these mean values are introduced by sampling the initial field modes according to Gaussian Wigner distributions (see Sect. 2.2 and App. A). The type of initial conditions shown in Fig. 6.1 induces transport of particles and energy, which leads to vortex creation and turbulence. We point out, that by varying the number and geometry of initially occupied modes, we probe the initial-state dependence of our observables.

6.1 Creation of vortices and turbulence

In the presence of a non-vanishing coupling g the initial states depicted in Fig. 6.1 are far from thermal equilibrium. During the first stages of the evolution coherent scattering into higher excited modes dominates. In Fig. 6.2 (left panel), we show the time evolution of the ensemble-averaged single-particle momentum occupation numbers $n(\mathbf{k}, t) = \langle |\phi(\mathbf{k}, t)|^2 \rangle$ as a function of time, for several momenta $\mathbf{k} = (k_i, 0)$

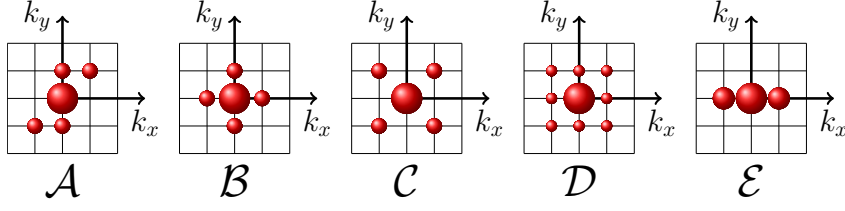


Figure 6.1: Panels $\mathcal{A} - \mathcal{E}$ illustrate the initially occupied momentum modes \mathbf{k}_{ini} (shaded discs) with $n(\mathbf{k}_{\text{ini}}, t = 0) \gg 1$, for 5 different mean field configurations. The areas of the discs are proportional to the mean number of particles. A sixth initial condition \mathcal{A}^* is geometrically the same as \mathcal{A} , but with initially occupied momenta $\mathbf{k}_{\text{ini}}^* = 4\mathbf{k}_{\text{ini}}$. If not stated otherwise, on average half of the total number of particles occupies the zero mode.

along the k_x -axis. One observes a power-law growth for momenta with $k_x \neq 0$ until $t \simeq 10^2$. This process, exhibiting fast power-law growth $\sim t^{2n}$ of occupations can be understood from analytic mean-field calculations by approximating strong initial occupations to be time-independent. This computation is carried out in Chap. 7. It is present for all our initial conditions and independent of spatial dimension.

In Fig. 6.2 (right), we continue to follow the time evolution of the condensate mode, $n(0, t)$. The decay of the zero-mode occupation is part of a non-local energy and particle transport to higher momenta. In coordinate space, this process leads to the formation of shock waves, which decay into large numbers of vortices, see Chap. 3 and Ref. [32] and videos of the evolution [311]. In addition, we study the

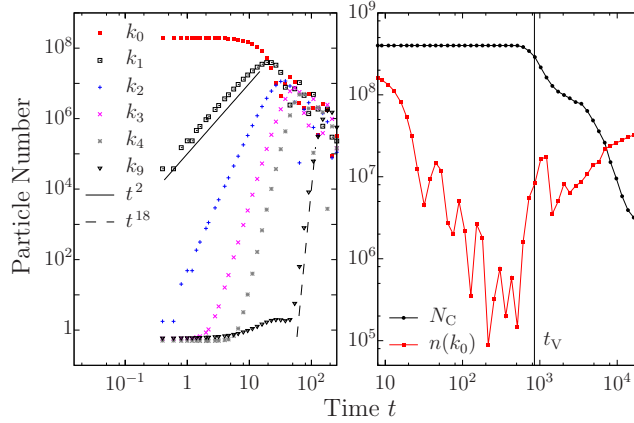


Figure 6.2: Left panel: Single-particle occupation numbers $n(\mathbf{k}, t) = \langle |\phi(\mathbf{k}, t)|^2 \rangle$ as a function of time t (in lattice units), for different discrete momentum modes $\mathbf{k} = (k_n, 0)$, $k_n = 2 \sin(n\pi/N_s)$ along the k_x -axis. Results are computed on a grid of size $N_s = 512$, from initial field configuration \mathcal{A} . Note the double-logarithmic scale. Lines show different power-law evolutions $\sim t^{2n}$. Right panel: Zero-mode occupation number $n(k_0, t)$ and coherent population $N_C = \int d^2x |\langle \phi(\mathbf{x}, t) \rangle|^2$ as a function of time t (double-log. scale), for an average over 100 runs, grid size $N_s = 512$ and initial condition \mathcal{A} . t_V marks the time of vortex creation.

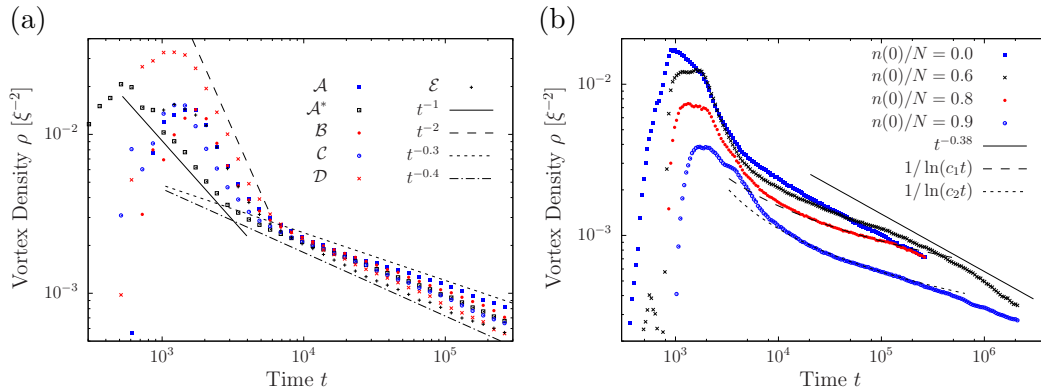


Figure 6.3: Vortex density ρ as a function of time t (in lattice units). Note the double logarithmic scale. (a) Evolution for various initial conditions as given in Fig. 6.1, averaged over 20 runs on a grid of size $N_s = 1024$. Lines show different power-law evolutions. Assuming the area of a vortex to be given by $V_V = (2\xi)^2\pi$, a maximally dense packing of vortices would correspond to the vortex density $\rho_{\max} = 1/V_V = 1/(4\pi\xi^2)$. (b) Evolution for different initial zero-mode populations $n(0)/N$. Averages were taken over 20 runs on a lattice of size $N_s = 1024$, for initial condition \mathcal{A} . Fitted parameters are $c_1 = 0.0026$ and $c_2 = 0.0012$. The closest approach to the non-thermal fixed point is reached at $t \simeq (5 \dots 10) \times 10^5$.

coherent population $N_C = \int d^2x |\langle \phi(\mathbf{x}, t) \rangle|^2$ for an initially phase coherent ensemble $N_C(t=0) = N$. The dynamics preserve coherence until vortices form around time $t = t_V \simeq 10^3$. This can be understood by considering that the local phase angle $\varphi(\mathbf{x}, t)$ of the complex field $\phi = |\phi|\exp\{i\varphi\}$ is determined by the positions of the vortices. Since vortices strongly interact, their trajectories in position space quickly randomise. Hence, in the ensemble average the coherent population decays. Beyond this time, density fluctuations are significant only at momenta larger than the inverse healing length, $k > 1/\xi$, whereas long-range fluctuations of the Bose gas are dominated by vortical flow. For $t \gtrsim t_V$, the zero-mode population $n(0, t)$ starts to increase, signalling the onset of phase ordering associated with vortex annihilations. This process will be studied in the following sections.

6.2 Vortex density decay

After the creation of vortices, the dynamical evolution exhibits a dual cascade in momentum space, transporting particles from intermediate to small momenta and energy from intermediate to large momenta [32]. The single-particle momentum spectrum develops a quasi-stationary bimodal scaling, with characteristic exponents corresponding to the respective cascade processes, see Chap. 5. The system approaches a non-thermal fixed point [29, 32]. The low-momentum scaling of the single-particle momentum distribution can be related to the presence of randomly distributed vortices and antivortices [32]. In this chapter, the evolution towards and away from the non-thermal fixed point is investigated. First, we will show that

the approach to the non-thermal fixed point is accompanied by a change of the characteristic scaling of the ensemble averaged vortex density $\rho(t)$ with time.

Fig. 6.3a shows the time evolution of the vortex density

$$\rho(t) = \langle N^V(t) + N^A(t) \rangle / V \quad (6.1)$$

with $N^{V(A)}(t)$ being the number of vortices (antivortices) in the volume V at time t , found in simulations starting from the initial conditions defined in Fig. 6.1. Vortices are counted by detecting their characteristic density and phase profiles, see Sect. 2.2.1 and App. A. In all runs, vortex formation occurs around $t_V \simeq 10^3$, apparent from the steep increase of vortex density around this time. For $t \gtrsim t_V$, two distinct stages in the vortex density decay are observed, a rapid early stage and a slow late stage. Specifically, the vortex density follows power laws $\rho(t) \sim t^{-\alpha_i}$ with two different exponents α_i , $i = 1, 2$. The exponent during the early stage depends considerably on initial conditions $1 \lesssim \alpha_1 \lesssim 2$, whereas the late stage features a decay exponent in a narrow interval $0.3 \lesssim \alpha_2 \lesssim 0.4$. From our analysis given in Sect. 6.7 below, we estimate that the closest approach to the non-thermal fixed point is reached at $t \simeq (5 \dots 10) \times 10^5$.

We have repeated our simulations on various grid sizes, $N_s \in \{256, 512, 1024, 4096\}$. Thereby, we found that decay exponents saturate for and above $N_s = 512$. We attribute deviations on smaller grids to effects from regular (integrable) dynamics of few-vortex systems [330]. We remark that the onset of the slow decay coincides with the development of a particular scaling behaviour in the single-particle momentum distribution $n(k) \sim k^{-4}$, which in Refs. [29,31,32] was shown to signal the approach to the non-thermal fixed point and the formation of a set of randomly distributed vortices. In this context, the reduction of the vortex density decay exponent, compared to the early stage of rapid decay, is interpreted as a (critical) slowing down of the nonlinear dynamics near the non-thermal fixed point.

As shown in Fig. 6.3b, the vortex density decay at late times is not always given by a power law. By considerably increasing the initial population of the zero-mode, e.g. $n(0)/N \in \{0.6, 0.8, 0.9\}$, we find that for some time the vortex density is better described by an inverse ln-function $\rho(t) \sim 1/\ln(t)$. However, at a late times $t \gtrsim t^*$, the decay seems to converge to a power law from the slow-decay regime. By analyzing the dynamics of the single-particle momentum distribution, we could identify the time t^* to be the time when compressible excitations have thermalised the high-momentum tail of the spectrum (for details see Fig. 10 in Ref. [32]). This is consistent with the observation that the inverse-ln decay could not be observed for initial conditions with small zero-mode occupation where the high-momentum thermalisation happens faster.

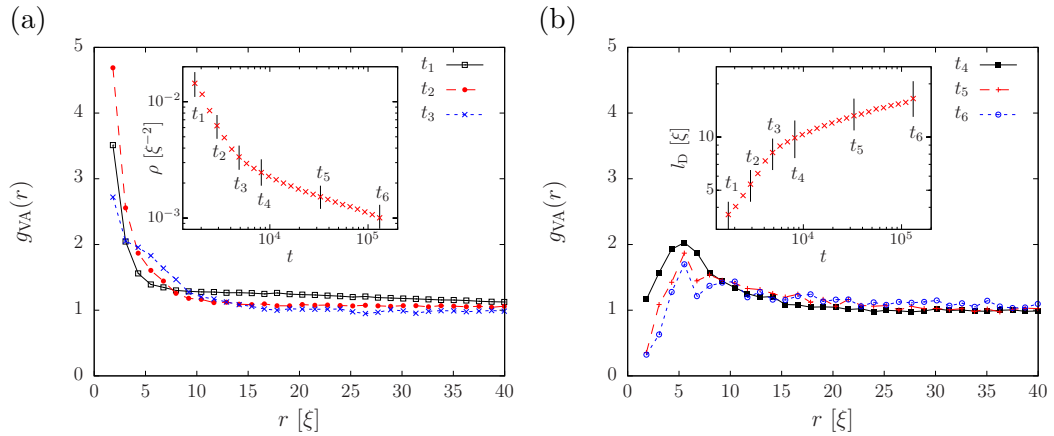


Figure 6.4: Normalised vortex-antivortex correlation functions g_{VA} defined in Eq. (6.2) as a function of radial coordinate r , for six different times t_i (in lattice units). (a) $g_{\text{VA}}(r)$ at times t_i , $i = 1, 2, 3$ during the rapid-decay stage, averaged over 174 runs on a grid of size $N_s = 1024$, using initial condition \mathcal{A} . Inset: Vortex density ρ as a function of time t , taken from the simulations for Fig. 6.3a. (b) $g_{\text{VA}}(r)$ at times t_i , $i = 4, 5, 6$ during the slow-decay stage, averaged over 174 runs on a grid of size $N_s = 1024$, using initial condition \mathcal{A} . Inset: Mean vortex-antivortex pair distance l_{D} as a function of time, from the simulations for Fig. 6.3a.

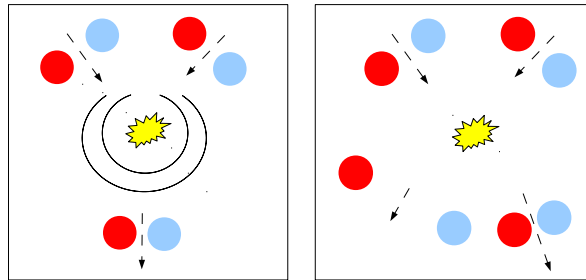


Figure 6.5: Sketch of different scattering events between two vortex-antivortex pairs in $d = 2$ dimensions. Left panel: Scattering of two vortex pairs resulting in mutual annihilation of two vortices and the emission of density waves. Right panel: Scattering of two vortex pairs, leading to a change in the vortex anti-vortex distance l_{D} and pair velocity \bar{v} . We remark, that once $l_{\text{D}} \sim \xi$ a vortex pair decays rapidly under the emission of density waves.

6.3 Vortex correlations

In the following, the dynamical transition in the vortex annihilation dynamics is discussed in terms of characteristic features of the vortex-antivortex correlation function

$$g_{\text{VA}}(\mathbf{x}, \mathbf{x}', t) = \frac{\langle \rho^{\text{V}}(\mathbf{x}, t) \rho^{\text{A}}(\mathbf{x}', t) \rangle}{\langle \rho^{\text{V}}(\mathbf{x}, t) \rangle \langle \rho^{\text{A}}(\mathbf{x}', t) \rangle}, \quad (6.2)$$

where $\rho^{V(A)}(\mathbf{x}, t) = \sum_i \delta(\mathbf{x} - \mathbf{x}_i(t))$ is the distribution of vortices (antivortices) at time t in a single run. For sufficiently large ensembles, g_{VA} is a function of $r = |\mathbf{x} - \mathbf{x}'|$ only.

In Fig. 6.4a, we show the evolution of $g_{VA}(r, t)$ as a function of r for different times during the fast-decay stage. At early times, one finds a strong pairing peak near $r = 0$. This peak gets quickly reduced and a hole is ‘burned’ into the correlation function near the origin, see Fig. 6.4b. Following the time evolution of the spatial vortex distribution we observe that this involves qualitatively different processes: Mutual annihilations of closely positioned vortices and antivortices occur under the emission of sound waves. Further separated vortices can approach each other in different ways as illustrated in Fig. 6.5. The scattering of two pairs can directly lead to the annihilation of one pair under the emission of sound waves. We consider this to include events where the pair distance of one dipole reduces below a certain threshold, so that it looks like a density dip rather than a vortex-pair. This density dip can still interact with other vortices, but it will quickly vanish. Alternatively, the scattering reduces the vortex-antivortex separation within one pair while it increases it within the other, in accordance with the Onsager point-vortex model [73]. We refer to this characteristic change in $g_{VA}(r)$ as a vortex unbinding process. The scattering of a closely bound vortex off an isolated vortex is not shown, because it is included as a collision between a closely and a loosely bound pair. At around the time $t_3 \lesssim t \lesssim t_4$ the power-law exponent of the vortex density decay changes to about a third of its previous value, see the inset of Fig. 6.4a. Next, we compute the mean vortex-antivortex pair distance l_D , by averaging over distances between each vortex and its nearest antivortex. In accordance to the previous discussion, l_D grows continuously, exhibiting two characteristic stages, see inset of Fig. 6.4b. At times $t \gtrsim 10^4$, $l_D(t)$ approaches the power-law solution $l_D \sim \rho^{-1/2}$, as expected for uncorrelated vortices.

6.4 Energy equilibration

The main result of the previous section was the relation of different stages in the evolution of the vortex density $\rho(t)$ to characteristic features in the vortex-antivortex correlation function $g_{VA}(r, t)$. The vortex density decay, was shown to be accompanied by a dynamical vortex unbinding. This finding can be supplemented by considering the evolution of different energies contained in the gas. In Refs. [114,115] it was suggested to decompose the kinetic energy into an incompressible and a compressible component, which, for conciseness, we give details of in Sect. 2.2.2. In this way, contributions from vortical excitations can be separated from other excitations such as sound waves. In Fig. 6.6, we show the time evolution of different energy components for initial condition \mathcal{A} . One observes that the decay of the incompressible energy during the early-time stage can be estimated to follow a power-law $\sim t^{-1.25}$ and in the late-time stage $\sim t^{-0.2}$. This decay happens considerably slower than the vortex density decay in the early- (late-)time stage $\sim t^{-1.7}$ ($\sim t^{-0.3}$), discussed in Sect. Sect. 6.2. As a result, the incompressible en-

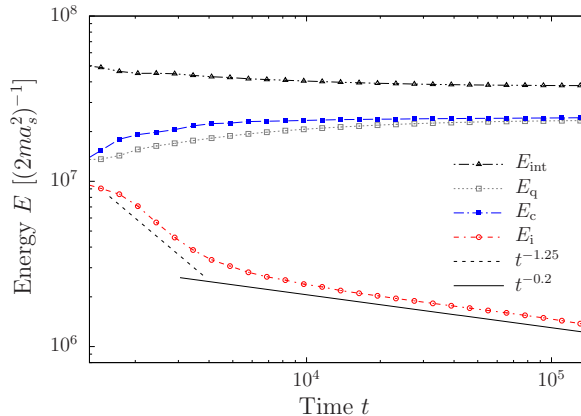


Figure 6.6: Contributions to the total energy as functions of time t (in lattice units), averaged over 174 runs. We show the interaction energy E_{int} , compressible energy E_c , incompressible energy E_i , and quantum pressure E_q , as defined in Sect. 2.2.2, derived on a grid of size $N_s = 1024$ and for initial condition \mathcal{A} defined in Fig. 6.1. Note the double-logarithmic scale. See Sect. 6.4 for a discussion of the power-law evolutions.

energy per vortex grows as $\sim t^{0.45}$ at early times and as $\sim t^{0.1}$ at late times. Since the energy of a vortex pair increases with distance, this is in agreement with the phenomenon of increasing vortex-antivortex pair distance l_D . At late times, compressible and quantum-pressure energy components develop into an equi-partitioned state, also observed in decaying superfluid turbulence starting from a Taylor-Green vortex configuration [119].

6.5 Possible relation to classical turbulence

In the following, we discuss a similarity between our results and findings in classical fluid turbulence. Great efforts have been made to investigate freely decaying turbulence in two-dimensional classical fluids, see, e.g., Refs. [331–338]. In this context, special focus was set on the decay of the enstrophy $\Omega(t)$, which is related to the vorticity $\omega = \nabla \times \mathbf{v}$ of the velocity field $\mathbf{v}(\mathbf{x}, t)$ by

$$\Omega(t) = \frac{1}{2} \int d^2x |\omega(\mathbf{x}, t)|^2. \quad (6.3)$$

It was found by different methods that the long-time decay of the enstrophy is given by a power-law $\Omega(t) \sim t^{-\gamma}$, with $\gamma \simeq 0.35 - 0.4$ [331–338].

In superfluids, vorticity is concentrated in the vortex cores. The vorticity of a turbulent flow consisting of M vortices with circulations κ_i and positions \mathbf{x}_i , for $i < M$, is given by $\omega(\mathbf{x}, t) = \sum_i \kappa_i \delta(\mathbf{x} - \mathbf{x}_i(t))$. Hence, in a flow consisting of

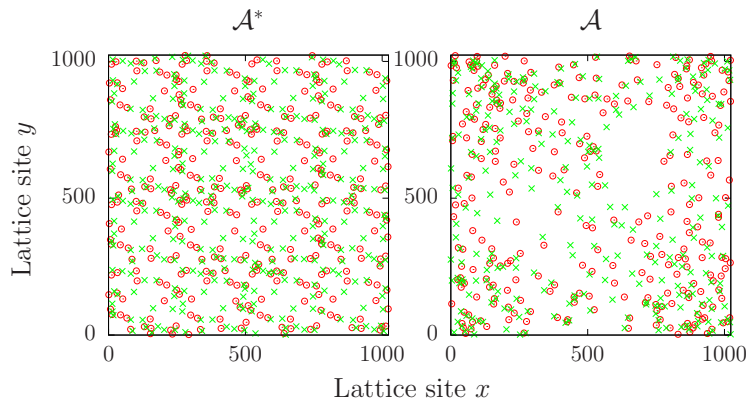


Figure 6.7: Vortex and antivortex positions shortly after turbulence creation at $t \simeq t_V$, for two single runs of the simulations on a grid of size $N_s = 1024$. Left panel: Initial condition \mathcal{A}^* . Right panel: Initial condition \mathcal{A} , as defined in Fig. 6.1.

vortices with circulations $\kappa_i = \pm \hbar/m$ the enstrophy reads

$$\Omega(t) = \frac{\hbar^2}{2m^2} \delta(\mathbf{0}) M(t), \quad (6.4)$$

which is, with $\delta(\mathbf{0}) \sim 1/V$, proportional to the vortex density, $\Omega(t) \propto \rho(t)$. As shown in Fig. 6.3a, in the late-time stage, our results are in accordance with the results from classical turbulence. However, we point out that the mechanisms of enstrophy decay in the two systems are fundamentally different. Whereas in superfluids vortices annihilate, the main process of vorticity decay in classical two-dimensional fluids is the merging into larger vortices.

We finally remark that in numerical simulations of freely decaying classical turbulence a crossover between two stages of power-law decay similar to our findings has been reported in Ref. [338].

6.6 Kinetic theory of vortex scattering

The decay of the vortex density has been investigated in two-dimensional classical fluids [331–338] and superfluids [106, 324, 339, 340], mainly in the presence of driving or dissipation. Several authors have proposed kinetic theories building upon assumptions about the decay process [331, 336, 337, 341]. The vortex decay cannot be explained by a simple model of independent vortices and antivortices moving towards each other to minimise the energy. Neglecting interactions with sound vortex-antivortex pairs perform a collective motion perpendicular to their relative distance vector without changing their distance. This motion quickly leads to pair-pair collisions and establishes a kinetic-theory picture for vortex pairs. In Fig. 6.5, we showed two examples of vortex-pair scattering processes altering the vortex density $\rho(t)$ and vortex correlation functions $g_{VA}(r, t)$.

Assuming that the vortices are moving in pairs and that annihilations happen as the result of collisions of vortex pairs, the decay rate for the number N_V of vortices follows from the number of dipoles $N_D \sim N_V$ and $\partial_t N_D(t) \sim -N_D(t)/\tau$, with mean free collision time τ . The mean free collision time $\tau = l_{\text{mfp}}/\bar{v}$ is given by the mean velocity of the pairs \bar{v} and the mean free path $l_{\text{mfp}} = V/(\sigma N_D)$ with cross section σ . Both, mean velocity and cross section depend on the number of vortices via the mean vortex-antivortex pair distance l_D according to $\bar{v} \sim 1/l_D$ and $\sigma \sim l_D$. These considerations result in a rate equation

$$\partial_t N_V(t) = -cN_V^2 \quad (6.5)$$

with dimensionfull constant c . Eq. (6.5) has the power-law solution $N_V(t) \sim t^{-1}$. This decay law can only be observed for specific initial conditions \mathcal{A}^* in the early-time stage. We attribute deviations from t^{-1} scaling during this period to an inhomogeneous distribution of vortices, encountered for certain initial conditions. To give an example, we show the vortex distributions created from the two different initial conditions \mathcal{A}^* and \mathcal{A} in Fig. 6.7.

During the late-time stage, only a few vortices are bound in pairs, while most vortices are loosely bound and interact equally with a larger number of vortices around them. We heuristically take this into account by considering a modified scattering cross section $\sigma \sim l_D N_D^2$. The resulting kinetic equation reads $\partial_t N_V(t) \sim -N_V^4$, with solution $N_V(t) \sim t^{-1/3}$, and hence yields the reduction of the decay exponent observed at late times in our simulations.

6.7 Phase correlations

In the remainder of this chapter, we focus on the growth of long-range coherence at late times, associated with the annihilation of topological defects [44–46, 48–50, 105, 106]. From this point of view freely decaying superfluid turbulence is a particular example of phase-ordering dynamics after a quench into the ordered phase [342]. Whereas in three dimensions a second-order phase transition connects a normal-fluid and a superfluid phase, a Bose gas in two dimensions experiences a Berezinskii-Kosterlitz-Thouless transition [126, 127]. For the two-dimensional ultracold Bose gas, experimental and theoretical results support the understanding of the phase transition in terms of vortices undergoing an unbinding-binding transition [124, 125, 138, 242–245].

In this context, we are interested in a comparison between correlation properties observed in the non-equilibrium dynamics near a non-thermal fixed point and those known from equilibrium studies. We compute the dynamical trajectory of the vortex gas in the space of inverse coherence length and inverse mean vortex-antivortex pair distance. We compare our results to simulations of a thermal two-dimensional Bose gas specifically for our system parameters. For this, we evolve field configurations in time which are initially close to a thermal Rayleigh-Jeans distribution at

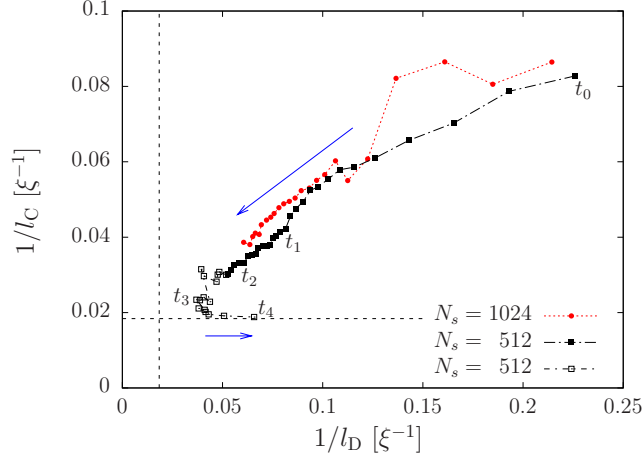


Figure 6.8: Trajectories of multi-vortex states in the space of inverse coherence length $1/l_C$ and inverse mean vortex-antivortex distance $1/l_D$, starting from $t = t_V$. Arrows are added to guide the eye along the time direction. Dashed lines mark the minimal values $2/L = 0.018\xi^{-1}$, available on a grid of size $N_s = 512$. Our understanding of the non-thermal fixed point as a configuration with a few, maximally separated pairs on an otherwise maximally coherent background implies it to be located near the crossing of the dashed lines. Hence, the non-thermal fixed point is approached most closely between $t \simeq 5 \times 10^5$ and $t \simeq 10^6 = t_3$. Closed (red) circles mark an average over 174 runs, $N_s = 1024$, initial time $t_V = 2.3 \times 10^3$ and final time $t_f = 1.3 \times 10^5$; closed squares an average over 1223 runs, with $N_s = 512$, $t_V = 1.7 \times 10^3$ and $t_f = 2.6 \times 10^5$; open squares an average over 16 runs, $N_s = 512$, $t_i = 2.6 \times 10^5$, and $t_f = 4.2 \times 10^6$. Note that the symbols are equally spaced on a logarithmic time scale. We indicate the times $t_0 = 1.7 \times 10^3$, $t_1 = 1.6 \times 10^4$, $t_2 = 1.3 \times 10^5$, $t_3 = 1.0 \times 10^6$, $t_4 = 4.2 \times 10^6$. The average number $N_V(t)$ of vortices left in the system is $N_V(t_0) = 97.7$, $N_V(t_1) = 21.8$, $N_V(t_2) = 11.7$, $N_V(t_3) = 5.8$ and $N_V(t_4) = 2.1$.

a temperature T . After equilibration is reached, we compute the position of the states in the above phase space for different T .

We define a coherence length l_C in terms of the participation ratio [343] of the angle-averaged first-order coherence function

$$g^{(1)}(r) = \int d\theta \frac{\langle \phi^*(\mathbf{x})\phi(\mathbf{x} + \mathbf{r}) \rangle}{\sqrt{\langle n(\mathbf{x}) \rangle \langle n(\mathbf{x} + \mathbf{r}) \rangle}},$$

$$l_C = \left(\mathcal{N} \int dr [g^{(1)}(r)]^2 \right)^{-1}, \quad (6.6)$$

with $\mathcal{N} = [\int dr g^{(1)}(r)]^{-2}$. l_C measures the spatial extension of the first order coherence function. Contrary to $r_{\text{coh}} = \int dr r^2 g^{(1)}(r) / \int dr r g^{(1)}(r)$, the quantity l_C does not sum up values of $g^{(1)}(r)$ weighted by the distance, which would enlarge insignificant contributions at large r . In addition, it gives meaningful results also in the case of large coherence $g^{(1)}(r) \simeq 1$, where for instance the FWHM-measure

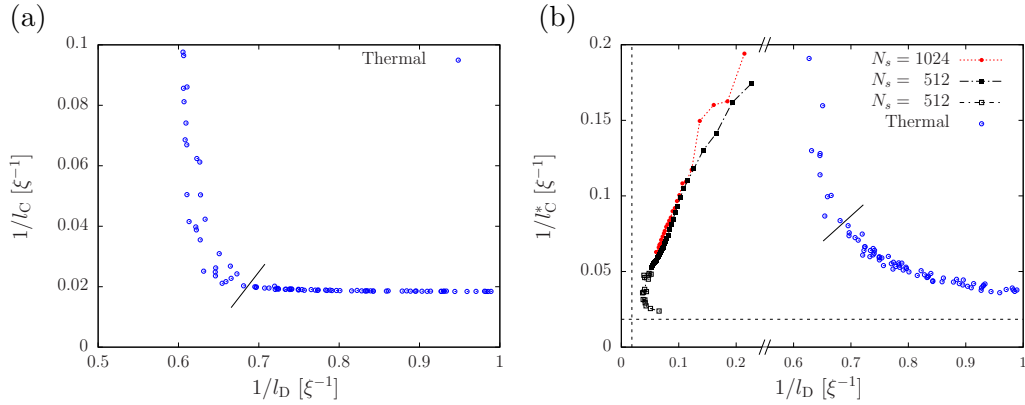


Figure 6.9: Multi-vortex states in the space of inverse coherence length and inverse mean vortex-antivortex distance. (a) Thermal configurations $(l_D^{-1}(T), l_C^{-1}(T))$ for a range of temperatures T , increasing from bottom right to top left. The solid line marks the point where the decay of the $g^{(1)}(r)$ -function changes from algebraic to exponential, signalling the Berezinskii-Kosterlitz-Thouless transition. (b) Comparison of the thermal line $(l_D^{-1}(T), l_C^{*-1}(T))$ for the same range of temperatures T with the corresponding dynamical evolution. (Same data as in Fig. 6.8.) Dashed lines mark the minimal values $2/L = 0.018\xi^{-1}$, available on a grid of size $N_s = 512$. Note that the $(1/l_D)$ -axis interval $[0.25, 0.55]$ has been cut out.

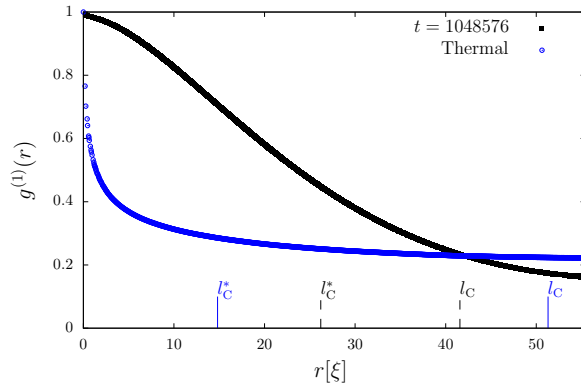


Figure 6.10: First order coherence function $g^{(1)}$ as a function of radial coordinate r . We show one example for the system during the equilibration process at time $t = 1.05 \times 10^6$, with $l_C = 41.6\xi$, $l_C^* = 26.2\xi$, and one for a thermal configuration, giving $l_C = 51.3\xi$, $l_C^* = 14.8\xi$.

can not be applied any more. Note that in equilibrium this quantity smoothly interpolates between the regime of exponential decay of $g^{(1)}$ above the Berezinskii-Kosterlitz-Thouless transition, where the exponential coherence length ξ_C is defined as $g^{(1)}(r) \sim \exp(-r/\xi_C)$, and its power-law decay in the superfluid regime.

In Fig. 6.8, we follow the time evolution of the gas for $t > t_V$. One can observe, that a state of low coherence and small mean vortex-antivortex pair distance evolves

towards larger coherence and larger vortex-antivortex separation. As discussed in Sects. 6.2 and 6.3, this is due to vortex annihilations and vortex-antivortex unbinding. For times $t > 10^4$, the coherence length grows as $l_C \sim \rho^{-1/2}$, in the same way as l_D shown in Fig. 6.4b. The evolution considerably slows down for $1/l_C \sim 1/l_D \rightarrow 0$. In this regime, the Bose gas shows characteristic scaling properties, see Refs. [31, 32], which indicate the presence of the non-thermal fixed point [29]. After spending a long time near this point, the mean vortex-antivortex pair distance declines. This is a sign that the last remaining vortex-antivortex pairs reduce their size prior to their annihilation and the equilibration of the system. Around the same time the power-law in the vortex density decay shown in Fig. 6.3 breaks down.

Our understanding of the non-thermal fixed point as a configuration with a few, maximally separated pairs on an otherwise maximally coherent background implies it to be located near the crossing of the dashed lines. Hence, the non-thermal fixed point is approached most closely between $t \simeq 5 \times 10^5$ and $t \simeq 10^6 = t_3$.

To set the above evolution in relation to equilibrium configurations, we show, in Fig. 6.9a, the thermal line $(l_D^{-1}(T), l_C^{-1}(T))$ for a range of temperatures T for which the system shows a non-vanishing zero-mode population. Note that, in order to define what counts as a bound vortex pair, we filter out field fluctuations on scales smaller than 0.55ξ before detecting vortices and antivortices. Hence, the resulting inverse of the mean vortex-antivortex distance represents a lower bound. By reducing the size of the filter the curve shifts to the left and the separation of the non-thermal fixed point from the thermal configurations becomes larger.

In view of the thermal results it is useful to consider an alternative definition for the coherence length. The length $l_C^* = \int dr g^{(1)}(r)$ shares the above mentioned advantages of the participation ratio. In addition, it does not overestimate the coherence of flat distributions. The thermal $g^{(1)}(r)$ functions show a fast decay at short distances r_s to a value $g_c^{(1)}$ and are almost constant for $r > r_s$. Fig. 6.10 shows two typical $g^{(1)}$ -functions, one for the system during the equilibration process at time $t = 1.05 \times 10^6$, with $l_C = 41.6\xi$, $l_C^* = 26.2\xi$, and one for a thermal configuration, giving $l_C = 51.3\xi$, $l_C^* = 14.8\xi$. Due to the small area under $g^{(1)}(r)$ up to r_s the normalisation \mathcal{N} in the definition of the participation ratio enlarges the integrand of Eq. (6.6) close to unity. Hence, l_C becomes large while l_C^* is less affected by this effect. In Fig. 6.9b we compare the thermal line $(l_D^{-1}(T), l_C^{*-1}(T))$ for the same range of temperatures T with the corresponding dynamical evolution.

In Fig. 1.2, our findings are summarised qualitatively in a reduced phase space of the vortex gas. In this way, the ‘Dynamical evolution’ of decaying superfluid turbulence is compared to an estimate of the expected equilibrium configurations illustrated by the dashed line marked ‘Thermal states’ along which the temperature T varies. The most significant difference between these two lines is that the non-equilibrium dynamics is characterised by an increase of the mean vortex-antivortex pair distance with increasing coherence, whereas equilibrium configurations are expected to feature a decrease in pair distance with increasing coherence. A slow-down of

the dynamics together with characteristic scaling of the single-particle momentum distribution, observed in the regime of large coherence and large vortex-antivortex pair distance, marks the position of the non-thermal fixed point. Finally, when all vortices have annihilated, the system reaches the ‘Thermal states’-line deep in the superfluid regime.

6.8 Summary

We have studied the non-equilibrium dynamics of a two-dimensional dilute ultra-cold Bose gas towards and away from a non-thermal fixed point. Following an initial quench, evolution towards a fixed point appears to be a generic feature of the (quasi-) condensation process and the build-up of coherence. In the course of a critically slowed evolution, vortex excitations evolved into an almost random distribution reflected in the scaling of the single-particle spectra at the non-thermal fixed point. We showed that the vortex-density decay is directly related to a non-equilibrium vortex unbinding process [33].

Our results allow to draw a picture of the evolution path towards and away from the fixed point, see Fig. 1.2. This picture allows to compare our results with quasi-equilibrium studies of a two-dimensional vortex gas. The non-thermal fixed point is characterised by a few - in the extreme case one - pairs of far separated anti-circulating vortices and bears similarities with the equilibrium Berezinskii-Kosterlitz-Thouless fixed point. However, while the phase transition also features unbinding of vortices, finite temperature implies the simultaneous excitation of many rotons, i.e. strongly bound vortex-antivortex pairs. The non-thermal fixed point is clearly identified by strong wave turbulent scaling in the infrared limit [29], $n(k) \sim k^{-4}$. At the same time, the high-energy modes can be populated in a much weaker way, e.g., far below the Berezinskii-Kosterlitz-Thouless critical temperature or remain out of equilibrium. The details of the UV mode populations are determined by the way the non-thermal fixed point is being approached.

The way we force the system here as in the work reported in Chaps. 3 and 5 [31,32] to approach the non-thermal fixed point generalises that of Kibble and Zurek. A strong sudden quench replaces the adiabatic approach of the Berezinskii-Kosterlitz-Thouless phase transition. To what extent the Berezinskii-Kosterlitz-Thouless phase transition can be understood as happening within a class of thermal states near the non-thermal fixed point studied here needs to be clarified by analysing full out-of-equilibrium renormalisation-group equations in comparison with standard descriptions in thermal equilibrium. As a first step, the dynamical evolution in the vicinity of the Berezinskii-Kosterlitz-Thouless critical point [126,127] was studied in Refs. [344], in terms of a perturbative renormalisation group analysis. The route to a non-perturbative analysis also for the strong-coupling regime is provided by out-of-equilibrium functional techniques [259,260,345].

In a recent experiment, a strong reduction of the vortex decay rate at late times

has been reported [90]. Quantitative experimental observation of the predictions made here could give new insight into the character of the non-thermal fixed point and its relation to quantum turbulence.

A three-dimensional Bose gas near a non-thermal fixed point

Triggered by the new IR-correspondence of topological defects and wave turbulence, we have thoroughly investigated vortex dynamics in $d = 2$ dimensions in Chap. 6. Here, we extend this study to three dimensions. We present analytic mean-field calculations to describe the evolution prior to vortex formation. After vortices are created, their influence becomes apparent through rapid isotropisation and mean field decay. Our main goal is to clarify the dynamics of vortex density decay in this system. We show numerically that the dynamical process involving the non-thermal fixed point [29,31,32] features three stages in the vortex density decay. Each stage will be discussed in detail. Beyond that, we show results on the evolution of the condensate fraction and draw a connection between vortex decay and phase ordering.

Turbulence is created by depleting an equilibrium Bose-Einstein condensate. Only a few modes near $\mathbf{k} = 0$ were chosen to be occupied at the initial time with $n(\mathbf{k}, 0) \gg 1$, see Fig. 7.1. We compare results from a quasi-two-dimensional initial condition \mathcal{A}_3 to an almost isotropic case \mathcal{B}_3 . As we will show in the following, the subsequent dynamics leads to strong depletion of the condensate and the creation of superfluid turbulence.

7.1 Mean field scattering dynamics

First, we discuss the initial scattering dynamics leading to the depletion of the condensate. In Fig. 7.2 (left), we show the early time evolution of occupation numbers for a few initially empty modes. Their dynamics is driven by the strongly occupied low momentum modes. One observes a power law increase of occupation numbers $n(k, t) \sim t^{2n}$, $n \in \mathbb{N}$, with n the order of the scattering process in the cascade. To explain this feature, we study the classical field equation, Eq. (2.5), in

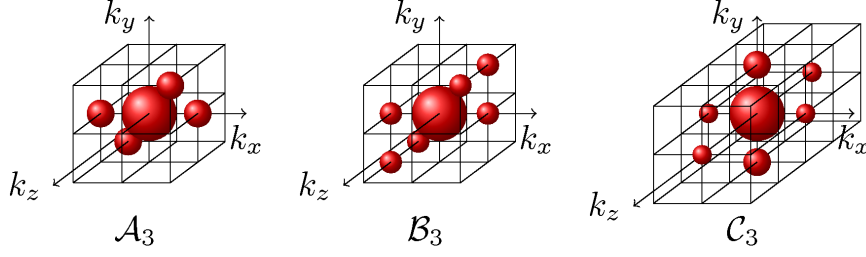


Figure 7.1: Panels $\mathcal{A}_3 - \mathcal{C}_3$ illustrate the initially occupied momentum modes \mathbf{k}_{ini} (shaded spheres) with $n(\mathbf{k}_{\text{ini}}, t = 0) \gg 1$, for 3 different mean field configurations. The volumes of the spheres are proportional to the mean number of particles. If not stated otherwise, on average half of the total number of particles occupies the zero mode.

momentum space

$$i\dot{\phi}_{\mathbf{k}} = \omega_{\mathbf{k}}\phi_{\mathbf{k}} + g \int d^3p d^3q d^3r \delta(\mathbf{p} + \mathbf{r} - \mathbf{q} - \mathbf{k}) \phi_{\mathbf{p}}\phi_{\mathbf{q}}^*\phi_{\mathbf{r}}, \quad (7.1)$$

with $\omega_{\mathbf{k}} = -k^2/2m$. Now, assume mode \mathbf{k} to be weakly occupied, modes $\mathbf{p}, \mathbf{q}, \mathbf{r}$ strongly occupied and momentum conservation fulfilled, $\mathbf{p} + \mathbf{q} - \mathbf{r} - \mathbf{k} = 0$. If we neglect any feedback of the evolution of $\phi_{\mathbf{k}}$ on the strongly occupied modes, the equations of motion read

$$\begin{aligned} i\dot{\phi}_{\mathbf{k}} &= \omega_{\mathbf{k}}\phi_{\mathbf{k}} + g\phi_{\mathbf{p}}\phi_{\mathbf{p}}^*\phi_{\mathbf{k}} + g\phi_{\mathbf{q}}\phi_{\mathbf{q}}^*\phi_{\mathbf{k}} + g\phi_{\mathbf{r}}\phi_{\mathbf{r}}^*\phi_{\mathbf{k}} + g\phi_{\mathbf{p}}\phi_{\mathbf{q}}^*\phi_{\mathbf{r}} \\ i\dot{\phi}_{\mathbf{p}} &= \omega_{\mathbf{p}}\phi_{\mathbf{p}} + g\phi_{\mathbf{p}}\phi_{\mathbf{p}}^*\phi_{\mathbf{p}} + g\phi_{\mathbf{q}}\phi_{\mathbf{q}}^*\phi_{\mathbf{p}} + g\phi_{\mathbf{r}}\phi_{\mathbf{r}}^*\phi_{\mathbf{p}}, \\ i\dot{\phi}_{\mathbf{q}} &= \omega_{\mathbf{q}}\phi_{\mathbf{q}} + g\phi_{\mathbf{q}}\phi_{\mathbf{q}}^*\phi_{\mathbf{q}} + g\phi_{\mathbf{p}}\phi_{\mathbf{p}}^*\phi_{\mathbf{q}} + g\phi_{\mathbf{r}}\phi_{\mathbf{r}}^*\phi_{\mathbf{q}}, \\ i\dot{\phi}_{\mathbf{r}} &= \omega_{\mathbf{r}}\phi_{\mathbf{r}} + g\phi_{\mathbf{r}}\phi_{\mathbf{r}}^*\phi_{\mathbf{r}} + g\phi_{\mathbf{p}}\phi_{\mathbf{p}}^*\phi_{\mathbf{r}} + g\phi_{\mathbf{q}}\phi_{\mathbf{q}}^*\phi_{\mathbf{r}}, \end{aligned} \quad (7.2)$$

The last term in the first equation is the only occupation number changing term. Higher order scattering terms are suppressed, since they depend on higher orders of empty field modes. It can be read off Eq. (7.2) that macroscopically occupied fields $\phi_{\mathbf{p}}, \phi_{\mathbf{q}}, \phi_{\mathbf{r}}$ will only evolve with a phase. If we set their initial occupation for simplicity all equal to N , this phase is $i(\omega_{\mathbf{p}, \mathbf{q}, \mathbf{r}} + 3gN)t$. Then, the equation for the empty mode $\phi_{\mathbf{k}}(t) = \eta(t)e^{i(\omega_{\mathbf{k}} + 3gN)t}$ is given by

$$\dot{\eta} = -ig\sqrt{N}^3 e^{i\delta\omega t}, \quad (7.3)$$

where we want to allow for $\delta\omega = \omega_{\mathbf{k}} + \omega_{\mathbf{p}} - \omega_{\mathbf{q}} - \omega_{\mathbf{r}} \neq 0$. Integration yields,

$$\eta(t) = g\sqrt{N}^3 \left(\frac{1}{\delta\omega} e^{i\delta\omega t} - \frac{1}{\delta\omega} \right) + \eta(0). \quad (7.4)$$

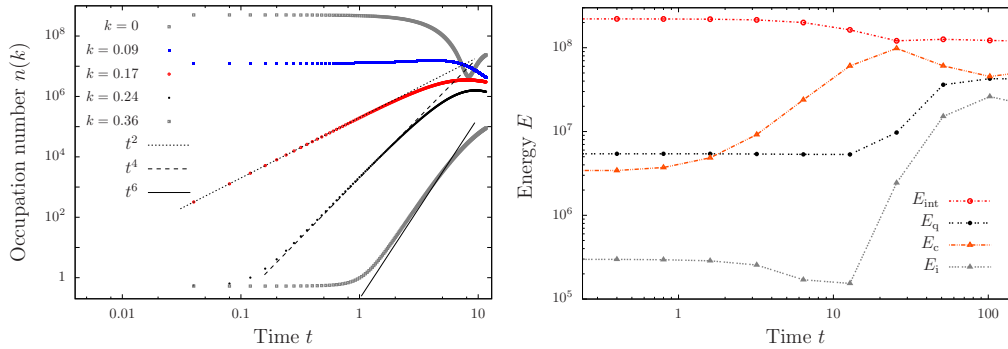


Figure 7.2: Early-time dynamics shown for initial conditions \mathcal{A}_3 . Parameters are: $\bar{g} = 4 \cdot 10^{-4}$, $N = 10^9$, $N_s = 128$. Note the double-logarithmic scale. Left: Single-particle mode occupation numbers as functions of time t . Right: Energies as functions of time t for times until vortices are created. Shown are the interaction energy E_{int} , compressible energy E_{c} , incompressible energy E_{i} , quantum pressure E_{q} , as defined in section Sect. 2.2. Observations: 1. Coherent scattering leads to an increase in compressible energy until $t \sim 5 \cdot 10$. 2. Vortex generation increases the incompressible energy at $t \sim 10^2$.

For times $t < \delta\omega^{-1}$ the exponential can be expanded, yielding a power law growth of the occupation number $n_{\mathbf{k}} \simeq \text{const.} + g^2 N^3 t^2$ until dephasing or out-scattering sets in. The even stronger growth of the next higher empty mode \mathbf{k}' can be understood, by reinserting $\phi_{\mathbf{k}}(t)$ into a resonant combination where $\mathbf{p} + \mathbf{q} - \mathbf{k} - \mathbf{k}' = 0$ and $\phi_{\mathbf{p},\mathbf{q}} = \sqrt{N} e^{i\omega_{\mathbf{p},\mathbf{q}} t}$. It follows, that $n_{\mathbf{k}'} = \text{const.} + g^4 N^5 t^4$. In this way, a cascade forms that transports particles to higher momenta.

The numerical simulations in Fig. 7.2 (left) confirm this analysis until the break down of the cascade at times $\bar{t} \sim 10$, which is caused by a depletion of the condensate mode and dephasing (e.g. $\delta\omega \sim 0.01$).

Having discussed the initial non-equilibrium scattering dynamics, we will now follow the system in time into the vortex dominated regime. The early time evolution of the different energy components (see Sect. 2.2) is plotted in Fig. 7.2 (right). Note, that initially over 95% of the energy is stored in the interactions. The scattering processes described in Sect. 7.1 converts half of the interaction energy in compressible energy. Incompressible energy is created on the expense of compressible energy at $\bar{t} \sim 10^2$, signalling the appearance of vortical excitations.

7.2 Isotropisation and mean field decay

In the following, we want to discuss two striking dynamical features connected to the appearance of vortices. The first interesting observation is that vortical excitations strongly isotropise the system in momentum space. In Fig. 7.3 (left), we plot the total number of excited particles in modes along the x, y, z -directions as a function

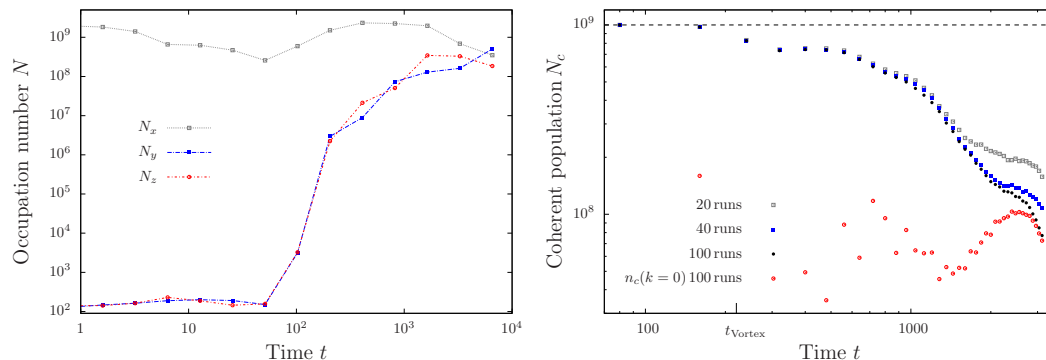


Figure 7.3: Isotropisation and mean field decay for initial conditions \mathcal{A}_3 . Parameters are: $\bar{g} = 4 \cdot 10^{-4}$, $N = 8 \cdot 10^9$. Note the double-logarithmic scale. Left: Occupation numbers of excited states summed over three different directions k_x, k_y, k_z , as defined in Eq. (7.5), as a function of time t for a single run. Lattice size is $N_s = 256$. Isotropisation is observed to set in around the time when vortices are created, $t \sim 3 \cdot 10^2$. Right: Time evolution of the coherent population N_c , as defined in Eq. (7.6), is shown for three different numbers of trajectories used to evaluate the expectation value. The time t_{Vortex} is marked as the time when vortices appear.

of time

$$N_i = \sum_{\mathbf{k}_i \neq 0} n(\mathbf{k}_i), \quad i = x, y, z, \quad (7.5)$$

for initial condition \mathcal{A}_3 , see Fig. 7.1. Initially, N_x shows macroscopic occupations, while N_y, N_z are only occupied by quantum noise. Around the time $t \sim 10^2$, N_y and N_z become rapidly populated. This coincides with the time t_{Vortex} when vortex lines are created. At times $t \gtrsim 10^3$ the observable indicates that the system has isotropised in momentum space. A possible explanation of this might be the influence of the crow-instability acting on parallel anti-circulating vortex lines [76].

A second interesting observation concerns the nonlinear dynamics of vortices. The Gross-Pitaevskii-Equation without statistical averaging conserves the integrated mean field, which we call the coherent population N_c ,

$$N_c = \int d^d x |\langle \phi(\mathbf{x}) \rangle|^2. \quad (7.6)$$

This description breaks down when non-linearities destroy the coherence between different realisations and the mean field is depopulated. To demonstrate this, we prepare a micro-canonical ensemble which is initially fully phase coherent. The time evolution of the average field is shown in Fig. 7.3 (right). Until $\bar{t} = 100$ essentially all particles populate the mean field. This regime can therefore be simulated with a single run of the Gross-Pitaevskii equation. The breakdown of the mean field description coincides with the formation of vortices at $t = t_{\text{Vortex}}$. In the following phase, dominated by the motion of the vortices the mean field decays monotonously.

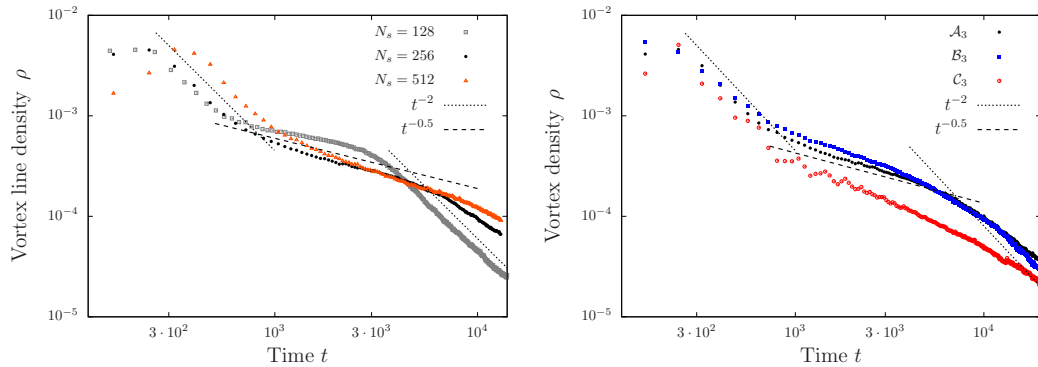


Figure 7.4: Vortex density $\rho(t)$ as a function of time t . Parameters are: $\bar{g} = 4 \cdot 10^{-4}$, $N/N_s^3 = 476$. Note the double-logarithmic scale. Left: Averaged $\rho(t)$ for three different lattice sizes. Initial conditions are \mathcal{A}_3 , but differ in energy. Right: Averaged $\rho(t)$ (10 runs) for three geometrically different initial conditions. Lattice size $N_s = 256$.

Since the local phase $\varphi(\mathbf{x}, t)$ of the field is determined by the positions of the whole set of vortices the decay of the mean field can be related to chaotic vortex motion and understood as the onset of turbulence. The dependence of the average field on the number of runs used in the averaging procedure is explicitly shown. By plotting the contribution from the average zero-mode separately, one can see that at times $\bar{t} \gtrsim 2000$ all excited modes have completely dephased.

7.3 Vortex density decay

In Chaps. 3, 4, and 5 [31, 32], the vortex bearing phase of the dynamical evolution in $d = 3$ dimensions was shown to exhibit non-thermal fixed point behaviour. Specifically, the single-particle momentum spectrum was observed to develop a quasi-stationary bimodal scaling, see Fig. 5.4, that was explained from an unstructured, dilute tangle of vortex loops. At late times, the scaling exponent decreased due to the dominance of small vortex loops.

In Chap. 6, the approach of the non-thermal fixed point in two dimensions was related to vortex-antivortex unbinding and characteristic behaviour of the vortex density decay. In the following, we discuss the analogous dynamical transition in the time evolution of the vortex density in three dimensions. To this end, we follow the decay of the vortex density $\rho(t) \sim L/V$ for various initial conditions. The vortex line length L is numerically determined by counting the number of lattice points with $n(x) < 0.02n$. In our simulations of the three-dimensional gas, see Fig. 7.4, three regimes are observed in the evolution of initial conditions \mathcal{A}_3 and \mathcal{B}_3 : a rapid initial decay, a slow intermediate time ρ decay and a fast late decay. Note that the specified grid sizes correspond to different initial kinetic energies. For initial condition \mathcal{C}_3 , the decay happens much faster and only two stages can be identified. In the analysis of the dynamics following initial conditions \mathcal{A}_3 and \mathcal{B}_3 , we assume

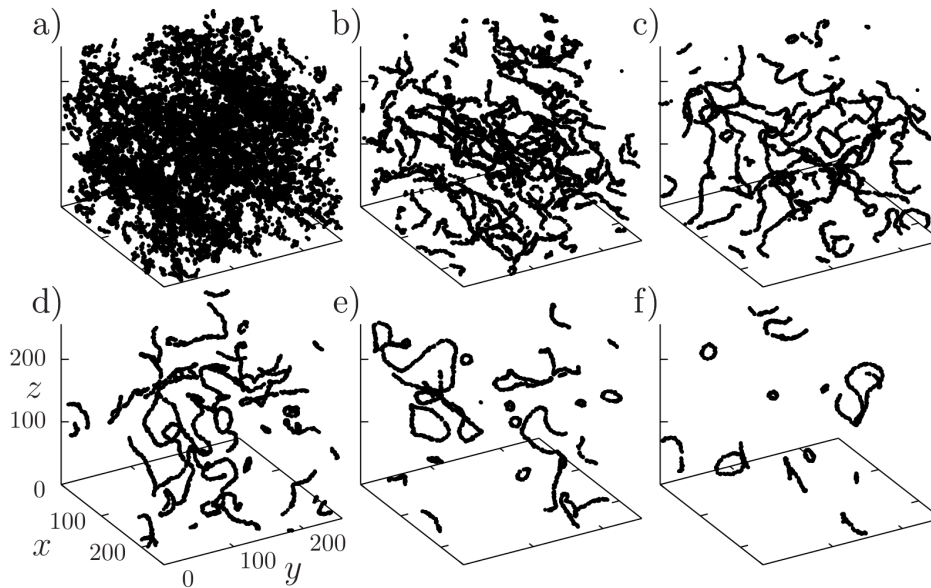


Figure 7.5: Snapshots of the vortex tangle for six different times of a single run in $d = 3$ dimensions. Initial conditions are \mathcal{A}_3 with the same parameters as Fig. 7.4. a) $t = 410$ and b) $t = 819$ are taken from the initial rapid decay regime. c) $t = 1640$ and d) $t = 3276$ are taken from the intermediate regime. The tangle has diluted and features large interacting rings with coherent transversal flow around them. Here, the system is close to the non-thermal fixed point characterised by $n(k) \sim k^{-5}$. e) $t = 6554$ and f) $t = 13107$ are taken from the late regime. The system is populated by small rings that decay almost independently.

the vortex densities to follow power laws $\rho(t) \sim t^{-\alpha}$ with different exponents α . The exponent of the initial decay regime is estimated by $\alpha \sim 2 \pm 0.2$. At intermediate times, a decay exponent of $\alpha \sim 0.45 \pm 0.05$ is observed. The late time regime approximately exhibits an exponent $1.5 < \alpha < 2$. In Fig. 7.5, we show snapshots of the vortex tangle of a single run in order to give an interpretation of the three decay regimes. The initial regime, depicted in snapshots a) and b) is characterised by a dense packing of density depressions. Some of which build vortices, some of which decay into other excitations. Snapshots c) and d) are taken from the intermediate decay regime which features the smallest decay exponent $\alpha \sim 0.45 \pm 0.05$. The snapshot shows the presence of a tangle of large, well separated vortex loops. We remark that during this period the single-particle momentum distribution shows a well established k^{-5} -scaling, originating from coherent transversal flow around the vortices. Hence, we interpret the reduction of the decay exponent as a slowing-down near the non-thermal fixed point [29]. Typical configurations from the late time regime are presented in e) and f). Here, a dilute gas of small vortex ellipses propagates through the gas. During this regime, the momentum distribution scales like $n(k) \sim k^{-3}$ which was interpreted as the departure from the non-thermal fixed point in Sect. 5.1.1.

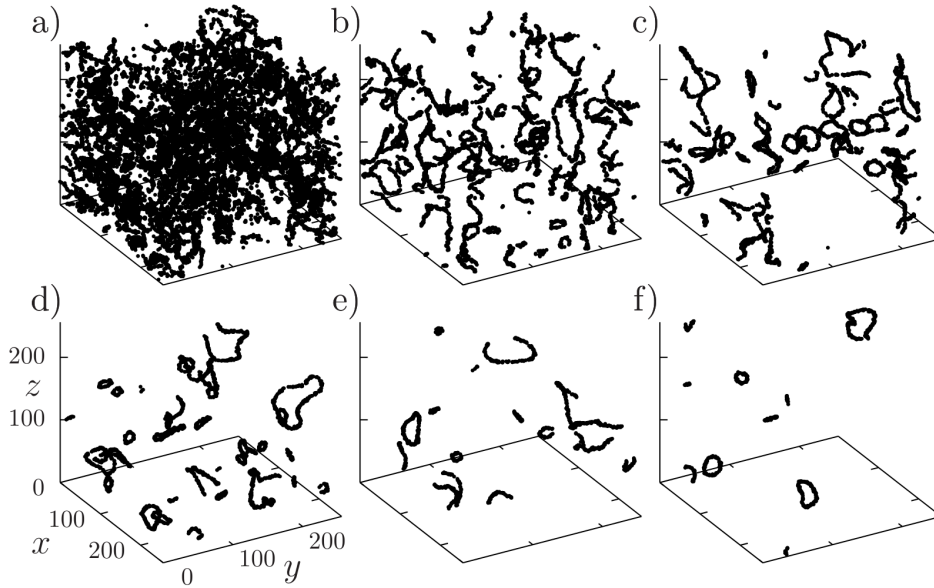


Figure 7.6: Snapshots of the vortex tangle for six different times of a single run in $d = 3$ dimensions. Initial conditions are \mathcal{C}_3 with the same parameters as Fig. 7.4. a) $t = 410$ and b) $t = 819$ are taken from the initial rapid decay regime. c) $t = 1640$ and d) $t = 3276$ are taken from the intermediate regime. In contrast to the evolution depicted in Fig. 7.5, we can not see the development of a dilute gas of large interacting rings. The system features a large number of small rings. e) $t = 6554$ and f) $t = 13107$ are taken from the late regime. The system is populated by small rings that decay almost independently.

Now, we want to turn our attention to the vortex density decay following initial condition \mathcal{C}_3 , see Fig. 7.4 (right). In this scenario, the reduction of the decay exponent from initial to intermediate times is less strong than for initial conditions \mathcal{A}_3 and \mathcal{B}_3 . Also a change of the behaviour from intermediate to late times is absent. In Fig. 7.6, a sequence of snapshots of the vortex tangle is presented. From these pictures we infer that the key difference between this dynamics (\mathcal{C}_3) and the one discussed in Fig. 7.5 (\mathcal{A}_3) is the absence of a clear enlargement of vortex rings at intermediate times. Interpreting these observations in the language of non-thermal fixed points, we state that the dynamics following initial condition \mathcal{C}_3 does not get as close to the non-thermal fixed point as for the \mathcal{A}_3 -case, before the departure towards equilibrium. This conclusion is supported by looking at the momentum spectrum at intermediate times for the two runs shown in Fig. 7.7. One observes a bimodal scaling in both cases. However, the IR-scaling $n(k) \sim k^{-5}$ associated with the non-thermal fixed point is more pronounced at low momenta for initial condition \mathcal{A}_3 than for \mathcal{C}_3 .

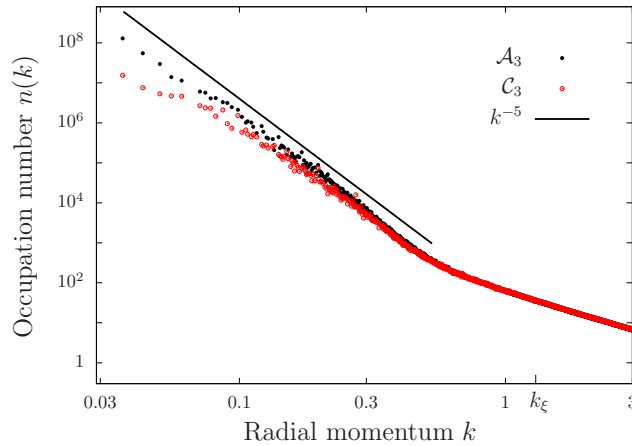


Figure 7.7: Single-particle mode occupation numbers as functions of the radial momentum k at intermediate times of the evolution, $t = 3276$. Note the double-logarithmic scale. Parameters are the same as Fig. 7.4. One observes a bimodal scaling in both cases. However, the IR-scaling $n(k) \sim k^{-5}$ associated with the non-thermal fixed point is more pronounced for initial condition \mathcal{A}_3 than for \mathcal{C}_3 . This is in accordance with snapshots of the respective vortex tangles in Fig. 7.5 and Fig. 7.6 and the slowing-down phenomenon discussed in Fig. 7.4. See text for more details.

7.4 Energy equilibration and condensation

The dynamical picture of vortex density decay close to the non-thermal fixed point that we have gained so far has three stages: At first, the turbulence is accompanied by strong density and phase fluctuations and experiences a rapid decay. At intermediate times $t \gtrsim 10^3$, the tangle reaches a quasi-stationary state characterised by a dilute gas of vortex loops of large radius. The long-range interactions of these loops slows down the decay considerably. At $t \gtrsim 10^4$, when only very few small size vortex rings are present in the gas, a third stage develops that features fast decay of vortex density.

The turbulent dynamics in the intermediate to long time regime, can be further visualised by plotting the different energy components, see Fig. 7.8 (left). Characteristic exponent for the decaying incompressible energy is slightly smaller than the exponent for decaying vortex density, see Fig. 7.4. We attribute the growth of the incompressible energy per vortex to the increase of the mean vortex ring radius. Note that the effect is smaller than in the two-dimensional scenario, Sect. 6.4. Simultaneously, compressible and quantum pressure energy components run into an equi-partitioned state, also observed in decaying superfluid turbulence starting from a Taylor-Green vortex [119]. The numerical simulations under consideration, started out by depleting a Bose-Einstein condensate, leading to a turbulent state of vortices featuring non-thermal fixed point behaviour. Although the initial perturbation drove the system far from thermal equilibrium, the total energy in the gas merely changed. Hence, the gas develops phase coherence and eventually Bose-

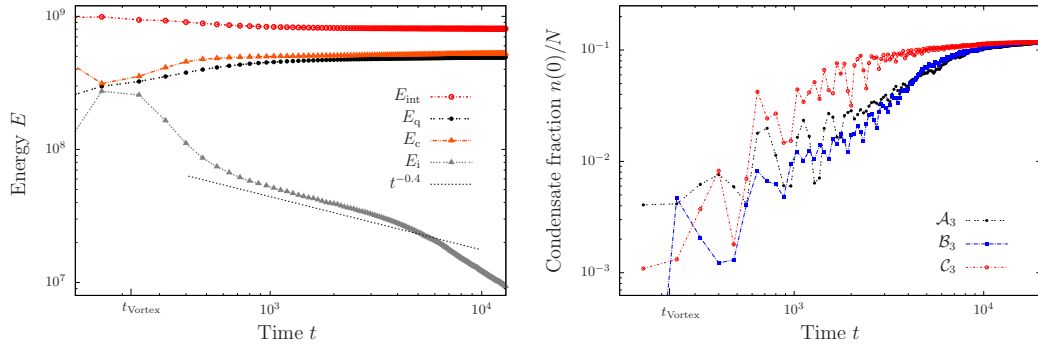


Figure 7.8: Energy equilibration and condensation. Parameters are: $\bar{g} = 4 \cdot 10^{-4}$, $N/N_s^3 = 476$. Left: Energies as functions of time t . Initial conditions are \mathcal{A}_3 and lattice size is $N_s = 128$. Shown are the interaction energy E_{int} , compressible energy E_{c} , incompressible energy E_{i} , quantum pressure E_{q} , as defined in section Sect. 2.2. Right: Zero mode $n(\mathbf{k} = 0)$ as a function of time t . Lattice size is $N_s = 256$.

Einstein condensation at late times. To make this explicit, we discuss the time evolution of the condensate fraction $n(0)/N$ in Fig. 7.8 (right). During the early-time scattering dynamics the initial zero-mode population $n(0, t = 0)/N = 0.5$ gets destroyed (not shown). We observe an increase of zero-mode population after the time t_{Vortex} . All three initial conditions feature approximately the same condensate fraction at final time. From the collected statistics (5 runs for each initial condition), we can not extract the functional form of the time evolution. At this point, we are satisfied with the identification of condensate formation in decaying three-dimensional superfluid turbulence. In the next chapter, Chap. 8, a thorough statistical analysis will be performed for the process of condensate formation out of a random phase initial condition.

7.5 Summary

In summary, we presented an analysis of the nonlinear dynamical evolution towards and away from the non-thermal fixed point in three dimensions. The dynamics of violent depletion of a Bose-Einstein condensate due to scattering was described by analytic mean field calculations. Then, we discussed the creation of turbulence from the transformation of compressible energy into incompressible energy. Subsequently, the nonlinear dynamics of vortices lead to isotropisation and a break down of the mean field approach, which was quantified by the decay of the average field. As reported in Chap. 6, see Refs. [33], the system undergoes a dynamical vortex unbinding, leading to an almost random vortex distribution, which constitutes the turbulent scaling at the non-thermal fixed point. We focused on the monitoring of vortex density decay during equilibration of the turbulent gas. We observed three scaling regimes in time. At intermediate times, the system gets close to the non-thermal fixed point which is characterised by critical slowing down and power-law

scaling of the momentum distribution at low momenta. We found that the departure from the non-thermal fixed point leads to the formation of a Bose-Einstein condensate. To study the non-equilibrium condensation dynamics, we investigated the time evolution of the condensate fraction. In the next chapter, the condensation process is investigated in more detail in the experimentally relevant setting of rapid evaporative cooling, see e.g. [137–139]. There, we will explain how the presence of a non-thermal fixed point effects the equilibration dynamics and clarify the role of superfluid turbulence in this process.

Dynamics of Bose-Einstein condensation

In the preceding chapter, Chap. 7, the decay of superfluid turbulence was shown to involve dynamical Bose-Einstein condensation. This observation brings up the longstanding question on the role of vortices in the formation of a Bose-Einstein condensate from a completely disordered initial state [45, 46, 48, 106, 130]. Note that also turbulence in acoustic excitations has been discussed in this context [44, 46, 47, 49, 50]. Here, we study this phenomenon under the experimentally relevant condition of rapid evaporative cooling, see Fig. 8.1 and Refs. [137–139, 227].

Suppose we start with a dilute, incoherent homogeneous gas in three dimensions, at a temperature close to and above the phase transition. Apply a cooling quench by removing particles from the higher-energy modes as depicted in Fig. 8.1 (right). After this, the system re-equilibrates to thermal equilibrium, with a temperature given by the total energy of the system after the quench which we chose to be below the critical temperature.

As a main result, we show that two different scenarios are possible: If a sufficiently small amount of energy is removed, the induced scattering of particles into the low-energy modes builds up a thermal Rayleigh-Jeans distribution in a quasi-adiabatic way. The chemical potential increases, and a fraction of particles is deposited in the lowest mode, forming a condensate. During this process, tangles of defect lines can be found in the Bose field by filtering out short-wavelength fluctuations [48]. While the field has a phase winding around these defects, the flow pattern in their vicinity is distorted by strong phase fluctuations.

In the second scenario, after a sufficiently strong cooling quench, the resulting superthermal population of the higher-energy modes results in a vigorous transport towards lower energies that has the form of a strong-wave-turbulence inverse cascade. This cascade induces a long-lived, power-law single-particle spectrum $n(k) \sim k^{-\zeta}$, with an exponent $\zeta = 5$ distinctly larger than the exponent $\zeta = 2$ which characterises a thermal Rayleigh-Jeans distribution. The emergence of the strong cascade can be explained by the dominance of incompressible, transverse, vortical superfluid flow over compressible, longitudinal sound excitations and density fluctuations in

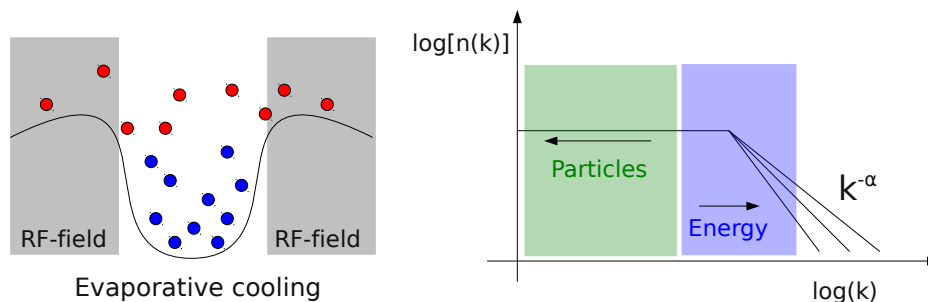


Figure 8.1: Left: Illustration of the evaporative cooling technique for magnetically trapped ultracold quantum gases [347, 348]. In rf-evaporation, a near-resonant radio-frequency field flips the atomic spin. As a result, the attractive trapping force turns into a repulsive force and expels the atoms from the trap. This scheme cools the gas, since it can be tuned such that the resonance condition is only fulfilled at the wings of the trap. [294]. Right: Momentum distribution after the initial evaporative cooling quench. The strength of the quench is parametrised by the exponent α . Subsequent particle and energy flows are indicated.

the respective regime of wave lengths. The power law k^{-5} is traced back to the flow pattern around the vortex lines [32] in the Vinen tangles [346] (see Sect. 2.3.2) which become visible without filtering out short-wavelength fluctuations. The possibility of a strong cascade was pointed out in Refs. [28, 29, 53], where this quasi-stationary scaling solution was referred to as a non-thermal fixed point. The two possible paths to BE condensation are shown schematically in Fig. 1.3. Whether the system, during the condensation dynamics, can approach the NTFP where the process critically slows down, or whether it moves in a direct way to thermal equilibrium depends on the initial conditions, i.e., on the strength of the cooling quench.

To reveal this dynamics we study a dilute Bose gas, in the classical-wave limit, using the Gross-Pitaevskii equation (see Eq. (2.5)). We consider a gas of N atoms in a box of size L^3 , with periodic boundary conditions and mean density $\bar{n} = N/L^3$. In the following, we measure length in units of the healing length $\xi = (2mg\bar{n})^{-1/2}$ and time in units of $\tau = m\xi^2$. Simulations were done on a cubic grid with 256^3 points.

The initial field in momentum space, $\phi(\mathbf{k}, 0) = \sqrt{n(\mathbf{k}, 0)}\exp\{i\varphi(\mathbf{k}, 0)\}$, is parametrised in terms of a randomly chosen phase $\varphi(\mathbf{k}, 0) \in [0, 2\pi)$ and a density $n(\mathbf{k}, 0) = f(k)\nu_{\mathbf{k}}$, with $\nu_{\mathbf{k}} \geq 0$ drawn from an exponential distribution $P(\nu_{\mathbf{k}}) = \exp(-\nu_{\mathbf{k}})$ for each \mathbf{k} . We choose the structure function

$$f(k) = \frac{f_\alpha}{k_0^\alpha + k^\alpha}, \quad (8.1)$$

for different values of α , with cutoff $(k_0\xi)^\alpha = 0.2/0.44^\alpha$ and normalisation $f_\alpha = 400/0.44^\alpha$. We compare results for a range of different cooling quenches defined by the power-laws $\alpha = 2.5, \dots, 10.0$, varying the total number between $N = 10^9$

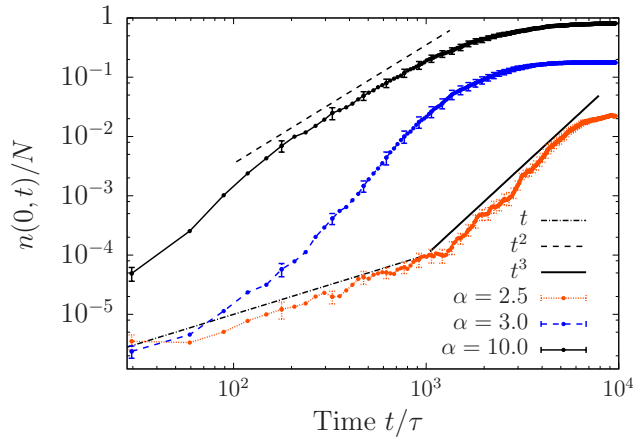


Figure 8.2: Build-up of the condensate fraction $n(\mathbf{k} = 0, t)/N$ on a double-logarithmic scale, for different strengths of the initial cooling quench, parametrised by the exponent α , cf. Eq. (8.1). Depending on α , a different power-law behaviour is observed. Standard averaging errors are shown.

($\alpha = 2.5$) and $N = 4.3 \times 10^8$ ($\alpha = 10$).

8.1 Evolution of the zero mode

The initial power-law fall-off of $f(k)$ chosen above is close to or steeper than that expected by a self-similar solution of the wave Boltzmann equation, $\alpha \simeq 2.4$ [65], corresponding to an inverse particle cascade in weak wave turbulence theory [45, 130]. $\alpha = 2$ would correspond to a stable initial thermal distribution at finite chemical potential, and thus any $\alpha > 2$ is required to set off a re-equilibration to a lower temperature. In Fig. 8.2 we show the ensuing time evolution of the condensate occupation number $n(0, t)$ for the different α . In each case, the evolution leads to a BEC characterised by a non-vanishing ratio $n(0, t)/N$. As we keep f_α and k_0^α constant $n(0, t)/N$ grows with α . This is because larger α cut off more high-momentum particles and leave less energy to be thermally redistributed. Power-law growths $n(0, t) \sim t$ [130], $\sim t^3$ [105], and $\sim t^2$ are seen.

8.2 Momentum distribution

Beyond the zero mode, the occupation spectrum of the non-zero momentum modes allows to follow the dynamical process of potentially turbulent particle transport to lower energies. In Fig. 8.3 we show the time evolution of the single-particle distribution $n(k, t)$ over the radial momenta $k = |\mathbf{k}|$ at four different times and for the different α . During the initial evolution ($t \lesssim 10^2 \tau$) the mode occupations gradually spread to lower wave numbers, at the same time depositing energy into the high-momentum tail. Our dynamic range does not allow to identify a weak-turbulence inverse particle cascade with $n(k) \sim k^{-2.4}$ [65]. At late times, the spectra

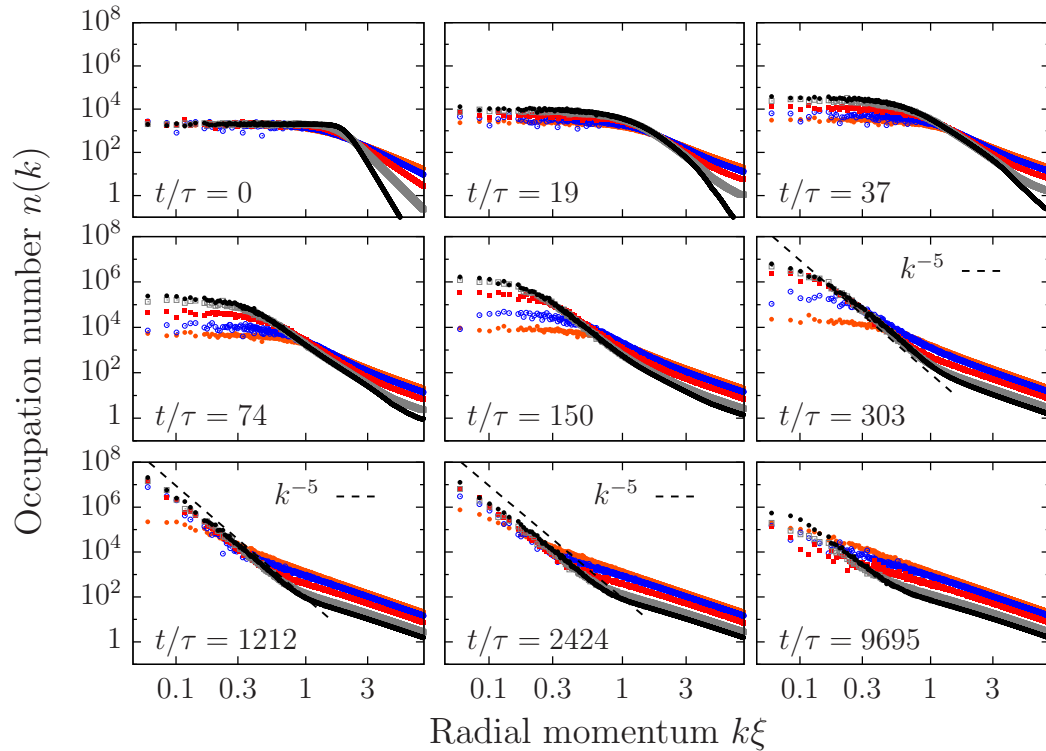


Figure 8.3: Particle momentum spectra at nine different times, on a double-logarithmic scale as functions of the radial momentum $k = |\mathbf{k}|$ for different $\alpha = 2.5$ (orange), 3.0 (blue), 4.0 (red), 6.0 (grey), 10 (black), from top to bottom at $k\xi = 1$. Averages over 3..7 runs. A steep infrared power-law $n(k) \sim k^{-5}$ appears for $\alpha > 3$.

developing from the different initial α differ strongly. For $\alpha \gtrsim 3$, the distribution develops a bimodal structure, with a power-law behaviour $n(k) \sim k^{-5}$ in the IR and $n(k) \sim k^{-2}$ in the UV. At very long times, this bimodal structure decays towards a global $n(k) \sim k^{-2}$ (not shown). For $\alpha \lesssim 3$, the distribution directly reaches a thermal Rayleigh-Jeans scaling $n(k) \sim T/k^2$. The transient non-thermal k^{-5} power law is in agreement with the strong wave turbulence scenario discussed in Sect. 2.3.3 [28, 29]. Its relation to a dilute gas of vortices has been laid out in Chaps. 3 - 7 [31, 32].

8.3 Hydrodynamic condensation

To interpret our results in the context of superfluid turbulence we analyse kinetic-energy spectra as defined in Sect. 2.2.2. In Fig. 8.4a, we show the evolution of the different components $n_\delta(k)$, $\delta \in \{i, c, q\}$, for the weak initial quench $\alpha = 2.5$. At early times, $t \lesssim 10^3\tau$, due to the absence of phase coherence [32] the resulting spectra do not add up to the single-particle spectrum $n(k) \neq n_i(k) + n_c(k) + n_q(k)$. Compressible and incompressible components are roughly of equal

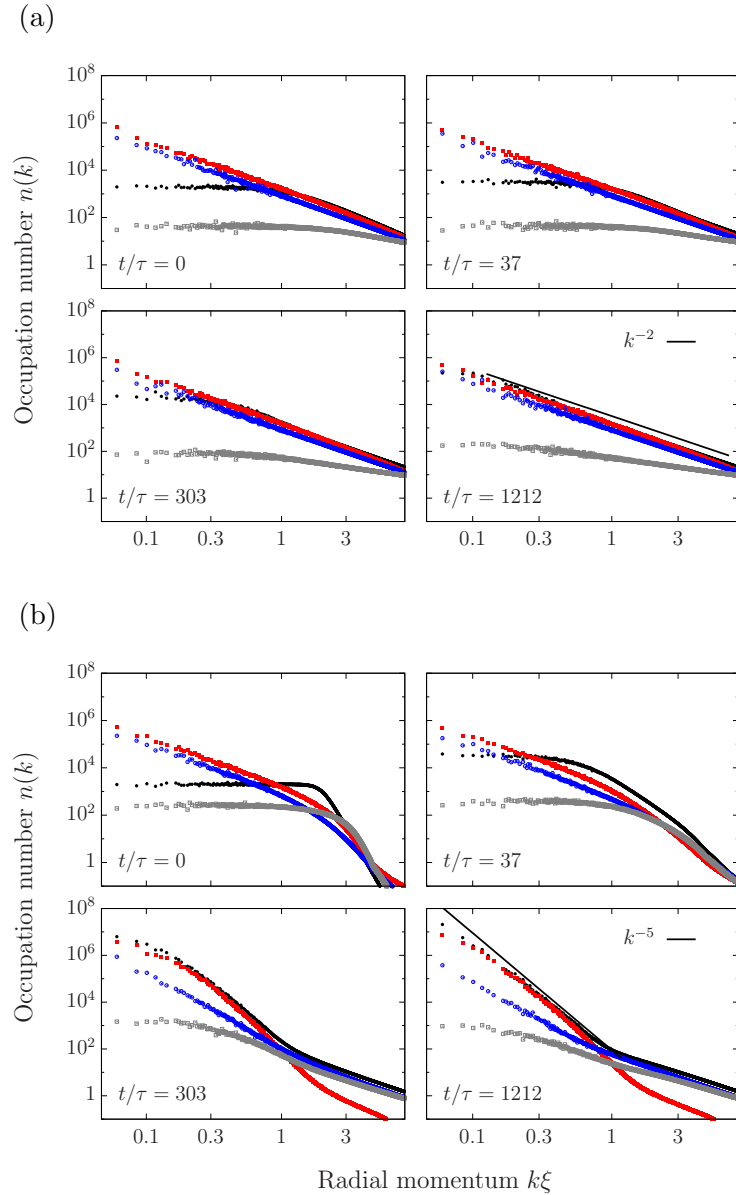


Figure 8.4: Decomposition of particle spectra $n(k)$ (black) into incompressible (red), compressible (blue), and ‘quantum-pressure’ (grey) components, see text for definitions, on a double-log scale, at four different times. (a) Weak cooling quench, $\alpha = 2.5$. Average of 3 runs (b) Strong quench, $\alpha = 10$. Average of 7 runs

magnitude while the quantum pressure component is insignificant on all scales. $n(k)$ grows in the regime of low momenta while phase coherence is being established and a condensate fraction appears (Fig. 8.2). For the case of the strongly non-thermal initial distribution, $\alpha = 10$, the evolution is shown in Fig. 8.4b. In contrast to Fig. 8.4a, two macroscopic flows can be observed, one to the UV, and one to the IR.

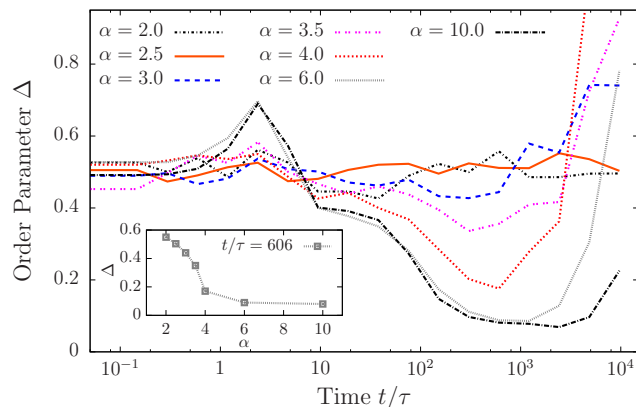


Figure 8.5: Evolution of the fraction Δ of integrated compressible to incompressible components below a momentum scale $k_\lambda \xi = 0.35$, for different initial conditions. Note the semi-log scale. For $\alpha \lesssim 4$, $\Delta(t)$ stays approximately constant. For $\alpha \gtrsim 4$, $\Delta(t)$ approaches zero at intermediate times, signalling the non-thermal fixed point and a superfluid hydrodynamic condensation process. Averages over 1...7 runs. Inset: $\Delta(t = 606\tau)$ as a function of α .

Conservation of particle and energy imply immediately that, when sent out from the regime of intermediate frequencies, energy is deposited in the UV while particles are predominantly transferred to the IR. This leads to an inverse particle cascade with approximately k -independent radial particle flux $Q(k) \equiv Q$ and a corresponding direct energy cascade to the UV [32]. The inverse particle cascade reflects strong wave turbulence, characterised by $n(k) \sim k^{-5}$ [29]. The decomposition in Fig. 8.4a makes clear that this power-law is caused by incompressible excitations only [31,32], establishing a dominantly ideal *hydrodynamic* Bose-Einstein condensation process. In the UV, the excitations follow a thermal $n(k) \sim k^{-2}$ and are dominated by the compressible and quantum-pressure components.

Our results show that during the hydrodynamic condensation process incompressible flow temporally dominates at the expense of compressible excitations in the IR regime. The opposite occurs for the compressible excitations in the UV. This dynamical separation marks the approach to the non-thermal fixed point and disappears when the system finally approaches thermal equilibrium. The evolution of the integrated fraction $\Delta(t) = N_c(k_\lambda, t)/N_i(k_\lambda, t)$, with $N_\delta(k_\lambda, t) = \int_{|\mathbf{k}| < k_\lambda} d\mathbf{k} n_\delta(\mathbf{k}, t)$, of compressible to incompressible occupations below a momentum scale $k_\lambda \xi = 0.35$ is shown in Fig. 8.5. Initially, $\Delta \sim 0.5$. Starting from $\alpha \leq 3$, Δ stays approximately constant while for $\alpha > 3$, Δ decreases for $t \gtrsim 10^2 \tau$ towards zero before increasing again when thermal equilibrium is approached. The inset shows $\Delta(t = 606)$ as a function of α in which one identifies a transition to a separation of the components, depending on the strength of the initial cooling quench.

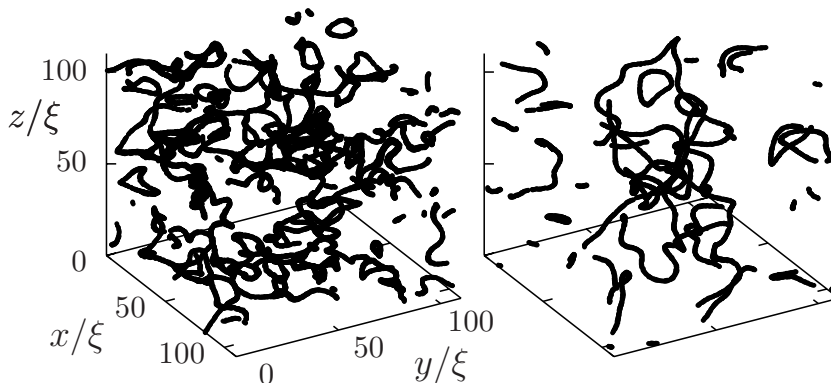


Figure 8.6: Vortex tangle structures emerging in the gas for the two different extremes of initial conditions, $\alpha = 2.5$, at time $t = 2424\tau$ (left) and $\alpha = 10$, at time $t = 606\tau$ (right).

8.4 Defect formation

In Fig. 8.6 we show the three dimensional distribution of points where the density falls below 0.2% of the average density \bar{n} , for the systems quenched with $\alpha = 2.5$ and $\alpha = 10$, at the times $t = 2424\tau$ and 606τ , respectively. We filtered out modes with wave number larger than $k\xi = 0.45$ but in the hydrodynamic case the high-momentum fluctuations barely distort the figure. The vortex tangles corroborate the findings of [48] for both cases of α . However, a remarkable difference exists in the distribution of the phase angle $\varphi(\mathbf{x})$ of the Bose field as can be inferred from Fig. 8.4. While in the direct condensation case, the circular flow has strong longitudinal (compressible) fluctuations, in the hydrodynamic condensation via the non-thermal fixed point macroscopic quantised vortical flow and thus Vinen turbulence of the superfluid are built up. Fig. 8.2 indicates a change in the power-law rise $n(0, t) \sim t^\nu$ from $\nu \sim 3$ to $\nu \sim 2$ to be associated with the approach of the non-thermal fixed point. Similar features have been found to characterise the dynamics of a two-dimensional superfluid near a non-thermal fixed point [33].

8.5 Summary

We find Bose-Einstein condensation in a dilute ultracold gas to occur in two different forms. Hydrodynamic condensation involves a distinct dominance of incompressible flow bearing chaotic (Vinen) turbulence, corresponding to an approach of a non-thermal fixed point. In this regime, particles can not be deposited quickly enough into the zero mode and form an excess population with a characteristic power-law fall-off within the low-energy modes. In contrast, direct condensation can exhibit the appearance of vortical motion but lacks its separation from compressible sound-like excitations. The found characteristic power-law growth of the condensate fraction allows to distinguish the regimes in experiment.

Non-thermal fixed points and solitons

The preceding chapters were committed to the study of turbulence in two- and three-dimensional uniform Bose gases. Now, we will turn our attention to one-dimensional trapped Bose gases, whose non-equilibrium dynamics is under intense investigation by the quantum gas community [2, 7, 149–154]. Specifically, we propose and test the possibility of solitonic states in one-dimensional trapped systems to act as a non-thermal fixed point. To this end, we analyse momentum spectra obtained from a random soliton model and from the non-equilibrium time evolution after a quench. A comparison of our findings to field theoretic predictions as well as turbulence in higher dimensions is made [51].

9.1 Momentum spectra of soliton ensembles

In Chaps. 3, 4, and 5, it was discussed how turbulent features of the single-particle spectrum can be understood from the statistics of vortices. Thereby, correlations between vortices and antivortices played a crucial role. Numerical simulations revealed, that due to vortex-vortex- as well as vortex-sound interactions, the system naturally evolves into a random distribution. As outlined in Sect. 2.2.1, vortices and solitons are both (quasi-) topological excitations of the classical field. They interact with other defects and show quasi-particle behaviour concerning their movement in a trap. Following this analogy, we propose that a random state of solitons can be understood as a non-thermal fixed point in one-dimensional bosonic systems. Similar to vortices we expect solitons to be driven towards this fixed point by soliton-soliton and soliton-sound interactions.

To begin with we develop a model of randomly positioned grey solitons, locally being solutions of the Gross-Pitaevskii equation. Single-particle momentum spectra are derived in a homogeneous system and under the constraint of a trapping potential.

9.1.1 Random-soliton model: uniform gas

Here, we consider the case of a dilute ensemble of solitons with random velocities and positions. The wave function of a single grey soliton in a homogeneous bulk background condensate is given in Eq. (2.6). Using this we write down an expression for a set of N_s uncorrelated solitons with density minima at $\{x_i, i = 1, \dots, N_s\}$ and (dimensionless) velocities ν_i , on a background of constant bulk density n :

$$\phi^{(N_s)}(x, t) = \sqrt{n} \prod_{i=1}^{N_s} \left[n^{-1/2} \phi_{\nu_i}(x - x_i) \right] \quad (9.1)$$

Note that due to the negligence of correlations this field does in general not represent a solution of the Gross-Pitaevskii equation in which the solitons remain non-dispersive.

We make use of the assumption that the ensemble is dilute, i.e., that the distance between each pair of neighbouring solitons is much larger than the healing length. This assumption, for grey solitons, is not valid as soon as two oppositely moving solitons encounter each other but for simplicity we will assume that these collisional configurations can be neglected in view of a majority of well-separated solitons. Since, for any i , $\phi'_{\nu_i}(x - x_i) \equiv d\phi_{\nu_i}(x - x_i)/dx \simeq 0$ as $|x - x_i| \gg 1$ we can rewrite the spatial derivative of the field Eq. (9.1) as

$$\begin{aligned} \phi^{(N_s)'}(x, t) &= \sum_{i=1}^{N_s} \phi'_{\nu_i}(x - x_i, t) \prod_{j \neq i} \left[n^{-1/2} \phi_{\nu_j}(x - x_j, t) \right] \\ &\simeq \sum_{i=1}^{N_s} \left[\delta(x - x_i(t)) \prod_{j \neq i} e^{i\beta_j \theta(x - x_j(t))} \right] \star \phi'_{\nu_i}(x, 0). \end{aligned} \quad (9.2)$$

Here $x_i(t) = x_i(0) - \nu_i t$, $\beta_j = 2 \arccos \nu_j$, \star denotes the convolution over the spatial dependence on x , $\theta(x)$ the Heaviside function, and we have neglected an irrelevant overall phase. Note that the sign of β_i indicates the direction of the propagation of the i -th soliton. The term in square brackets in the second line of Eq. (9.2) is proportional to the spatial derivative of the field describing an ensemble of N_s infinitely thin solitons ($\xi \rightarrow 0$), at the positions $\{x_i\}$,

$$\phi^{(N_s)'}(x, t) \simeq \sum_i \frac{i\gamma_i}{2n_s \sqrt{n}} \phi_{\xi \rightarrow 0}^{(N_s)'}(x_i, t) \delta(x - x_i) \star \phi'_{\nu_i}(x, 0) \quad (9.3)$$

where n_s is the number of solitons per unit length and the pre-factor containing γ_i takes into account that the phase jump by $\exp\{i\beta_i \theta(x - x_i)\}$ is itself proportional to a theta function $\gamma_i \theta(x - x_i)$. Note that although the derivative $\phi_{\xi \rightarrow 0}^{(N_s)'}(x_i, t)$ gives a sum of terms, each being proportional to a delta distribution, only one of these remains when evaluated at x_i , which gives the term in square brackets in Eq. (9.2). We take the Fourier transform of $\langle \phi^{(N_s)'}(x) \star \phi^{(N_s)'}(y) \rangle$ with respect to

$x - y$, integrate over $R = (x + y)/2$, and divide by k^2 ,

$$n(k, t) = \frac{n}{4n_s^2} \left\langle \sum_{i,j=1}^{N_s} \gamma_i \gamma_j e^{ik(x_i - x_j)} \phi_{\nu_i}^*(k) \phi_{\nu_j}(k) \right. \\ \left. \times \partial_{x_i} \partial_{x_j} e^{-n_s |x_i - x_j| \{1 - \int_{\beta} P(\beta) \exp[i\beta \operatorname{sgn}(x_i - x_j)]\}} \right\rangle. \quad (9.4)$$

Here, P is the probability for finding a soliton with greyness $\nu = \cos(\beta/2)$, and averaging over the random positions of all solitons other than those at x_i and x_j has been done in order to obtain the exponential decay of the coherence function. Combining Eq. (9.4) with the Fourier transform of $\phi_{\nu}(x, 0)$,

$$\phi_{\nu}(k, t) = i \sqrt{\frac{2\pi n}{L}} \left[2\pi\nu \delta(k) + \frac{\sqrt{2}\pi\xi}{\sinh(\pi\gamma k\xi/\sqrt{2})} \right], \quad (9.5)$$

one derives the single-particle momentum distribution for a set of N_s solitons defined by greyness and position, $\{\nu_i, x_i \mid i = 1, \dots, N_s\}$, as

$$n(k, t) \simeq \frac{n}{4n_s^2} \int \frac{dk'}{2\pi} \sum_{i,j=1}^{N_s} \gamma_i \gamma_j e^{i(k-k')(x_i - x_j)} \\ \times \left[2\pi\nu_i \nu_j \delta(k) + \frac{2\delta(0)\pi^2\xi^2}{\sinh(\pi\gamma_i k\xi/\sqrt{2}) \sinh(\pi\gamma_j k\xi/\sqrt{2})} \right] \\ \times \frac{4k'^2 n_s \operatorname{Re} \alpha}{4n_s^2 (\operatorname{Re} \alpha)^2 + (k' - 2n_s \operatorname{Im} \alpha)^2} e^{-ik'(\nu_i - \nu_j)t} \quad (9.6)$$

Here, the inverse volume $\delta(0) = L^{-1}$ appears as we first choose the $\phi_{\nu_i}^*$ and ϕ_{ν_j} in Eq. (9.4) different and take the identity limit only at the end. α is the average over all $\alpha_i = (1 - \exp\{i\beta_i\})/2$.

Assuming the dependence of $\gamma_i / \sinh(\pi\gamma_j k\xi/\sqrt{2})$ on ν_i to be negligible we obtain an approximate stationary distribution

$$n(k) \simeq \frac{4n_s n \operatorname{Re} \alpha}{4n_s^2 (\operatorname{Re} \alpha)^2 + (k - 2n_s \operatorname{Im} \alpha)^2} \frac{(\pi\gamma k\xi)^2/2}{\sinh^2\left(\frac{\pi\gamma k\xi}{\sqrt{2}}\right)}, \quad (9.7)$$

with a yet to be determined parameter γ . For black solitons ($\nu_i \equiv 0$) one obtains the exact expression

$$n(k)|_{\nu=0} = \frac{4n_s n}{4n_s^2 + k^2} \frac{(\pi k\xi)^2/2}{\sinh^2\left(\pi k\xi/\sqrt{2}\right)}. \quad (9.8)$$

For an ensemble of grey solitons of identical $|\nu_i| \equiv \nu$, travelling with probabilities

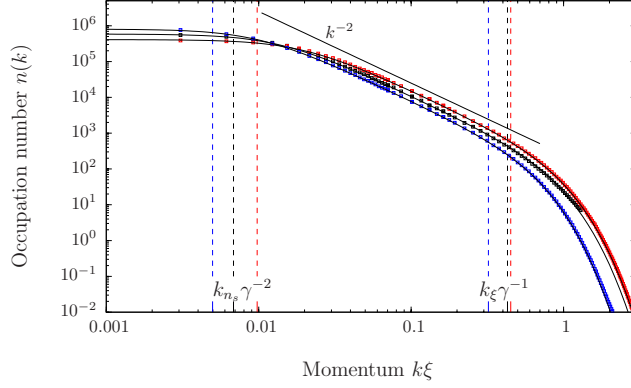


Figure 9.1: Single-particle momentum spectrum as a function of k on a double-logarithmic scale for an ensemble of 5×10^3 configurations with $N_s = 20$ solitons each distributed according to a flat distribution across phase-space defined by the positions in the box and the maximum greyness $|\nu_{\max}| = 0.99$. We chose $\xi = 8a_s$. Solid (black) squares: numerical ensemble averages, solid (black) line: Eq. (9.7) with $\alpha = 0.7$, $\gamma = 1.05$, shown up to $k\xi \simeq 1.3$ where a finite-size effect sets in due to the random set of solitons not matching periodic boundary conditions. For comparison, results for $N_s = 20$ purely black solitons (red squares and line) are shown as well as for $N_s = 20$ solitons with fixed greyness $|\nu| = 0.707$, i.e., $\gamma = 1.4$, (blue squares and line) choosing an equal number of right- and left-movers, $P = Q = 1/2$. The comparison validates the approximate expressions Eq. (9.7)–Eq. (9.9) which exhibit scaling behaviour in the regime of momenta $k_{n_s}\gamma^{-2} \ll k \ll k\xi\gamma^{-1}$.

P into the positive x -direction and $Q = 1 - P$ into the negative direction one finds

$$n(k) = \frac{4n_s n}{4n_s^2\gamma^{-4} + [k + 2(1 - 2Q)n_s\nu\gamma^{-1}]^2} \frac{(\pi k\xi)^2/2}{\sinh^2\left(\pi\gamma k\xi/\sqrt{2}\right)}. \quad (9.9)$$

Here, $\gamma = (1 - \nu^2)^{-1/2}$. To demonstrate the applicability of the above analytic expressions we construct ensembles of phase-space distributions of spatially well-separated solitons in a box with periodic boundary conditions and compute the ensemble averaged correlations. These simulations are done on a 1D grid of $N = 2^{14}$ sites, generating 5×10^3 configurations for taking ensemble averages. For this we multiply $N_s = 20$ single-soliton solutions Eq. (2.6) with positions x_i and greyness ν_i chosen randomly according to a given phase-space distribution. To make sure that their relative distance on the average is much larger than their widths we chose the phase-space distribution to allow for a maximum greyness, $|\nu_i| < |\nu_{\max}| < 1$, such that the diluteness criterion requires an approximate minimum box length of $L = 4(1 - \nu_{\max}^2)^{-1/2}N_s$.

Fig. 9.1a shows the single-particle momentum spectrum $n(k)$ on a double-logarithmic scale for an ensemble of 5×10^3 configurations with $N_s = 20$ solitons each distributed according to a flat distribution across phase-space defined by the positions in the box and the maximum greyness $|\nu_{\max}| = 0.99$. Solid (black) squares represent the

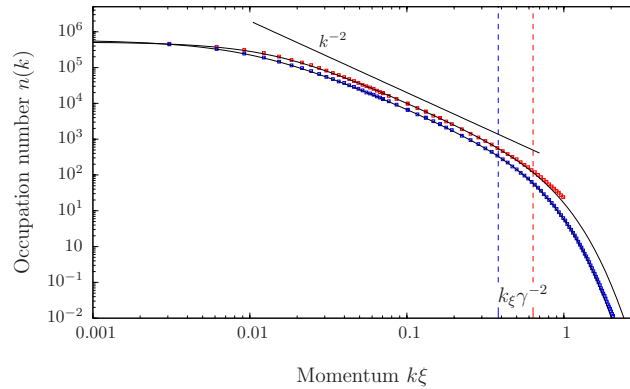


Figure 9.2: Single-particle momentum spectrum as a function of k on a double-logarithmic scale for an ensemble of $N = 5 \times 10^3$ configurations with $N_s = 20$ solitons each distributed according to a phase-space distribution with an unequal weight for solitons with positive ν (right-movers) and negative ν (left-movers). The greyness is uniformly distributed within $0 = \nu_{\min} \leq \nu \leq \nu_{\max} = 0.99$. All other parameters are chosen as for Fig. 9.1. Red squares and black line show the ensemble average and compare with Eq. (9.9) for $Q = 0.2$, $\gamma = 1.179$, and $\nu = 0.412$, shown up to $k\xi \simeq 1$ where a finite-size effect sets in due to the random set of solitons not matching periodic boundary conditions. For comparison, results for $N_s = 20$ solitons with fixed greyness $\nu = 0.707$, i.e., $\gamma = 1.41$, (blue squares and line) are shown.

results of the numerical ensemble average while the solid line corresponds to the analytical formula Eq. (9.7), with fitted parameters $\alpha = 0.7$, $\gamma = 1.05$. Compare this to the analytical average $\alpha = 2/3$. For comparison, we give the results for the same number of purely black solitons (red squares and line) as well as for a fixed greyness $|\nu| = 0.707$ (blue squares and line), choosing an equal number of right- and left-movers. The comparison validates the approximate expressions Eq. (9.7)–Eq. (9.9) which exhibit scaling behaviour in the regime of momenta $k_{n_s}\gamma^{-2} \ll k \ll k_\xi\gamma^{-1}$.

In Fig. 9.2 we show the single-particle momentum spectrum for an ensemble of 5×10^3 configurations with $N_s = 20$ solitons each distributed according to a phase-space distribution with an unequal weight for solitons with positive ν (right-movers) and negative ν (left-movers). We specifically restricted the greyness to the interval $0 = \nu_{\min} \leq \nu \leq \nu_{\max} = 0.99$ and besides that chose the same parameters as for Fig. 9.1. Black squares and line show the ensemble average and compare with Eq. (9.9) for $Q = 0.2$, $\gamma = 1.179$, and $\nu = 0.412$. For comparison, results for $N_s = 20$ solitons with fixed greyness $\nu = 0.707$, i.e., $\gamma = 1.41$, (blue squares and line) are shown.

9.1.2 Relation to non-thermal fixed points and vortices

Universal scaling behaviour in a many-body system far from equilibrium points to the appearance of turbulence phenomena. In the following, we discuss the power-law spectra derived for soliton ensembles in this context.

In Chaps. 3, 4 and 5 [31, 32], it was shown that a new class of non-thermal fixed points can also be understood, in two and three dimensions, in terms of vortex excitations of the superfluid. As a consequence, within a window in momentum space, i.e. the inertial range, which is limited by the inverse mean distance between different vortices and the inverse core size, the single-particle occupation number spectrum shows the power law predicted in [29].

Before we discuss this in more detail let us first turn back to the soliton spectra derived in the previous section. Assuming an equal number of solitons travelling with positive and negative velocities, $P = Q = 1/2$, i.e., assuming $\text{Im } \alpha = 0$, the single-particle spectrum Eq. (9.9) is characterised by a maximum of two scales. Consider the case $n_s \ll \gamma/(\sqrt{2}\pi\xi)$. For momenta greater than the reduced soliton density but smaller than the reduced inverse healing length, $k_{n_s}\gamma^{-2} \ll k \ll k_\xi\gamma^{-1}$, with $k_{n_s} = 2n_s$, and $k_\xi = \sqrt{2}/(\pi\xi)$, the momentum distribution exhibits a power-law behaviour, $n(k) \sim k^{-2}$. This reflects, first, the random position of the kink-like phase jump across the centre of the soliton, and second, that these momenta cannot resolve the spatial width of the kink. In other words, looking within a spatial window of size between $\gamma^2 k_\xi^{-1}$ and $\gamma k_{n_s}^{-1}$, the appearance of a single sharp solitonic phase jump inside the window is observed in a random manner. Hence, for any of these window sizes, the system looks identical, it appears self-similar. This self-similarity is at the base of the scaling momentum distribution. Already for a single soliton, the momentum distribution does not know anything about the position of the kink (this information appears as a phase in the momentum-space Bose field which is irrelevant for $n(k)$), and thus the single-soliton distribution is self-similar, too.

For black solitons, the self-similar scaling region is limited by the scales k_{n_s} and k_ξ . Below k_{n_s} , the distribution is constant because too low wave numbers cannot resolve the kink-structure. This corresponds to the first-order coherence function decaying exponentially in space, with the decay scale set by the soliton distance $1/n_s$,

$$\langle \phi^*(x)\phi(y) \rangle \sim \exp\{-2n_s|x - y|\}. \quad (9.10)$$

Above k_ξ , the momentum spectrum resolves the finite width of the soliton density dip which results in an exponential suppression of the mode occupations. We recall that also in equilibrium, at sufficiently high temperatures where quasi-particle mode occupations are large, $n^{(\text{qp})}(k) = k_B T / (c_s k) \gg 1/2$, the first-order coherence function decays exponentially, $g^{(1)}(s) \sim \exp[-s/r_0]$, where the scale is set by the coherence length $r_0 = 2n/(mk_B T)$. Hence, the corresponding momentum spectrum has the same shape

$$n^{\text{eq}}(k) \sim \frac{2r_0^{-1}}{r_0^{-2} + k^2}, \quad (9.11)$$

as for a set of random thin solitons. We emphasise, however, that the transition scale k_{n_s} above which scaling $\sim k^{-2}$ sets in (see, e.g. Eq. (9.8)) can be made larger than for a thermal ensemble by increasing the soliton density n_s above the inverse thermal coherence length $1/r_0$. Moreover, the thermal distribution Eq. (9.11) does

not show an exponential decay above k_ξ . This allows to identify non-equilibrium soliton vs. thermal scaling in experiment.

We finally compare the universal and non-universal aspects of the soliton momentum spectra found here with the corresponding spectra in $d = 2$ and 3 dimensions. As discussed in detail in the previous chapters [31, 32], the universal exponent $\zeta = d + 2$, $d = 2, 3$, found for the particle spectra $n(k) \sim k^{-\zeta}$ during the dynamical relaxation of an initially strongly quenched gas reflected the appearance of vortices in two and vortex lines in three dimensions. In two dimensions, this can be seen in an easy way looking at the flow velocity field $\mathbf{v} \sim \nabla\varphi = \mathbf{e}_\theta/r$ at the distance r from the core of a singly quantised vortex, where \mathbf{e}_θ is the local tangential unit vector and φ the phase angle of the complex Bose field. The r -dependence implies a k^{-1} scaling of $|\mathbf{v}(k)|$ and thus a k^{-2} scaling of the kinetic energy $E(k) \sim k^2 n(k) \sim v(k)^2$, i.e., $n(k) \sim k^{-4}$ [32, 115]. Similar arguments lead to $n(k) \sim k^{-5}$ for the radial momentum distribution in the presence of a vortex line in three dimensions, see Chap. 4 [32]. Extending these arguments, the scaling $n(k) \sim k^{-d-2}$ was shown to appear for ensembles of randomly positioned vortices/vortex lines in a range of momenta $l_v^{-1} \lesssim k \lesssim \xi^{-1}$ between the inverse of the inter-vortex distance l_v and the inverse of the healing length ξ which is a measure for the core width.

As pointed out in Sect. 2.3, the power-law spectrum $n(k) \sim k^{-d-2}$, in turn, had been predicted by use of non-perturbative field-theory methods in [28, 29] where it resulted for a strong-wave-turbulence cascade in the IR, characterising the scaling behaviour at a non-thermal fixed point. This cascade was shown in [32] to be caused by particles being transported towards the IR where they build up high mode occupations and thus coherence in the sample, see also [44–46, 48–50]. Note that in the picture of the evolving Bose field this momentum-space transport corresponds to the mutual annihilation of vortices and anti-vortices in the system which results in an increase of the inter-vortex distance and thus of the range over which phase coherence is established.

Having recalled all this, we note that solitonic states in one dimension resemble the turbulent phenomena in $d = 2, 3$. Firstly, the presence of metastable solitons induces a quasi-stationary power-law momentum distribution. Secondly, inverse momentum-space transport corresponds to soliton decay, which increases the inter-soliton distance and extends the self-similar regime towards smaller momenta. However, there is a discrepancy between the predicted scaling $\sim k^{-d-2}$, which was found consistent with the vortex picture for $d = 2$ and 3, and the scaling $\sim k^{-2}$ obtained here for the solitons in $d = 1$. To gain more insight into this issue we consider the spatial decay of the phase coherence for a system in two dimensions over distances considerably larger than the inter-vortex spacing. In analogy to the soliton ensembles discussed in Sect. 9.1.1 and Sect. 9.1.3, we consider randomly positioned and well-separated vortices. One finds that the decay of the phase coherence follows the same exponential law,

$$\langle \phi^*(\mathbf{x})\phi(\mathbf{y}) \rangle \sim \exp\{-2n_{v,1}|\mathbf{x} - \mathbf{y}|\}, \quad (9.12)$$

where $n_{v,1}$ is the one-dimensional uniform vortex density along the straight line through \mathbf{x} and \mathbf{y} . Fourier transforming Eq. (9.12) with respect to $\mathbf{x} - \mathbf{y}$ results in a momentum spectrum $n_c(k) \sim (4n_{v,1}^2 + k^2)^{-3/2}$ which scales as k^{-3} for momenta considerably larger than the inverse vortex distance¹ $n_{v,1} = 1/l_v$. Analogously, one finds $n_c(k) \sim k^{-4}$ for vortex line tangles in three dimensions. We use the subscript ‘c’ to distinguish these spectra from the $n(k)$ discussed above.

The apparent contradiction between the respective scalings of $n(k)$ and $n_c(k)$ whose exponents differ by 1, is resolved by observing the following: While the exponential decay Eq. (9.12) is valid over large distances $|\mathbf{x} - \mathbf{y}| \gg l_v$, it is the algebraic dependence of the flow field \mathbf{v} as a function of distance from the vortex core which matters on length scales below the inter-vortex distance, causing the steeper power law $n(k) \sim k^{-d-2}$ at momenta $k \gg 1/l_v$. Hence, we find an important qualitative difference between the physical properties underlying the universal scaling $n(k) \sim k^{-2}$ in one dimension and the scalings $n(k) \sim k^{-d-2}$ in $d = 2$ and 3 dimensions: While black solitons in one dimensions are at rest and no particle flow can occur, in higher dimensions, transverse flow circling around the vortex cores gives rise to an additional contribution to the kinetic energy. As far as this transverse flow dominates over a possible additional longitudinal flow component for which $\mathbf{v} \cdot \nabla \mathbf{v} \neq 0$, see [32], this comparison also holds when allowing for grey solitons, which are moving opposite to the (longitudinal) particle flow across the soliton dip.

9.1.3 Random-soliton model: trapped gas

In our dynamical simulations we will consider soliton formation in a harmonic trapping potential rather than in a homogeneous system, see Sect. 9.2. We therefore need to take into account, in the random-soliton model, the inhomogeneous bulk distribution of the gas.

Assuming a sufficiently shallow harmonic potential, $l_{\text{ho}}/\xi = (m\omega_{\text{ho}}\xi^2)^{-1/2} \gg n_s^{-1}$ we can describe the Bose field in local-density approximation with respect to a bulk density distribution given in Thomas-Fermi approximation, $n_{\text{TF}}(x) \simeq n_0[1 - (x/R)^2]$, with $R = \sqrt{2}c_s/(\omega_{\text{ho}}\xi) = 2g_{1\text{D}}n/\omega_{\text{ho}}$ being the Thomas-Fermi radius in units of ξ . We take the maximum density n_0 large enough to ensure $k_\xi \gg k_{n_s}$ for solitons not too close to the edge of the cloud. In such a bulk density distribution, single solitons oscillate harmonically between classical turning points where the solitons “touch ground”, i.e., momentarily turn black [163]. Their oscillation frequency is by a factor of $\sim 1/\sqrt{2}$ smaller than the trap frequency, $\omega_s \simeq \omega_{\text{ho}}/\sqrt{2}$.

In leading order in $\epsilon \sim \ddot{x}_s/\dot{x}_s$, the field of a single soliton can locally be written in the simple form given in Eq. (2.6), with ν , and thus γ replaced by local quantities,

$$\nu \rightarrow \nu(x_s) = \nu_{s,\text{max}} \left[1 - \left(\frac{x_s}{x_{s,\text{max}}} \right)^2 \right], \quad (9.13)$$

¹This behaviour can indeed be observed for a short intermediate time of the evolution right after vortex generation, see Fig. 5.3 (top right).

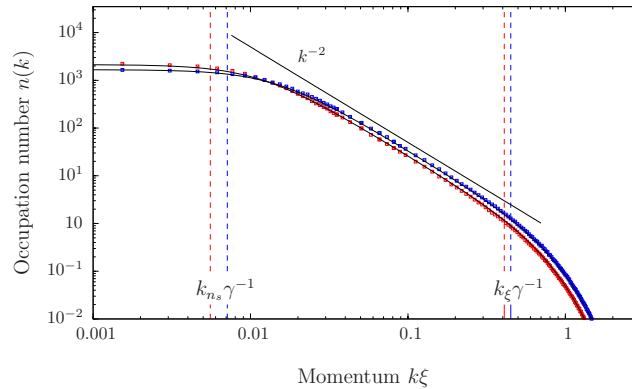


Figure 9.3: Single-particle momentum spectrum $n(k)$ on a double-logarithmic scale for an ensemble of 5×10^3 configurations with $N_s = 20$ solitons each distributed according to a flat distribution in phase-space $\{x/R, \nu\}$, circularly symmetric around $(x = 0, \nu = 0)$ with radius $\bar{R}_s = 1$. We chose $\xi = 4a_s, N_0$. Solid (red) squares: results of numerical ensemble average; solid line through these points: analytical spectrum Eq. (9.17), with $\gamma = 1.1$. (Blue) squares and line: Corresponding results for the same number of black solitons distributed randomly across the trap.

$\gamma \rightarrow \gamma(x_s) = [1 - \nu(x_s)^2]^{-1/2}$, evaluated at the position $x_s = x_s(t)$ of the soliton [163]. $\nu_{s,\max}$ is the maximum greyness the soliton acquired in the centre of the trap, and $x_{s,\max} = \nu_{s,\max}R$ is the distance of the soliton's turning point from the trap centre. Only solitons whose velocity does not exceed the Landau critical velocity, i.e., for which $\nu_{s,\max} \leq 1$, can oscillate in the trap for more than a quarter of the period $T_s = 2\pi/\omega_s$. This limits the maximum greyness at a distance x from the trap centre to a range between 0 and $\nu_{\max}(x) = 1 - (x/R)^2$.

At a given time t , we assume a particular set $\{x_i(t)\}$ of N_s well-separated solitons across the trapped gas. The single-particle momentum spectrum corresponding to an ensemble of such sets depends on the distribution of the solitons over the greyness for each position in the trap. This distribution is best visualised in phase space which is parametrised by the (x, ν) , or, equivalently and in dimensionless form, by $(x/R, \nu)$, with both, x/R and ν ranging between -1 and 1 . In this space, the trajectory of a single soliton is a circle with radius $\nu_{s,\max}$ which is traced out with constant angular velocity ω_s . Hence, a stationary distribution of the N_s solitons is given by a circularly symmetric distribution in phase space, i.e., a distribution over the different possible maximum greyness $\nu_{s,\max}$ or turning points $x_{s,\max}$. The simplest assumption would be that of a uniform distribution of the solitons in phase space, which amounts to a uniform distribution over the different possible ν at each distance x from the trap centre and an integrated soliton density distribution $n_s(x) \propto 1 - (x/R)^2$.

Following the above considerations we can obtain approximate expressions for the momentum spectrum. For instance, for a uniform density $P[\bar{x}, \nu] \equiv n_{s,0}/\bar{R}_s$ of solitons within a radius $\bar{R}_s = R_s/R$ in phase space, i.e., for all (\bar{x}, ν) with

$\sqrt{\bar{x}^2 + \nu^2} \leq \bar{R}_s \leq 1$, with $n_{s,0} = N_s/(\bar{R}_s\pi)$, the first-order coherence function for thin solitons becomes

$$\langle \phi^{(N_s)}(\bar{x})^* \phi^{(N_s)}(\bar{y}) \rangle_{\xi \rightarrow 0} = \sqrt{n_{\text{TF}}(\bar{x})n_{\text{TF}}(\bar{y})} \exp\{-2n_{s,0} \int_{\bar{y}}^{\bar{x}} d\bar{z} \alpha(\bar{z})\} \quad (9.14)$$

with a local average dephasing of

$$\begin{aligned} \alpha(\bar{x}) &= \frac{1}{2\bar{R}_s} \int_{-\sqrt{\bar{R}_s^2 - \bar{x}^2}}^{\sqrt{\bar{R}_s^2 - \bar{x}^2}} d\nu \left(1 - \nu^2 \pm i\nu\sqrt{1 - \nu^2}\right) \\ &= \sqrt{1 - \frac{\bar{x}^2}{\bar{R}_s^2}} \left(1 - \frac{\bar{R}_s^2 - \bar{x}^2}{3}\right). \end{aligned} \quad (9.15)$$

Using this, the integral over α to linear order in \bar{x} reads $\int_0^{\bar{x}} d\bar{z} \alpha(\bar{z}) = \alpha^{(1)}\bar{x} + \mathcal{O}(\bar{x}^3)$, $\alpha^{(1)} = 1 - \bar{R}_s^2/3$. This approximation is best for $\bar{R}_s \rightarrow 1$, in which limit we obtain

$$\langle \phi^{(N_s)}(\bar{x})^* \phi^{(N_s)}(\bar{y}) \rangle_{\xi \rightarrow 0} \simeq \sqrt{n_{\text{TF}}(\bar{x})n_{\text{TF}}(\bar{y})} e^{-4N_s|\bar{x}-\bar{y}|/(3\pi\bar{R}_s)}. \quad (9.16)$$

Analogously, one calculates the exponential dephasing factor for more complicated soliton phase-space distributions. Taking the above results together one derives the momentum distribution in local-density-approximation as the convolution of the spectrum for a homogeneous distribution of thin solitons with the Fourier transform of the bulk density, multiplied with the momentum spectrum of a single soliton:

$$n(k) \simeq \left(n_{\text{TF}}(k) \star \frac{4n_{s,0}\alpha^{(1)}}{4n_{s,0}^2\alpha^{(1)2} + k^2} \right) \frac{(\pi\gamma k\xi)^2/2}{\sinh^2(\pi\gamma k\xi/\sqrt{2})}, \quad (9.17)$$

where the parameter γ is to be determined and \star denotes the convolution with respect to k .

In the case that single soliton distributions contributing to the ensemble are not uniform throughout phase space, the ensemble-averaged $n(k)$ would rather be a sum of ($k \rightarrow -k$)-asymmetric distributions such that on the average the momentum distribution can have local maxima at finite $|k| > 0$.

To study the quality of the above analytic expressions we construct ensembles of phase-space distributions of spatially well-separated solitons inside a harmonic trap and compute the ensemble averaged correlations. For this, we multiply N_s single-soliton solutions Eq. (2.6) with positions x_i and greyness ν_i chosen according to a given phase-space probability distribution and ensure that their relative distance on the average is much larger than their widths. Fig. 9.3 shows the single-particle momentum spectrum $n(k)$ on a double-logarithmic scale for an ensemble of 5×10^3 configurations with $N_s = 20$ solitons each distributed according to a flat distribution in phase-space $\{x/R, \nu\}$, circularly symmetric around $(x = 0, \nu = 0)$ with radius $\bar{R}_s = 1$. Solid (red) squares represent the results of the numerical ensemble average

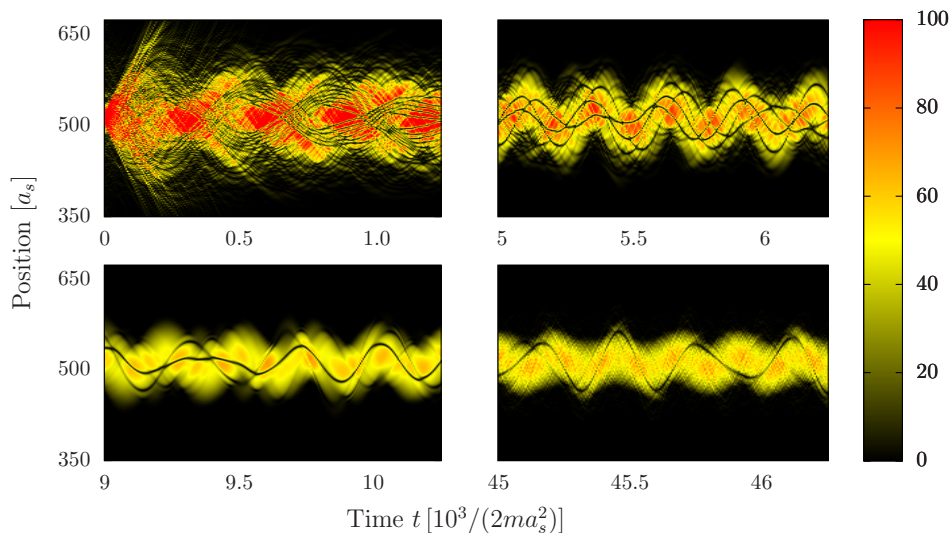


Figure 9.4: Snapshots of a single run of the non-linear classical field equation, showing solitons which oscillate inside a trapped one-dimensional ultracold Bose gas. The gas is initially non-interacting and thermalised, with $T = 360\omega_{\text{ho}}$, in a trap with oscillator length $l_{\text{ho}} = 8.5$ (in grid units). At time $t = 0$ the interaction is switched to $g_{1\text{D}} = 7.3 \times 10^{-3}$, and a cooling period using a high-energy knife is applied, see Sect. 9.2 for details on grid units, the chosen parameters and protocol. The panels show the one-dimensional colour-encoded density distribution as a function of time. Top left panel: The initially imposed interaction quench causes strong breathing-like oscillations and the creation of many solitons. Top right panel: Breathing oscillations have damped out, leaving a dipolar oscillation of the bulk distribution in the trap. Clearly distinct solitons have formed. Bottom left panel: After the end of the cooling period (here at $t = t_c = 9.1 \times 10^3$) only a few solitons are left oscillating within the oscillating bulk. Bottom right panel: A single soliton is left at late times.

while the solid line corresponds to the analytical formula Eq. (9.17), with $\gamma = 1.1$. For comparison, we give corresponding results for the same number of black solitons distributed randomly across the trap (blue squares and line).

9.2 Soliton spectra in dynamical simulations

We study the formation and evolution of soliton excitations in trapped one-dimensional Bose gases by means of the classical field equation Eq. (2.5), see also Sect. 2.2. For the simulations, we map the system onto a grid of $N = 1024$ lattice sites with a lattice constant a_s . If not stated otherwise, quantities are given in grid units based on a_s , see Sect. 2.2 and App. A. The parameters are chosen as $g_{1\text{D}} = 7.3 \times 10^{-3}$ for the coupling, $t_c = 9.1 \times 10^3$ for the cooling time, and $l_{\text{ho}} = 8.5$ for the harmonic oscillator length.

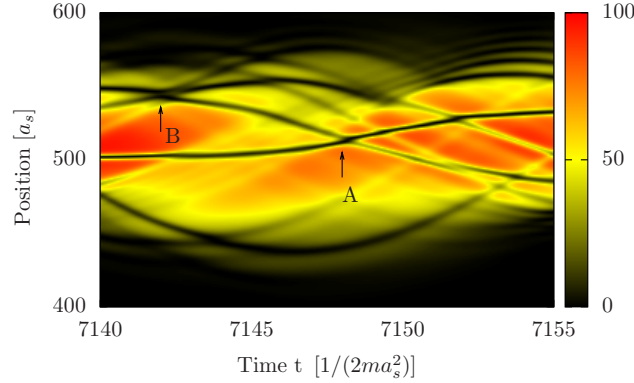


Figure 9.5: Snapshots of a single run of the non-linear classical field equation, showing solitons which oscillate inside the trap, thereby showing signs of mutual scattering and passing through each other (examples marked by letters). Parameters are chosen as in Fig. 9.4.

9.2.1 Soliton formation and tracking in position space

At the initial time, we take the gas to be non-interacting and thermalised and impose an interaction quench. To allow the emerging collective excitations to form solitons at a desired density we furthermore apply evaporative cooling by opening the trapping potential at the edges in a controlled fashion. During the first, cooling period, $t \leq t_c$, the potential is given by the inverted Gaussian $V(x, t) = m\omega_{\text{ho}}^2 U(t) \{1 - \exp[-x^2/2U(t)]\}$ with its maximum being ramped down by sweeping $U(t) = U_0 + (U_c - U_0)t/t_c$ linearly in time from U_0 to U_c . At the same time, highly energetic particles near the edge of the potential are removed by adding a loss term $i\Gamma(x, t)/2 = i\Gamma_\infty[V(x, t)/U(t)]^r/2$ to the trapping potential. Thereafter, during the interval $t_c \leq t \leq t_{\text{max}}$ the loss is switched off and the potential is ramped up again to harmonic shape across the extension of the gas, $U(t) = U_c + (U_{\text{max}} - U_c)(t - t_c)/(t_{\text{max}} - t_c)$. We choose $r = 10$, $U_0 = 2.75$, $\Gamma_\infty = 0.1U_0$, $U_c = U_0/3$, and $U_{\text{max}} = 10U_0$. The times t_c and t_{max} vary and are given in the following. This protocol corresponds to the one used in Ref. [349]. Different cooling schemes have been used in experiments, see, e.g., [350, 351], but as we are primarily interested in the one-dimensional dynamics, we here restrict ourselves to purely 1D calculations.

Three stages of the induced dynamical evolution can be observed, see Fig. 9.4:

Initial Oscillations. See the top left panel of Fig. 9.4. Following the interaction quench potential energy is transferred to kinetic energy. One observes strong breathing-like oscillations of the gas. These oscillations decay on a timescale of $t \approx 2 \times 10^3$, leaving a dipolar oscillation of the bulk in the harmonic trap. Solitons are formed in the wake of the decaying breathing oscillations.

Solitonic Regime. See the top right panel of Fig. 9.4. The initial collective oscillations have largely decayed except for an overall dipole mode, and many solitons

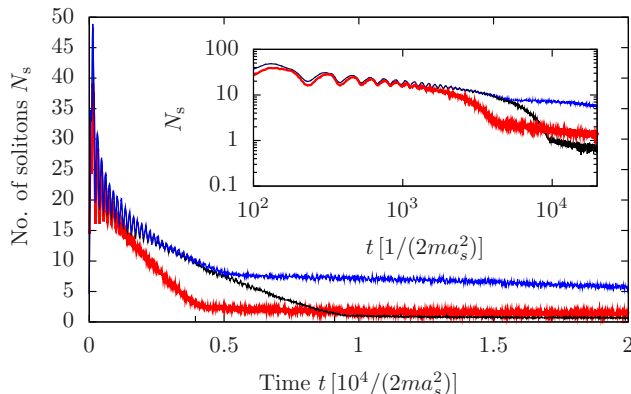


Figure 9.6: Time evolution of the mean number N_s of solitons, for an ensemble of 100 runs. Strong initial oscillations occur during the breathing like bulk oscillations after the interaction quench, until $t \simeq 10^3$. The number of solitons decreases while the gas is evaporatively cooled. After the end of the cooling, at $t = t_c$ the decay is considerably slowed down and the number of solitons remains largely stable. Three different cooling times and two ramp speeds are shown, with $t_c = 3.9 \times 10^3$ (red), $t_c = 4.55 \times 10^3$ (blue), and $t_c = 9.1 \times 10^3$ (black).

appear. The bottom left graph shows the evolution around $t = t_c = 9.1 \times 10^3$ when only very few solitons have survived. The solitons oscillate in the trap, being nearly black at the edges and grey in the centre of the trap corresponding to a nonzero velocity. Fig. 9.5 magnifies a short period of the evolution. On mutual encounters, the solitons get phase-shifted, such that collisions show signs of scattering or passing through each other. Collisions with different such shifts are marked by letters A and B in Fig. 9.5.

Final stage: At times $t \gg t_c$, a soliton is still visible, see the bottom right panel of Fig. 9.4. Comparing runs we find different numbers of solitons remaining during the late stage.

The shortest relevant time scale is the time of sound crossing the trap² $t_s = l_{\text{HO}}/c \approx 10$, then comes the oscillation period in the trap $T_{\text{ho}} \approx 230$, which leads to an initial collective oscillation with period $T_{\text{oscillation}} \approx 300$ (cf. Fig. 9.4). The collective breathing motion dies out after $\tau \approx 2000$. The oscillation period of a soliton in the Thomas Fermi bulk is $T_s \approx \sqrt{2} T_{\text{ho}} \approx 320$. The longest time scale in our setup is the cooling time $t_c = 9100$. Comparing these time scales to the total time of the simulation $t > 10^5$, at the end of which solitons are still present, we see that the solitons are quasi-stationary in the system. They emerge soon after the initial quench and remain throughout the whole evolution while thermalisation of the high-momentum modes is proceeding as we will see in the following.

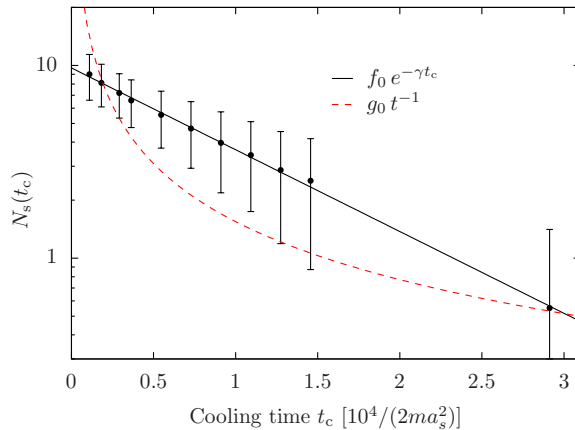


Figure 9.7: The number of solitons $N_s(t_c)$ at the end of the cooling period, $t = t_c$, as a function of t_c , for ensembles of 200 runs each (black dots and error bars). The function $f_0 \exp\{-\gamma t_c\}$, with $f_0 = 9.7$ and $\gamma = 9.77 \cdot 10^{-5}$, was fitted with $\chi^2 = 0.006$ (black line). The function $g_0 t_c^{-1}$, with $g_0 = 1.55 \cdot 10^5$, was fitted with $\chi^2 = 1.28$ (red dashed line). Hence, other than for the Kibble-Zurek scheme of Ref. [349], cooling after the initial quench results in an exponential dependence of $N_s(t_c)$ on t_c .

9.2.2 Number of solitons after cooling ends

In order to study the statistics of the solitons emerging during the evolution we have set up an efficient tracking algorithm which identifies the trajectories of the solitons oscillating in the gas, see App. A. Fig. 9.6 shows the evolution of the mean number of solitons, for an ensemble of 200 runs. The three stages described above can be identified. The strong initial oscillations give an oscillating number of solitons until $t \simeq 10^3$. The number of solitons decreases while the gas is evaporatively cooled. After the end of the cooling, at $t = t_c$ the decay is considerably slowed down and the number of solitons remains largely stable. Three different cooling times and two ramp speeds are shown, with $t_c = 3.9 \times 10^3$ (red), $t_c = 4.55 \times 10^3$ (blue), and $t_c = 9.1 \times 10^3$ (black), where the same speed is chosen to obtain the blue and black data.

Kibble and Zurek have predicted that the number of defects created in the near-adiabatic crossing of a phase transition scales with the crossing rate according to a power law which depends on the universal properties of the transition [182, 353]. This was studied numerically in [349] using the cooling protocol described above. While the interacting gas was chosen to be in thermal equilibrium initially, with a temperature well above the critical point, we start our simulations, motivated by earlier work on vortex dynamics [31, 32], with an interaction quench driving the system strongly out of equilibrium. To compare the dynamics induced in this way with the results of [349] we show, in Fig. 9.7, the dependence of the number of solitons created on the cooling ramp time t_c . We find that, within the error bars

²Taking $l_{\text{HO}} \simeq 10 \mu\text{m}$ and $c \simeq 10^4 \mu\text{m/s}$ [352], a typical experimental value for would be $t_s = 10^{-3} \text{s}$

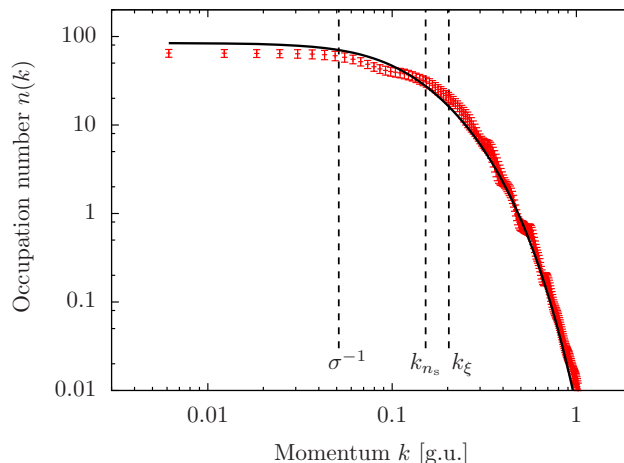


Figure 9.8: Momentum spectrum $n(k, t)$ at time $t = 5 \cdot 10^3$ with statistical errors (ensemble average over 100 runs). k and t are in grid units as defined in Sect. 9.2.1 where also all other simulation parameters are given. Solitons have formed at high density such that the scales k_{n_s} and k_ξ are close together, as indicated in the graph. Solid line: fit of the analytical model spectrum Eq. (9.17), with $n_{s,0} = 0.076$, $\gamma = 1$, $\sigma^{-1} = 0.036$ where Gaussian of width σ was used to describe the bulk distribution in position space. A Rayleigh-Jeans tail is absent as the cooling is still on. Due to the proximity of k_{n_s} and k_ξ no k^{-2} power law is seen in between the low-energy plateau and the high-energy exponential fall-off.

which indicate the variance over 200 runs, the data is rather fitted by an exponential dependence $N_s(t_c) = f_0 \exp\{-\gamma t_c\}$ than by a power law $N_s(t_c) = g_0/t_c$ as predicted in Ref. [158]. We emphasise however that in our system, solitons mainly form during the initial stage following the interaction quench.

9.2.3 Time evolution of single-particle spectra

We finally discuss the relaxation dynamics with respect to the evolution of the respective single-particle momentum spectra. The initial state chosen in the simulations is given by a thermal canonical ensemble of distributions over the single-particle eigenstates of the trap. In Fig. 9.8 we show the momentum spectrum at time $t = 5 \cdot 10^3$.

Solitons have formed at high density such that the scales $k_{n_s} \simeq 0.15$ and $k_\xi \simeq 0.2$ are close together, as indicated in the graph. The solid line represents a fit of the analytical model spectrum Eq. (9.9). A Rayleigh-Jeans tail is absent as the cooling is still on. Due to the proximity of k_{n_s} and k_ξ no k^{-2} power law is seen in between the low-energy plateau and the high-energy exponential fall-off.

In Fig. 9.9 we showed the spectrum for a wider trap with $l_{ho} = 17$ which allows the solitons to be diluted more across the trap and results in $k_{n_s} \simeq 0.15$ and $k_\xi \simeq 0.65$. This allows for a k^{-2} scaling to appear clearly, indicating a self-similar random distribution of the solitons. For $t > t_c$, the gas enters the final stage: The number

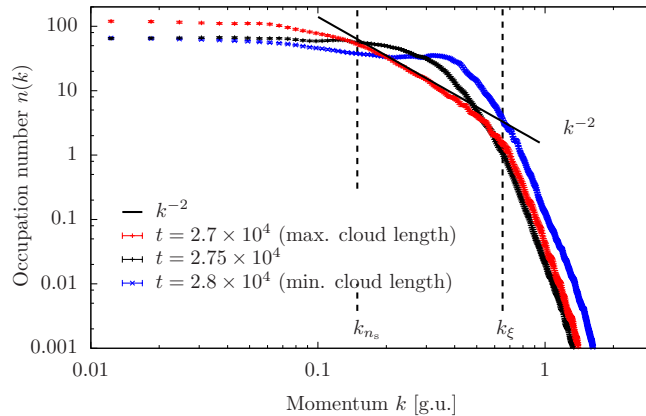


Figure 9.9: Momentum spectrum $n(k, t)$ at different times t as indicated, with statistical errors (ensemble averages over 1000 runs). Momentum scales defined by the inverse healing length, k_{ξ} , as well as by the density of solitons, k_{n_s} , are marked by dashed lines. A power-law dependence $\sim k^{-2}$ is indicated by the black solid line. Here, a larger trap oscillator length was chosen, $l_{\text{ho}} = 17$, such that around the outer turning point of the breathing oscillation the solitons become diluted and thus the scales k_{n_s} and k_{ξ} sufficiently far away from each other to allow for a k^{-2} power law to be seen in between (red points). Momentum k and time t are measured in grid units as defined in Sect. 9.2 where also all other simulation parameters are given.

of particles and the energy are now conserved and the healing length is ‘frozen out’. Fig. 9.10 shows the development of $n(k, t)$ from $t \gtrsim t_c$ to late times. Once the cooling and thus the removal of particles with high energy is terminated, a transport process from low to high momenta starts and thermalisation takes place. There are still solitons in the gas for the times displayed in Fig. 9.10 which contribute with their spectral profile to the total spectrum and broaden the plateau at low momenta up to $k_{\xi} \simeq 0.1$.

9.3 Summary

We have studied the formation of dark solitary waves in one-dimensional Bose-Einstein condensates as well as their relaxation dynamics towards equilibrium. The corresponding single-particle momentum spectra were predicted in the framework of a static model of well-separated grey solitons. For comparison with these predictions, semi-classical simulations of the relaxation dynamics of one-dimensional Bose gases after an initial interaction quench and a cooling period were used to determine the respective spectra numerically. The so found spectra compared well with the analytical predictions, giving insight into the many-body dynamics from the point of view of statistics of (quasi-) topological defects.

In Sect. 9.1, we have discussed the power-law behaviour of the momentum spectra, which appears in a range between the inverse of the inter-soliton distance and

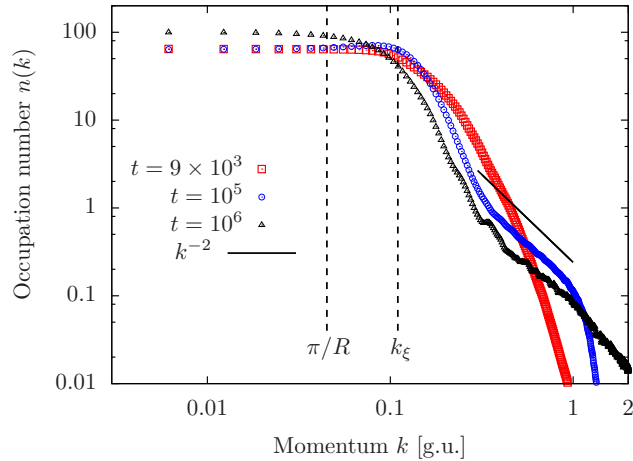


Figure 9.10: The spectrum $n(k)$ is shown for three different times from $t \approx t_c = 9 \times 10^3$ to $t = 10^6$, for an ensemble of 5×10^3 (10^3 for $t = 10^6$) realisations. k and t are in grid units as defined in Sect. 9.2.1 where also all other simulation parameters are given. Momentum scales defined by the inverse Thomas-Fermi radius R as well as by the healing length ξ are marked by dashed lines. A power-law dependence $\sim k^{-2}$ of the thermal tail is indicated by the black solid line.

the inverse healing length. Qualitatively, the result is the same as found for vortex statistics in $d = 2, 3$ dimensions, see Chap. 4. However, with regard to the universal scaling laws predicted in non-perturbative field-theory approaches to strong wave turbulence, the observed power-law exponent $\zeta = 2$ differs by 1 from the exponent $\zeta = 3$ predicted for an inverse particle cascade in $d = 1$ spatial dimensions. In Sect. 9.1.2, we traced this discrepancy back to the different flow patterns possible in $d > 1$ versus $d = 1$ dimensions. To recover this discrepancy within a field-theory approach to strong wave turbulence is an important topic for future research.

We point out that the single-particle momentum spectra discussed here could be used in experiment to study solitary-wave dynamics in one-dimensional Bose gases without the necessity to detect solitons in-situ. Studying in this way universal properties during the relaxation dynamics from a non-equilibrium initial state or under a constant driving force opens a new access to strong wave turbulence and non-thermal fixed points.

From cosmological inflation to table-top experiments

The purpose of this chapter, is to highlight our recent studies on non-thermal fixed points and superfluid turbulence in the context of reheating after cosmological inflation and quenched two-component Bose gases. Finally, the chapter ends with an overview of experimental prospects for experimental studies on non-thermal fixed points with ultracold alkali atoms.

10.1 Charge separation in reheating after inflation

In cosmological models of the universe, reheating describes the epoch starting at the end of inflation [354]. During this epoch the potential energy of the inflaton field is redistributed into a homogeneous and isotropic hot plasma of particle excitations. These become a substantial part of the further expanding universe. Simple models describing reheating after inflation invoke self-interacting scalar fields. One of the popular scenarios involves the parametrically resonant amplification of quantum fluctuations of the macroscopically oscillating inflaton field. The amplified modes represent the emerging matter content of the universe [355, 356]. Various theoretical approaches have been proposed to model reheating. As both, the inflaton and the amplified modes are strongly populated, classical field simulations can be applied to describe their evolution [357–359]. Alternatively, Kadanoff-Baym dynamic equations, as derived from 2PI effective actions in non-perturbative approximation, can describe the resonant excitation and the ensuing thermalisation [250]. The exponentially fast excitation process is followed by a slower equilibration, possibly with transient turbulent behaviour transporting the energy deposited in the low-momentum modes of the system to higher momenta. Previously, classical field simulations and scaling solutions of kinetic equations were used to analyse possible turbulent evolution during reheating and thermalisation [52, 64].

As we have discussed in Sect. 2.3, recent analytical predictions of new non-thermal fixed points of the field dynamics provided an extension of the above turbulence

scenarios into the regime beyond perturbative quantum-Boltzmann approximations [29, 53]. Their relevance for the non-equilibrium dynamics of ultracold matter fields has been explored in detail in this thesis. For relativistic fields, the scaling predictions [28] have been confirmed by numerical simulations [28, 30] for the case of $O(4)$ -symmetric scalar fields in $d = 3, 4$ dimensions. Here, we demonstrate that, in some cases, these non-thermal fixed points are characterised by metastable configurations of the underlying inflaton field with a soliton-like charge distribution.

We study parametric resonance in a globally $O(2)$ or, equivalently, $U(1)$ symmetric relativistic scalar field theory in $d = 2, 3$ dimensions. Shortly after the resonant excitations have set in we find spatial separation of charges. Both, charge and anti-charge overdensities become uniformly distributed within slowly varying regions which are separated by sharp boundary walls of grossly invariant thickness. These walls have a character similar to topological defects and appear for generic initial conditions. We observe that the presence of charge domains coincides with the visibility of the non-thermal stationary scaling solutions. In this way a link is established between wave turbulence phenomena as discussed, e.g., in [28–30, 52, 53, 58, 64] and long-lived quasi-topological structures in the inflaton field.

10.1.1 The model

The action of the model considered here is given by

$$S = \int d^d x dt \left\{ \frac{1}{2} [(\partial_t \varphi)^2 - (\partial_i \varphi)^2 - m^2 \varphi^2] - \frac{\lambda}{4!N} (\varphi^2)^2 \right\} \quad (10.1)$$

where $\varphi^2 \equiv \varphi_a(x)\varphi_a(x)$, $(\partial_i \varphi)^2 \equiv \partial_i \varphi_a(x)\partial_i \varphi_a(x)$, sums over $i = 1, \dots, d$ and $a = 1, \dots, N$, $N = 2$, implied. To describe the dynamics of the scalar field φ in the rapidly expanding universe one works in conformal coordinates in which the metric is defined through $ds^2 = a(t)^2(dt^2 - dx^2)$, with a scale parameter $a(t)$ depending on the conformal time t . We choose the bare mass scale to vanish, $m^2 = 0$, such that the equation of motion for the rescaled field $\varphi' = a\varphi$ reads (in $d = 3$):

$$\left[\partial_t^2 - \Delta + \frac{\lambda}{6N} \varphi'^2 - \frac{\ddot{a}}{a} \right] \varphi'_a = 0 \quad (10.2)$$

During the parametric reheating epoch the universe is close to being radiation dominated [357], such that the scale dependent term can be neglected, $\ddot{a} = 0$. Hence, the equation of motion for the rescaled field $\Phi = \varphi'/\varphi'_0$, with $\varphi'_0 = \varphi'(t = 0)$ the initial value of the inflaton field, can be approximated as

$$[\partial_t^2 - \Delta + \Phi^2] \Phi_a = 0 \quad (10.3)$$

where the coupling has been absorbed by the rescaling $\sqrt{\lambda/6N}\varphi'_0 x \rightarrow x$ and $\sqrt{\lambda/6N}\varphi'_0 t \rightarrow t$. Due to the global $O(2)$ symmetry of the action the charge-current

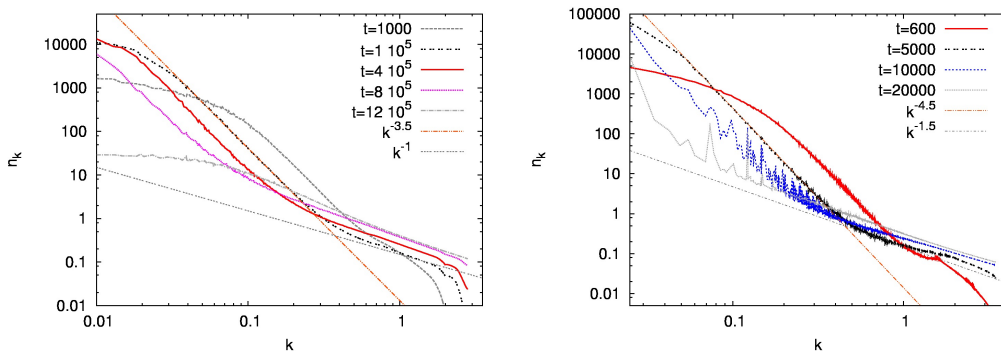


Figure 10.1: Occupation-number spectrum Eq. (10.5) of the system in $d = 2$ (left panel) and $d = 3$ (right) spatial dimensions at different times t (in lattice units). Averages were taken over 69 (84) runs on a 960^2 (256^3) grid. The double-log scale exhibits the bimodal power-law $n(k, t) \sim k^{-\kappa}$. For $d = 2$ we find $\kappa \simeq d + 1.5$ in the infrared, and thermal scaling, $\kappa \simeq 1$, for large k . For $d = 3$ we also observe, at late times and intermediate momenta, the UV weak wave turbulence exponent $\kappa \simeq 1.5$. Note that the physical particle number spectrum is $6Nn(k, t)/\lambda$. See the main text for further details.

density

$$j_\mu(x) = \Phi_1(x)\partial_\mu\Phi_2(x) - \Phi_2(x)\partial_\mu\Phi_1(x). \quad (10.4)$$

is conserved, $\partial^\mu j_\mu = 0$.

To induce parametrically resonant reheating, we start our simulation from a configuration where only the zero mode of the inflaton field is populated. Fluctuating non-zero momentum modes act as seeds for the ensuing instabilities. Choosing $m^2 = 0$ and $\lambda > 0$, which corresponds to an equilibrium configuration in the symmetric phase, subsequent oscillation of the inflaton field induces parametrically resonant exponential growth of certain modes. Scattering between these modes causes the entire spectrum to fill up. Our simulations of Eq. (10.3) were performed on a cubic space-time lattice of L^d gridpoints using periodical boundary conditions in $d = 2$ and 3 spatial dimensions.

10.1.2 Scaling of the momentum distribution

The time evolution of the system after the instabilities have set in was found to be best described by a turbulent stage followed by thermalisation on the largest time scales. The turbulent phases feature universal scaling of the (solid-)angle-averaged momentum-space occupation numbers

$$n(k, t) = \frac{1}{4L^d} \int d^{d-1}\Omega_{\mathbf{k}} \sqrt{\langle |\partial_t \Phi(\mathbf{k}, t)|^2 \rangle \langle |\Phi(\mathbf{k}, t)|^2 \rangle}. \quad (10.5)$$

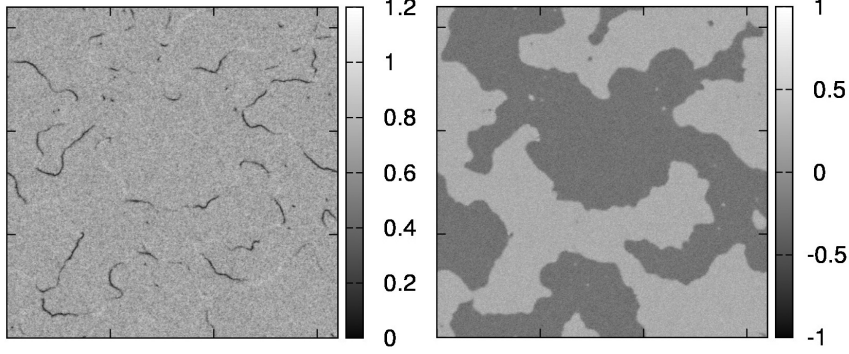


Figure 10.2: Charge separation at lattice time $t = 9 \times 10^3$ in $d = 2$ dimensions on a 960^2 lattice. Left: Modulus $|\Phi(\mathbf{x}, t)| = [\Phi_1^2(\mathbf{x}, t) + \Phi_2^2(\mathbf{x}, t)]^{1/2}$. “Defect” lines with substantially reduced $\rho = j_0$ (cf. Eq. (10.4)), contrast with a fairly constant bulk $\rho_{\text{bulk}} \simeq 0.7$. Right: Charge density $\rho(\mathbf{x}, t) = j_0(\mathbf{x}, t)$ (cf. Eq. (10.4)). Note the evenly distributed charge overdensities with opposite sign, separated by lines which include the “defect” lines shown on the left.

By means of analytical studies based on quantum Boltzmann equations [41], one expects to find weak wave turbulence during these phases. One finds the possible exponents [28, 29, 41]

$$\kappa_P = d + \frac{3}{2}(z - 2), \quad \kappa_Q = d + z - 3. \quad (10.6)$$

for constant radial flow of energy $P(k) \equiv P$, or constant radial flow of (quasi-)particle number, $Q(k) \equiv Q$. Here, z is the homogeneity index of the dispersion $\omega(s\mathbf{k}) = s^z \omega(\mathbf{k})$ of mode \mathbf{k} . Note that in thermal equilibrium one expects $\kappa_{th} = z$, corresponding to the Rayleigh-Jeans law. In the non-perturbative IR-regime, new scaling exponents similar to the ones found for non-relativistic scalars [29] have been proposed [28]:

$$\kappa_P^{\text{IR}} = d + 2z, \quad \kappa_Q^{\text{IR}} = d + z \quad (10.7)$$

As was first brought forward in [28] for the case of an $O(4)$ model, numerical simulations of parametric resonance confirm both, the IR and the UV scaling exponents. Corresponding results for the model studied here are shown in Fig. 10.1 for $d = 2$ and $d = 3$ at different instances of time t .

As was shown in [41], for our model Eq. (10.1), in wave turbulence, either energy flows with rate P towards larger k or quasi-particles flow with rate Q towards lower k . In our simulations, the resonantly induced momentum distribution is observed to act, during the further evolution, as a source at intermediate momenta, $k \simeq 0.1..0.3$, see Fig. 10.1. Our model implies $z = 1$ such that we expect from Eq. (10.7), in the infrared, the exponent $\kappa_Q^{\text{IR}} = d + 1$, assuming a constant quasi-particle number flow towards the IR. We note that in contrast to cases with smaller $1/N$ discussed in [28, 30] we find, in the IR, $\kappa \simeq 3.5$ ($d = 2$) and 4.5 ($d = 3$). In the UV, assuming a constant flow P from intermediate to larger momenta one expects, from

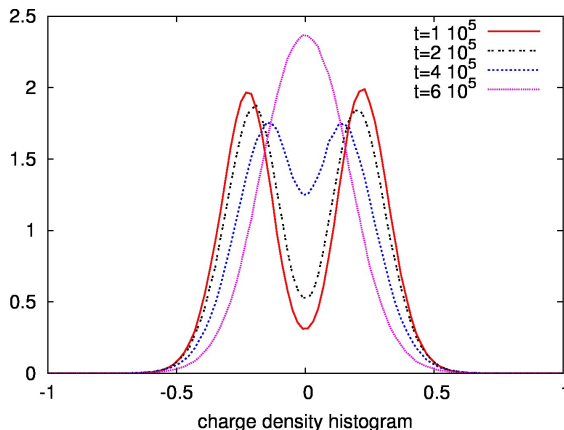


Figure 10.3: Histogram of the charge density distribution of the system in $d = 2$, at points of time for which Fig. 10.1 shows the corresponding spectra. We find that a clear charge separation goes together with the strong IR scaling with $\kappa = 3.5$.

Eq. (10.6), $\kappa_P^{\text{UV}} = d - 3/2$. Numerically we find that in the UV the occupation number distribution approaches, at large times, thermal scaling $\kappa_{th} = 1$. For $d = 3$ we also observe, at late times and intermediate momenta, the expected UV weak wave turbulence exponent $\kappa \simeq 1.5$.

10.1.3 Charge separation

Having recovered scaling behaviour we present, in the following, our central result: Looking at the real-space structure of the emerging critical configuration we find patterns similar to topological defects giving rise to quasi-stationary charge separation. We find a correspondence between the appearance of the strong scaling exponent and of the defect-separated charge patterns. In Fig. 10.2 (left) we depict, for $d = 2$, a typical real-space configuration in the turbulent stage, plotting the modulus of the $O(2)$ scalar field, $|\Phi(\mathbf{x}, t)| = [\Phi_1^2(\mathbf{x}, t) + \Phi_2^2(\mathbf{x}, t)]^{1/2}$. Localised regions appear, specifically “defect” lines where the absolute value of the field is much smaller than its average. Fig. 10.2 (right) shows the corresponding charge density $\rho(\mathbf{x}, t) = j_0(\mathbf{x}, t)$, Eq. (10.4). Clearly, both uniform charge and anti-charge overdensities appear within distinctly separated regions, showing only small fluctuations as compared to their bulk values. This separation of charges is confirmed by the histogram of local charge densities shown in Fig. 10.3.

Moreover, we see that the “defect” lines in Fig. 10.2 (left) are lying along the boundary limits between the regions of opposite charge. Note that only part of the boundaries is clearly visible as “defect” lines. Following the time evolution of the defect lines [360] we find that they appear and disappear with a period of $T/2 \simeq 6$ determined by the effective mass $m_{\text{eff}} = 2\pi/T$ of the mean field theory, at every point along the boundaries between the oppositely charged domains.

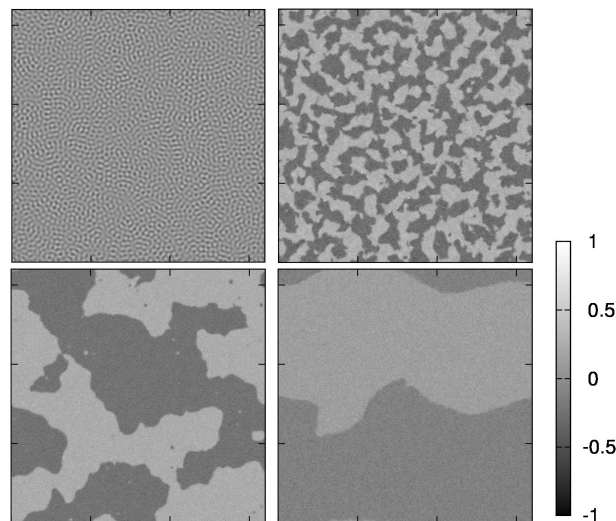


Figure 10.4: Charge density $\rho(\mathbf{x}, t) = j_0(\mathbf{x}, t)$ (cf. Eq. (10.4)) for the same run as shown in Fig. 10.2 at the times $t = 300$ (upper left), $t = 10^3$ (upper right), $t = 10^4$ (lower left), $t = 6 \times 10^4$ (lower right). The scale of the largest structures is found not to depend on the total lattice size.

The explanation for the appearance of these lines is as follows: The charge density ρ can be interpreted as field angular momentum in the $N = 2$ dimensional field space. Hence, d -dimensional configuration space can be divided into regions according to the sign of ρ . On the lines separating these regions the local field variable has neighbours of opposite charge which therefore possess opposite “circular polarisation” in field space. Thus, at a particular point on the boundary the rotations add to a linear oscillation of the field through zero, giving rise to spatially and temporally oscillating defect lines. While such an evolution could similarly occur in a free theory ($\lambda = 0$) interactions are responsible for rendering the transition between the opposite charges sharp as can be seen in Fig. 10.2 (left).

Following the evolution of the system starting from the homogeneous initial configuration we find the defect lines to appear once the instability has saturated. The lines can reconnect with each other while they propagate slowly through configuration space, such that the number of spatially connected charged regions changes in time. On the average, the total length of the defect lines as well as the number of connected regions is found to decrease with time, see Fig. 10.4. During the late stage of the evolution the separation of opposite charges gradually disappears while the system finally thermalises. This can also be seen in the histogram in Fig. 10.3 where the central well gradually disappears while the spectrum $n(k, t)$ approaches thermal equilibrium, see Fig. 10.1. We note that the sharp step between the opposite charges remains (Fig. 10.4, bottom right panel). This, as well as the histogram in Fig. 10.3 suggest that topological defects occur according to the homotopy group of the charge density space C instead of the order parameter space. Although C , for the $O(2)$ model, equals the real numbers, our results show, that the system remains,

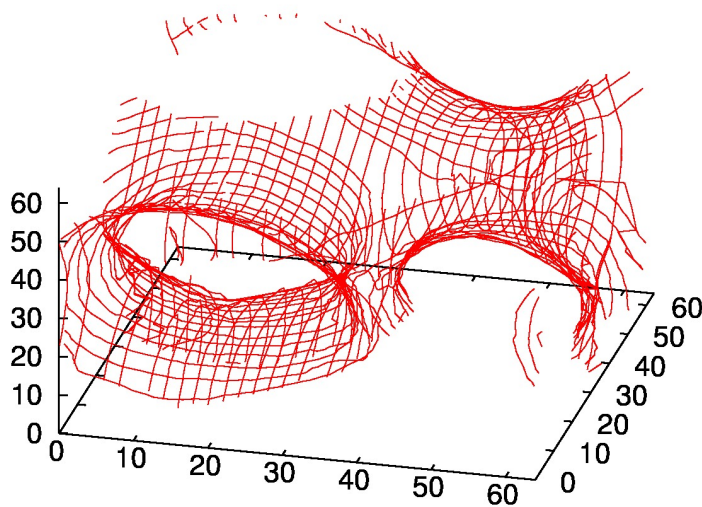


Figure 10.5: Bubbles of approximately constant and opposite charge separated by thin walls on a 64^3 lattice at $t = 1500$. Plotted are surface lines which are fitted to lattice points having $|\Phi|^2 < 0.05$.

for a long time, in a subspace which is topologically equivalent to $S_0 = \{-1, 1\} \in C$. Hence, one expects defect lines (walls) to separate regions corresponding to the two unconnected parts of C .

For $d = 3$, starting from an equivalent initial configuration, we find bubbles of opposite charge separated by thin walls (Fig. 10.5) [360] as well as charge density histograms similar to the case $d = 2$. These bubbles are seen to appear in coincidence with the strong IR scaling in the spectra (Fig. 10.1, right panel).

We emphasise that the structures found are distinctly different from the known topological defects appearing in $O(2)$ theories such as vortices in $d = 2$ and vortex strings in $d = 3$ which one obtains in the case of equilibrium symmetry breaking, i.e., $m^2 < 0$ [359]. The bubble walls reported here form for vanishing or positive mass squared.

To summarise, we have studied the non-equilibrium dynamics of an $O(2)$ -symmetric scalar field theory in two and three spatial dimensions. We have found structures similar to (quasi-) topological defects to emerge on intermediate time scales, breaking charge symmetry locally while the classical action implies an equilibrium configuration without symmetry breaking. These structures were found to appear in direct correspondence with strong wave-turbulent scaling behaviour of occupation numbers in the IR regime of low momenta. It is an interesting question for future studies whether similar structures exist in more complicated theories, such as gauge theories.

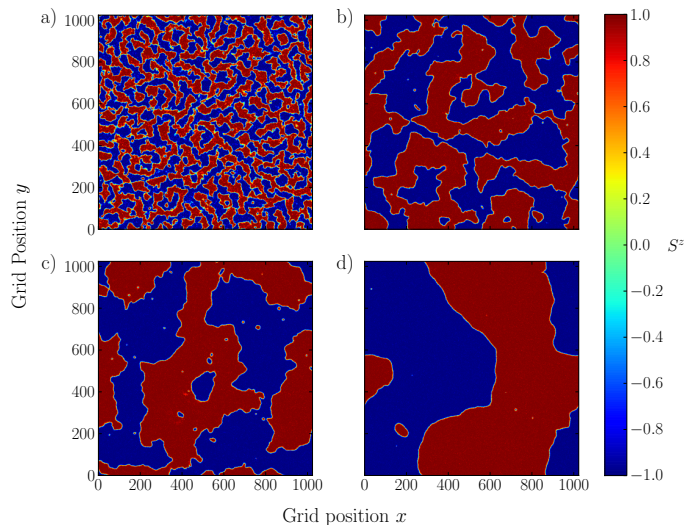


Figure 10.6: The figure shows the time evolution of the spin density $S^z(\mathbf{x})$ in the immiscible regime. Numerical parameters are $L = 1024$, $N_1 = N_2 = 3.2 \cdot 10^9$, $g = 3 \cdot 10^{-5}$ and $\alpha = 2$. The panels a) to d) correspond to snapshots of a single run at different grid times $t = 500, 5000, 10000, 100000$. Quickly after the start of the simulation domains of oppositely signed S^z emerge in a rather regular pattern. In the following evolution towards the equilibrium state these domains merge until the configuration of minimal energy in the spin system is reached, constrained by strict particle conservation in each component and the system ends up in a state with two large domains (see panel d).

10.2 Domain formation in a two-component Bose gas

In the last section we have presented evidence for a relation between turbulent scaling and domain formation in a relativistic scalar field. In the following we illustrate that similar phenomena occur in the non-relativistic regime. The results sketched in this section are unpublished and are the subject of a forthcoming publication [167].

In ultracold two-component Bose gases the existence of domain structures has been proposed [168, 169] and measured in experiments with different hyperfine species of optically trapped ultracold ^{87}Rb atoms [202, 361, 362]. Even control on the number of domains is within reach via a Kibble-Zurek scheme [6, 7, 363]. In addition, the two-component Bose gas can feature angular-momentum carrying vortices and skyrmions [364].

We consider the dynamics of two complex scalar fields $\phi_1(\mathbf{x}, t)$ and $\phi_2(\mathbf{x}, t)$ describing the bosonic gas, with self interactions $g_1 = g_2 \equiv g$ and inter-species coupling g_{12} . For the beginning it is instructive to concentrate on the degrees of freedom which describe the relative evolution of the two components. Writing the fields in the polar representation $\phi_i = \sqrt{\rho_i} \exp(i\varphi_i)$ these are given by the local phase difference

$\theta_r = \varphi_1 - \varphi_2$ and by the local density difference $\rho_1 - \rho_2$. With the Pauli matrices σ_a a meaningful mapping from the original two-component complex field to the relative degrees of freedom can be defined by $S^a = \phi_j \sigma_{ij}^a \phi_i$ (sum over repeated indices implied) [364]. This results in a three-component vector of (pseudo-)spin densities S^a for $a \in \{x, y, z\}$

$$S^x = 2\sqrt{\rho_1 \rho_2} \cos(\theta_r), \quad (10.8a)$$

$$S^y = -2\sqrt{\rho_1 \rho_2} \sin(\theta_r), \quad (10.8b)$$

$$S^z = \rho_1 - \rho_2, \quad (10.8c)$$

where the modulus corresponds to the total density $|\mathbf{S}| = \rho_1 + \rho_2 \equiv \rho_T$. For convenience, we apply the redefinition $S^a \rightarrow \rho_T S^a$ such that $|\mathbf{S}| \equiv 1$.

The two-component Bose gas is well known to possess two different ground states depending on the choice for the parameter $\alpha = g/g_{12}$ [168–170]. For the case $\alpha > 1$, which is called the immiscible regime, the inter-species interaction energy overcomes the intra-species interaction and thus for energetic reasons the preferable ground state of the system has to minimise the spatial overlap of the components. Thus configurations with $S^z = \pm 1$ are preferred which leads not only to spin polarised ground states but also to the formation of domains with oppositely signed S^z due to a discrete symmetry $S^z \rightarrow -S^z$ in the energy functional. In the miscible regime, i.e. $\alpha \leq 1$, a spatial overlap of both densities is energetically favourable. Hence, in the zero temperature ground state both densities are constant with their individual mean particle density and $S^z = 0$. Note that in both regimes the dynamic evolution is constrained by exact particle conservation in each component.

10.2.1 Dynamics in the immiscible regime

For the simulations in the immiscible regime we choose the parameter $\alpha = 2$ and initial configurations which are unpolarised $S^z(\mathbf{x}, t = 0) \equiv 0$ up to quantum noise. Initial configurations of such type are far from the zero temperature ground state and therefore lead to instabilities that drive the system dynamically towards spatial demixing [168–170]. We observe that the demixing process occurs on a very fast timescale and the main part of the long-time evolution is dominated by merging of domains, see Fig. 10.6. During this process, we monitor the single-particle momentum distribution. The results are presented in Fig. 10.7. Here, we observe that already at an early stage of the evolution a scaling distribution in the IR has developed. The scaling behaviour terminates in the IR at a scale π/L_D given by the mean domain size L_D , while the cut-off in the UV at π/ξ_s is set by the width of the domain walls, i.e. the spin healing length $\xi_s = \xi(2/|1 - \alpha|)^{\frac{1}{2}}$. In between a scaling region with an exponent of $\zeta \simeq 3.5$ is visible. Consistent with domain growth the IR cut-off of the scaling regime moves towards lower momenta with time whereas in the UV thermalisation of the distribution sets in, signalled by the appearance of a new scaling exponent $\zeta = 2$. During the whole time evolution the IR scaling exponent stays at $\zeta \simeq 3.5$, in contrast to the prediction for a non-relativistic scalar

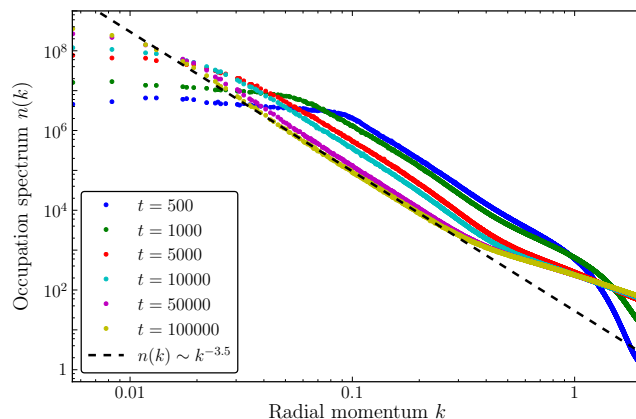


Figure 10.7: The figure shows the single particle momentum distribution at different grid times. Numerical parameters correspond to Fig. 10.6 and the spectra are averaged over 100 runs. After the onset of domain formation a scaling region $n \sim k^{-3.5}$ forms at intermediate momenta. At a time $t = 5000$ this region begins to move towards the IR while a new scaling region with $n \sim k^{-2}$ develops in the UV. The latter signals the onset of thermalisation of the UV modes. At late times a stable bimodal power law behaviour has formed with a scaling exponent $\zeta = 2$ in the UV and a IR scaling exponent $\zeta \simeq 3.5$.

field theory in $d = 2$ dimensions $\zeta^{IR} = 4$. This discrepancy can be resolved by decomposing the momentum distribution into compressible-, incompressible- and spin excitations. It turns out that the exponent $\zeta \simeq 3.5$ is caused by a superposition of two scalings, an incompressible component with exponent $\zeta \simeq 4$ originating from vortex-like topological objects called skyrmions and anti-skyrmions [364] and a spin-domain component with exponent $\zeta \simeq 3$ [167]. This hints at the possibility that a similar effect accounts for the observed discrepancy in the relativistic case between the numerically determined exponent 3.5, see Fig. 10.1, and the field theoretic prediction, Eq. (10.7).

10.2.2 Outlook into the miscible regime

To gain a complete picture of possible non-thermal fixed points in a two-component Bose gas in two dimensions, we have further carried out dynamical simulations in the miscible regime ($\alpha \leq 1$). Here, the system is driven out of equilibrium by making use of the counter-superflow instability [365, 366]. Deep in the miscible regime ($\alpha < 1$), we recover $\zeta \simeq 4$ scaling behaviour at late times, which is caused by vortices [167]. On the contrary, at the transition point $\alpha = 1$, the life time of domain like density fluctuations seems strongly enhanced. We expect this effect to be connected to additional conservation laws arising from the spin symmetry [67]. The associated scaling exponent $\zeta \simeq d+1 = 3$ can be dominant beyond experimental time scales. Note that this state bears similarities with soliton turbulence in one dimension, where $\zeta = d + 1 = 2$ is also observed, see Chap. 9.

A similar phenomenon might also occur in the two-component Bose gas in one dimension, where the counter-superflow instability was previously shown to produce so called dark-bright solitons in the miscible regime [367]. A variety of (quasi-) topological features is also known to exist in trapped spinor Bose gases [368–370], allowing for turbulence in spin as well as fluid degrees of freedom [175, 371, 372].

10.3 Experimental prospects

The concept of a non-thermal fixed point has strong interdisciplinary aspects. Besides ultracold atoms, it has for example been extensively studied in models for reheating of the early-universe [28, 30, 52, 53, 55, 64] and heavy-ion collisions. In the latter, the non-equilibrium regime of a quark-gluon plasma is predicted to develop quasi-stationary scaling behaviour [56–59, 373]. However, the prospects for a direct experimental observation of the non-thermal fixed point in these systems are very limited. Therefore, experiments with trapped ultracold atoms are in a unique position. Various groups across the world have the potential to create and identify essential non-equilibrium dynamics. As examples, we briefly introduce the setups by the groups in Vienna, Austria (1D) [150, 178, 179], Heidelberg, Germany (1D) [7, 151, 374], Tucson, USA (2D) [89, 90, 138] and Sao Carlos, Brazil (3D) [109, 111].

Experiments at the Technische Universität Wien take place on an atom chip with a highly anisotropic trapping potential [178, 179]. Non-equilibrium states can for example be created by rapid evaporative cooling of the transversal degrees of freedom. A typical set-up has trap frequencies $\omega_T \simeq 3300\text{Hz}$ for the transversal confinement and $\omega_L \simeq 23\text{Hz}$ ($l_L \simeq 10\mu\text{m}$) in the longitudinal direction. The initial sample might contain $N \simeq 10^5$ ^{87}Rb atoms at temperature $T \simeq 10^3\text{nK}$ which is above the critical temperature of a quasi one-dimensional condensate. The healing length is estimated as $0.3\mu\text{m}$. The dynamics of the momentum distribution after the quench can be investigated by time-of-flight imaging with an expansion time of $\tau \simeq 46\text{ms}$ performed after different hold times τ_{hold} . On the other hand, the in-situ imaging of the cloud is difficult due to the coarse resolution scale of $\simeq 4\mu\text{m}$.

This problem is less significant in the Heidelberg experiment, which has a spatial resolution of $\simeq 1\mu\text{m}$ [7, 151, 374]. Atoms are trapped in a one-dimensional wave guide with $\omega_T \simeq 10^3\text{Hz}$ generated by a red-detuned laser beam. The longitudinal confinement is $\omega_L \simeq 10^2\text{Hz}$ ($l_L \simeq 5\mu\text{m}$). The set-up has been shown to reliably create solitonic states from the interference of two ^{87}Rb condensates [151, 374]. Furthermore, it offers the possibility to study dynamics across the miscible-immiscible transition of a two-component Bose gas of $N \simeq 10^4$ atoms by addressing the hyperfine states $|1\rangle = |F = 1, m_F = 1\rangle$ and $|2\rangle = |F = 2, m_F = -1\rangle$. The inter- and intraspecies scattering lengths are $(a_{11}, a_{22}, a_{12}) = (95.0, 100.4, 97.7)$ in units of the Bohr radius. Using a Feshbach resonance can change a_{12} by $\sim 10\%$ into both directions. In principle, these techniques can readily be extended to two-dimensional geometries. In this context it would be especially interesting to explore the possibil-

ity of relative phase measurements between the two species in order to investigate the dynamics and correlations of vortices.

An experiment that studies two-dimensional superfluid turbulence is currently operating in Tucson [89, 90, 138]. $N \sim 10^6$ atoms are confined in a harmonic trap with $\omega_T \simeq 500\text{Hz}$ and $\omega_L \simeq 50\text{Hz}$ ($l_L \simeq 8\mu\text{m}$). The turbulence is created by rapid evaporative cooling [138], or circular stirring with a blue-detuned (repulsive) laser that irradiates the clouds from above [90].

Similar stirring techniques are used by the group in São Carlos to create turbulence in three dimensions [109, 111]. Here, a cigar-shaped ($\omega_T \simeq 10^3\text{Hz}$, $\omega_L \simeq 10^2\text{Hz}$) Bose-Einstein condensate of $N \simeq 10^5$ atoms is excited by rotating the confining magnetic field coils, leading to a superposition of rotations around the longitudinal and transversal axis.

We remark that the creation of non-equilibrium states is much easier than their observation and characterisation. For example, in three dimensions vortices can not be easily observed since absorption-imaging does not allow to unambiguously identify vortices which are not aligned along the imaging axis. Measuring the momentum distribution by time-of-flight imaging is corrupted by interactions between atoms. This effect becomes less dramatic in lower dimensions where the rapid transversal expansion quickly dilutes the gas and reduces interactions. It becomes clear that the development of new imaging techniques of non-equilibrium states is essential for the prospects of future experimental studies with cold atoms.

Finally, we would like to remark that the phenomena discussed in this thesis might also be present in experiments with superfluid helium [76, 82, 103, 104, 375]. Superfluid helium which is created in macroscopic containers (length $L \sim 1\text{cm}$) can be stirred and develops large numbers of interacting vortices. However, an accurate theoretical description of helium is beyond the scope of this thesis. More suitable might be the application of our analysis to bosonic excitations in solid-state devices, for example in magnon- or polariton condensates [141, 142, 145, 146].

Summary and outlook

In this thesis, we studied the non-equilibrium dynamics of ultracold quantum gases numerically and analytically in one, two, and three spatial dimensions. We focused on the regime of high occupation numbers, where the system can be described by an ensemble of non-linear waves. A goal of this work was to investigate the existence of non-thermal fixed points in the dynamics of ultracold Bose gases.

It was shown in Chaps. 3, 4, and 5 that a two- or three-dimensional Bose gas features a non-thermal fixed point which is characterised by a state of a dilute random distribution of vortices or vortex lines. This state is accompanied by particle and energy fluxes and decays via the formation of vortex-antivortex correlations. The evolution from a non-equilibrium initial state towards a non-thermal fixed point was first presented in Chap. 3. In Chap. 4 quasi-stationary scaling properties of the momentum distribution were explained from a model of uncorrelated point/line vortices. We derived further scaling exponents by taking vortex-antivortex correlations into account and discussed Onsager's picture of equilibrium configurations. In Chap. 5, a detailed analysis of the momentum distribution and flux spectra was given. We investigated signatures of vortex correlations in the momentum distribution. We also paid attention to non-thermal scaling in the compressible energy which was shown to survive beyond the lifetime of the vortex bearing phase. Finally, we discussed the power-law tail in the velocity probability distribution of a vortex-dominated flow.

We gave a detailed analysis of the vortex dynamics near the non-thermal fixed point in Chap. 6. According to our analysis the approach of the non-thermal fixed point is related to characteristic behaviour in the vortex density decay. The observations were compared to results from a kinetic theory of vortex scattering. Moreover, we showed that the inverse particle cascade is associated with a decay of vortex density and an increase of mean vortex-antivortex distance. This was followed by a comparison between the non-equilibrium trajectory and equilibrium states of the ultracold Bose gas in two dimensions. In Chap. 7, we reported on analogous studies for the case of an ultracold Bose gas in three dimensions. A similar picture compared to $d = 2$ arose, evident in a slowing-down of vortex density decay and

increase of mean vortex ring radius near the non-thermal fixed point.

Furthermore, we focused on the relevance of the non-thermal fixed point for the dynamics of phase ordering, discussed in Chaps. 6, 7 and 8. The main finding of Chap. 8 concerns the role of superfluid turbulence during Bose-Einstein condensation starting from an initial state above the critical temperature. For a strong cooling quench, random phase fluctuations evolve into coherent vortical flow observable in characteristic power-law dependence of the momentum distribution and associated to the non-thermal fixed point. This stage is transient and decays towards a homogeneous Bose-Einstein condensate. We found a characteristic power-law growth of the condensate fraction during this process.

Then, we investigated the possibility of a non-thermal fixed point in a one-dimensional ultracold Bose gas realised by a dilute gas of solitons, see Chap. 9. A model of random solitons was applied to a homogeneous as well as a trapped Bose gas and compared with numerical simulations for a quenched system subject to a cooling mechanism.

We also discussed the presence of a non-thermal fixed point in a relativistic scalar field theory in the form of transient charge separation in Chap. 10. This led to the investigation of the non-equilibrium dynamics of an ultracold two-component Bose gas in the miscible and immiscible regime. We presented evidence for the dynamical approach of various non-thermal scaling solutions and pointed out their microscopic origin. Finally, we briefly discussed different experimental set-ups to study non-equilibrium quantum gases and motivated that a verification of our results is readily feasible.

In order to emphasise the importance of our results, we would like to point out the possibility of a universal duality between decaying topological defects and a non-perturbative wave-turbulence inverse cascade. This requires the generation of (quasi-) topological configurations far from thermal equilibrium and their slow decay for an increase of coherence and defect separation. Under these conditions, we expect power-law scaling in between scales $1/\xi$, with ξ the microscopic extend of the defect core, and $1/l_{\text{COH}}$, with l_{COH} being the coherence length approximated by the mean distance between defects. In this setting, an inverse particle cascade is generated by defect dilution and the associated power-laws can be found from the scaling properties of the respective single defect. We have shown this mechanism to exist in soliton- and vortex dominated single-component Bose gases [31, 32, 51, 140], decaying domain walls and vortices in two-component Bose gases [167] as well as transient charge domains in complex relativistic scalar theory [55]. We want to emphasise that the stability of these defects does not need to be topological, as our examples of solitons, see Chap. 9, and charge domains, see Chap. 10, indicate. See e.g. Ref. [67] for a review of non-topological solitons.

A variety of (quasi-) topological excitations are known to exist in superconductors, magnets, and cosmic fields [67–70]. Specific examples are monopoles in gauge fields [376, 377] and exotic magnets [378] as well as skyrmions in Bose-Einstein con-

(Quasi-) topological defect	Field	d	Momentum scaling
Soliton/Domain	$\phi \in \mathbb{C}, S_z \in \mathbb{R}$	1	$\langle \phi(k) ^2 \rangle, \langle S_z(k) ^2 \rangle \sim k^{-2}$
Soliton line/Domain	$\phi \in \mathbb{C}, S_z \in \mathbb{R}$	2	$\langle \phi(k) ^2 \rangle, \langle S_z(k) ^2 \rangle \sim k^{-3}$
Soliton surface/Domain	$\phi \in \mathbb{C}, S_z \in \mathbb{R}$	3	$\langle \phi(k) ^2 \rangle, \langle S_z(k) ^2 \rangle \sim k^{-4}$
Vortex	$\phi \in \mathbb{C}$	2	$\langle \phi(k) ^2 \rangle \sim k^{-4}$
Vortex line	$\phi \in \mathbb{C}$	3	$\langle \phi(k) ^2 \rangle \sim k^{-5}$
Skyrmion	$\mathbf{S} \in \mathbb{R}^3$	2	$\langle S_{x(y)}(k) ^2 \rangle \sim k^{-2}$
Skyrmion line	$\mathbf{S} \in \mathbb{R}^3$	3	$\langle S_{x(y)}(k) ^2 \rangle \sim k^{-3}$
Monopole	$\mathbf{B} \in \mathbb{R}^2$	2	$\langle B(k) ^2 \rangle \sim k^{-2}$
Monopole	$\mathbf{B} \in \mathbb{R}^3$	3	$\langle B(k) ^2 \rangle \sim k^{-2}$

Table 11.1: Angle-averaged field as a function of radial momentum k in d spatial dimensions. The scaling behaviour is calculated from the Fourier transform of a single defect configuration and valid for $k < 1/\xi$, with ξ describing the size of the defect core.

densates [364, 379] and liquid crystals [380]. A list of expected scaling properties is given in Table 11.1.

We expect that the phase ordering process can be formulated and understood from the analysis of non-perturbative dynamic equations for correlation functions. This includes scaling of momentum spectra, fluxes, and higher order correlation functions. To describe the defect-induced scaling solutions as renormalisation group fixed points and, thereby, to establish a new notion of criticality out-of-equilibrium, is an exciting topic for future work.

The study of multi-component fields is certainly among the most interesting new directions of research. We have taken a first step in this direction by investigating the two-component Bose gas [167]. The possibility of different non-thermal fixed points depending on inter- and intraspecies couplings opens a path towards out-of-equilibrium control [7, 168–170]. Relating (quasi-) topological field configurations known from ground state analysis of spinor Bose gases [370] to transient scaling phenomena observed in correlation functions provides a great challenge for experiments and theory. Fortunately, experimental studies of ultracold spin-1 and spin-2 Bose gases, including the detection of spin domains, are highly developed [133, 171, 172, 174, 175, 177] and supported by theoretical work [173, 176]. Multi-component fields are important far beyond ultracold atomic physics. For example, multi-component inflatons and their associated topological defects are discussed in early-universe expansion scenarios [249, 354, 381]. Especially exciting are recent developments in the field of heavy-ion collisions, where the non-equilibrium regime of a quark-gluon plasma can be investigated by multi-component gauge field simulations [56–61]. The possibility for defect-induced non-thermal fixed points in

this system has yet to be explored. The rapid expansion of the quark-gluon plasma adds a completely new aspect to the dynamical description. Similar processes can be studied by releasing ultracold gases from their trapping potential. Specifically, we are interested in the behaviour of expanding turbulent clouds [109, 111, 382, 383].

Ultimately, non-thermal fixed points have to be included into a global picture of non-equilibrium dynamics of interacting many-body systems [1, 2]. The concept points out a way towards universal phenomena far away from equilibrium. To understand its relations to non-thermal equilibrium states [13–17], generalised Gibbs states [13–15], or prethermalised states [19–23] are essential steps towards a unifying framework of complex dynamical many-body systems.

A

Numerical techniques

A large part of this thesis consists of the analysis of results from numerical simulations in the framework of the classical field method introduced in 2.2. In the following, we give information on some of the numerical techniques.

A.1 Dimensionless quantities

Our numerical simulations are performed on space-time lattices with spatial side lengths $L = N_s a_s$, with lattice spacing a_s and in total N_s^d gridpoints in position space. We use periodic boundary conditions and $N_s \in \{1024\}$ for $d = 1$, $N_s \in \{256, 512, 1024\}$ for $d = 2$ and $N_s \in \{128, 256, 512\}$ for $d = 3$. Eq. (2.5) is written in terms of the dimensionless variables $\bar{g} = 2mga_s^{2-d}$, $\bar{t} = t/(2ma_s^2)$ and $\bar{\phi}_n(t) = \phi_n \sqrt{a_s^d} \exp(2i\bar{t})$. Where not otherwise stated, all quantities in the figures are either dimensionless or shown in lattice units, with the length unit given by a_s . In some places the length unit a_s has been converted into healing length $\xi = (2mng)^{-1/2}$, which is the natural length scale in experiments. The lattice momenta (units of a_s^{-1}) are $k = [\sum_{i=1}^d 4\sin^2(k_i/2)]^{1/2}$, $\mathbf{k} = 2\pi\mathbf{n}/N_s$, $\mathbf{n} = (n_1, \dots, n_d)$, $n_j = -N_s/2, \dots, N_s/2$. This is derived from the discrete Fourier transform of the kinetic term on the lattice

$$\sum_i \partial_{x_i}^2 \phi(\mathbf{x}) \equiv \sum_i \phi(\mathbf{x}_{\mathbf{n}+\Delta_i}) + \phi(\mathbf{x}_{\mathbf{n}-\Delta_i}) - 2\phi(\mathbf{x}_{\mathbf{n}}), \text{ with } \Delta_{i,l} = \delta_{il}. \quad (\text{A.1})$$

In order to relate our simulations to a typical situation in experiment, we give parameters for ^{78}Rb . We estimate the total energy of the gas in equilibrium to be given by the interaction energy which, by equipartition is related to the temperature, $2E_{\text{int}} = L^d g n^2 = N_s^d a_s^d g n^2 = N_s^d T$. At the transition to degeneracy the thermal de Broglie wave length $\lambda_{\text{dB}} = \sqrt{2\pi\hbar^2/mT}$ is of the order of the interparticle spacing and hence $T_{\text{deg}} \sim 2\pi n^{2/d}/m$. Inserting this into the expression for the interaction energy allows to express the lattice spacing in terms of the density

and the scattering length as

$$\begin{aligned} a_s &= \frac{1}{2n} \sqrt{\ln 4 - \ln(\mu m a_{2D})} \quad (d = 2), \\ a_s &= (n^{4/3} a)^{-1/3} \quad (d = 3). \end{aligned} \quad (\text{A.2})$$

Inserting parameters for a typical Rb-87 experiment in $d = 3$, viz., $a = 5 \text{ nm}$, $m = 1.4 \times 10^{-25} \text{ kg}$, $n = 10^{20} \text{ m}^{-3}$ we obtain $a_s = 1 \mu\text{m}$. Hence, the time scale is $t/\bar{t} = 2ma_s^2 = 3 \times 10^{-3} \text{ s}$. Our lattice time typically runs until $\bar{t} \simeq 1000$, which represents a realistic observation timescale in experiments.

A.2 Sampling the initial state

As described in Sect. 2.2, initial state configurations $\{\phi(\mathbf{x}_{\mathbf{n}}) | \mathbf{n} = (n_1, \dots, n_d), n_j = -N_s/2, \dots, N_s/2\}$ are sampled from the Wigner function corresponding to certain quantum states. They are determined by expanding $\phi(\mathbf{x})$ in a series of mode functions $\{M_{\mathbf{n}}(x) | \mathbf{n} = (n_1, \dots, n_d), n_j = -N_s/2, \dots, N_s/2\}$,

$$\phi(\mathbf{x}_{\mathbf{m}}) = \sum_{\mathbf{n}} \alpha_{\mathbf{n}} M_{\mathbf{n}}(\mathbf{x}_{\mathbf{m}}), \quad (\text{A.3})$$

with coefficients $\{\alpha_{\mathbf{n}} | \mathbf{n} = (n_1, \dots, n_d), n_j = -N_s/2, \dots, N_s/2\}$, which are taken to be given by uncorrelated Gaussian distributions

$$W(\{\alpha_{\mathbf{n}}, \alpha_{\mathbf{n}}^*\}) = \prod_{\mathbf{n}} W_{\mathbf{n}}(\alpha_{\mathbf{n}}, \alpha_{\mathbf{n}}^*) \quad (\text{A.4})$$

$$W_{\mathbf{n}}(\alpha_{\mathbf{n}}, \alpha_{\mathbf{n}}^*) = \frac{1}{2\pi\sigma_{\mathbf{n}}^2} \exp\left(-\frac{|\alpha_{\mathbf{n}}|^2}{2\sigma_{\mathbf{n}}^2}\right) = \frac{1}{2\pi\sigma_{\mathbf{n}}^2} \exp\left(-\frac{\mathcal{R}(\alpha_{\mathbf{n}})^2 + \mathcal{I}(\alpha_{\mathbf{n}})^2}{2\sigma_{\mathbf{n}}^2}\right) \quad (\text{A.5})$$

For the case of a non-interacting thermal gas, the occupation number $|\alpha_{\mathbf{n}}|^2$ of mode \mathbf{n} is given by the Bose-Einstein distribution for mode energy $E_{\mathbf{n}}$ and chemical potential μ . In the Wigner distribution half a quantum of noise is added to each mode [121], which determines the variance $\sigma_{\mathbf{n}}$ to be

$$2\sigma_{\mathbf{n}}^2 = \frac{1}{\exp\frac{E_{\mathbf{n}} - \mu}{k_B T} - 1} + \frac{1}{2} = \left(2 \tanh \frac{E_{\mathbf{n}} - \mu}{k_B T}\right)^{-1}. \quad (\text{A.6})$$

The chemical potential $\mu = \mu(T, V, N)$ is determined implicitly by the condition of fixed particle number $N + N_s^d/2$. Numerically, it is determined iteratively until $\langle \hat{N} \rangle = N$. To reduce particle number fluctuations, pre-selection of ensemble members with particle number close to N can be implemented. For $T < T_c$ it is sufficient to use $\mu = E_0$. In most of our simulations, we assume distributions at $T = 0$. Note, that in a harmonic trap, mode functions are not given by plain waves,

but harmonic oscillator eigenstates

$$\alpha_{\mathbf{n}}(\mathbf{x}) = \prod_{i=1}^d \frac{1}{\sqrt{\sqrt{\pi}l_{\text{T}}}} H_{n_i}(x_i/l_{\text{T}}) \exp\left(-\frac{x_i^2}{2l_{\text{T}}}\right). \quad (\text{A.7})$$

A.3 Split-step method

After sampling initial mode occupation numbers $\alpha_{\mathbf{n}}$, we can construct our initial field distribution $\phi(x)$ from Eq. (A.3). The time evolution of ϕ is determined by the Gross-Pitaevskii equation, Eq. (2.5), which is formally solved by

$$\phi(\mathbf{x}, t - t_0) = \phi(\mathbf{x}, t_0) \mathcal{T} \exp\left(-i \int_{t_0}^t dt' h(\phi(\mathbf{x}, t'), \partial_{\mathbf{x}}, \mathbf{x}, t')\right), \quad (\text{A.8})$$

for $h(\phi(\mathbf{x}, t), \partial_{\mathbf{x}}, \mathbf{x}, t) = h_0(\partial_{\mathbf{x}}) + h_1(\phi(\mathbf{x}, t), \mathbf{x}, t) = -\nabla^2/2m + V(\mathbf{x}) + |\phi(\mathbf{x}, t)|^2$ and \mathcal{T} the time ordering operator. For an infinitesimal time step δt this simplifies to

$$\phi(\mathbf{x}, t_0 + \delta t) = \phi(\mathbf{x}, t_0) \exp(-ih(\phi(\mathbf{x}, t_0), \partial_{\mathbf{x}}, \mathbf{x}, t_0)\delta t). \quad (\text{A.9})$$

However, the time evolution is still non-trivial, since the arguments of the exponential function are operators. An efficient way of simulating such a time step is called the split-step method [384]. It uses the Baker-Campbell-Hausdorff formula to write the exponential of a sum of operators in terms of a product of exponentials. One obtains

$$e^{-ih(\phi(\mathbf{x}, t_0), \partial_{\mathbf{x}}, \mathbf{x}, t_0)\delta t + \mathcal{O}(\delta t^3)} = e^{-ih_0(\partial_{\mathbf{x}})/2\delta t} e^{-ih_1(\phi(\mathbf{x}, t_0), \mathbf{x}, t_0)\delta t} e^{-ih_0(\partial_{\mathbf{x}})/2\delta t}. \quad (\text{A.10})$$

Splitting the time-evolution operator enables us to calculate the three terms in position or momentum space separately. We choose to evaluate the terms including h_0 in momentum space, since the derivative operator becomes diagonal $\partial_{\mathbf{x}} \rightarrow i\mathbf{k}$. The h_1 -term is conveniently calculated in position space. Hence, each time step consists of multiple Fourier transformations bringing the field from position into momentum space and back.

Fourier Transforms can be efficiently carried out by using the FFTW-package¹, which also includes useful parallelisation options. Additionally, we use make use of OpenMP² and CUDA³ parallelisation algorithms.

A.4 Detection of vortices and solitons

The study of non-equilibrium states requires reliable algorithms for the detection of (quasi-) topological defects. Here, we outline our strategy to identify solitons,

¹<http://www.fftw.org>

²www.openmp.org/

³www.nvidia.com/object/cuda_home_new.html

vortices and vortex lines in the complex field $\phi(\mathbf{x})$.

In one-dimensional systems, solitons are found by checking for their characteristic features, see Sect. 2.2.1, a density minimum and a phase jump of $\approx \pi$. In an evaporatively cooled cloud, see Chap. 9, the total number of particles changes with time. Therefore, we have to determine the characteristic length scale for the soliton density dip $\xi = \xi(t) = \sqrt{2mn(t)g}$ dynamically. Spatial variations of ξ are neglected. However, spatial variations have to be taken into account in the section of the algorithm which detects the presence of a density dip. This is accomplished by defining a new density profile $\tilde{n}(x, t)$ as the envelope of the fluctuating density $n(x)$. Then, we check for density dips by scanning the lattice and comparing $n(x)$ with $\tilde{n}(x)$. Once a point x_s with $n(x) \ll \tilde{n}(x)$ is found, we check the local minimum condition $\phi(x_{s+1}) > \phi(x_s)$. If this is fulfilled, a region of size ξ around x_s is analysed for phase jumps of about π magnitude. If the algorithm concludes that there is a phase jump, x_s is characterised as hosting a soliton. Note, that optimal threshold values for density dips and phase jumps are difficult to estimate at high soliton densities, since overlap effects become relevant especially for grey solitons.

In two-dimensional systems, vortices are identified by a density minimum and a characteristic phase change of 2π , see Sect. 2.2.1. First, density minima are detected, where the density falls below 5% of the average density. Then, the algorithm performs the path integral of the phase gradient for a circle of radius ξ around the density minimum. If this give 0, no vortex has been found, for $2\pi\kappa$, a vortex of circulation κ has been found. This method can only resolve structures of order ξ , which means that closely bound vortex-antivortex pairs might be artificially removed.

Vortex lines in three dimensions are found by checking for points where the density falls below 5% of the average density. A determination of the circulation of superfluid flow around the vortex line is considerably more difficult than in two dimensions, due to the lack of an efficient algorithm for the determination of the vortex line orientation.

A.5 Helmholtz decomposition

To visualise vortical flow we use the Helmholtz decomposition of the generalised velocity

$$\mathbf{w} = \mathbf{w}_i + \mathbf{w}_c, \quad (\text{A.11})$$

as described in Sect. 2.2.2. The incompressible \mathbf{w}_i and compressible \mathbf{w}_c parts can be determined in the following way. Since \mathbf{w}_c is rotationless, $\nabla \times \mathbf{w}_c = 0$ it can be written as a scalar potential $\mathbf{w}_c = \nabla\Theta$. By applying a divergence onto Eq. (A.11), it transforms into a Poisson equation

$$\nabla \times \mathbf{w} = \Delta\Theta. \quad (\text{A.12})$$

In Fourier space $\nabla \rightarrow i\mathbf{k}$ and $\Delta \rightarrow -k^2$, this equation can be solved and yields the compressible (longitudinal) field

$$\mathbf{w}_c(\mathbf{k}) = \mathbf{k}\Theta(\mathbf{k}) = \mathbf{k} \cdot \frac{\mathbf{k} \cdot \mathbf{w}(\mathbf{k})}{k^2}. \quad (\text{A.13})$$

Finally, the incompressible (transversal) part is calculated from $\mathbf{w}_i(\mathbf{k}) = \mathbf{w}(\mathbf{k}) - \mathbf{w}_c(\mathbf{k})$.

B

Condensation

In Sect. 2.2, we have described the classical nature of the macroscopically occupied region of the ultracold Bose gas. We recall that this is an effective theory which is not valid for arbitrarily high momenta. Here, we briefly discuss equilibrium Bose-Einstein condensation in $d = 3$ dimensions in the effective classical theory. A detailed discussion also including particle interactions can be found in Refs. [136, 272–274]. In the following, we chose $k_B = \hbar = 2m = 1$.

B.1 Critical temperature

In classical bosonic field theory the equilibrium distribution of free particles over radial momenta $k = |\mathbf{k}| \in [0, k_c]$

$$n(k) = \frac{T}{k^2 - \mu}, \quad (\text{B.1})$$

has to be regularised by a momentum cut-off k_c . Otherwise, one encounters the Rayleigh-Jeans catastrophe of diverging total energy E and total particle number N . In our lattice simulations, see App. A, this cut-off is given by the inverse lattice spacing a_s . The real uniform Bose-gas does not suffer from this divergence, because of the exponential tail of the Bose-Einstein distribution, Eq. (2.2).

At the phase transition, the chemical potential $\mu(T_c) = 0$ and the zero-mode population $N_0(T_c) = 0$. Hence, we can compute

$$N = \frac{V}{(2\pi)^3} \int_0^{k_c} d^3k \frac{T}{k^2} = \frac{V}{(2\pi)^3} 4\pi k_c T_c, \quad (\text{B.2})$$

which yields the critical temperature

$$T_c = \frac{N}{V} \frac{2\pi^2}{k_c}. \quad (\text{B.3})$$

This can be compared to the critical temperature in a real uniform Bose gas

$$T_c = 4\pi \left(\frac{N}{2.612V} \right)^{2/3}. \quad (\text{B.4})$$

B.2 Condensate fraction

Below T_c , the condensate fraction $N_0(T)/N$ becomes non-vanishing. We compute its behaviour by

$$N = N_0 + \frac{V}{(2\pi)^3} \int_0^{k_c} d^3k \frac{T}{k^2} = N_0 + \frac{V}{(2\pi)^3} 4\pi k_c T, \quad (\text{B.5})$$

which leads to

$$N_0/N = 1 - T/T_c. \quad (\text{B.6})$$

Again, this can be compared to the condensate growth in a real uniform Bose gas

$$N_0/N = 1 - (T/T_c)^{3/2}. \quad (\text{B.7})$$

References

- [1] A. Polkovnikov, K. Sengupta, A. Silva, and M. Vengalattore, Colloquium: Nonequilibrium dynamics of closed interacting quantum systems, *Rev. Mod. Phys.* **83**, 863 (2011).
- [2] T. Gasenzer, Ultracold gases far from equilibrium, *Eur. Phys. J. ST* **168**, 89 (2009).
- [3] T. Schäfer and D. Teaney, Nearly perfect fluidity: from cold atomic gases to hot quark gluon plasmas, *Rep. Prog. Phys.* **72**, 126001 (2009).
- [4] J. Berges, J. Blaizot, and F. Gelis, EMMI rapid reaction task force on thermalization in non-abelian plasmas, *J. Phys. G: Nucl. Part. Phys.* **39**, 085115 (2012).
- [5] M. Müller, S. Diehl, G. Pupillo, and P. Zoller, Engineered open systems and quantum simulations with atoms and ions, in E. A. Paul Berman and C. Lin, eds., *Advances in Atomic, Molecular, and Optical Physics*, volume 61, 1, Academic Press (2012).
- [6] J. Sabbatini, W. H. Zurek, and M. J. Davis, Phase separation and pattern formation in a binary Bose-Einstein condensate, *Phys. Rev. Lett.* **107**, 230402 (2011).
- [7] E. Nicklas, H. Strobel, T. Zibold, C. Gross, B. A. Malomed, P. G. Kevrekidis, and M. K. Oberthaler, Rabi flopping induces spatial demixing dynamics, *Phys. Rev. Lett.* **107**, 193001 (2011).
- [8] W. H. Zurek, Cosmological experiments in condensed matter systems, *Phys. Rep.* **276**, 177 (1996).
- [9] J. Dziarmaga, Dynamics of a quantum phase transition and relaxation to a steady state, *Adv. Phys.* **59**, 1063 (2010).
- [10] T. Kinoshita, T. Wenger, and D. S. Weiss, A quantum Newton's cradle, *Nature* **440**, 900 (2006).

- [11] M. Rigol, V. Dunjko, and M. Olshanii, Thermalization and its mechanism for generic isolated quantum systems, *Nature* **452**, 854 (2008).
- [12] M. Cramer, C. Dawson, J. Eisert, and T. Osborne, Exact relaxation in a class of nonequilibrium quantum lattice systems, *Phys. Rev. Lett.* **100**, 30602 (2008).
- [13] M. Rigol, V. Dunjko, V. Yurovsky, and M. Olshanii, Relaxation in a completely integrable many-body quantum system: An ab initio study of the dynamics of the highly excited states of 1d lattice hard-core bosons, *Phys. Rev. Lett.* **98**, 050405 (2007).
- [14] M. Eckstein and M. Kollar, Nonthermal steady states after an interaction quench in the Falicov-Kimball model, *Phys. Rev. Lett.* **100**, 120404 (2008).
- [15] M. Kollar and M. Eckstein, Relaxation of a one-dimensional Mott insulator after an interaction quench, *Phys. Rev. A* **78**, 013626 (2008).
- [16] M. Rigol, Breakdown of thermalization in finite one-dimensional systems, *Phys. Rev. Lett.* **103**, 100403 (2009).
- [17] M. Kronenwett and T. Gasenzer, Far-from-equilibrium dynamics of an ultracold Fermi gas, *Appl. Phys. B* **102**, 469 (2011).
- [18] M. Tsubota, Quantum turbulence, *J. Phys. Soc. Jpn.* **77**, 111006 (2008).
- [19] J. Berges, S. Borsanyi, and C. Wetterich, Prethermalization, *Phys. Rev. Lett.* **93**, 142002 (2004).
- [20] R. Barnett, A. Polkovnikov, and M. Vengalattore, Prethermalization in quenched spinor condensates, *Phys. Rev. A* **84**, 023606 (2011).
- [21] T. Kitagawa, A. Imambekov, J. Schmiedmayer, and E. Demler, The dynamics and prethermalization of one-dimensional quantum systems probed through the full distributions of quantum noise, *New J. Phys.* **13**, 073018 (2011).
- [22] M. Gring, M. Kuhnert, T. Langen, T. Kitagawa, B. Rauer, M. Schreitl, I. Mazets, D. A. Smith, E. Demler, and J. Schmiedmayer, Relaxation and prethermalization in an isolated quantum system, *Science* **337**, 1318 (2012).
- [23] M. Kollar, F. A. Wolf, and M. Eckstein, Generalized Gibbs ensemble prediction of prethermalization plateaus and their relation to nonthermal steady states in integrable systems, *Phys. Rev. B* **84**, 054304 (2011).
- [24] J.-P. Blaizot, F. Gelis, J.-F. Liao, L. McLerran, and R. Venugopalan, Bose-Einstein condensation and thermalization of the quark-gluon plasma, *Nucl. Phys.* **A873**, 68 (2012).
- [25] N. Goldenfeld, *Lectures on phase transitions and the renormalization group*, Addison-Wesley (1992).
- [26] N. Philipp, *Scaling of an ultracold Bose gas out of equilibrium*, Master's thesis,

- Universität Heidelberg (2012).
- [27] J. Berges and D. Mesterházy, Introduction to the nonequilibrium functional renormalization group, Nucl. Phys. B Suppl. **228**, 37 (2012).
 - [28] J. Berges, A. Rothkopf, and J. Schmidt, Non-thermal fixed points: Effective weak-coupling for strongly correlated systems far from equilibrium, Phys. Rev. Lett. **101**, 041603 (2008).
 - [29] C. Scheppach, J. Berges, and T. Gasenzer, Matter-wave turbulence: Beyond kinetic scaling, Phys. Rev. A **81**, 033611 (2010).
 - [30] J. Berges and D. Sexty, Strong versus weak wave-turbulence in relativistic field theory, Phys. Rev. D **83**, 085004 (2011).
 - [31] B. Nowak, D. Sexty, and T. Gasenzer, Superfluid turbulence: Nonthermal fixed point in an ultracold Bose gas, Phys. Rev. B **84**, 020506(R) (2011).
 - [32] B. Nowak, J. Schole, D. Sexty, and T. Gasenzer, Nonthermal fixed points, vortex statistics, and superfluid turbulence in an ultracold Bose gas, Phys. Rev. A **85**, 043627 (2012).
 - [33] J. Schole, B. Nowak, and T. Gasenzer, Critical dynamics of a two-dimensional superfluid near a non-thermal fixed point, Phys. Rev. A **86**, 013624 (2012).
 - [34] A. N. Kolmogorov, The local structure of turbulence in incompressible viscous fluid for very large Reynolds numbers, Proc. USSR Acad. Sci. **30**, 299 (1941), [Proc. R. Soc. Lond. A 434, 9 (1991)].
 - [35] A. M. Obukhov, Spectral energy distribution in a turbulent flow, Izv. Akad. Nauk S.S.S.R., Ser. Geogr. Geofiz. **5**, 453 (1941).
 - [36] V. Yakhot and S. A. Orszag, Renormalization group analysis of turbulence. I. Basic theory, J. Sci. Comp. **1**, 3 (1986).
 - [37] U. Frisch, *Turbulence: The Legacy of A. N. Kolmogorov*, CUP, Cambridge, UK (1995).
 - [38] G. Eyink and N. Goldenfeld, Analogies between scaling in turbulence, field theory, and critical phenomena, Phys. Rev. E **50**, 4679 (1994).
 - [39] L. Smith and S. Woodruff, Renormalization-group analysis of turbulence, Ann. Rev. Fl. Mech. **30**, 275 (1998).
 - [40] L. F. Richardson, The supply of energy from and to atmospheric eddies, Proc. Roy. Soc. Lond. Ser. A **97**, 354 (1920).
 - [41] V. E. Zakharov, V. S. L'vov, and G. Falkovich, *Kolmogorov Spectra of Turbulence I: Wave Turbulence*, Springer-Verlag, Berlin (1992).
 - [42] S. Nazarenko, *Wave turbulence*, number 825 in Lecture Notes in Physics, Springer, Heidelberg (2011).

- [43] A. Newell, Wave turbulence, *Ann. Rev. Fluid Mech.* **43** (2011).
- [44] E. Levich and V. Yakhot, Time development of coherent and superfluid properties in the course of a λ -transition, *J. Phys. A: Math. Gen.* **11**, 2237 (1978).
- [45] Y. Kagan, B. V. Svistunov, and G. V. Shlyapnikov, Kinetics of Bose condensation in an interacting Bose gas, [*Zh. Eksp. Teor. Fiz.* 101, 528 (1992)] *Sov. Phys. JETP* **74**, 279 (1992).
- [46] Y. Kagan and B. V. Svistunov, Kinetics of the onset of long-range order during Bose condensation in an interacting gas, [*Zh. Eksp. Teor. Fiz.* 105, 353 (1994)] *Sov. Phys. JETP* **78**, 187 (1994).
- [47] Y. Kagan and B. V. Svistunov, Evolution of correlation properties and appearance of broken symmetry in the process of Bose-Einstein condensation, *Phys. Rev. Lett.* **79**, 3331 (1997).
- [48] N. G. Berloff and B. V. Svistunov, Scenario of strongly nonequilibrated Bose-Einstein condensation, *Phys. Rev. A* **66**, 013603 (2002).
- [49] B. Svistunov, in C. Barenghi, R. Donnelly, and W. Vinen, eds., *Quantized Vortex Dynamics and Superfluid Turbulence*, number 571 in *Lecture Notes in Physics*, Springer, Berlin (2001).
- [50] E. V. Kozik and B. V. Svistunov, Theory of decay of superfluid turbulence in the low-temperature limit, *J. Low Temp. Phys.* **156**, 215 (2009).
- [51] M. Schmidt, S. Erne, B. Nowak, D. Sexty, and T. Gasenzer, Nonthermal fixed points and solitons in a one-dimensional Bose gas, *New J. Phys.* **14**, 075005 (2012).
- [52] R. Micha and I. I. Tkachev, Relativistic turbulence: A long way from preheating to equilibrium, *Phys. Rev. Lett.* **90**, 121301 (2003).
- [53] J. Berges and G. Hoffmeister, Nonthermal fixed points and the functional renormalization group, *Nucl. Phys.* **B813**, 383 (2009).
- [54] J. Berges, D. Gelfand, and J. Pruschke, Quantum theory of fermion production after inflation, *Phys. Rev. Lett.* **107**, 61301 (2011).
- [55] T. Gasenzer, B. Nowak, and D. Sexty, Charge separation in reheating after cosmological inflation, *Phys. Lett.* **B710**, 500 (2012).
- [56] P. B. Arnold and G. D. Moore, QCD plasma instabilities: The nonabelian cascade, *Phys. Rev.* **D73**, 025006 (2006).
- [57] J. Berges, S. Scheffler, and D. Sexty, Turbulence in nonabelian gauge theory, *Phys. Lett.* **B681**, 362 (2009).
- [58] M. Carrington and A. Rebhan, Perturbative and nonperturbative Kolmogorov turbulence in a gluon plasma, *Eur. Phys. J.* **C71**, 1787 (2011).

-
- [59] K. Fukushima and F. Gelis, The evolving glasma, Nucl. Phys. **A874**, 108 (2012).
- [60] K. Fukushima, Evolving glasma and Kolmogorov spectrum, Acta Phys. Polon. **B42**, 2697 (2011).
- [61] J. Berges and D. Sexty, Bose condensation far from equilibrium, Phys. Rev. Lett. **108**, 161601 (2012).
- [62] G. Düring, C. Josserand, and S. Rica, Weak turbulence for a vibrating plate: can one hear a Kolmogorov spectrum?, Phys. Rev. Lett. **97**, 25503 (2006).
- [63] E. Falcon, C. Laroche, and S. Fauve, Observation of gravity-capillary wave turbulence, Phys. Rev. Lett. **98**, 94503 (2007).
- [64] R. Micha and I. I. Tkachev, Turbulent thermalization, Phys. Rev. D **70**, 043538 (2004).
- [65] D. Semikoz and I. Tkachev, Condensation of bosons in the kinetic regime, Phys. Rev. D **55**, 489 (1997).
- [66] V. Lvov and S. Nazarenko, Spectrum of Kelvin-wave turbulence in superfluids, JETP Letters **91**, 428 (2010).
- [67] T. Lee and Y. Pang, Nontopological solitons, Phys. Rep. **221**, 251 (1992).
- [68] D. Thouless, *Topological quantum numbers in nonrelativistic physics*, World Scientific, Singapore (1998).
- [69] L. M. Pismen, *Vortices in nonlinear fields: From liquid crystals to superfluids, from non-equilibrium patterns to cosmic strings*, CPO, Oxford (1999).
- [70] D. Nelson, *Defects and geometry in condensed matter physics*, CUP, Cambridge, UK (2002).
- [71] N. Mermin, The topological theory of defects in ordered media, Rev. Mod. Phys. **51**, 591 (1979).
- [72] C. Lin, On the motion of vortices in 2d i. existence of the kirchoff-routh function, Proc. Nat. Acad. Sci. **27**, 570 (1941).
- [73] L. Onsager, Statistical hydrodynamics, Nuovo Cim. Suppl. **6**, 279 (1949).
- [74] R. P. Feynman, Applications of quantum mechanics to liquid helium, in C. J. Gorter, ed., *Progress in Low Temperature Physics Vol 1.*, 17, North Holland, Amsterdam (1955).
- [75] W. Vinen, The detection of single quanta of circulation in liquid helium II, Proc. Roy. Soc. Lond. Ser. A: Math. Phys. Sci. **260**, 218 (1961).
- [76] R. J. Donnelly, *Quantized Vortices in Liquid He II*, CUP, Cambridge, UK (1991).

- [77] L. Pitaevskii, Vortex lines in an imperfect Bose gas, *Sov. Phys. JETP* **13**, 451 (1961).
- [78] E. P. Gross, Structure of a quantized vortex in boson systems, *Nuovo Cim.* **20**, 454 (1961).
- [79] F. Dalfovo, S. Giorgini, L. P. Pitaevskii, and S. Stringari, Theory of Bose-Einstein condensation in trapped gases, *Rev. Mod. Phys.* **71**, 463 (1999).
- [80] A. L. Fetter and A. A. Svidzinsky, Vortices in a trapped dilute Bose-Einstein condensate, *J. Phys.* **13**, R135 (2001).
- [81] A. Aftalion, *Vortices in Bose-Einstein Condensates*, Birkhäuser, Boston (2006).
- [82] W. P. Halperin and M. Tsubota, eds., *Progress in Low Temperature Physics Vol. 16: Quantum Turbulence*, Elsevier, Amsterdam (2008).
- [83] N. Berloff and A. Youd, Dissipative dynamics of superfluid vortices at nonzero temperatures, *Phys. Rev. Lett.* **99**, 145301 (2007).
- [84] M. R. Matthews, B. P. Anderson, P. C. Haljan, D. S. Hall, C. E. Wieman, and E. A. Cornell, Vortices in a Bose-Einstein condensate, *Phys. Rev. Lett.* **83**, 2498 (1999).
- [85] K. W. Madison, F. Chevy, W. Wohlleben, and J. Dalibard, Vortex formation in a stirred Bose-Einstein condensate, *Phys. Rev. Lett.* **84**, 806 (2000).
- [86] J. R. Abo-Shaeer, C. Raman, J. M. Vogels, and W. Ketterle, Observation of vortex lattices in Bose-Einstein condensates, *Science* **292**, 476 (2001).
- [87] B. P. Anderson, P. C. Haljan, C. A. Regal, D. L. Feder, L. A. Collins, C. W. Clark, and E. A. Cornell, Watching dark solitons decay into vortex rings in a Bose-Einstein condensate, *Phys. Rev. Lett.* **86**, 2926 (2001).
- [88] J. A. Seman, E. A. L. Henn, M. Haque, R. F. Shiozaki, E. R. F. Ramos, M. Caracanhas, P. Castilho, C. Castelo Branco, P. E. S. Tavares, F. J. Poveda-Cuevas, G. Roati, K. M. F. Magalhães, and V. S. Bagnato, Three-vortex configurations in trapped Bose-Einstein condensates, *Phys. Rev. A* **82**, 033616 (2010).
- [89] T. W. Neely, E. C. Samson, A. S. Bradley, M. J. Davis, and B. P. Anderson, Observation of vortex dipoles in an oblate Bose-Einstein condensate, *Phys. Rev. Lett.* **104**, 160401 (2010).
- [90] T. W. Neely, A. S. Bradley, E. C. Samson, S. J. Rooney, E. M. Wright, K. J. H. Law, R. Carretero-González, P. G. Kevrekidis, M. J. Davis, and B. P. Anderson, Characteristics of two-dimensional quantum turbulence in a compressible superfluid, arXiv:1204.1102 [cond-mat.quant-gas] (2012).
- [91] E. A. Novikov, Dynamics and statistics of a system of vortices, *Zh. Eksp.*

- Teor. Fiz. **68**, 1868 (1975).
- [92] V. Berdichevsky, Statistical mechanics of point vortices, Phys. Rev. E **51**, 4432 (1995).
- [93] V. Berdichevsky, Statistical mechanics of vortex lines, Phys. Rev. E **57**, 2885 (1998).
- [94] S. Nemirovskii and L. Kondaurova, Langevin dynamics of vortex lines and thermodynamic equilibrium of vortex tangle, J. Low Temp. Phys. **156**, 182 (2009).
- [95] M. Paoletti and D. Lathrop, Quantum turbulence, Ann. Rev. Cond. Mat. Phys. **2**, 213 (2011).
- [96] W. Vinen, Mutual friction in a heat current in liquid helium II. III. Theory of the mutual friction, Proc. Roy. Soc. Lond. Ser. A: Math. Phys. Sci. **242**, 493 (1957).
- [97] W. Vinen, Mutual friction in a heat current in liquid helium II. II. Experiments on transient effects, Proc. Roy. Soc. Lond. Ser. A: Math. Phys. Sci. **240**, 128 (1957).
- [98] W. Vinen, Mutual friction in a heat current in liquid helium II. IV. Critical heat currents in wide channels, Proc. Roy. Soc. Lond. Ser. A: Math. Phys. Sci. **243**, 400 (1958).
- [99] K. W. Schwarz, Turbulence in superfluid helium: Steady homogeneous counterflow, Phys. Rev. B **18**, 245 (1978).
- [100] K. Schwarz, Three-dimensional vortex dynamics in superfluid ^4He : Homogeneous superfluid turbulence, Phys. Rev. B **38**, 2398 (1988).
- [101] W. F. Vinen, Classical character of turbulence in a quantum liquid, Phys. Rev. B **61**, 1410 (2000).
- [102] W. F. Vinen and J. J. Niemela, Quantum turbulence, J. Low Temp. Phys. **128**, 167 (2002).
- [103] P. Walmsley, A. Golov, H. Hall, A. Levchenko, and W. Vinen, Dissipation of quantum turbulence in the zero temperature limit, Phys. Rev. Lett. **99**, 265302 (2007).
- [104] P. Walmsley and A. Golov, Quantum and quasiclassical types of superfluid turbulence, Phys. Rev. Lett. **100**, 245301 (2008).
- [105] K. Damle, S. Majumdar, and S. Sachdev, Phase ordering kinetics of the Bose gas, Phys. Rev. A **54**, 5037 (1996).
- [106] S. Nazarenko and M. Onorato, Wave turbulence and vortices in Bose-Einstein condensation, Phys. D: Nonlin. Phen. **219**, 1 (2006).

- [107] T.-L. Horng, C.-H. Hsueh, and S.-C. Gou, Transition to quantum turbulence in a Bose-Einstein condensate through the bending-wave instability of a single-vortex ring, *Phys. Rev. A* **77**, 063625 (2008).
- [108] T.-L. Horng, C.-H. Hsueh, S.-W. Su, Y.-M. Kao, and S.-C. Gou, Two-dimensional quantum turbulence in a nonuniform Bose-Einstein condensate, *Phys. Rev. A* **80**, 023618 (2009).
- [109] E. A. L. Henn, J. A. Seman, G. Roati, K. M. F. Magalhães, and V. S. Bagnato, Emergence of turbulence in an oscillating Bose-Einstein condensate, *Phys. Rev. Lett.* **103**, 045301 (2009).
- [110] V. Yukalov, Turbulent superfluid as continuous vortex mixture, *Las. Phys. Lett.* **7**, 467 (2010).
- [111] J. A. Seman, E. A. L. Henn, R. F. Shiozaki, G. Roati, F. J. Poveda-Cuevas, K. M. F. Magalhães, V. I. Yukalov, M. Tsubota, M. Kobayashi, K. Kasamatsu, and V. S. Bagnato, Route to turbulence in a trapped Bose-Einstein condensate, *Las. Phys. Lett.* **8**, 691 (2011).
- [112] J. Maurer and P. Tabeling, Local investigation of superfluid turbulence, *Europhys. Lett.* **43**, 29 (1998).
- [113] S. Stalp, L. Skrbek, and R. Donnelly, Decay of grid turbulence in a finite channel, *Phys. Rev. Lett.* **82**, 4831 (1999).
- [114] C. Nore, M. Abid, and M. E. Brachet, Kolmogorov turbulence in low-temperature superflows, *Phys. Rev. Lett.* **78**, 3896 (1997).
- [115] C. Nore, M. Abid, and M. E. Brachet, Decaying Kolmogorov turbulence in a model of superflow, *Phys. Fl.* **9**, 2644 (1997).
- [116] T. Araki, M. Tsubota, and S. K. Nemirovskii, Energy spectrum of superfluid turbulence with no normal-fluid component, *Phys. Rev. Lett.* **89**, 145301 (2002).
- [117] M. Kobayashi and M. Tsubota, Kolmogorov spectrum of superfluid turbulence: Numerical analysis of the Gross-Pitaevskii equation with a small-scale dissipation, *Phys. Rev. Lett.* **94**, 065302 (2005).
- [118] M. Kobayashi and M. Tsubota, Kolmogorov spectrum of quantum turbulence, *J. Phys. Soc. Jpn.* **74**, 3248 (2005).
- [119] G. Krstulovic and M. Brachet, Energy cascade with small-scale thermalization, counterflow metastability, and anomalous velocity of vortex rings in fourier-truncated Gross-Pitaevskii equation, *Phys. Rev. E* **83**, 066311 (2011).
- [120] J. Berges and T. Gasenzer, Quantum versus classical statistical dynamics of an ultracold Bose gas, *Phys. Rev. A* **76**, 033604 (2007).
- [121] P. Blakie, A. Bradley, M. Davis, R. Ballagh, and C. Gardiner, Dynamics and

- statistical mechanics of ultra-cold Bose gases using c-field techniques, *Adv. Phys.* **57**, 363 (2008).
- [122] A. Polkovnikov, Phase space representation of quantum dynamics, *Ann. Phys.* **325**, 1790 (2010).
- [123] C. Timm, Generalization of the Berezinskii–Kosterlitz–Thouless theory to higher vortex densities, *Phys. C: Supercond.* **265**, 31 (1996).
- [124] R. N. Bisset, M. J. Davis, T. P. Simula, and P. B. Blakie, Quasicondensation and coherence in the quasi-two-dimensional trapped Bose gas, *Phys. Rev. A* **79**, 033626 (2009).
- [125] C. J. Foster, P. B. Blakie, and M. J. Davis, Vortex pairing in two-dimensional Bose gases, *Phys. Rev. A* **81**, 023623 (2010).
- [126] V. Berezinskii, Destruction of long-range order in one-dimensional and two-dimensional systems having a continuous symmetry group i. classical systems, *JETP* **32**, 493 (1971).
- [127] J. Kosterlitz and D. Thouless, Ordering, metastability and phase transitions in two-dimensional systems, *J. Phys. C: Sol. St. Phys.* **6**, 1181 (1973).
- [128] E. Levich and V. Yakhot, Time evolution of a Bose system passing through the critical point, *Phys. Rev. B* **15**, 243 (1977).
- [129] H. T. C. Stoof, Formation of the condensate in a dilute Bose gas, *Phys. Rev. Lett.* **66**, 3148 (1991).
- [130] B. Svistunov, Highly nonequilibrium Bose condensation in a weakly interacting gas, *J. Mosc. Phys. Soc.* **1**, 373 (1991).
- [131] D. Snoke and J. Wolfe, Population dynamics of a Bose gas near saturation, *Phys. Rev. B* **39**, 4030 (1989).
- [132] C. W. Gardiner, M. D. Lee, R. J. Ballagh, M. J. Davis, and P. Zoller, Quantum kinetic theory of condensate growth: Comparison of experiment and theory, *Phys. Rev. Lett.* **81**, 5266 (1998).
- [133] H. Miesner, D. Stamper-Kurn, M. Andrews, D. Durfee, S. Inouye, and W. Ketterle, Bosonic stimulation in the formation of a Bose-Einstein condensate, *Science* **279**, 1005 (1998).
- [134] P. Drummond and J. Corney, Quantum dynamics of evaporatively cooled Bose-Einstein condensates, *Phys. Rev. A* **60**, 2661 (1999).
- [135] M. Köhl, M. J. Davis, C. W. Gardiner, T. Hänsch, and T. Esslinger, Growth of Bose-Einstein condensates from thermal vapor, *Phys. Rev. Lett.* **88**, 080402 (2002).
- [136] C. Connaughton, C. Josserand, A. Picozzi, Y. Pomeau, and S. Rica, Condensation of classical nonlinear waves, *Phys. Rev. Lett.* **95**, 263901 (2005).

- [137] S. Ritter, A. Öttl, T. Donner, T. Bourdel, M. Köhl, and T. Esslinger, Observing the formation of long-range order during Bose-Einstein condensation, *Phys. Rev. Lett.* **98**, 090402 (2007).
- [138] C. N. Weiler, T. W. Neely, D. R. Scherer, A. S. Bradley, M. J. Davis, and B. P. Anderson, Spontaneous vortices in the formation of Bose-Einstein condensates, *Nature* **455**, 948 (2008).
- [139] R. P. Smith, S. Beattie, S. Moulder, R. L. D. Campbell, and Z. Hadzibabic, Condensation dynamics in a quantum-quenched Bose gas, *Phys. Rev. Lett.* **109**, 105301 (2012).
- [140] B. Nowak and T. Gasenzer, On a new twist in the dynamics of Bose-Einstein condensation, arXiv:1206.3181 [cond-mat.quant-gas] (2012).
- [141] V. E. Demidov, O. Dzyapko, S. O. Demokritov, G. A. Melkov, and A. N. Slavin, Thermalization of a parametrically driven magnon gas leading to Bose-Einstein condensation, *Phys. Rev. Lett.* **99**, 037205 (2007).
- [142] V. E. Demidov, O. Dzyapko, M. Buchmeier, T. Stockhoff, G. Schmitz, G. A. Melkov, and S. O. Demokritov, Magnon kinetics and Bose-Einstein condensation studied in phase space, *Phys. Rev. Lett.* **101**, 257201 (2008).
- [143] J. Keeling and N. Berloff, Spontaneous rotating vortex lattices in a pumped decaying condensate, *Phys. Rev. Lett.* **100**, 250401 (2008).
- [144] P. Nowik-Boltyk, O. Dzyapko, V. Demidov, N. Berloff, and S. Demokritov, Spatially non-uniform ground state and quantized vortices in a two-component Bose-Einstein condensate of magnons, *Sci. Rep.* **2** (2012).
- [145] J. Kasprzak, M. Richard, S. Kundermann, A. Baas, P. Jeambrun, J. M. J. Keeling, F. M. Marchetti, M. H. Szymaska, R. Andrel, J. L. Straehli, V. Savona, P. B. Littlewood, B. Deveaud, and L. S. Dang, Bose-Einstein condensation of exciton polaritons, *Nature* **443**, 409 (2006).
- [146] R. Balili, V. Hartwell, D. Snoke, L. Pfeiffer, and K. West, Bose-Einstein condensation of microcavity polaritons in a trap, *Science* **316**, 1007 (2007).
- [147] K. Lagoudakis, M. Wouters, M. Richard, A. Baas, I. Carusotto, R. André, L. Dang, B. Deveaud-Plédran et al., Quantized vortices in an exciton-polariton condensate, *Nature Phys.* **4**, 706 (2008).
- [148] J. Keeling and N. Berloff, Exciton-polariton condensation, *Cont. Phys.* **52**, 131 (2011).
- [149] G. Theocharis, P. Kevrekidis, M. Oberthaler, and D. Frantzeskakis, Dark matter-wave solitons in the dimensionality crossover, *Phys. Rev. A* **76** (2007).
- [150] S. Hofferberth, I. Lesanovsky, B. Fischer, T. Schumm, and J. Schmiedmayer, Non-equilibrium coherence dynamics in one-dimensional Bose gases, *Nature* **449**, 324 (2007).

-
- [151] A. Weller, J. P. Ronzheimer, C. Gross, J. Esteve, M. K. Oberthaler, D. J. Frantzeskakis, G. Theocharis, and P. G. Kevrekidis, Experimental observation of oscillating and interacting matter wave dark solitons, *Phys. Rev. Lett.* **101**, 130401 (2008).
- [152] C. Becker, S. Stellmer, P. Soltan-Panahi, S. Dörscher, M. Baumert, E.-M. Richter, J. Kronjäger, K. Bongs, and K. Sengstock, Oscillations and interactions of dark and dark bright solitons in Bose–Einstein condensates, *Nature Phys.* **4**, 496 (2008).
- [153] D. Frantzeskakis, Dark solitons in atomic Bose–Einstein condensates: From theory to experiments, *J. Phys. A: Math. Theo.* **43**, 213001 (2010).
- [154] R. G. Scott, F. Dalfovo, L. P. Pitaevskii, and S. Stringari, Dynamics of dark solitons in a trapped superfluid fermi gas, *Phys. Rev. Lett.* **106**, 185301 (2011).
- [155] R. K. Smith, Travelling waves and bores in the lower atmosphere: The morning glory and related phenomena, *Earth-Sci. Rev.* **25**, 267 (1988).
- [156] A. Scheffers and D. Kelletat, Sedimentologic and geomorphologic tsunami imprints worldwide: A review, *Earth-Sci. Rev.* **63**, 83 (2003).
- [157] L. F. Mollenauer, R. H. Stolen, and J. P. Gordon, Experimental observation of picosecond pulse narrowing and solitons in optical fibers, *Phys. Rev. Lett.* **45**, 1095 (1980).
- [158] W. H. Zurek, Causality in condensates: Gray solitons as relics of bec formation, *Phys. Rev. Lett.* **102**, 105702 (2009).
- [159] B. Damski and W. H. Zurek, Soliton creation during a Bose-Einstein condensation, *Phys. Rev. Lett.* **104**, 160404 (2010).
- [160] S. Burger, L. D. Carr, P. Öhberg, K. Sengstock, and A. Sanpera, Generation and interaction of solitons in Bose–Einstein condensates, *Phys. Rev. A* **65**, 043611 (2002).
- [161] L. D. Carr, J. Brand, S. Burger, and A. Sanpera, Dark-soliton creation in Bose-Einstein condensates, *Phys. Rev. A* **63**, 051601 (2001).
- [162] P. O. Fedichev, A. E. Muryshev, and G. V. Shlyapnikov, Dissipative dynamics of a kink state in a Bose-condensed gas, *Phys. Rev. A* **60**, 3220 (1999).
- [163] T. Busch and J. R. Anglin, Motion of dark solitons in trapped Bose-Einstein condensates, *Phys. Rev. Lett.* **84**, 2298 (2000).
- [164] A. Rajantie and A. Tranberg, Looking for defects in the 2-PI correlator, *JHEP* **11**, 020 (2006).
- [165] A. Rajantie and A. Tranberg, Counting defects with the two-point correlator, *JHEP* **1008**, 086 (2010).

- [166] J. Berges and S. Roth, Topological defect formation from 2-PI effective action techniques, *Nucl. Phys.* **B847**, 197 (2011).
- [167] M. Karl, B. Nowak, and T. Gasenzer, in preparation .
- [168] E. D. Siggia and A. E. Ruckenstein, Bose condensation in spin-polarized atomic hydrogen, *Phys. Rev. Lett.* **44**, 1423 (1980).
- [169] E. Timmermans, Phase separation of Bose-Einstein condensates, *Phys. Rev. Lett.* **81**, 5718 (1998).
- [170] K. Kasamatsu and M. Tsubota, Modulation instability and solitary-wave formation in two-component Bose-Einstein condensates, *Phys. Rev. A* **74**, 013617 (2006).
- [171] H. Schmaljohann, M. Erhard, J. Kronjäger, M. Kottke, S. van Staa, L. Cacciapuoti, J. J. Arlt, K. Bongs, and K. Sengstock, Dynamics of $f = 2$ spinor Bose-Einstein condensates, *Phys. Rev. Lett.* **92**, 040402 (2004).
- [172] M.-S. Chang, C. D. Hamley, M. D. Barrett, J. A. Sauer, K. M. Fortier, W. Zhang, L. You, and M. S. Chapman, Observation of spinor dynamics in optically trapped ^{87}Rb Bose-Einstein condensates, *Phys. Rev. Lett.* **92**, 140403 (2004).
- [173] H. Saito and M. Ueda, Spontaneous magnetization and structure formation in a spin-1 ferromagnetic Bose-Einstein condensate, *Phys. Rev. A* **72**, 023610 (2005).
- [174] J. M. Higbie, L. E. Sadler, S. Inouye, A. P. Chikkatur, S. R. Leslie, K. L. Moore, V. Savalli, and D. M. Stamper-Kurn, Direct nondestructive imaging of magnetization in a spin-1 Bose-Einstein gas, *Phys. Rev. Lett.* **95**, 050401 (2005).
- [175] L. E. Sadler, J. M. Higbie, S. R. Leslie, M. Vengalattore, and D. M. Stamper-Kurn, Spontaneous symmetry breaking in a quenched ferromagnetic spinor Bose-Einstein condensate, *Nature* **443**, 312 (2006).
- [176] Y. Kawaguchi and M. Ueda, Spinor Bose-Einstein condensates, *Phys. Rep.* (in press) (2012).
- [177] J. Guzman, G.-B. Jo, A. N. Wenz, K. W. Murch, C. K. Thomas, and D. M. Stamper-Kurn, Long-time-scale dynamics of spin textures in a degenerate $f = 1$ ^{87}Rb spinor Bose gas, *Phys. Rev. A* **84**, 063625 (2011).
- [178] R. Folman, P. Krüger, D. Cassettari, B. Hessmo, T. Maier, and J. Schmiedmayer, Controlling cold atoms using nanofabricated surfaces: Atom chips, *Phys. Rev. Lett.* **84**, 4749 (2000).
- [179] R. Folman, P. Krüger, J. Schmiedmayer, J. H. Denschlag, and C. Henkel, Microscopic atom optics: From wires to an atom chip, *Adv. At. Mol. Opt. Phys.* **48**, 253 (2002).

-
- [180] A. Schakel, Entangled vortices: Onsager's geometrical picture of superfluid phase transitions, *J. Low. Temp. Phys.* **129**, 323 (2002).
- [181] T. W. B. Kibble, Topology of cosmic domains and strings, *J. Phys. A: Math. Gen.* **9**, 1387 (1976).
- [182] W. H. Zurek, Cosmological experiments in superfluid helium?, *Nature* **317**, 505 (1985).
- [183] L. Mathey, K. Günter, J. Dalibard, and A. Polkovnikov, Dynamic Kosterlitz-Thouless transition in 2d Bose mixtures of ultra-cold atoms, arXiv:1112.1204 [cond-mat.quant-gas] (2011).
- [184] S. N. Bose, Plancks Gesetz und Lichtquantenhypothese, [*Am. J. Phys.* **44**, 1056 (1976)] *Z. Phys.* **26**, 178 (1924).
- [185] A. Einstein, Quantentheorie des einatomigen idealen Gases, *Sitzungsber. Kgl. Preuss. Akad. Wiss., Phys. Math. Kl.* **1924**, 261 (1924).
- [186] A. Einstein, Quantentheorie des einatomigen idealen Gases. Zweite Abhandlung, *Sitzungsber. Preuss. Akad. Wiss.* **1925**, 3 (1925).
- [187] M. H. Anderson, J. R. Ensher, M. R. Matthews, C. E. Wieman, and E. A. Cornell, Observation of Bose-Einstein condensation in a dilute atomic vapor, *Science* **269**, 198 (1995).
- [188] K. B. Davis, M.-O. Mewes, and W. Ketterle, An analytical model for evaporative cooling of atoms, *Appl. Phys. B* **60**, 155 (1995).
- [189] C. C. Bradley, C. A. Sackett, J. J. Tollett, and R. G. Hulet, Evidence of Bose-Einstein condensation in an atomic gas with attractive interactions, *Phys. Rev. Lett.* **75**, 1687 (1995).
- [190] J. R. Anglin and W. Ketterle, Bose-Einstein condensation of atomic gases, *Nature* **416**, 211 (2002).
- [191] A. J. Leggett, Bose-Einstein condensation in the alkali gases: Some fundamental concepts, *Rev. Mod. Phys.* **73**, 307 (2001).
- [192] M. Drechsler and W. Zwerger, Crossover from BCS-superconductivity to Bose-condensation, *Ann. d. Phys.* **504**, 15 (1992).
- [193] S. Jochim, M. Bartenstein, A. Altmeyer, G. Hendl, C. Chin, J. H. Denschlag, and R. Grimm, Pure gas of optically trapped molecules created from Fermionic atoms, *Phys. Rev. Lett.* **91**, 240402 (2003).
- [194] C. Chin, M. Bartenstein, A. Altmeyer, S. Riedl, S. Jochim, J. Denschlag, and R. Grimm, Observation of the pairing gap in a strongly interacting Fermi gas, *Science* **305**, 1128 (2004).
- [195] J. Chin, D. Miller, Y. Liu, C. Stan, W. Setiawan, C. Sanner, K. Xu, and W. Ketterle, Evidence for superfluidity of ultracold fermions in an optical

- lattice, *Nature* **443**, 961 (2006).
- [196] S. Diehl, H. Gies, J. Pawłowski, and C. Wetterich, Flow equations for the BCS-BEC crossover, *Phys. Rev. A* **76**, 021602 (2007).
- [197] T. Dao, A. Georges, J. Dalibard, C. Salomon, and I. Carusotto, Measuring the one-particle excitations of ultracold fermionic atoms by stimulated Raman spectroscopy, *Phys. Rev. Lett.* **98**, 240402 (2007).
- [198] M. Punk and W. Zwerger, Theory of rf-spectroscopy of strongly interacting fermions, *Phys. Rev. Lett.* **99**, 170404 (2007).
- [199] S. Floerchinger, M. Scherer, S. Diehl, and C. Wetterich, Particle-hole fluctuations in BCS-BEC crossover, *Phys. Rev. B* **78**, 174528 (2008).
- [200] S. Giorgini, L. P. Pitaevskii, and S. Stringari, Theory of ultracold fermi gases, *Rev. Mod. Phys.* **80**, 1215 (2008).
- [201] T.-L. Ho and V. B. Shenoy, Binary mixtures of Bose condensates of alkali atoms, *Phys. Rev. Lett.* **77**, 3276 (1996).
- [202] D. S. Hall, M. R. Matthews, J. R. Ensher, C. E. Wieman, and E. A. Cornell, Dynamics of component separation in a binary mixture of Bose-Einstein condensates, *Phys. Rev. Lett.* **81**, 1539 (1998).
- [203] Z. Hadzibabic, C. A. Stan, K. Dieckmann, S. Gupta, M. W. Zwierlein, A. Görlitz, and W. Ketterle, Two-species mixture of quantum degenerate Bose and Fermi gases, *Phys. Rev. Lett.* **88**, 160401 (2002).
- [204] T. Köhler, T. Gasenzer, and K. Burnett, Microscopic theory of atom-molecule oscillations in a Bose-Einstein condensate, *Phys. Rev. A* **67**, 013601 (2003).
- [205] T. Köhler, K. Góral, and P. S. Julienne, Production of cold molecules via magnetically tuneable Feshbach resonances, *Rev. Mod. Phys.* **78**, 1311 (2006).
- [206] E. Braaten and H. Hammer, Efimov physics in cold atoms, *Ann. Phys.* **322**, 120 (2007).
- [207] S. Diehl, H. Krahl, and M. Scherer, Three-body scattering from nonperturbative flow equations, *Phys. Rev. C* **78**, 034001 (2008).
- [208] L. Carr, D. DeMille, R. Krems, and J. Ye, Cold and ultracold molecules: science, technology and applications, *New J. Phys.* **11**, 055049 (2009).
- [209] S. Floerchinger, R. Schmidt, and C. Wetterich, Three-body loss in lithium from functional renormalization, *Phys. Rev. A* **79**, 053633 (2009).
- [210] I. Boettcher, J. Pawłowski, and S. Diehl, Ultracold atoms and the functional renormalization group, *Nucl. Phys. B Suppl.* **228**, 63 (2012).
- [211] M. K. Oberthaler, R. Abfalterer, S. Bernet, J. Schmiedmayer, and A. Zeilinger, Atom waves in crystals of light, *Phys. Rev. Lett.* **77**, 4980 (1996).

-
- [212] M. Greiner, O. Mandel, T. Esslinger, T. W. Hänsch, and I. Bloch, Quantum phase transition from a superfluid to a Mott insulator in a gas of ultracold atoms, *Nature* **415**, 39 (2002).
- [213] O. Morsch and M. K. Oberthaler, Dynamics of Bose-Einstein condensates in optical lattices, *Rev. Mod. Phys.* **78**, 179 (2006).
- [214] M. Lewenstein, A. Sanpera, V. Ahufinger, B. Damski, A. Sen, and U. Sen, Ultracold atomic gases in optical lattices: Mimicking condensed matter physics and beyond, *Adv. Phys.* **56**, 243 (2007).
- [215] K. Temme and T. Gasenzer, Non-equilibrium dynamics of condensates in a lattice from the 2PI effective action in $1/\mathcal{N}$ expansion, *Phys. Rev. A* **74**, 053603 (2006).
- [216] M. A. Cazalilla and M. Rigol, Focus on dynamics and thermalization in isolated quantum many-body systems, *New J. Phys.* **12**, 055006 (2010).
- [217] A. V. Gorshkov, M. Hermele, V. Gurarie, C. Xu, P. S. Julienne, J. Ye, P. Zoller, E. Demler, M. D. Lukin, and A. M. Rey, Two-orbital SU(N) magnetism with ultracold alkaline-earth atoms, *Nature Phys.* **6**, 289 (2010).
- [218] J. Dalibard, F. Gerbier, G. Juzeliūnas, and P. Öhberg, Colloquium: Artificial gauge potentials for neutral atoms, *Rev. Mod. Phys.* **83**, 1523 (2011).
- [219] A. Sørensen, L.-M. Duan, J. I. Cirac, and P. Zoller, Many-particle entanglement with Bose-Einstein condensates, *Nature* **409**, 63 (2001).
- [220] J. Estève, C. Gross, A. Weller, S. Giovanazzi, and M. K. Oberthaler, Squeezing and entanglement in a Bose-Einstein condensate, *Nature* **455**, 1216 (2008).
- [221] C. Gross, T. Zibold, E. Nicklas, J. Estève, and M. K. Oberthaler, Nonlinear atom interferometer surpasses classical precision limit, *Nature* **464**, 1165 (2010).
- [222] C. Bodet, J. Estève, M. K. Oberthaler, and T. Gasenzer, Two-mode Bose gas: Beyond classical squeezing, *Phys. Rev. A* **81**, 063605 (2010).
- [223] W. D. Phillips, Laser cooling and trapping of neutral atoms, *Rev. Mod. Phys.* **70**, 721 (1998).
- [224] A. S. Parkins and D. F. Walls, The physics of trapped dilute-gas Bose-Einstein condensates, *Phys. Rep.* **303**, 1 (1998).
- [225] Y. Castin, Bose-Einstein condensates in atomic gases: Simple theoretical results, in R. Kaiser, C. Westbrook, and F. David, eds., *Coherent atomic matter waves*, Lecture Notes of Les Houches Summer School, 1, Springer (2001).
- [226] P. W. Courteille, V. S. Bagnato, and V. I. Yukalov, Bose-Einstein condensation of trapped atomic gases, *Las. Phys.* **11**, 659 (2001).
- [227] L. P. Pitaevskii and S. Stringari, *Bose-Einstein Condensation*, Clarendon

- Press (2003).
- [228] H. Stoof, K. Gubbels, and D. Dickerscheid, *Ultracold quantum fields*, Springer, Dordrecht (2009).
- [229] J. Weiner, V. S. Bagnato, S. Zilio, and P. S. Julienne, Experiments and theory in cold and ultracold collisions, *Rev. Mod. Phys.* **71**, 1 (1999).
- [230] W. Ketterle and N. J. van Druten, Evaporative cooling of trapped atoms, *Adv. At. Mol. Opt. Phys.* **37**, 181 (1996).
- [231] P. Courteille, R. S. Freeland, D. J. Heinzen, F. A. van Abeelen, and B. J. Verhaar, Observation of a Feshbach resonance in cold atom scattering, *Phys. Rev. Lett.* **81**, 69 (1998).
- [232] S. Inouye, M. R. Andrews, J. Stenger, H.-J. Miesner, D. M. Stamper-Kurn, and W. Ketterle, Observation of Feshbach resonances in a Bose-Einstein condensate, *Nature* **392**, 151 (1998).
- [233] P. F. Bedaque, E. Braaten, and H.-W. Hammer, Three-body recombination in Bose gases with large scattering length, *Phys. Rev. Lett.* **85**, 908 (2000).
- [234] T. Weber, J. Herbig, M. Mark, H.-C. Nägerl, and R. Grimm, Three-body recombination at large scattering lengths in an ultracold atomic gas, *Phys. Rev. Lett.* **91**, 123201 (2003).
- [235] P. Kapitza, Viscosity of liquid helium below the λ -point, *Nature* **141**, 74 (1938).
- [236] J. F. Allen and A. D. Misener, Flow of liquid helium II, *Nature* **141**, 75 (1938).
- [237] F. London, On the Bose-Einstein condensation, *Phys. Rev.* **54**, 947 (1938).
- [238] F. London, The λ -phenomenon of liquid helium and the Bose-Einstein degeneracy, *Nature* **141**, 643 (1938).
- [239] L. Landau, Theory of the superfluidity of helium II, *Phys. Rev.* **60**, 356 (1941).
- [240] P. C. Hohenberg and P. C. Martin, Microscopic theory of superfluid helium, *Ann. Phys.* **34**, 291 (1965).
- [241] W. Mullin, Bose-Einstein condensation in a harmonic potential, *J. Low Temp. Phys.* **106**, 615 (1997).
- [242] Z. Hadzibabic, P. Krüger, M. Cheneau, B. Battelier, and J. Dalibard, Berezinskii–Kosterlitz–Thouless crossover in a trapped atomic gas, *Nature* **441**, 1118 (2006).
- [243] T. P. Simula and P. B. Blakie, Thermal activation of vortex-antivortex pairs in quasi-two-dimensional Bose-Einstein condensates, *Phys. Rev. Lett.* **96**, 020404 (2006).

-
- [244] V. Schweikhard, S. Tung, and E. A. Cornell, Vortex proliferation in the Berezinskii–Kosterlitz–Thouless regime on a two-dimensional lattice of Bose-Einstein condensates, *Phys. Rev. Lett.* **99**, 30401 (2007).
- [245] L. Giorgetti, I. Carusotto, and Y. Castin, Semiclassical field method for the equilibrium Bose gas and application to thermal vortices in two dimensions, *Phys. Rev. A* **76**, 013613 (2007).
- [246] S. Floerchinger and C. Wetterich, Superfluid Bose gas in two dimensions, *Phys. Rev. A* **79**, 013601 (2009).
- [247] J. Armijo, T. Jacqmin, K. Kheruntsyan, and I. Bouchoule, Mapping out the quasi-condensate transition through the 1d-3d dimensional crossover, *Mol. Opt. Phys.* **83**, 021605 (2011).
- [248] I. Bouchoule, N. J. van Druten, and C. I. Westbrook, Atom chips and one-dimensional Bose gases, in *Atom Chips*, 331, Wiley-VCH (2011).
- [249] J. Berges, Introduction to nonequilibrium quantum field theory, *AIP Conf. Proc.* **739**, 3 (2005).
- [250] J. Berges and J. Serreau, Parametric resonance in quantum field theory, *Phys. Rev. Lett.* **91**, 111601 (2003).
- [251] A. Arrizabalaga, J. Smit, and A. Tranberg, Tachyonic preheating using 2PI - 1/N dynamics and the classical approximation, *JHEP* **10**, 017 (2004).
- [252] J. Berges, S. Borsanyi, and J. Serreau, Thermalization of fermionic quantum fields, *Nucl. Phys.* **B660**, 51 (2003).
- [253] J. Berges, n-PI effective action techniques for gauge theories, *Phys. Rev. D* **70**, 105010 (2004).
- [254] G. Aarts and J. M. Martinez Resco, Transport coefficients from the 2PI effective action: Weak coupling and large N analysis, *J. Phys. Conf. Ser.* **35**, 414 (2006).
- [255] T. Gasenzer, J. Berges, M. G. Schmidt, and M. Seco, Non-perturbative dynamical many-body theory of a Bose-Einstein condensate, *Phys. Rev. A* **72**, 063604 (2005).
- [256] A. M. Rey, B. L. Hu, E. Calzetta, and C. W. Clark, Quantum kinetic theory of a Bose-Einstein gas confined in a lattice, *Phys. Rev. A* **72**, 023604 (2005).
- [257] J. Berges and T. Gasenzer, Quantum versus classical statistical dynamics of an ultracold Bose gas, *Phys. Rev. A* **76**, 033604 (2007).
- [258] A. Branschädel and T. Gasenzer, 2PI nonequilibrium versus transport equations for an ultracold Bose gas, *J. Phys. B* **41**, 135302 (2008).
- [259] T. Gasenzer and J. M. Pawłowski, Towards far-from-equilibrium quantum field dynamics: A functional renormalisation-group approach, *Phys. Lett.*

- B670**, 135 (2008).
- [260] T. Gasenzer, S. Kessler, and J. M. Pawłowski, Far-from-equilibrium quantum many-body dynamics, *Eur. Phys. J. C* **70**, 423 (2010).
- [261] H. Carmichael, *Statistical Methods in Quantum Optics 1: Master Equations and Fokker-Planck Equations*, Springer Verlag, Berlin (1999).
- [262] E. H. Lieb and W. Liniger, Exact analysis of an interacting Bose gas. I. The general solution and the ground state, *Phys. Rev.* **130**, 1605 (1963).
- [263] M. Girardeau, Relationship between systems of impenetrable bosons and fermions in one dimension, *J. Math. Phys.* **1**, 516 (1960).
- [264] H. Buljan, R. Pezer, and T. Gasenzer, Fermi-Bose transformation for the time-dependent Lieb-Liniger gas, *Phys. Rev. Lett.* **100**, 080406 (2008).
- [265] D. Jukić, R. Pezer, T. Gasenzer, and H. Buljan, Free expansion of a Lieb-Liniger gas: Asymptotic form of the wave functions, *Phys. Rev. A* **78**, 053602 (2008).
- [266] D. S. Petrov, M. Holzmann, and G. V. Shlyapnikov, Bose-Einstein condensation in quasi-2D trapped gases, *Phys. Rev. Lett.* **84**, 2551 (2000).
- [267] M. Olshanii, Atomic scattering in the presence of an external confinement and a gas of impenetrable bosons, *Phys. Rev. Lett.* **81**, 938 (1998).
- [268] J. D. Jackson, *Classical Electrodynamics*, Wiley (1998).
- [269] M. Brewczyk, M. Gajda, and K. Rzażewski, Classical fields approximation for bosons at nonzero temperatures, *J. Phys. B: At. Mol. Opt. Phys.* **40**, R1 (2007).
- [270] E. Gross, Classical theory of boson wave fields, *Ann. Phys.* **4**, 57 (1958).
- [271] L. P. Pitaevskii, Vortex lines in an imperfect Bose gas, [*Zh. Eksp. Teor. Fiz.* **40**, 646 (1961)] *Sov. Phys. JETP* **13**, 451 (1961).
- [272] M. J. Davis, S. A. Morgan, and K. Burnett, Simulations of Bose fields at finite temperature, *Phys. Rev. Lett.* **87**, 160402 (2001).
- [273] I. Carusotto and Y. Castin, An exact stochastic field method for the interacting Bose gas at thermal equilibrium, *J. Phys. B: At. Mol. Opt. Phys.* **34**, 4589 (2001).
- [274] N. Proukakis and B. Jackson, Finite-temperature models of Bose-Einstein condensation, *J. Phys. B: At., Mol. Opt. Phys.* **41**, 203002 (2008).
- [275] M. J. Steel, M. K. Olsen, L. I. Plimak, P. D. Drummond, S. M. Tan, M. J. Collett, D. F. Walls, and R. Graham, Dynamical quantum noise in trapped Bose-Einstein condensates, *Phys. Rev. A* **58**, 4824 (1998).
- [276] A. Sinatra, C. Lobo, and Y. Castin, Classical-field method for time dependent

- Bose-Einstein condensed gases, Phys. Rev. Lett. **87**, 210404 (2001).
- [277] S. P. Cockburn, D. Gallucci, and N. P. Proukakis, Quantitative study of quasi-one-dimensional Bose gas experiments via the stochastic Gross–Pitaevskii equation, Phys. Rev. A **84**, 023613 (2011).
- [278] P. Bienias, K. Pawłowski, M. Gajda, and K. Rzążewski, Statistical properties of one-dimensional Bose gas, Phys. Rev. A **83**, 033610 (2011).
- [279] S. P. Cockburn, H. E. Nistazakis, T. P. Horikis, P. G. Kevrekidis, N. P. Proukakis, and D. J. Frantzeskakis, Matter-wave dark solitons: Stochastic versus analytical results, Phys. Rev. Lett. **104**, 174101 (2010).
- [280] V. E. Zakharov and A. B. Shabat, Exact theory of two-dimensional self-focusing and one-dimensional self-modulation of waves in nonlinear media, JETP **34**, 62 (1972).
- [281] J. Brand and W. P. Reinhardt, Solitonic vortices and the fundamental modes of the “snake instability”: Possibility of observation in the gaseous Bose-Einstein condensate, Phys. Rev. A **65**, 043612 (2002).
- [282] E. B. Sonin, Vortex oscillations and hydrodynamics of rotating superfluids, Rev. Mod. Phys. **59**, 87 (1987).
- [283] D. Kivotides, J. C. Vassilicos, D. C. Samuels, and C. F. Barenghi, Kelvin waves cascade in superfluid turbulence, Phys. Rev. Lett. **86**, 3080 (2001).
- [284] W. F. Vinen, M. Tsubota, and A. Mitani, Kelvin-wave cascade on a vortex in superfluid ^4He at a very low temperature, Phys. Rev. Lett. **91**, 135301 (2003).
- [285] G. Krstulovic, Kelvin-wave cascade and dissipation in low-temperature superfluids vortices, arXiv:1209.3210 [cond-mat.other] (2012).
- [286] M. Lesieur, *Turbulence in fluids*, volume 84, Springer, Dordrecht (2008).
- [287] G. F. Bonini and C. Wetterich, Time evolution of correlation functions and thermalization, Phys. Rev. D **60**, 105026 (1999).
- [288] G. Aarts, G. F. Bonini, and C. Wetterich, Exact and truncated dynamics in nonequilibrium field theory, Phys. Rev. D **63**, 025012 (2000).
- [289] P. Davidson, Y. Kaneda, K. Moffatt, and K. Sreenivasan, *A voyage through turbulence*, CUP, Cambridge, UK (2011).
- [290] S. Z. Alamri, A. J. Youd, and C. F. Barenghi, Reconnection of superfluid vortex bundles, Phys. Rev. Lett. **101**, 215302 (2008).
- [291] A. W. Baggaley, The importance of vortex bundles in quantum turbulence at absolute zero, Phys. Fl. **24**, 055109 (2012).
- [292] C. F. Barenghi, S. Hulton, and D. C. Samuels, Polarization of superfluid turbulence, Phys. Rev. Lett. **89**, 275301 (2002).

- [293] K. Morris, J. Koplik, and D. W. I. Rouson, Vortex locking in direct numerical simulations of quantum turbulence, *Phys. Rev. Lett.* **101**, 015301 (2008).
- [294] W. Ketterle, D. S. Durfee, and D. M. Stamper-Kurn, Making, probing and understanding Bose-Einstein condensates, in M. Inguscio, S. Stringari, and C. E. Wieman, eds., *Proceedings of the International School of Physics - Enrico Fermi*, 67, IOS Press, Amsterdam (1999).
- [295] V. Gurarie, Probability density, diagrammatic technique, and epsilon expansion in the theory of wave turbulence, *Nucl. Phys. B* **441**, 569 (1995).
- [296] V. Gurarie, Field theory and the phenomenon of turbulence, arXiv:9501021 [hep-th] (1995).
- [297] J. M. Luttinger and J. C. Ward, Ground-state energy of a many-fermion system. II, *Phys. Rev.* **118**, 1417 (1960).
- [298] G. Baym, Self-consistent approximations in many-body systems, *Phys. Rev.* **127**, 1391 (1962).
- [299] J. M. Cornwall, R. Jackiw, and E. Tomboulis, Effective action for composite operators, *Phys. Rev. D* **10**, 2428 (1974).
- [300] C. Bodet, M. Kronenwett, B. Nowak, D. Sexty, and T. Gasenzer, Non-equilibrium Quantum Many-Body Dynamics: Functional Integral Approaches, in N. Proukakis, S. Gardiner, M. Davis, and M. Szymanska, eds., *Proc. Int. Workshop FINESSE 2009, Durham, UK*, Quantum Gases: Finite Temperature and Non-Equilibrium Dynamics (Vol. 1 Cold Atoms Series), Imperial College Press, London (in press) (2012).
- [301] C. Wetterich, Exact evolution equation for the effective potential, *Phys. Lett.* **B301**, 90 (1993).
- [302] J. Berges, N. Tetradis, and C. Wetterich, Non-perturbative renormalization flow in quantum field theory and statistical physics, *Phys. Rept.* **363**, 223 (2002).
- [303] H. Gies, Introduction to the functional RG and applications to gauge theories (2006).
- [304] J. M. Pawłowski, Aspects of the functional renormalisation group, *Ann. Phys.* **322**, 2831 (2007).
- [305] J. Zanella and E. Calzetta, Renormalization group study of damping in nonequilibrium field theory, arXiv:061122[hep-th] (2006).
- [306] H. Schoeller, A perturbative nonequilibrium renormalization group method for dissipative quantum mechanics. Real-time RG in frequency space, *Eur. Phys. J. ST* **168**, 179 (2009).
- [307] L. Canet, H. Chaté, B. Delamotte, and N. Wschebor, Nonperturbative renor-

- malization group for the Kardar-Parisi-Zhang equation, *Phys. Rev. Lett.* **104**, 150601 (2010).
- [308] W. L. Bragg, The diffraction of short electromagnetic waves by a crystal, *Proc. Cambridge Philos. Soc.* **17**, 43 (1912).
- [309] P. J. Martin, B. G. Oldaker, A. H. Miklich, and D. E. Pritchard, Bragg scattering of atoms from a standing light wave, *Phys. Rev. Lett.* **60**, 515 (1988).
- [310] S. Kunze, S. Dürr, and G. Rempe, Bragg scattering of slow atoms from a standing light wave, *Europhys. Lett.* **34**, 343 (1996).
- [311] See: <http://www.thphys.uni-heidelberg.de/~smp/gasenzler/videos/boseqt.html>.
- [312] A. White, C. Barenghi, N. Proukakis, A. Youd, and D. Wacks, Nonclassical velocity statistics in a turbulent atomic Bose-Einstein condensate, *Phys. Rev. Lett.* **104**, 75301 (2010).
- [313] M. S. Paoletti, M. E. Fisher, K. R. Sreenivasan, and D. P. Lathrop, Velocity statistics distinguish quantum turbulence from classical turbulence, *Phys. Rev. Lett.* **101**, 154501 (2008).
- [314] G. Eyink and K. Sreenivasan, Onsager and the theory of hydrodynamic turbulence, *Rev. Mod. Phys.* **78**, 87 (2006).
- [315] P. Chavanis, *Statistical mechanics of two-dimensional vortices and stellar systems*, Springer, Berlin (2002).
- [316] A. S. Bradley and B. P. Anderson, Energy spectra of vortex distributions in two-dimensional quantum turbulence, arXiv:1204.1103 [cond-mat.quant-gas] (2012).
- [317] S. Nemirovskii, Gaussian model of vortex tangle in He II, *Phys. Rev. B* **57**, 5972 (1998).
- [318] S. Nemirovskii, M. Tsubota, and T. Araki, Energy spectrum of the random velocity field induced by a gaussian vortex tangle in He II, *J. Low Temp. Phys.* **126**, 1535 (2002).
- [319] A. Chorin and J. Akao, Vortex equilibria in turbulence theory and quantum analogues, *Phys. D: Nonlin. Phen.* **52**, 403 (1991).
- [320] V. Berdichevsky, On statistical mechanics of vortex lines, *Int. J. Eng. Sci.* **40**, 123 (2002).
- [321] J. B. Weiss, A. Provenzale, and J. C. McWilliams, Lagrangian dynamics in high-dimensional point-vortex systems, *Phys. Fl.* **10**, 1929 (1998).
- [322] I. A. Min, I. Mezic, and A. Leonard, Lévy stable distributions for velocity and velocity difference in systems of vortex elements, *Phys. Fl.* **8**, 1169 (1996).

- [323] P.-H. Chavanis and C. Sire, The spatial correlations in the velocities arising from a random distribution of point vortices, *Phys. Fl.* **13**, 1904 (2001).
- [324] R. Numasato, M. Tsubota, and V. L'vov, Direct energy cascade in two-dimensional compressible quantum turbulence, *Phys. Rev. A* **81**, 063630 (2010).
- [325] S. Khlebnikov, Strong acoustic turbulence and the speed of Bose-Einstein condensation, *Phys. Rev. A* **66**, 063606 (2002).
- [326] S. Dyachenko, A. C. Newell, A. Pushkarev, and V. E. Zakharov, Optical turbulence: weak turbulence, condensates and collapsing filaments in the non-linear Schrödinger equation, *Phys. D: Nonlin. Phen.* **57**, 96 (1992).
- [327] K. E. Daniels and E. Bodenschatz, Statistics of defect motion in spatiotemporal chaos in inclined layer convection, *Chaos* **13**, 55 (2003).
- [328] D. Proment, S. Nazarenko, and M. Onorato, Sustained turbulence in the three-dimensional Gross–Pitaevskii model, *Phys. D: Nonlin. Phen.* (2011).
- [329] M. Leadbeater, T. Winiecki, D. Samuels, C. Barenghi, and C. Adams, Sound emission due to superfluid vortex reconnections, *Phys. Rev. Lett.* **86**, 1410 (2001).
- [330] H. Aref, Integrable, chaotic, and turbulent vortex motion in two-dimensional flows, *Ann. Rev. Fl. Mech.* **15**, 345 (1983).
- [331] G. F. Carnevale, J. C. McWilliams, Y. Pomeau, J. B. Weiss, and W. R. Young, Evolution of vortex statistics in two-dimensional turbulence, *Phys. Rev. Lett.* **66**, 2735 (1991).
- [332] J. B. Weiss and J. C. McWilliams, Temporal scaling behavior of decaying two-dimensional turbulence, *Phys. Fluids A* **3**, 608 (1993).
- [333] A. Bracco, J. C. McWilliams, G. Murante, A. Provenzale, and J. B. Weiss, Revisiting freely decaying two-dimensional turbulence at millennial resolution, *Phys. Fl.* **12**, 2931 (2000).
- [334] P. Tabeling, S. Burkhart, O. Cardoso, and H. Willaime, Experimental study of freely decaying two-dimensional turbulence, *Phys. Rev. Lett.* **67**, 3772 (1991).
- [335] R. Benzi, M. Colella, M. Briscolini, and P. Santangelo, A simple point vortex model for two-dimensional decaying turbulence, *Phys. Fluids A* **4**, 1036 (1992).
- [336] C. Sire, P.-H. Chavanis, and J. Sopik, Effective merging dynamics of two and three fluid vortices: Application to two-dimensional decaying turbulence, *Phys. Rev. E* **84**, 056317 (2011).
- [337] C. Sire and P.-H. Chavanis, Numerical renormalization group of vortex aggregation in two-dimensional decaying turbulence: The role of three-body

- interactions, *Phys. Rev. E* **61**, 6644 (2000).
- [338] V. Yakhot and J. Wanderer, Crossover in the enstrophy decay in two-dimensional turbulence in a finite box, *Phys. Rev. Lett.* **93**, 154502 (2004).
- [339] H.-C. Chu and G. A. Williams, Quenched Kosterlitz–Thouless superfluid transitions, *Phys. Rev. Lett.* **86**, 2585 (2001).
- [340] S. Nazarenko and M. Onorato, Freely decaying turbulence and Bose–Einstein condensation in Gross–Pitaevskii model, *J. Low Temp. Phys.* **146**, 31 (2007).
- [341] V. Ambegaokar, B. I. Halperin, D. R. Nelson, and E. D. Siggia, Dynamics of superfluid films, *Phys. Rev. B* **21**, 1806 (1980).
- [342] A. J. Bray, Theory of phase-ordering kinetics, *Adv. Phys.* **43**, 357 (1994).
- [343] B. Kramer and A. MacKinnon, Localization: theory and experiment, *Rep. Progr. Phys.* **56**, 1469 (1993).
- [344] L. Mathey and A. Polkovnikov, Supercritical superfluid and vortex unbinding following a quantum quench, *Phys. Rev. A* **80**, 041601 (2009).
- [345] L. Canet and H. Chate, Non-perturbative approach to critical dynamics, *J. Phys. A* **40**, 1937 (2007).
- [346] G. Volovik, On developed superfluid turbulence, *J. Low Temp. Phys.* **136**, 309 (2004).
- [347] D. E. Pritchard, K. Helmerson, and A. Martin, Atom traps, in S. Haroche, J. C. Gay, and G. Grynberg, eds., *Atomic Physics XI*, Proceedings of the Eleventh International Conference on Atomic Physics, 4-8 July 1988, Paris, France, 179, World Scientific (1989).
- [348] T. W. Hijmans, O. J. Luiten, I. D. Setija, and J. T. M. Walraven, Optical cooling of atomic hydrogen in a magnetic trap, *J. Opt. Soc. Am. B* **6**, 2235 (1989).
- [349] E. Witkowska, P. Deuar, M. Gajda, and K. Rzażewski, Solitons as the early stage of quasicondensate formation during evaporative cooling, *Phys. Rev. Lett.* **106**, 135301 (2011).
- [350] S. Hofferberth, I. Lesanovsky, B. Fischer, T. Schumm, and J. Schmiedmayer, Non-equilibrium coherence dynamics in one-dimensional Bose gases, *Nature* **449**, 324 (2007).
- [351] T. Kitagawa, A. Imambekov, J. Schmiedmayer, and E. Demler, The dynamics and prethermalization of one-dimensional quantum systems probed through the full distributions of quantum noise, *New Journal of Physics* **13**, 073018 (2011).
- [352] M. R. Andrews, C. G. Townsend, H.-J. Miesner, D. S. Durfee, D. M. Kurn, and W. Ketterle, Observation of interference between two Bose condensates,

- Science **275**, 637 (1997).
- [353] T. Kibble, Topology of cosmic domains and strings, *J. Phys. A: Math. Gen.* **9**, 1387 (1976).
- [354] R. Allahverdi, R. Brandenberger, F.-Y. Cyr-Racine, and A. Mazumdar, Reheating in Inflationary Cosmology: Theory and Applications, *Ann. Rev. Nucl. Part. Sci.* **60**, 27 (2010).
- [355] L. Kofman, A. D. Linde, and A. A. Starobinsky, Reheating after inflation, *Phys. Rev. Lett.* **73**, 3195 (1994).
- [356] J. H. Traschen and R. H. Brandenberger, Particle production during out-of-equilibrium phase transitions, *Phys. Rev. D* **42**, 2491 (1990).
- [357] S. Y. Khlebnikov and I. I. Tkachev, Classical decay of inflaton, *Phys. Rev. Lett.* **77**, 219 (1996).
- [358] T. Prokopec and T. G. Roos, Lattice study of classical inflaton decay, *Phys. Rev. D* **55**, 3768 (1997).
- [359] I. Tkachev, S. Khlebnikov, L. Kofman, and A. D. Linde, Cosmic strings from preheating, *Phys. Lett.* **B440**, 262 (1998).
- [360] For videos see: <http://www.thphys.uni-heidelberg.de/~sixty/videos>.
- [361] C. J. Myatt, E. A. Burt, R. W. Ghrist, E. A. Cornell, and C. E. Wieman, Production of two overlapping Bose-Einstein condensates by sympathetic cooling, *Phys. Rev. Lett.* **78**, 586 (1997).
- [362] D. S. Hall, M. R. Matthews, C. E. Wieman, and E. A. Cornell, Measurements of relative phase in two-component Bose-Einstein condensates, *Phys. Rev. Lett.* **81**, 1543 (1998).
- [363] C. Lee, Universality and anomalous mean-field breakdown of symmetry-breaking transitions in a coupled two-component Bose-Einstein condensate, *Phys. Rev. Lett.* **102**, 070401 (2009).
- [364] K. Kasamatsu, M. Tsubota, and M. Ueda, Spin textures in rotating two-component Bose-Einstein condensates, *Phys. Rev. A* **71**, 043611 (2005).
- [365] H. Takeuchi, S. Ishino, and M. Tsubota, Binary quantum turbulence arising from countersuperflow instability in two-component Bose-Einstein condensates, *Phys. Rev. Lett.* **105**, 205301 (2010).
- [366] S. Ishino, M. Tsubota, and H. Takeuchi, Countersuperflow instability in miscible two-component Bose-Einstein condensates, *Phys. Rev. A* **83**, 063602 (2011).
- [367] C. Hamner, J. J. Chang, P. Engels, and M. A. Hoefer, Generation of dark-bright soliton trains in superfluid-superfluid counterflow, *Phys. Rev. Lett.* **106**, 065302 (2011).

-
- [368] J. Stenger, S. Inouye, D. Stamper-Kurn, H. Miesner, A. Chikkatur, and W. Ketterle, Spin domains in ground-state Bose-Einstein condensates, *Nature* **396**, 345 (1998).
- [369] H.-J. Miesner, D. M. Stamper-Kurn, J. Stenger, S. Inouye, A. P. Chikkatur, and W. Ketterle, Observation of metastable states in spinor Bose-Einstein condensates, *Phys. Rev. Lett.* **82**, 2228 (1999).
- [370] M. Ueda, Bose gases with nonzero spin, *Ann. Rev. Cond. Mat. Phys.* **3**, 263 (2012).
- [371] M. Vengalattore, S. R. Leslie, J. Guzman, and D. M. Stamper-Kurn, Spontaneously modulated spin textures in a dipolar spinor Bose-Einstein condensate, *Phys. Rev. Lett.* **100**, 170403 (2008).
- [372] K. Fujimoto and M. Tsubota, Spin turbulence in a trapped spin-1 spinor Bose-Einstein condensate, *Phys. Rev. A* **85**, 053641 (2012).
- [373] J. Berges, S. Schlichting, and D. Sexty, Overpopulated gauge fields on the lattice, *Phys. Rev. D* **86**, 074006 (2012).
- [374] A. Weller, *Dynamics and interaction of dark solitons in Bose-Einstein condensates*, Ph.D. thesis, Rupprechts-Karls-Universität Heidelberg (2009).
- [375] W. Vinen and J. Niemela, Quantum turbulence, *J. Low Temp. Phys.* **128**, 167 (2002).
- [376] A. Rajantie, Formation of topological defects in gauge field theories, *Int. J. Mod. Phys. A* **17**, 1 (2002).
- [377] A. Rajantie, Introduction to magnetic monopoles, *Cont. Phys.* **53**, 195 (2012).
- [378] C. Castelnovo, R. Moessner, and S. Sondhi, Magnetic monopoles in spin ice, *Nature* **451**, 42 (2008).
- [379] J. Ruostekoski and J. R. Anglin, Creating vortex rings and three-dimensional skyrmions in Bose-Einstein condensates, *Phys. Rev. Lett.* **86**, 3934 (2001).
- [380] I. Dierking, *Textures of liquid crystals*, Wiley-VCH (2003).
- [381] A. Rajantie, Defect formation in the early universe, *Cont. Phys.* **44**, 485 (2003).
- [382] M. Caracanhas, A. Fetter, S. Muniz, K. Magalhães, G. Roati, G. Bagnato, and V. Bagnato, Self-similar expansion of the density profile in a turbulent Bose-Einstein condensate, *J. Low Temp. Phys.* **166**, 49 (2012).
- [383] P. Weckesser, *Expansion turbulenter Bose-Einstein-Kondensate*, Master's thesis, Universität Heidelberg (2012).
- [384] J. Fleck, J. Morris, and M. Feit, Time-dependent propagation of high energy laser beams through the atmosphere, *Appl. Phys. A* **10**, 129 (1976).

